2015

Synthesis, Surface Functionalization, and Biological Testing of Iron Oxide Nanoparticles for Development as a Cancer Therapeutic

Stanley E. Gilliland III
Virginia Commonwealth University

Synthesis, Surface Functionalization, and Biological Testing of Iron Oxide Nanoparticles for Development as a Cancer Therapeutic

A Dissertation submitted in partial fulfillment of the requirements for the degree of Doctor of Philosophy at Virginia Commonwealth University.

By
Stanley Eugene Gilliland III
Bachelor of Science
James Madison University
December 2015

Director: Dr. Everett E. Carpenter
Professor, Department of Chemistry
Co-Director: Dr. Michael D. Shultz
Research Biologist - McGuire VA Medical Center
& Adjunct Faculty, Department of Chemistry

Virginia Commonwealth University

Richmond, Virginia
December 2015

Acknowledgment

While working towards my PhD in Nanoscience and Nanotechnology I received exceptional support, help and advice from numerous people. First, I would like to thank my beautiful wife Ruthie and our daughter Emily for their unwavering support and affection. Ruthie has always given me confidence to achieve my goals. Our daughter Emily was born in May 2013 and has been a source of rejuvenation and laughter which has made the writing of this dissertation so much easier. I would also like to give thanks to my family that has always been encouraging and supportive in all of my life's endeavors.

I have received invaluable advising for the Nanoscience and Nanotechnology PhD program, research, and career advice from Dr. Carpenter. Dr. Shultz, my co-advisor, has always been optimistic about all aspects of the research and has given great advice and inspiration for the research project and for career and life decisions. My committee members and the VCU Chemistry Department all deserve my appreciation for allowing me the opportunity to study and research this interesting topic. My lab mates 'across town' have always been helpful in my research and teaching me new research techniques. I would like to specifically thank Zach Huba for teaching me so many techniques, Dustin Clifford for helping with TEM imaging, and Sarah Smith for running and analyzing XPS data and running so many TGA samples. Lastly, I would like to thank the VCU Nanomaterials Core Characterization Facility and Hunter Holmes McGuire VA Medical center, as none of this research would have been possible without access to these facilities.

Table of Contents

List of Tables

Chapter 2.

Chapter 3.

Chapter 4.

List of Figures

Chapter 1.

Chapter 2.

Chapter 3.

Chapter 4.

Chapter 5.

List of Abbreviations and Symbols

$\left(\frac{\Delta T}{\Delta t}\right)$ -	Initial linear temperature increase per unit time
$\langle \Gamma \rangle$-	average decay rate
$\frac{1}{\tau}$-	Effective relaxation time
a-	Radius
A-	Amperes
$\mathbf{A_H}$-	Hamacker constant
ABA-	γ-aminobutryic acid
AC-	Alternating Current
ANOVA-	Analysis of variance
APTS-	(3-Aminopropyl)trimethoxy silane
APTES-	(3-aminominopropyl)triethoxysilane
Arg-	DL-arginine
Asn-	L-(+)-asparagine
ATR-	Attenuated total reflectance
b-	Full Width Half Maximum (FWHM)
$\mathbf{c_{H2O}}$-	Specific heat capacity of water
$\mathbf{c_{np}}$-	Specific heat capacity of nanoparticles
CED-	Convection enhanced delivery
CM-	Complete cell medium
CMPVA-	Carboxymethylated polyvinyl alcohol
CSF-	Artificial cerebral spinal fluid
CVD-	Chemical Vapor Deposition
Cys-	L-cysteine
$\mathbf{D_b}$-	Einstein's Brownian diffusion coefficient
$\mathbf{D_f}$-	Diffusion coefficient
$\mathbf{d_{hkl}}$-	distance between atomic planes of lattice
$\mathbf{D_p}$-	Particle Size
$\mathbf{d_p}$-	Depth of penetration
DLS-	Dynamic Light Scattering
DLVO-	Derjaguin, Landua, Verwey, and Overbeek
DMEM-	Eagle's minimal essential medium
DOTA-	S-2-(4-Aminobenzyl)-1,4,7,10-tetraazacyclododecane tetraacetic acid
DPBS-	Dulbecco's phosphate buffered saline
$\mathbf{E_A}$-	Energy Barrier
$\left(\frac{\mathbf{E_A}}{k_B \mathbf{T}}\right)$-	Exponential term
EDA-	Ethylenediamine
EDC-	1-Ethyl-3-(3-dimethylaminopropyl)carbodiimide

EPR-	Enhanced Permeation and Retention
EtOH-	Ethanol
eV-	Electronvolt
f-	frequency
FBS-	Fetal bovine serum
FCC-	Face Centered Cubic
$Fe(acac)_3$-	Iron (III) acetylacetonate
$FeCl_2$-	Iron (II) Chloride
Fe_3O_4-	Magnetite
FeOx-	Iron Oxide
FTIR-	Fourier transform infrared
g-	Gram
Gly-	Glycine
GLYMO-	(3-Glycidyloxypropyl)trimethoxysilane
Gln-	L-glutamine
H-	Magnetic field strength
H_C-	Coercivity
HCl-	Hydrochloric acid
HPLC-	High-performance liquid chromatography
HS-	Human serum
HSD-	Honest significant difference
I-	Current
IACUC-	Institutional Animal Care and Use Committee
IC_{50}-	Half maximal inhibitory concentration
ICP-	Inductively coupled plasma
ILP-	Intrinsic Loss of Power
IRE-	Internal reflectance element
K-	Magnetocrystalline anisotropy constant
K-	Shape factor
K_B-	Boltzmann constant
k_BT-	Thermal energy
L-	Length of a coil
Lys-	DL-lysine monohydrochloride
M-	Magnetization
m_{H2O}-	Mass of water
m_{np}-	Mass of nanoparticles
M_R-	Remnant Magnetization
M_S-	Magnetization Saturation
MCL_{hkl}-	Coherently scattering domain that is perpendicular to the hkl plane
MES-	2-(*N*-morpholino)ethanesulfonic acid
MFH-	Magnetic Fluid Hyperthermia
MRI-	Magnetic Resonance Imaging
MWCO-	Molecular weight cutoff
n-	Integer
N-	Number of turns in a coil
n-	Refractive index

N_2-	Nitrogen
$NaHCO_3$-	Sodium bicarbonate
nm-	Nanometer
NaCl-	Sodium Chloride
NaOH-	Sodium Hydroxide
O-	Oxygen
OH-	Hydroxide
PBS-	Phosphate buffered saline
PDI-	Polydispersity index
PVA-	Polyvinyl alcohol
q-	Magnitude of scattering wave
R_H-	Hydrodynamic radius
r-	Distance between particles, center-to-center
$\frac{r}{a}$-	**E**quilibrium separation distance
RF-	Radiofrequency
S-NHS-	N-hydroxysulfosuccinimide
SAHBA-	(S)-(-)-4-Amino-2-hydroxybutyric acid
SAR-	Specific Absorption Rate
Ser-	DL-serine
Δt-	Change in time
T-	Temperature
T_B-	Brownian relaxation time
T_M-	Morin Temperature
T_N-	Néel relaxation time
T_N-	Néel Temperature
TEM-	Transmission Electron Microscopy
TEPA-	Tetraethylenepentamine
TGA-	Thermogravimetric analysis
Thr-	DL-threonine
TMAOH-	Tetramethylammonium hydroxide
V_C-	Volume of the core particle
V_H-	Hydrodynamic Volume
VSM-	Vibrating Sample Magnetometery
W-	Watt
X-	Magnetic Susceptibility
Δx-	Extent of three dimensional Brownian motion displacement
XRD-	X-ray Diffraction
γ-Fe_2O_3-	Maghemite
ε-	Permittivity
ε_0-	Permittivity of free space
ε_r-	Relative permittivity
ζ-	Zeta potential
η-	Viscosity
κ-	Debye Hückel parameter
$\frac{1}{\kappa}$	Double layer thickness
θ-	Incident Angle

θ_{DLS}-	Range of scattering angle
λ-	Wavelength
μ-	Solution viscosity
μ_2-	Variance of the decay rate distribution
μ_B-	Bohr magneton
μL-	Microliter
μ_o-	Permeability of free space
$\tau_o E_A$-	Pre-exponential factor
ψ_A-	Van der Waal attractive forces
ψ_R-	Van der Waal repulsive forces
ψ_{TOT}-	Total interparticle potential

Abstract

SYNTHESIS, SURFACE FUNCTIONALIZATION, AND BIOLOGICAL TESTING OF IRON OXIDE NANOPARTICLES FOR DEVELOPMENT AS A CANCER THERAPEUTIC

By Stanley Eugene Gilliland III, B.S., M.S.

A dissertation submitted in partial fulfillment of the requirements for the degree of Doctor of Philosophy at Virginia Commonwealth University.

Virginia Commonwealth University, 2015.

Major Director: Dr. Everett E. Carpenter, Professor,
Director of the Nanoscience and Nanotechnology Program,
Director of the NCC
Department of Chemistry
Research Director: Dr. Everett E. Carpenter
Professor, Department of Chemistry
Research Co-Director: Dr. Michael D. Shultz
Research Biologist - McGuire VA Medical Center
& Adjunct Faculty, Department of Chemistry

Iron oxide nanoparticles are highly researched for their use in biomedical applications such as drug delivery, diagnosis, and therapy. The inherent biodegradable and biocompatible nanoparticle properties make them highly advantageous in nanomedicine. The magnetic properties of iron oxide nanoparticles make them promising candidates for magnetic fluid hyperthermia applications. Designing an efficient iron oxide nanoparticle for hyperthermia

requires synthetic, surface functionalization, stability, and biological investigations. This research focused on the following three areas: optimizing synthesis conditions for maximum radiofrequency induced magnetic hyperthermia, designing a simple and modifiable surface functionalization method for specific or broad biological stability, and *in vitro* and *in vivo* testing of surface functionalized iron oxide nanoparticles in delivering effective hyperthermia or radiotherapy.

The benzyl alcohol modified seed growth method of synthesizing iron oxide nanoparticles using iron acetylacetonate as an iron precursor was investigated to identify significant nanoparticle properties that effect radiofrequency induced magnetic hyperthermia. Investigation of this synthesis under atmospheric conditions revealed a combination of thermal decomposition and oxidation-reduction mechanisms that can produce nanoparticles with larger crystallite sizes and decreased size distributions.

Nanoparticles were easily surface functionalized with (3-Glycidyloxypropyl) trimethoxysilane (GLYMO) without the need for organic-aqueous phase transfer methods. The epoxy ring on GLYMO facilitated post-modifications via a base catalyzed epoxy ring opening to obtain nanoparticles with different terminal groups. Glycine, serine, γ-aminobutryic acid (ABA), (S)-(-)-4-amino-2-hydroxybutyric acid (SAHBA), ethylenediamine, and tetraethylenepentamine were successful in modifying GLYMO coated-iron oxide nanoparticles to provide colloidal and varying biological stability while also allowing for further conjugation of chemotherapeutics or radiotherapeutics. The colloidal stability of cationic and anionic nanoparticles in several biologically relevant media was studied to address claims of increased cellular uptake for cationic nanoparticles.

The surface functionalized iron oxide nanoparticles were investigated to determine effects on cellular uptake and viability. *In vitro* tests were used to confirm the ability of iron oxide nanoparticles to provide effective hyperthermia treatment. S-2-(4-Aminobenzyl)-1,4,7,10-tetraazacyclododecane tetraacetic acid (DOTA) was coupled to SAHBA and carboxymethylated polyvinyl alcohol surface functionalized iron oxide nanoparticles and radiolabeled with ^{177}Lu. The capability of radiolabeled iron oxide nanoparticles for delivering radiation therapy to a U87MG murine orthotopic xenograft model of glioblastoma was initially investigated.

Chapter 1: Introduction and Background

1.1 Radiofrequency Induced Hyperthermia: Treatment of Cancer

The hyperthermia treatment of cancer with magnetic particles was first introduced by Gilchrist in 1957.[4] Hyperthermia can be subcategorized into three temperature ranges: mild hyperthermia, moderate hyperthermia, and thermoablation. Each of these has varying degrees of effects and can interact with different therapies.[5,6] Increasing the body temperature above 37°C to non-lethal ranges of 39-42°C is referred to as mild hyperthermia and can increase drug perfusion and oxygenation which can sensitize cells to radiotherapy or chemotherapy.[6-8] When the temperature is increased to moderate hyperthermia temperatures, 41-46°C, the heat stress will stimulates degradation of proteins, interferes with essential cell processes, and causes programed cell death or apoptosis.[9-11] Further increase of temperature above 45°C is termed thermoablation.[9,11-14] At these extreme temperatures cells will begin to die as a direct result of the temperature increase causing carbonization, coagulation and necrosis.[9,11-14] In terms of heat sensitivity there has been no reported evidence of a difference between normal and cancerous tissue.[15,16] However, due to the vasculature of cancerous tumors there are regions of low pH and hypoxia that sensitize tumors to hyperthermia at temperatures between 40-44°C.[15] These levels of hyperthermia can be achieved utilizing magnetic particles in an external radiofrequency (RF)

alternating current (AC) magnetic field. Heating is produced by eddy currents, hysteretic heating, and dielectric losses, but the material characteristics and properties such as conductivity, size, and magnetic properties determine the extent of heating for a given magnetic field strength and frequency.[4,5,17-20] Dielectric loss can damage tissue when high magnetic field strengths and frequencies are applied.[4] To maximize the amount of hysteretic heating of the particles and limit unwanted damage to normal tissues it has been suggested that the frequency be kept below 100 MHz as they have the required RF penetration with minimal RF absorption and are used in magnetic resonance imaging (MRI).[21] The magnetic field strength and frequency product (Hxf) of $5\times10^9 \frac{A}{ms}$ is considered the maximum threshold for safe heating of a human torso for 1 hour.[22] Above this threshold nonspecific and potentially detrimental eddy current heating can occur.[22] In the treatment of smaller tissues of a healthy patient and depending on the location of the tumor the H×f product can be surpassed in some cases.[22] Therefore, the goal of magnetic hyperthermia with particles has focused on maximizing achievable heating rates while minimizing the magnetic field strengths and/or frequencies required.[22] The RF coil used within this research was designed so that small solution volumes in microcentrifuge tubes or similar containers could be easily heated. Reports have indicated that there is a linear relationship between increased heating and H×f values, however these higher H×f values require the time of heating to be reduced to limit possible detrimental side effects or patient discomfort.[23]The RF heating values reported in this work were conducted under $1.01\text{x}10^{10} \frac{A}{ms}$ H×f values. This was deemed to be acceptable for *in vitro* and small animal *in vivo* studies.[24] Additionally, the heating times used were well below one hour.

1.2 Néel and Brownian Relaxation Mechanisms

Since Gilchrist's research there has been a significant change in magnetic particle based hyperthermia. Multi-domain particles have been replaced by the use of superparamagnetic nanomaterials. Nanoparticles small size lends them a tremendous advantage in navigating the complexities of biological systems. Superparamagnetic nanoparticles are beneficial because of their greater efficiency of absorbing the applied radiofrequency to generate heat.[5] The ability to generate more heat with lower required power reduces the nonspecific heating of normal tissue that may occur with prolonged treatment times.

Néel and Brownian relaxation mechanisms are responsible for producing heat in superparamagnetic nanoparticles exposed to a RF alternating current (AC) magnetic field. When an AC magnetic field is applied, the superparamagnetic nanoparticles will adjust the magnetic moment orientation to match the direction of the applied field. This reorientation results from either rapid alteration of magnetic moment directions within the crystal lattice (Néel mechanism) (**Figure 1.1 A**) or by the nanoparticle physically rotating to align the internal magnetic moments with the external magnetic field (Brownian mechanism) (**Figure 1.1 B**).[9,25,26] The Néel mechanism is also referred to as internal heating; as heat is first generated by internal friction between the crystal lattice and the rotating magnetic spins and is then lost as thermal energy to the surrounding medium.[25,26] More specifically, the Néel mechanism produces heat when the AC magnetic field provides a sufficient amount of energy for the dipole to overcome an energy barrier and alter directions.[25,27] The volume of the nanoparticle and the magnetocrystalline anisotropy are determining factors of the energy barrier.[25,27] **Equation 1a** shows the relationship between the magnetocrystalline anisotropy constant (K), volume of the core particle (V_c), and the

energy barrier (E_A). The Brownian mechanism generates and releases mechanical heat generated from friction

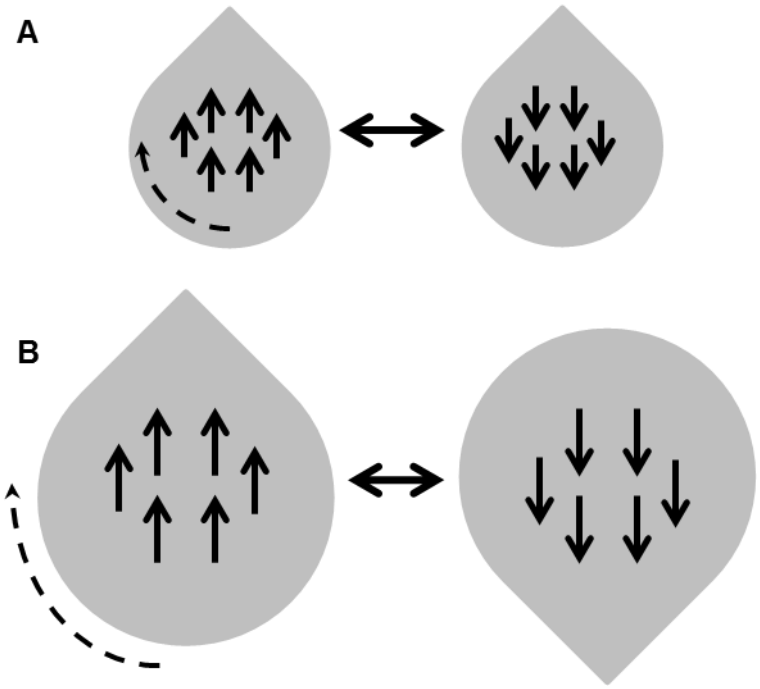

Figure 1.1. Illustration of (A) Néel and (B) Brownian mechanisms in response to an alternating current magnetic field. The dashed arrow represents either the internal magnetic spins (A) or the entire nanoparticle (B) rotating in response to a 180° magnetic field direction change.

between the rotating nanoparticle and solution.[25,26] The amount of friction is dependent upon the viscosity of the solution.[25,26] Heat is generated simultaneously by both mechanisms at all relevant superparamagnetic nanoparticle sizes.[17,18,25,28-31] Depending on the crystallite size of the nanoparticle one mechanism will have a faster relaxation time and is thus the dominate source of heating.[17,18,25,28-31] The effective relaxation time ($1/\tau$) (**Equation 1b**) is used to describe the combination of heating mechanisms. Néel heating is dominant at smaller nanoparticle sizes. For example, this heating mechanism dominates below 15-16 nanometers (nm) for iron oxide (FeOx) nanoparticles. In the equation for Néel relaxation time (τ_N)[28] (**Equation 1c)** it can be seen that

below 8 nm crystallite diameters the Néel relaxation time is dictated by the pre-exponential term ($\tau_o E_A$) and at crystallite diameters between 8 and 15-16 nm the relaxation time is dictated by the exponential term $\left(\frac{E_A}{k_B T}\right)$.[17,27,29,32,33] Above 15-16 nm crystallite diameters the Brownian relaxation time (τ_B)[28,34] (**Equation 1d**) is much faster than Néel relaxation time and becomes dominant.[17,29,32,33] The Brownian relaxation time depends on the medium viscosity (η), hydrodynamic volume of the particle (V_h), and inversely on temperature (T) and Boltzmann constant (k_B).

$$E_A = KV_c \tag{1a}$$

$$\frac{1}{\tau} = \frac{1}{\tau_N} + \frac{1}{\tau_B} \tag{1b}$$

$$\tau_N = \tau_o E_A \exp\left(\frac{E_A}{k_B T}\right) \tag{1c}$$

$$\tau_B = \frac{3\eta V_h}{k_B T} \tag{1d}$$

From **Equations 1a-d** it becomes apparent that the heating mechanisms are determined by nanoparticle size, crystal structure, polydispersity, shape, and magnetocrystalline anisotropy.[25,26] When a large size distribution is used (large polydispersity) heat will be generated by a varying degree of combined heating mechanisms and is typically unfavorable.[25]

The ability to quantifiable measure and compare the effectiveness of hyperthermia between nanoparticles is important. In 1993 Jordan et al. attempted this through the use of determining what they termed the specific absorption rate (SAR).[17] However, SAR values are often misunderstood or improperly determined and lead to improperly reporting the efficiency of magnetic nanoparticles.[23] The SAR equation (**Equation 2a**) has since been expanded to normalize SAR values depending on the magnetic field strength and frequency of the coil

used.[23,35] The new equation is referred to as effective SAR (**Equation 2b**) or intrinsic loss of power (ILP) (**Equation 2c**).[23,35,36]

$$SAR = \frac{c}{m_{np}}\left(\frac{\Delta T}{\Delta t}\right) \tag{2a}$$

$$Effective\ SAR = \frac{c_{H_2O}m_{H_2O}+c_{np}m_{np}}{m_{np}}\left(\frac{\Delta T}{\Delta t}\right)\left(\frac{1}{H^2_{applied}\times f}\right) \tag{2b}$$

$$ILP = \frac{SAR}{H^2_{applied}\times f} \tag{2c}$$

In **Equations 2a-c**, specific heat capacity of water and nanoparticles are denoted c_{H_2O} and c_{np} with units of $\left(\frac{\mathrm{W\times s}}{\mathrm{g\times K}}\right)$, mass of total nanoparticles and water are denoted m_{np} and m_{H_2O}, initial linear increase in temperature per unit time is denoted $\left(\frac{\Delta T}{\Delta t}\right)$ in units of $\left(\frac{\mathrm{K}}{\mathrm{s}}\right)$, magnetic field strength is H in units of $\left(\frac{\mathrm{A}}{\mathrm{m}}\right)$, and AC magnetic field frequency (f) in units of kHz.[29,31] From **Equations 1 and 2** it has been determined that to maximize energy absorption and thus produce the most efficient heating, the crystallite size and monodispersity must be controlled.[20,37]

Additional benefits of switching to nanoparticles include more uniform heating, decreased invasiveness, and reduced chances of causing adverse damage to surrounding normal tissue.[5] The superparamagnetism of these small nanoparticles are additionally useful as they lose their magnetism when the external magnetic field is removed.[38] This is essential in biological applications as magnetic aggregation of stable nanoparticles are less likely to occur which prolongs the blood circulation time.[38] The advent of nanomedicine has allowed for numerous new targeting strategies specifically for cancer cells to provide confined local heating while limiting invasiveness.[5,9,20,39,40] The extraordinary advantages of nanoparticle hyperthermia are responsible for the vast amount of recent literature and research being conducted on magnetic

hyperthermia treatment of cancer. Several issues that must be addressed for successful clinical implementation of magnetic nanoparticle hyperthermia include increasing ILP values, biological stability, blood circulation, and cellular uptake while minimizing immunogenicity and toxicity.[22,24,25,41] Maximizing ILP values is essential to lower the required amount of nanoparticles for effective heating. However, there is evidence that hyperthermia without detectable temperature increases can provide sufficient treatment of cancer.[25,42,43] This gives evidence to suggest that SAR and ILP values are often misleading and may not always indicate the best magnetic hyperthermia.[25] Biocompatible nanomaterials with biologically suitable surface modifications may offer the best chance of addressing the current challenges of transitioning more nanoparticle hyperthermia into clinical trials.

1.3 Iron Oxide Nanoparticles for Magnetic Hyperthermia: Ideal Properties and Challenges to Overcome

Nanomaterials have remained an important research area in nanomedicine. Biocompatible nanomaterials make excellent nanomedicine therapeutics, such as magnetic fluid hyperthermia. For example, FeOx is a biocompatible material with RF induction heating potential that allow for its application in magnetic fluid hyperthermia (MFH).[25,38,41,44] FeOx nanoparticles can be cleared from the body by opsonization or through degradation via the body's metabolism forming iron ions that are then used by erythrocytes to form hemoglobin.[45,46] Biocompatible FeOx nanoparticles can furthermore act as a theranositc agent[47-50] by providing therapy via magnetic fluid hyperthermia[41,51,52] and diagnosis in the form of magnetic resonance imaging.[51,53] FeOx nanoparticles are one of the only US FDA approved nanoparticles for their use as MRI contrast agents[54] of the liver and as iron supplements[55-57]. In Germany, aminosilane

functionalized superparamagnetic FeOx nanoparticles are already being investigated for glioblastoma and prostate cancer treatment with MFH at the clinical level.[39,52,58]

MFH research using FeOx nanoparticles has revealed that the optimal crystallite size is 15-16 nm with minimal size distribution.[29,59] Within this size range Néel relaxation is still dominant, but has a fast Brownian relaxation time as well which results in the best theoretical superparamagnetic heating.[13] Crystallite sizes above 16 nm that have dominant Brownian heating usually have less effective heat generation.[13] Hyperthermia is not a new medical procedure and can be delivered via thermoseeds, water bath, microwave, infrared or ultrasound radiation.[25,60] However, nanoparticle delivered MFH offers the ability to less invasively deliver effective MFH to smaller cancerous regions.[25,60] Nanoparticles offer a unique solution to the problem that some conventional drugs have with regards to being ineffective due to poor solubility or bioavailability.[61] Due to their small size nanoparticles can in some cases cross biological membrane barriers such as mucus membranes or the absorptive epithelium in the small intestine.[62,63] Additionally, surface modifiable nanoparticle can be used as a nanoplatform or a nanocarrier to deliver a surface conjugated drug or drugs to the target of interest by either passive or active uptake.[64,65] Active uptake can be facilitated by surface functionalized targeting ligands that can direct nanoparticles to overexpressed targets in cancerous tissues.[63,66] An additional benefit of FeOx nanoparticles is that they are inherently biodegradable. This means that once the drug has been delivered the nanoparticles can be easy cleared from the body or metabolized. Also, due to the size range of superparamagnetic nanoparticles they can be passively uptaken by cancerous tissue through the enhanced permeation and retention (EPR) effect.[25,67]

Research on nanomaterials for biological applications continues to suffer from a lack of broad stability and/or ease of surface functionalization, which impedes the advancement of many

synthesized nanoparticles into actual nanomedical applications. Moreover, the definition of stability is often misused or misleading when claiming a "stable" nanomaterial surface functionalization. True stability is very complex and can be defined in regards to colloidal, chemical, physical, pharmaceutical, and/or biological stability.[68] For efficient magnetic hyperthermia stability should be defined as a combination of the above listed stability terms. The colloidal stability can most simply be defined as having higher repulsive forces than attractive forces with respect to solid nanoparticles dispersed in an aqueous medium (colloid). The pharmaceutical stability refers to how long the solution is physically and chemically stable, and can effectively deliver a pharmaceutical dose. Chemical and physical stability refers to the protection against factors such as temperature, pH, humidity, etc. that may alter the nanoparticle composition or render the nanoparticle inert. With respect to biological stability this refers to overcoming attractive forces that may arise from immersion into different biological environments where counter ions, proteins, pH, and other molecules vary.

An alarming number of studies on nanoparticles rely on the assumption that a surface coating will provide the required colloidal stability to properly investigate certain parameters of interest. It should be noted that nanoparticles displaying colloidal stability upon synthesis or after surface functionalization may aggregate and precipitate in when introduced to different biologically relevant medium or biological environments. This can drastically alter or affect the results of biological testing and investigations. Therefore, it is vital to understand what constitutes a stable nanoparticle solution, the biological and chemical challenges of surface functionalizing nanoparticles for stability, and ideal biological and chemical properties of surface functionalized nanoparticles for nanomedical applications. These topics will be covered in the following subsections.

1.3.1 Colloidal Stability

Nanoparticles small size lends them a tremendous advantage in navigating the complexities of biological systems. However, nanoparticles exhibit a greater propensity to aggregate in aqueous solutions, than their bulk counterparts, due to surface properties, interactions between nanoparticles, and size.[69] Aggregation must be addressed to achieve colloidal stability in buffered or saline based medium which is paramount to permit sterile filtration (or other sterilization methods; for example sterile buffer exchange) before use with *in vitro* studies or *in vivo* administration. Additionally, without proper colloidal stability in biologically relevant medium the nanoparticles may aggregate or interact unfavorably when administered *in vitro* or *in vivo*.[66,70] Colloidal stability in buffered solutions is also necessary for reactions involving conjugation to biological targets, such as proteins and antibodies, and for other reactions such as radiolabeling and chelation. Nanoparticles that do not possess intrinsic colloidal stability cannot be used effectively in biomedical applications, but colloidal stability can be provided by functionalizing the surface with hydrophilic ligands.[70-72]

Nanoparticle surface functionalization is most often used to overcome nanoparticles greater tendency to aggregate. The small size of nanoparticles and Brownian motion offers a simple explanation for nanoparticles propensity to aggregate.[69] In **Equations 3a and 3b** we can see the relationship between particle size (d_p) and extent of three dimensional Brownian motion displacement (Δx).[69] Where D_b is Einstein's Brownian diffusion coefficient, Δt is change in time, T is temperature, k_B is Boltzmann's constant, and μ is the solution viscosity.

$$\Delta x = \sqrt{6 D_b \Delta t} \tag{3a}$$

$$D_b = \frac{k_B T}{3\pi\mu d_p} \tag{3b}$$

Equation 3b clearly shows that as particle size decreases the displacement due to Brownian motion increases. This results in a greater chance for aggregation between nanoparticles due to Van der Waal attraction forces.[69] More precisely, there usually exists a relatively strong attraction between solid phase nanoparticles that are dispersed in an aqueous phase.[69,73] This attractive force can result in aggregation.[69,74] While the size of nanoparticles offers a simple explanation for greater aggregation probability, factors such as surface charge and chemistry can also influence aggregation tendency, further complicating obtaining colloidal stability. Therefore, the surface modification must sufficiently increase van der Waal repulsion to prevent aggregation and achieve colloidal stability.[72,73] Surface ligands can provide nanoparticles with steric, electrostatic, or electrosteric stability.[72,75] These types of stability are shown in **Figure 1.2**.

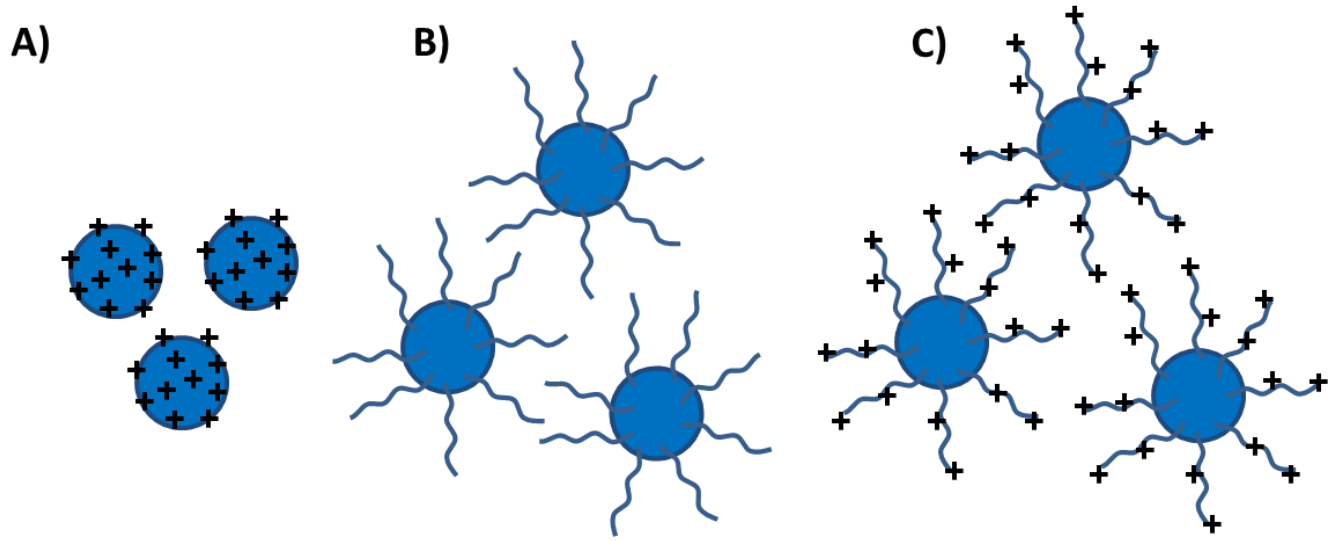

Figure 1.2. A) Electrostatic, B) steric, or C) electrosteric colloidal stabilization of nanoparticles provided by surface charge properties, surface ligands, or charged surface ligands respectively.

Electrostatic stability prevents aggregation due to charged nanoparticle surfaces that repel neighboring nanoparticles with greater force as they approach.[73] An electrostatic double layer, shown in **Figure 1.3,** forms due to counter ions in solution being attracted to the charged surface

forming the 'diffuse layer' and repelling nanoparticles with the same 'surface layer'.[76] The surface and diffuse layers are also termed Stern and Guoy layers respectively. Addition of surface ligands to the nanoparticle can also provide steric stability. Steric repulsion is provided by the steric hindrance of the ligands and is determined by how dense and compressed the ligands can pack as the nanoparticles approach.[73] Surface ligands with charged functional groups utilize both steric and electrostatic stabilization to prevent aggregation and are often referred to as electrosteric stabilization.[73]

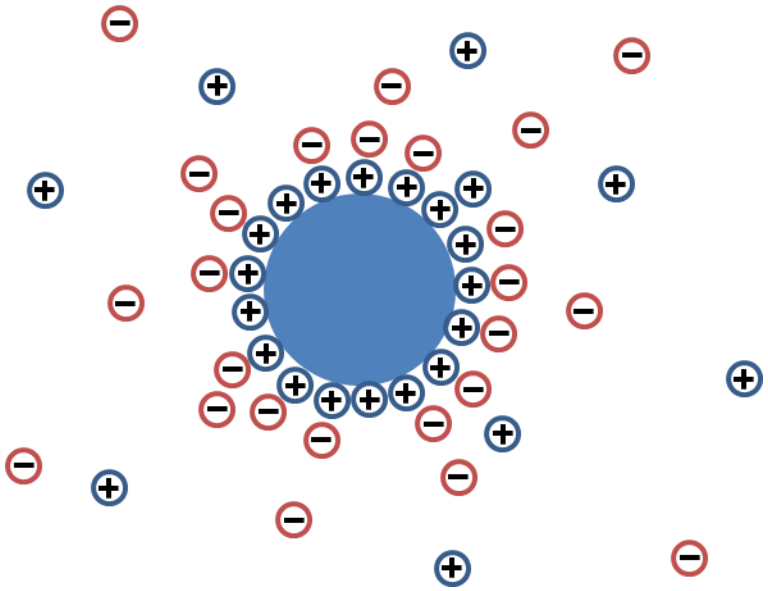

Figure 1.3. Scheme of the electrostatic double layer of small positively charged solid particle in an ionic liquids. The double layer is comprised of the positively charged (blue circle with + inside) surface layer and the surrounding negatively charged (red circle with – inside) layer (Stern layer). This is encompassed by a diffuse layer of equal positive and negative charges (Guoy layer).

The stabilization distance provided by the electrostatic double layer is typically between 1-100 nm for colloids and is compacted as the concentration of ionic electrolytes increases.[74,76] The formed layer of counter ions has a certain thickness ($1/\kappa$) or is inversely proportional to the Debye Hückel parameter (κ) which is dependent upon concentration of ions and the interaction between charged surfaces and ions.[74,76] Therefore, factors such as concentration of counter ions, and nanoparticle surface charges as well as the size of nanoparticles can play a crucial role in colloidal stability.[73] This offers a simple explanation for the nanoparticle instability upon transfer from water to biological medium such as PBS that contain higher ion concentrations. A model that is most commonly used to describe the repulsive force generated due to the electrostatic interactions is the Derjaguin, Landua, Verwey, and Overbeek (DLVO) model.[69,77-80] In this model several simplifications are used, mainly the co-ions, counter ions, and nanoparticle surface charges are represented as spheres that interact through short range potentials and Coulomb interactions.[73,80] The change of energy as charged nanoparticles approach each other is quantitated within the DLVO model and relates to the extent of stability.[73,80] The double layer thickness is used to calculate the amount of Coulomb repulsion between approaching nanoparticles.[73,80] The DLVO theory can be simply stated as the total interparticle potential (Ψ_{TOT}) which is the combination of overlapping electrostatic double layers providing repulsive forces (Ψ_R) and van der Waal attractive forces (Ψ_A), shown in **Equation 4a**.[73,80] The simplified equations for van der Waal attractive forces and repulsive forces are shown in **Equations 4 b and c.** The equation for attractive forces is simplified by assuming particles are of identical radius (a) and that the radius of particles is much greater than the distance between particles, center-to-center (r).[73,80] Likewise the equation for repulsive forces can be simplified by assuming the radius of particles and zeta potential (ζ) are identical.[73] The Hamacker constant (A_H)

describes the forces between two particles in solution and the interaction between the surface of the nanoparticle and solution medium.[73]

$$\Psi_{TOT} = \Psi_A + \Psi_R \quad (4a)$$

$$\Psi_A = -\frac{A_H a}{12r} \quad (4b)$$

$$\Psi_R = 2\pi\varepsilon a\zeta^2 \ln(1 + e^{-\kappa a}) \quad (4c)$$

It should be noted that the attractive force decreases drastically as the distance between nanoparticles increases ($1/r^2$) and that the attractive force exists over larger distances compared to the repulsive forces.[74,80] This can be represented by graphing r/a vs. interparticle potentials (**Figure 1.4**) where a positive potential represents repulsive forces and a negative potential represents an attractive force.

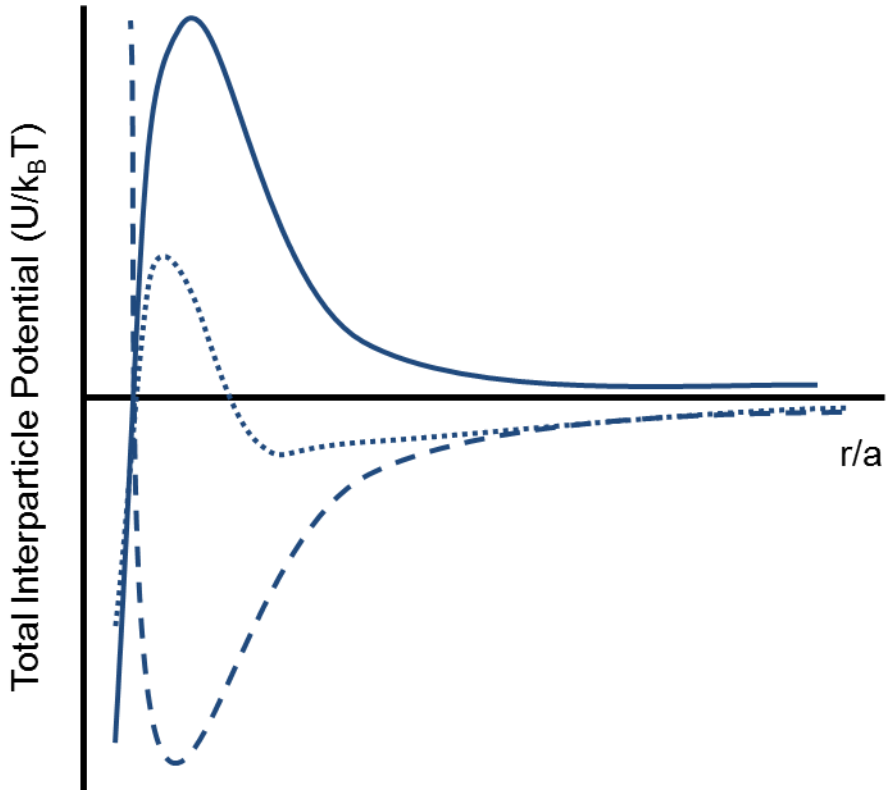

Figure 1.4. Graph illustrating interparticle potentials for stable dispersions (solid line), flocculated dispersions (dotted line), and aggregated dispersions (dashed line).

For stable dispersions (**Figure 1.4** solid line) the particles repel nanoparticles effectively at all distances.[74] Particles that are starting to flocculate or are starting to aggregate (**Figure 1.4** dotted line) have greater attractive forces at certain distances (r/a) which is termed the equilibrium separation distance.[74] Unstable particles (**Figure 1.4** dashed line) that do not have sufficient repulsive forces will have very large attractive forces as they approach and will irreversibly aggregate and precipitate.[74] This exemplifies why nanoparticles can be dispersed in solutions, but may require stabilization by means such as surface modifications to attain colloidal stability.[75] Dynamic light scattering (DLS) is a useful characterization tool that can determine the zeta potential of the nanoparticles and assess the stability of the nanoparticles in solution.

There are numerous different strategies for functionalizing the surface of FeOx nanoparticles to provide colloidal stability. Such strategies include modifying the surface with hydrophilic biomolecules, small molecules, dendrimers, surfactants, or polymers.[71] In addition to the electrostatic forces provided by the surface ligands, the stability is also due to an osmotic and elastic involvement.[61,81-85] When two nanoparticles with a surface coating approach each other the increase in concentration of surface ligands will cause water to enter the volume and force the nanoparticles apart to restore osmotic equilibrium.[81-84] Additionally, when the nanoparticles are in a confined area the surface ligands will have an reduction in conformational entropy which will ultimately repel the particles to increase entropy.[81-84] Once colloidal stability is achieved, it should be assessed in multiple biologically relevant media since colloidal stability in water or phosphate buffered saline (PBS) may not translate to stability when introduced to the biological environment of interest.

Effective use of nanoparticles for treatment of cancer requires colloidal stability. However, there are several additional factors that need to be addressed when choosing and designing a surface functionalization strategy. These challenges can be subcategorized into biological and chemical challenges of modifying the surface of nanoparticles.

1.3.2 Biological Challenges for Surface Functionalization

FeOx nanoparticles without post-modifications are generally not stable in biological conditions. Additionally, nanoparticles can exhibit low probability of reaching the desired target, non-specific interactions with proteins that can cause aggregation, adsorption of opsonins leading to phagocytosis and subsequent clearance from the body, and toxicity issues.[61,63] To prolong the circulation time and enhance passive uptake the optimal surface functionalized nanoparticle size should be between 30-100 nm.[61,86] Below this size range the nanoparticles are susceptible to leakage into the blood capillaries and above this size they become more likely to be opsonized and cleared by macrophages.[61,86,87] The ideal surface ligand should therefore provide colloidal stability in biological media while maintaining a small size to increase circulation time and enhance cellular uptake probability. It is also advantageous in radiofrequency magnetic hyperthermia to choose a surface functionalization that can be easily conjugate additional therapeutics, diagnostics, and targeting ligands to aid in delivery, treatment, and/or diagnosis. The biological concerns and requirements are addressed in further detail below.

Opsonization is the process by which opsonin tags a foreign object for phagocytosis and clearance from the body.[46] A potential way to overcome the challenge of avoiding opsonization is to use a surface functionalization technique using polymers.[46] Utilizing these biomolecules could prevent opsonization by mimicking biology to create ‘stealth’ like properties for the

nanoparticle.[61,81,88] Stealth property of some nanoparticles refers to a surface coating that increases the circulation time allowing for a greater chance of passive targeting by reduce protein adsorption and recognition by opsonin.[61,81,88] This is especially important in cancer treatment since some tumors are known to have leaky vasculature, as a result of reduced lymphatic drainage and increased angiogenesis, which improves the accumulation of nanoparticles in these regions.[61,63] The intercellular junctions of normal tissue is typically less than 10 nm reducing the potential for nanoparticles to accumulate.[61] In comparison it has been reported that tumor intercellular spaces can range from 0.5-2.5 μm.[89,89,90] The passive uptake resulting from both leaky vasculature and increased intercellular spaces is termed the enhanced permeation and retention (EPR) effect. Nanoparticles in the size range of about 20-150 nm can take advantage of the EPR effect most efficiently.[63]

While passive targeting via the EPR effect increases the accumulation of nanoparticles in tumors as compared to normal tissue it should not be exclusively relied upon. For this reason the ability for further conjugation of targeting moieties, therapeutics, and/or diagnostic agents is highly advantageous for medical applications. Addition of targeting moieties such as ligands, proteins, or antibodies facilitates active accumulation of nanoparticles by targeting overexpressed receptors on tumor cells.[63,66,91,92] One popular way of conjugating targeting moieties is to use 1-Ethyl-3-(3-dimethylaminopropyl)carbodiimide (EDC) coupling to form an amide bond between a carboxyl group and a primary amine.[93] This method is beneficial as amines and carboxyl groups aid in providing aqueous stability and are typically found on surface functionalizations used for biological stability.[93] Additionally, targeting biomolecules typically contain a primary amine and/or carboxyl group.

Another significant biological challenge that nanomaterials face is accurate assessment of stability. Nanoparticles' colloidal stability must be assessed not only in water and PBS, but also in biologically relevant medium before conducting any *in vitro* experiments, such as uptake or toxicity. This is important as colloidal instability due to the introduction of nanoparticles into cell medium can drastically alter results.[66,94] When the nanoparticles are introduced to cell culture medium, blood, cerebral spinal fluid, or other medium, aggregation can result. This can be caused by differences in pH, ion concentrations, or presence of interacting or adsorbing proteins. Instability due to aggregation reduces the circulation time and prevents the nanoparticles from reaching or remaining at the region of interest.[66] Aggregation can also decrease cellular uptake and internalization, or drastically reduce the effectiveness of targeting.[61,66] In some cases adsorption can lead to recognition by the immune system leading to clearance from the body. It is therefore very important that the biological stability of the surface functionalized FeOx nanoparticles be investigated in several relevant media such as complete tissue culture medium, cerebral spinal fluid, and human serum. For the treatment of glioblastoma multiform (GBM) it is important to modify the surface for stability in cerebral spinal fluid. This can be tested by using artificial cerebral spinal fluid (CSF). Additionally, the use of convection enhanced delivery (CED) reduces the need for active targeting as the nanoparticles are directly administered at the tumor site. The use of CED also reduces the issue of nanoparticles crossing the blood brain barrier.

Toxicity is another biological obstacle that must be kept in mind when modifying the surface of the nanoparticles.[63] It has been suggested that cationic surface functionalizations can improve the cellular uptake, however there is some evidence that suggests potential toxicity due to surface functionalizations containing positive amine groups.[63,95,96] The charge of the surface

modification is thought to not only affect cellular uptake of nanoparticles, but also where the nanoparticles localize within the cell.[95,96] Cellular toxicity can be significantly affected by where a nanoparticle localizes.[95,96] Therefore the possible tradeoff between potential toxicity and potential increased cellular uptake must be considered for specific applications.

In conclusion factors such as charge, size, chemical composition, and toxicity must all be considered when designing a nanoparticle surface for biological stability and targeting of cancerous cells. Further understanding of factors that influence biological stability and the ability to produce stable nanoparticle solutions in a broad range of medium is paramount in progressing nanomedical agents into the clinic. Ideally, surface functionalized nanoparticles will provide protection against clearance and aggregation as they interact with different biological environments, exhibit low toxicity, and offer potential for further conjugation of targeting ligands and/or additional therapeutic or diagnostic agents.

1.3.3 Chemical Challenges for Surface Functionalization

When choosing a surface functionalization strategy the chemical challenges of functionalizing the surface must also be considered and addressed. The nanoparticles surface chemistry can pose several challenges to surface modification. Such chemical issues to be avoided include use of toxic chemicals, difficult surface functionalization methods, and large surface functionalizations that cannot be sterile filtered. Other challenges include washing and isolating the surface functionalized nanoparticles, and retaining colloidal stability when conjugating additional targeting ligands or drugs.

Washing and isolating the stable surface functionalized nanoparticles is vital to remove unreacted ligands, chemicals, and partially or incomplete surface functionalized nanoparticles.

This becomes extremely necessary if toxic chemicals are used or toxic byproducts are present during surface functionalization. Additionally it is important to be able to buffer exchange the nanoparticles directly into different biologically relevant medium without the need to completely dry the nanoparticles. Often when surface functionalized nanoparticles are dried to a powder the surface chemistry is altered or even removed resulting in colloidal instability upon resuspension.

Difficult surface functionalizations are frequently required to obtain colloidal stability in water or PBS. The nanoparticles that usually require these difficult methods are synthesized by organic methods which result in only organic media stability. For these nanoparticles a phase transfer process is generally required to transition the nanoparticle from organic stability to aqueous stability. Facilitating this transition requires a mixture of organic and aqueous phases with a surface functionalization or stabilizer. The two phases are allowed to separate and then the nanoparticles in the aqueous phase are extracted. Additional steps must then be taken to ensure complete removal of these organic chemicals. If the chemical, polymer, or molecule used to modify the surface is soluble in the organic phase then removal of the chemical, polymer, or molecule is easily done by washing with the organic phase. Synthetic approaches with facile surface functionalization methods without the need for potentially toxic organic chemicals are highly sought after.

1.4 Methods of Synthesizing Iron Oxides

There is a plethora of synthetic methods reported in the literature including mechanical alloying or ball milling[97-99], electron beam lithography[100], laser pyrolysis[101-105], electrospray[106], and gas-phase deposition[107].[51] It is desirable to avoid these synthetic methods for FeOx nanoparticles used in hyperthermia because these methods are often complex and/or do not have

sufficient nanoscale size control. Synthetic methods that produce more applicable nanoparticles for hyperthermia include aqueous co-precipitation[108-113], sol-gel[114], hydrothermal reaction[115], flow injection synthesis[116], microemulsion[117], chemical vapor deposition (CVD)[118,119], glycol[53,120-122], thermal decomposition(83-86), and sonochemical syntheses[123].[27,124,125] Co-precipitation of iron salts is mentioned in spite of its sufficient lack of size distribution control because it produces nanoparticles that have some degree of water stability without post-modification steps.[27,126]

Thermal decomposition synthesis of FeOx nanoparticles are worthy of particular emphasis. This method is extremely versatile and the size and morphology can be controlled.[27] Synthesis parameters of time, reactant concentration, ratios of reactants, temperature, intrinsic solvent or iron precursor properties, and seed growth techniques can be utilized to obtain morphology and size control.[27,127] Utilizing non-polar solvents is beneficial to obtain highly crystalline FeOx nanoparticles with tunable size, narrow size distribution and facile scale-up potential. To produce 15 nm crystallite sizes, with non-polar solvents, the nanoparticles must be synthesized with seed growth steps that require multiple solvents, capping agents, and/or intermediate wash steps.[128,129] However, the downside of non-polar solvent use is that they require difficult or complex phase transfer steps to obtain aqueous dispersions and stability. It is crucial that a biologically stable colloidal solution of nanoparticle be easily obtain by post-synthetic methods such as surface functionalization. The importance of biological stability and conjugation potential of targeting ligands provided by surface functionalization is critical for FeOx nanoparticles for use in MFH or nanomedical applications especially where targeting to tumor cells is required.[39,40,130]

1.5 Benzyl Alcohol Synthesis of Metal Oxides

Benzyl alcohol, a polar solvent, provides the benefits of non-polar solvent synthetic methods of control of size, high crystallinity, narrow size distribution, and potential facile scale-up with the added benefit of being more easily surface functionalized for the required biological stability post synthesis.[131] Size control has been achieved for crystalline titania nanoparticles synthesized with benzyl alcohol from titanium tetrachloride by modifying the reaction temperature and precursor concentrations.[132] Scale-up was demonstrated in recent reports of benzyl alcohol synthesis with vanadium and tungsten chlorides to produce gram quantities.[133] Thermal decomposition of iron (III) acetylacetonate ($Fe(acac)_3$) in benzyl alcohol has several benefits. Benzyl alcohol is simultaneously acting as a solvent, capping agent, and reducing agent to synthesize FeOx nanoparticles. Furthermore, when the reaction is carried out under the presence of air the reduction of $Fe(acac)_3$ is increased due to increased oxidation of benzyl alcohol to benzaldehyde.[94] The oil of plants naturally contain benzyl alcohol.[134] Commercial applications have been found for benzyl alcohol in products such as cosmetics products[135], injectable drug preservative[134], and as fragrance and flavor additives[135-137].

Over 35 metal oxides have been synthesized using benzyl alcohol and metal precursor salts such as alkoxides, acetates, acetylacetonates, and halides.[138-143] Literature reports relatively few benzyl alcohol synthesis studies of FeOx nanoparticles especially using $Fe(acac)_3$ as a metal precursor.[138,139] FeOx has been synthesized in a microwave mediated benzyl alcohol synthesis with the metal precursor $Fe(acac)_3$ which had the benefits of producing highly crystalline nanoparticles very rapidly (5 minutes), but only 5 nm crystallite sizes were obtainable.[139] A more complicated benzyl alcohol synthesis with $Fe(acac)_3$ was recently done using an autoclave method and requiring a glovebox, and heating in a furnace for two days to obtain 15-25 nm

crystallite sizes.[143] A simple, well controlled and understood benzyl alcohol reaction that produces 15-16 nm crystallite sizes is highly desirable. Therefore, a simple benzyl alcohol synthesis under nitrogen and atmospheric conditions was used to gain mechanistic insight into the benzyl alcohol $Fe(acac)_3$ synthesis of FeOx nanoparticles. Initial studies will be used to acquire enhanced control over crystallite size and size distribution that is vital for increasing the effectiveness in radiofrequency hyperthermia.

1.6 Surface Functionalization of nanoparticles for Biological Applications

The initial stability of FeOx nanoparticles depends on whether they were synthesized by an aqueous or organic method. Aqueous synthesis such as co-precipitation typically results in some degree of aqueous stability. Organic synthesis such as thermal decomposition of $Fe(acac)_3$ results in stability in organic solvents and requires difficult phase transitions to modify the surface for aqueous stability.[144] However, organic synthesis is favored for producing FeOx nanoparticles where precise control of size and size distribution is required. FeOx nanoparticles synthesized by the benzyl alcohol modified seed growth synthesis have the advantages of organic synthesis of tunable size and size distribution and can be easily surface functionalized for aqueous stability without complicated phase transfer processes.[94] There is an ever increasing demand for surface functionalizations that provide true biologically relevant colloidal stability despite the numerous reported methods in literature.[124] Typical surface functionalizations have terminal amine and/or carboxyl groups to provide stability and have the added benefit of further conjugation of targeting ligands, chelates, or radiolabels.[94,124,145] Some examples of commonly used surface functionalizations for biological stability include use of polymers or organosilanes.

1.6.1 Carboxymethylated Polyvinyl Alcohol Surface Functionalization

Polyvinyl alcohol can be carboxymethylated to form carboxymethylated polyvinyl alcohol (CMPVA) a biodegradable, cheap, and hydrophilic biopolymer.[130] The carboxyl groups of CMPVA interact strongly with the surface of FeOx.[131] The carboxyl groups that do not interact with the surface provide the colloidal and biological stability as well as sites for further conjugation of targeting ligands, therapeutic and/or diagnostic agents. One possible disadvantage of using CMPVA is that the length of the polymer increases the possibility of bridging and/or multiple nanoparticles adsorbing the same polymer which will ultimately lead to clusters of stable nanoparticles or instability. Large stable clusters of nanoparticles are undesirable as this can potentially affect the cellular uptake, blood circulation time, and increase the chance of becoming opsonized.

1.6.2 Organosilane Surface Functionalization

Organosilanes offer the advantage of protecting the surface of FeOx from undesirable reactions and are often used to provide stability based on the terminal functional group of the organosilane.[146-148] Two of the more commonly used organosilanes for FeOx surface functionalization include (3-Aminopropyl)trimethoxy silane (APTS) and (3-aminominopropyl)triethoxysilane (APTES). These organosilanes offer an efficient and easy method to modifying the surface of FeOx nanoparticles through a silanization reaction resulting in a Fe-O-Si bond and a silica shell around each nanoparticle.[124,149] The resulting modified surface contains terminal amine groups giving the nanoparticles a positive zeta potential at neutral pH.[146] More specifically the charge of the nanoparticles offers stabilization through an electrostatic double layer and steric hindrance of the organosilane.[73-76] The number of silica shells

that form in addition to how quickly and effectively the silanization occurs depends on several factors such as time, pH, temperature, hydrolysis rate, concentration and type of catalyst used.[124,149,150] There is a plethora of reported methods for APTS or APTES surface functionalization of FeOx nanoparticles, however few have sufficiently been optimized or characterized to properly show biologically relevant stability or extent of silanization.[149] Additionally, the methods employed will need to be modified or optimized depending on the FeOx nanoparticle synthesis used.

Another organosilane of particular interest is (3-Glycidyloxypropyl)trimethoxysilane (GLYMO) which contains a terminal three membered epoxy ring that can be used to easily alter the chemistry at the surface. The epoxide ring initially prevents aqueous stability after silanization, but also hinders the possibility of creating additional silane shells, and bridging or coating of multiple nanoparticles. Through the use of acid or base-catalyzed epoxy ring opening reactions aqueous stability can be achieved by coupling different biomolecules containing an amine group or strong nucleophile.[151] When selecting an appropriate biomolecule it is advantageous to select one with only one reactive site to prevent possible bridging or cross linking between nanoparticles. This bridging would result in larger hydrodynamic diameters, wider size distributions, and ultimately aggregation and precipitation. Overall, modifying the surface of FeOx nanoparticles with GLYMO grants the ability to conjugate a wide array of biomolecules providing and even tuning the colloidal stability for specific biological environments.

1.7 Project Overview

Herein, the research into FeOx nanoparticles for radiofrequency induced magnetic hyperthermia treatment of cancer is split into three main objectives. The first objective was to design and optimize the benzyl alcohol synthesis of FeOx nanoparticles with ideal properties for hyperthermia applications. The second objective was to devise and tailor a simple surface functionalization strategy suitable for biological applications with further conjugation potential. The third objective was to conduct biological tests to determine the nanoparticles efficacy in for biological applications including RF hyperthermia and brachytherapy delivery.

Chapter 1 introduced the relevant and essential background information to understand radiofrequency induced magnetic hyperthermia. More specifically this chapter discussed the plethora of FeOx nanoparticle synthesis and surface functionalization strategies that are suitable for RF hyperthermia applications. The challenges and ideal properties of surface functionalization for translation to biological applications are also discussed.

In Chapter 2 the different FeOx nanoparticles are introduced. The numerous applications for FeOx nanoparticles and the different crystal structures are briefly reviewed with focus on the inverse spinel crystal structure of magnetite and maghemite ordinarily used in magnetic RF hyperthermia.

In Chapter 3 the results and discussion from the investigation into synthetic parameters of the benzyl alcohol synthesis are presented. Emphasis is placed on altering the reaction environment, concentration, and temperature to optimize the resulting FeOx nanoparticle properties. LaMer growth and Ostwald ripening principles are used to speculate on the observed effects of reaction parameters on nanoparticle properties. For further optimization and control of nanoparticle properties a modified seed growth method is investigated. The complex interactions

between reaction parameters and nanoparticle properties, as well as between nanoparticle properties and RF heating are analyzed using JMP effect screening models.

Chapter 4 presents the ease of surface functionalization for FeOx nanoparticles synthesized by the benzyl alcohol method. The surface functionalization with CMPVA, APTS, APTES, and GLYMO are discussed with emphasis on the stability properties in different biologically relevant media. The GLYMO modification with different amino acid and nucleophiles is investigated to obtain a method that allows for tailoring of stability properties. Additionally, the CMPVA-FeOx and SAHBA-FeOx nanoparticles are further functionalized with a DOTA chelate and radiolabeled with ^{177}Lu to confirm their use as a nanoplatform.

Chapter 5 presents biological testing of surface functionalized FeOx nanoparticles. *In vitro* cellular uptake, proliferation, and hyperthermia test results are presented and discussed. An initial *in vivo* survival study using a murine orthotopic xenograft model of glioblastoma multiforme is used to investigate the efficacy of CMPVA-FeOx and SAHBA-FeOx nanoparticles to deliver brachytherapy.

Chapter 6 concludes the dissertation with a brief summary of important findings. The combination of investigating synthetic methods, surface functionalization strategies, and biological testing in this project will be extremely beneficial to gain knowledge applicable to magnetic hyperthermia applications, nanotechnology, and nanomedicine. The work herein will be beneficial and intriguing to experts in areas of material synthesis, surface coating technology, medicine, physics, radiology, molecular biology, and other disciplines.

Chapter 2: Iron Oxide Nanoparticles

2.1 Iron Oxides in Nanotechnology

Nanotechnology, especially FeOx nanoparticles, can be utilized in countless ways. FeOx nanoparticles are useful materials in biosensors,[152-156] high density information data storage,[157-160] catalysts,[124,157,161-163] magnetic sensors,[164-167] and permanent magnets.[159,160,168,169] FeOx nanoparticles with specific surface functionalizations have proven very useful in biosensing applications using diagnostic magnetic resonance (DMR) technology to detect cells and biomolecules such as DNA, pathogens, mRNA, proteins, drugs, and tumors.[156] Understanding and manipulation of magnetocrystalline anisotropy of FeOx has given rise to innovative ways to magnetically store information data.[158] The high surface area to volume ratio property of nanoparticles has led to a significant interest in utilizing FeOx nanoparticles for catalysts and magnetic sensors.[161] Additionally, catalysts and magnetic sensors benefit from nanoparticles stability, selectivity, and increased efficiency as compared to bulk sized materials.[161] The magnetic properties of FeOx nanoparticles are often sought after because they can be magnetically extracted and recycled after use as catalysts, biosensors, or in other applications.[156,161] Significant amounts of research time have been invested into creating permanent magnets and finding new applications for them. Permanent magnet materials combine

the ideal properties of a soft magnet's large coercivity property and a hard magnet's large magnetization saturation property by exchange coupling.[160] FeOx nanoparticles are extremely advantageous in biotechnology and nanomedicine as they can be used in both theranostics and diagnostics. Diagnostically they are used as magnetic resonance imaging contrast agents due to their strong T_2-weighted and T_2* image improvement.[28,170,171] FeOx nanoparticles continue to be rigorously investigated to find new and better applications and improve their efficacy in applications such as magnetic hyperthermia where their superparamagnetic behavior, size, biocompatibility, and inherent imaging capabilities are utilized.[29,44,170,172-174]

2.2 Iron Oxide Crystal Structures

Iron oxides in nature typically consist of iron (II) and/or iron (III) cations and certain oxygen containing anions.[125,175,176] Iron oxides can be referred to as oxides, hydroxides, or oxide-hydroxides depending on if the crystal structure contains O^{2-} and/or OH^- anions. The term iron oxide is often used as an encompassing term of the many different iron oxides, hydroxides, or oxide-hydroxides.[125] Stoichiometry and crystal structures differences have been used to identify the sixteen known pure phase iron oxides.[1,125,175] **Table 2.1** lists the known iron oxides and are subcategorized into iron oxides, iron hydroxides, and iron oxide-hydroxides.[1] In the following sections hematite, wüstite, maghemite, and magnetite crystal structures are briefly introduced.

Table 2.1. The mineral name and formula for the sixteen known pure phase iron oxides subcategorized into iron oxide, iron hydroxide and iron oxide-hydroxide. Reproduced from [1].

Iron Oxide	
Mineral Name	**Formula**
Wüstite	FeO
Magnetite	Fe_3O_4
Hematite	α-Fe_2O_3
β-Maghemite	β-Fe_2O_3
Maghemite	γ-Fe_2O_3
ε-maghemite	ε-Fe_2O_3
High pressure iron oxide	Fe_4O_5
Iron Hydroxide	
Mineral Name	**Formula**
Iron(II) hydroxide	$Fe(OH)_2$
Bernalite (Iron(III) hydroxide)	$Fe(OH)_3$
Iron Oxide-Hydroxide	
Mineral Name	**Formula**
Goethite	α-FeOOH
Akaganéite	β-FeOOH
Lepidocrocite	γ-FeOOH
Feroxyhyte	δ-FeOOH
High Pressure FeOOH	FeOOH
Ferrihydrite	$Fe_5HO_8 \cdot 4H_2O$ approx.
Schwertmannite	$Fe_{16}O_{16}(OH)_y(SO_4)_z \cdot nH_2O$
Green Rusts	$Fe_x^{3+}Fe_y^{2+}(OH)_{3x+2y-z}(A^-)_z$; $A^-=Cl^-, 1/2SO_4^{2-}, CO3^{2-}$

2.2.1 Magnetite Crystal Structure

Magnetite is the preferred crystal structure for magnetic fluid hyperthermia. The inverse spinel structure of magnetite is depicted in **Figure 2.1**[2]. [1,28,157,175,177,178] The inverse spinel crystal structure consists of 32 oxygen atoms close packed in a face centered cubic (FCC) orientation with iron ions located within 16 of the 32 octahedral holes and 8 of the 64 tetrahedral holes.[28,177]

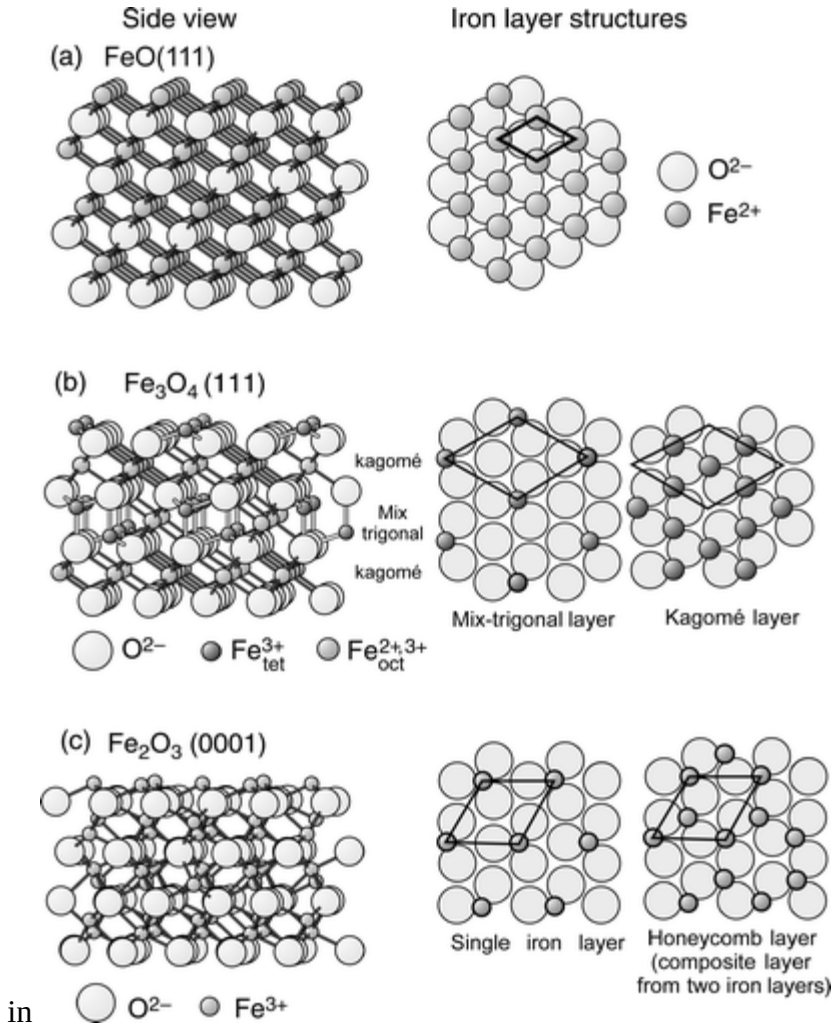

Figure 2.1. Diagram showing the side view and top view of wüstite (a), magnetite (b), and hematite(c). Two top views are shown for magnetite and hematite to visualize the different layers of the crystal structure. From [2]

The magnetite inverse spinel crystal structure contains eight Fe^{2+} and eight Fe^{3+} ions the octahedral vacancies, and eight Fe^{3+} ions in the tetrahedral vacancies.[28,175,177] The magnetite inverse spinel formula is therefore Fe_3O_4 or $Fe^{3+}(Fe^{2+}Fe^{3+})O_4$.[28,175,177] The octahedral and tetrahedral holes make up the sublattices within the oxygen FCC lattice. The ferrimagnetism intrinsic to magnetite results from the coupling between the iron ions.[175,177] More specifically, we

can see that from Hund's rule that Fe^{2+} and Fe^{3+} have magnetic moments of 4 and 5 Bohr magnetons (μ_B) respectively.[177] Magnetite has a calculated μ_B=4.07 per formula unit which is much closer to the 4 μ_B of Fe^{2+}.[177,178] This can be explained due to the antiferromagnetic arrangement of the Fe^{3+} in the octahedral and tetrahedral vacancies leaving the Fe^{2+} ions as the significant contributor to the magnetization.[177,178] In summary, the ferrimagnetic property is a result of the difference in Bohr magnetons of each iron ion, the arrangement between the two sublattices, and the unequal Fe^{2+} and Fe^{3+} amounts. The properties of magnetite, maghemite, Wüstite, and hematite are summarized in **Table 2.2**.[1]

Table 2.2. Properties of magnetite, maghemite, hematite and wüstite. Reproduced from [1].

Mineral Name	**Magnetite**	**Maghemite**	**Hematite**	**Wüstite**
	Cubic	Cubic or tetragonal	Rhombohedral hexagonal	Cubic
Cell Dimensions (nm)	a= 0.8396	a= 0.83474	a= 0.50356 c= 1.37489	a= 0.4302-0.4275
Formula units, per unit cell, Z	8	8	6	4
Density (g/cm^3)	5.18	4.87	5.26	5.9-5.99
Octahedral occupancy	-	-	2/3	-
Color	Black	Reddish-brown	Red	Black
Hardness	5.5	5	6.5	5
Magnetism	Ferrimagnetic	Ferrimagnetic	Weekly ferromagnetic or antiferromagnetic	Antiferromagnetic
Currie (Néel) Temperature (K)	850	820-986	956	203-211[1)]
Melting point (°C)	1583-1597		1350	1377
Boiling point (°C)	2623			2512

1) Néel Temperature

2.2.2 Maghemite Crystal Structure

Maghemite also displays an inverse spinel crystal structure and is more thermodynamically favored than magnetite.[1,2,157,179,180] The properties of maghemite are summarized in **Table 2.2**.[1] It is important to note that maghemite is a ferrimagnet and has a reddish-brown color. This color helps to first distinguish it from magnetite as the two inverse spinel structures cannot be differentiated by powder XRD. The metastable maghemite, γ-Fe_2O_3, cubic unit cell can be stoichemetrically written as $(Fe^{3+})_8[Fe^{3+}_{5/6}\square_{1/6}]_{16}O_{32}$ where $\square$ indicates a cation vacancy and the tetrahedral and octahedral positions are indicated by () and [] respectively.[1,175,179,180] Maghemite can be obtained from heating magnetite in organic compounds which causes the Fe^{2+} cations to become oxidized and result in some cation vacancies.[175,180,181] At high temperatures, around 400°C depending on crystallinity and size the crystal structure of maghemite can be converted to the more thermodynamically favored hematite crystal structure.[1,180]

2.2.3 Hematite Crystal Structure

The red colored ferromagnetic iron oxide, hematite (α-Fe_2O_3), is nature's most abundant iron oxide.[1,157,180,181] **Figure 2.1** depicts hematite's crystal structure which is similar to rhombohedral corundum.[1,2] Properties of hematite are summarized in **Table 2.2**.[1] It has a rhombohedrally centered hexagonal close packed crystal structure with two-thirds of the octahedral sites filled with Fe^{3+} ions.[1,157,180] Hematite's weak ferromagnetic state is due to the magnetic spins being canted about 5° at temperatures between the Morin Temperature (T_M) and the Néel Temperature (T_N).[180] The ferromagnetism of hematite transitions to antiferromagnetism below T_M=260 K, and to paramagnetism above T_N=950 K.[180] Hematite is the most

thermodynamically favored structure of all the iron oxides and so under the correct conditions magnetite, maghemite, etc. will all undergo oxidation and/or rearrangement to hematite.[180,181]

2.2.4 Wüstite Crystal Structure

Wüstite has a similar crystal structure to that of sodium chloride (NaCl) where the Fe^{2+} ions exist in octahedral sites of the oxygen anions closed packed FCC lattice.[1] The crystal structure is shown in **Figure 2.1** and the summarized properties are listed in **Table 2.2**.[1] Interestingly this crystal structure is only formed at temperatures exceeding 843K and the stoichiometric formula is $Fe_{1-x}O$ because of 5-15% oxidation of Fe^{2+} ions to Fe^{3+} ions.[175,182] The amount of oxidation is dependent upon the temperature and partial pressure of oxygen.[175,182] Below 843K this crystal structure will disproportionate to more thermodynamically favored states of Fe metal and Fe_3O_4.[1]

2.3 Magnetic Properties of Iron Oxide

The magnetic, biodegradable and biocompatible properties of magnetite (Fe_3O_4) and maghemite (γ-Fe_2O_3) make them the most desirable FeOx nanoparticles for magnetic hyperthermia.[9,25,28,183] Bulk FeOx particles are comprised of multi-domain particles, but as the size is decreased into the nanometer region the FeOx nanoparticles will behave as single-domain particles and eventually superparamagnets. For example it has been estimated that below 166 nm diameter the particles will behave as single-domain particles.[160] Likewise, magnetite has a theoretical multi-domain to single-domain transition at approximately 80-100 nm.[184,185] Further reduction in diameter below approximately 20-30 nm the nanoparticles will start to display superparamagnetism depending on the crystal structure.[184] Multi-domain particles will not be

discussed in detail as these are above the desirable size range for efficient magnetic hyperthermia.

Superparamagnetism is an interesting phenomenon that arises in certain magnetic materials when the size is sufficiently small. The non-interacting magnetic moments of superparamagnets will respond to thermal fluctuations when the thermal energy (K_BT) is greater than the anisotropic energy.[124,159,169] When the thermal energy exceeds the anisotropic energy the individual magnetic moments will alter directions in response to thermal fluctuations.[169] The nanoparticles magnetic spin direction will eventually reach an equilibrium comparable to thermal equilibrium.[169] It should be noted that the size limit of superparamagnetism depends on the material of interest and is termed the superparamagnetic limit.[28,124] Superparamagnets exhibit very large saturation magnetization and susceptibility values as a result of considering the nanoparticles total magnetic moments (as high as 10^4-10^5 Bohr magnetons) instead of the individual magnetic moment of a single atom.[28,169] A representative hysteresis loop for a superparamagnet is shown in **Figure 2.2**. The negligible coercivity and magnetic remanence can be seen in the hysteresis curve in **Figure 2.2**. Coercivity refers to force required in terms of magnetic field strength required to return the magnetization to zero.[28,124,169] Magnetic remanence defines the residual magnetism that remains after the magnetic field is removed.[28,124,169] These properties make FeOx superparamagnets ideal candidates for use in biological applications such as magnetic hyperthermia as they will not exhibit magnetization after removal of the externally applied magnetic field. Additionally, when the radiofrequency alternating current magnetic field is applied the nanoparticles will rapidly respond to changes in the applied external magnetic field. The negligible remnant magnetization is important to mention as this reduces the probability of aggregation due to room temperature magnetism between nanoparticles.[28,124] It

would be advantageous to use metallic nanoparticles instead of oxide nanoparticles because of their higher magnetization values, however they are generally toxic and not applicable in medical applications.[124]

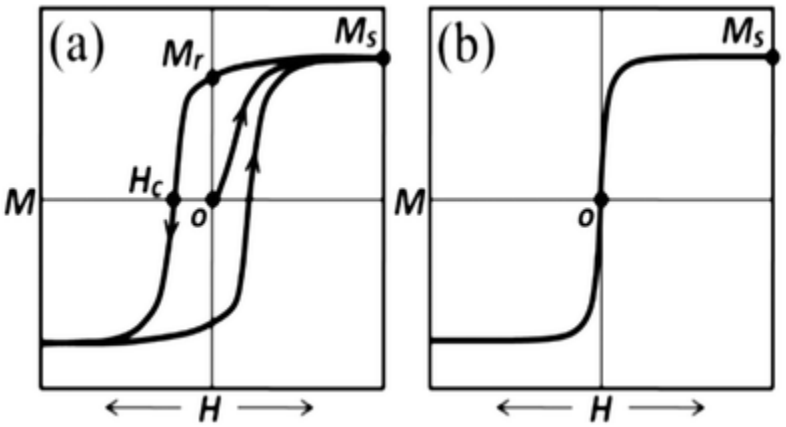

Figure 2.2. Representative hysteresis loop for single domain ferromagnetic (a) and superparamagnetic (b) crystals plotted as magnetization (M) versus magnetic field (H). M_S, M_r, and H_c correspond to magnetization saturation, remnant magnetization, and coercive field respectively. From [168]

Single-domain particles in the nanorange, outside of the superparamagnetic size range, are also useful in biomedical applications. Single-domain particles do not have domain walls and therefore exhibit large magnetic coercivities. [124,159,169] Also, these single-domain particles have a net magnetic spin direction.[124,159,169] The lack of domain walls is due to the unfavorable magnetostatic energy at such small volumes.[159] External magnetostatic energy is allowed rather than creating energetically unfavorable domain walls.[124] Therefore, when the size of the particle increases it will eventually become energetically favorable to create multiple walls resulting in multi-domain particles.[124,159] At these larger sizes several factors determine the size and shape of

the domains; these include anisotropy, energy of exchange and magnetostatic interactions.[159] It is worth mentioning that the coercivity can be increased with differing shape anisotropy of single-domain particles.[124]

Chapter 3: Benzyl Alcohol Synthesis of Iron Oxide Nanoparticles

3.1 Experimental Section

3.1.1 Reagents, Materials, and Equipment

All chemicals and materials were used as received. Tetramethylammonium hydroxide (TMAOH) solution (Alfa Aesar, 25% w/w aq.), iron (III) acetylacetonate ($Fe(acac)_3$) (Acros Organics, 99+%), benzyl alcohol (Alfa Aesar, 99%), copper TEM grids (Ted Pella Inc., 200 mesh Formvar carbon type B), Fe inductively coupled plasma (ICP) standard (Alfa Aesar, Iron, plasma standard solution, Specpure®, Fe 1000 µg/mL), hydrochloric acid solution (HCl) (Electron Microscopy Sciences, 2%), potassium ferrocyanide aqueous solution (Prussian Blue) (Electron Microscopy Sciences, 2%), two-neck 100 mL round bottom flask (Chemglass), coil style reflux condenser (Chemglass), and acetone (Fisher Scientific, ACS grade)

3.1.2 Modified Seed Growth of Iron Oxide Nanoparticles

Synthesis of FeOx nanoparticles in benzyl alcohol was conducted under nitrogen flow or open to air in a two-neck 100 mL round bottom flask (Chemglass) equipped with a coil style reflux condenser (Chemglass). The volume of benzyl alcohol (Alfa Aesar, 99%) for all reactions

was 20 mL. Iron (III) acetylacetonate ($Fe(acac)_3$) (1, 2, 3, 4, or 6 g) (Acros Organics, 99+%) was dissolved in benzyl alcohol with vigorous magnetic stirring and then immediately heated to reflux or a set temperature. In the nitrogen syntheses, nitrogen was initially bubbled in the benzyl alcohol and $Fe(acac)_3$ for 30 minutes prior to heating. After the solution color changed from a dark red to black, the reaction was carried out for 2 or 24 hours. At the end of the reaction, the round bottom flask was removed from heat and stirred for 15 minutes while cooling. Acetone (Fisher Scientific, ACS grade) was then used to precipitate and wash the FeOx nanoparticles with magnetic extraction. This wash step was repeated 3-5 times with intermittent and brief sonication (Cole Parmer, Ultrasonic Cleaner 8892) between wash steps. The nanoparticles were then dried down to a powder with nitrogen flow.

The modified seed growth procedures followed the procedure as stated above, but after the 24 hour reaction an additional amount of $Fe(acac)_3$ (1, 2, 3, 4, or 6 g) was added as a dry powder directly to the hot reaction. Reaction was then carried out for an additional 24 hours before removal from heat. The nanoparticles were then precipitated, washed, magnetically extracted, and dried as stated above.

The heating mantle (Thermoscientific, electrothermal heating mantle) used in initial studies was replaced with a silicone oil bath (Alfa Aesar) with the temperature controlled by a magnetic stirring hot plate (VWR, VMS-C7) equipped with a temperature control unit (VWR, VT-5 S40) to better and more precisely control the temperature. The maximum heating ramp rate was used for either the heating mantle or silicon oil bath and hotplate setup. The temperature and color of the solution was observed and documented every 60 seconds in the initial heating to reflux or set temperature. This was important to determine important temperature thresholds such as when high levels of nanoparticles were forming indicated by a solution color change to black.

3.2 Characterization Techniques

3.2.1 X-ray Diffraction (XRD)

Determining the crystal structure of a material by x-ray diffraction (XRD) characterization is advantageous as it is a non-destructive technique.[1,186-189] XRD utilizes x-rays that will interact with the sample and form a diffraction pattern that is used in determining the bulk crystalline structure.[188,189] More specifically, electromagnetic radiation in the form of x-rays are used to analyze the arrangement of the atoms within a crystal. Typically the wavelength (λ) of the x-rays is approximately 0.1 nm as this wavelength is similar to the crystal's interatomic distance resulting in elastically scattered x-rays.[1,188-190] The constructive and destructive interference of scattered x-rays produces a diffraction pattern that is unique to different crystal structures of crystalline materials.[1,188,189] The atoms in a crystalline material are consistently arranged resulting in the incident x-rays elastically scattering at specific angles and interatomic lattice distances which causes constructive interference in specific directions.[1,188] Bragg's law (**Equation 5**) states the distance between atomic planes of the lattice (d_{hkl}) and the incident angle (θ), specific to an incident x-ray wavelength (λ) spaced at integer multiples (n) of the path difference where constructive interference of elastically scattered x-rays occur.[1,188]

$$n\lambda = 2d_{hkl} \sin\theta \quad (5)$$

The resultant XRD pattern's peak positions are used to determine the lattice parameter, size, and symmetry.[188] Additionally, the peak intensities are useful in determining the organization of atoms.[188] The database of known crystallography data can be searched to find similar XRD patterns and thus verify the crystal structure of a material of interest.[188] Powder XRD is very useful for the characterization of crystalline nanomaterials. This technique exploits the large number of crystals present in a powder and allows the incident x-ray to interact with the material

at numerous orientations or angles at the same time.[189] A diffractometer investigates all possible crystal orientations of the powder by analyzing the resultant diffraction cones of the powder sample which are used to determine the diffraction pattern.[189] It is important to note that magnetite and maghemite crystal structures are indistinguishable by XRD.[1]

The crystallite size of nanoparticles can also be determined by analyzing the XRD line broadening with the Scherrer formula (**Equation 6**).[1] The Scherrer formula relates the corrected peak width at an angle in the XRD measurement to the crystallite size, but will underestimate the smaller crystallite sizes when multiple crystallites are present.[1] In other words, the formula is biased towards larger crystallite size when the mean crystallite size is determined from the coherently scattering domain perpendicular to the hkl plane (MCL_{hkl}).[1] This is due to larger crystallites more intensely scattering x-rays.

$$MCL_{hkl} = \frac{K\lambda}{b\ \cos\theta} \tag{6}$$

The formula uses the shape factor (K), full width half maximum (FWHM) of the measured peak (b), and wavelength of the x-ray (λ).[1] The instrument error is accounted for by subtracting the instrument width from the value of b.

A PANalytical X'Pert Pro Materials Research Diffractometer was used to obtain powder XRD patterns. The sample was prepared by drying the material to a powder with nitrogen and mild grinding to acquire a fine powder that was then transferred to a low background silicon disk. The material was scanned at 20-80° 2θ using a Cu Kα x-ray source. X'Pert High Score Plus software was used to analyze the pattern and calculate the crystallite size based on diffraction peak broadening using the Scherrer formula. Several of the peaks in the XRD pattern were used to calculate crystallite size and standard deviation.

3.2.2 Dynamic Light Scattering (DLS)

Characterizing nanoparticles in solution provides useful information about hydrodynamic size, size distribution, diffusion coefficients, and surface charge. Dynamic light scattering (DLS) is a technique that can be used to rapidly assess these properties of a nanoparticle solution without destroying the nanoparticles.[191,192] DLS requires a stable colloidal suspension for best results. DLS utilizes a monochromatic light source to probe the colloidal suspension and record the time variation of the intensity of the light scattered by diffusing nanoparticles throughout a solution.[191,192] The intensity at two specific time points are correlated by the intensity autocorrelation function.[192] Since, the colloidal nanoparticles have kinetic energy the diffusion coefficient can be measured.[191] The intensity of scattered light at certain angles over time is related to the diffusion of the nanoparticles throughout the solution.[191] Therefore, it is important to know the viscosity, refractive index, and temperature of the solution being analyzed to effectively characterize nanoparticles using DLS. The hydrodynamic diameter and size distribution in terms of polydispersity index (PDI) values are calculated from the measured diffusion coefficients.[192] In **Equation 7**, the magnitude of the scattering wave (q) is calculated using the range of scattering angles (θ_{DLS}), wavelength of the incident light (λ), and refractive index of the solution (n).[191]

$$q = \left(\frac{4\pi n}{\lambda}\right) sin\left(\frac{\theta_{DLS}}{2}\right) \tag{7}$$

The hydrodynamic radius (R_H) is calculated using the Stokes-Einstein equation shown in **Equation 8** where the following abbreviations are used: T is the solution temperature, K_B is Boltzmann constant, and η is the medium viscosity.[191,192] Thus it can be seen that the hydrodynamic radius is directly related to the diffusion coefficient (D_f).[191]

$$D_f = \frac{K_B T}{6\pi\eta R_H} \tag{8}$$

Next, the size distribution is calculated, in terms of the PDI, using the average decay rate (⟨Γ ⟩) and the variance of the decay rate distribution (μ_2) (**Equation 9**).[191]

$$PDI = \frac{\mu_2}{\langle\Gamma\rangle^2} \tag{9}$$

Absolute monodispersity is highly improbable, therefore the correlation function calculated ⟨Γ ⟩ and q values can be used to obtain an average hydrodynamic radius (**Equation 10**).[191] Depending on the instrument used, a weighted function can be used to calculate the summation of all possible decay rates for each nanoparticle to determine a size distribution.[192] The size distribution determined using a weighted average should be considered "semi-quantitative" representation of the size distribution and not an exact size distribution.[192]

$$R_H = \frac{K_B T}{6\pi\eta\langle\Gamma\rangle} q^2 \tag{10}$$

The DLS data can be presented based on the number, volume, or intensity of nanoparticles because the data is an average of the nanoparticles in solution. Larger nanoparticles more intensely scatter light than smaller nanoparticles causing a bias towards larger nanoparticles when the results are presented as intensity. For nanoparticles in solution, it is better to analyze the data presented based on number or volume of nanoparticles rather than intensity as this is a more indicative of the actual hydrodynamic diameter. Hydrodynamic diameter is also useful in determining the surface functionalization thickness on nanoparticles. This is accomplished by measuring the nanoparticles before and after surface functionalization and subtracting the non-surface functionalized nanoparticles. However, the nanoparticle surface and the surface functionalization ligands may interact with water differently and thus skew the thickness measurement.

Zeta potential (ζ) determined by dynamic light scattering is often used to characterize the electro-kinetic phenomenon of the stabilization offered by the double layer. This measurement

utilizes electrophoresis, the movement of charged particles in response to an external applied electric field, to calculate the mobility which is the velocity divided by the field intensity.[73] When spherical nanoparticles are sufficiently small (where κa is small enough that spherical nanoparticles can be considered a point charge) and are measured at low electrolyte concentrations and potentials the Hückel-Onsager equation (**Equation 11**) can be used to relate electrophoretic mobility (μ_E) to zeta potential.[73] The value of κa is a dimensionless term that represents the thickness of the double layer and nanoparticle radius respectively.[73] The viscosity (η) of the solution and permittivity (ε) also play key roles in determining the electrophoretic mobility. The permittivity is a combination of permittivity of free space (ε_0) and relative permittivity (ε_r) and is shown in **Equation 12**.

$$\mu_E = \frac{\varepsilon\zeta}{6\pi\eta} \tag{11}$$

$$\varepsilon = 4\pi\varepsilon_0\varepsilon_r \tag{12}$$

For particles too large to use the Hückel equation, a generalized equation (**Equation 13**) is used instead to relate electrophoretic mobility and zeta potential.

$$\mu_E = \frac{\varepsilon\zeta}{6\pi\eta} f(\kappa a) \tag{13}$$

A Malvern Zetasizer Nano-ZS (Malvern Instruments, U.K.) was used to analyze the hydrodynamic diameter, polydispersity index, and zeta potential of FeOx nanoparticles and surface functionalized FeOx nanoparticles at ambient conditions. This instrument uses a He-Ne laser (633 nm, max 4 mW) light source. For initial hydrodynamic diameter and PDI measurements the FeOx nanoparticles at a concentration of 20 mg/mL were dispersed by sonication for 180 minutes in a 0.25% tetramethylammonium hydroxide (TMAOH) solution. Next, the solution was incubated at room temperature overnight and then a 1 mL 1:100 dilution

with water was made for DLS analysis. These samples were transferred to a low volume disposable cuvette and DLS was run 5 times with each run containing 11 measurements. For zeta size measurements the surface functionalized nanoparticles were concentration and pH matched and then loaded into a folded capillary zeta cell (Malvern Instruments, U.K.) prewashed with ethanol and water to remove any contaminants.

Several concentrations of TMAOH solution were used to disperse the FeOx nanoparticles to verify that the hydrodynamic diameter was not significantly altered by the TMAOH concentration. Additionally, this is important because different concentrations of TMAOH may be required to efficiently disperse different sizes of nanoparticles. FeOx nanoparticles produced by a modified seed growth method were dispersed in several TMAOH concentrations and their hydrodynamic size and PDI values were measured using DLS, the results are shown in **Table 3.1**.

Table 3.1. Initial hydrodynamic diameters and PDI values for various v/v % concentration of TMAOH.

% TMAOH	**Hydrodynamic Diameter (nm)**	**PDI**[a]
0.0625	25.99	0.38
0.125	29.96	0.363
0.25	23.61	0.39
0.5	26.12	0.41

[a]Polydispersity Index (PDI) determined by DLS.

3.2.3 Vibrating Sample Magnetometry (VSM)

The magnetic properties of FeOx nanoparticles can be determined from vibrating sample magnetometry (VSM) determined hysteresis loop. A hysteresis loop is produced by loading a sample of known mass into a magnetometer and measuring the magnetization as the external magnetic field applied is increased from zero to a set magnetic field where the magnetization reaches a maximum or becomes saturated.[1,189] Once the magnetization saturation is reached for the positive external magnetic field, the direction of external magnetic field is then reversed to reach a "negative" magnetization saturation and reversed a second time to the original "positive" magnetic field direction to complete the hysteresis loop.[1,189] A representative hysteresis loop for superparamagnetic and ferromagnetic materials determined by VSM is displayed in **Figure 2.2**. Several important properties can be discerned from the shape, height, and width of the hysteresis loop. These properties include magnetization saturation (M_s), initial magnetic susceptibility (X), remnant magnetization (M_r), and coercivity (H_c). The magnetization saturation refers to the magnetization where all of the magnetic moments are oriented in the same direction of the externally applied magnetic field.[1,189] Furthermore, the magnetization will not increase above the magnetization saturation when the external magnetic field is increased.[1,189] The initial linear increase of the magnetization when the external magnetic field is increased from 0 is used to calculate the initial magnetic susceptibility. When the external magnetic field (H) is returned to 0 any remaining magnetization is termed the remnant magnetization.[1,189] The coercivity or coercive field refers to the magnetic field required to force the magnetization back to 0 or demagnetize the material after magnetization.[1,189] It is important to note that for FeOx nanoparticles the presence of ferrimagnetic magnetite and maghemite will overpower the magnetism of other iron oxides detected.[1]

VersaLab 3 Tesla Cryogen-Free Vibrating Sample Magnetometer (Quantum Design) was used to probe the iron oxide materials and determine their magnetic properties. VSM sample capsule (Quantum Design) were loaded with 5-15 mg of dry FeOx powder and scanned for an offset of 35 mm. Next, the moment versus field measurements were recorded at a purged pressure of <50 Torr, sweep rate of 150 Oersted/second (Oe/s), and scanned in 5 quadrants from 0 Oe to 15,000 Oe (Hmax) to -15,000 Oe (Hmin) without automatic centering. The hysteresis curve was examined to determine the magnetization saturation and was mass corrected using thermogravimetric analysis (TGA) in units of emu/g.

3.2.4 Thermal Gravimetric Analysis (TGA)

Thermal gravimetric analysis (TGA) characterization is beneficial in determining the weight loss of a material as the temperature is increased.[1] This technique can be used to correct the mass of impurities within a sample such as water, organic compounds, excess chemicals, surface functionalities, etc. in dry FeOx nanoparticles. Sample preparation for TGA involves first calibrating the tare weight of the TGA pan with a highly sensitive balance and then loading a sample (laden weight) on to the TGA pan and recording the sample weight as the temperature is increased at rates of 2-10 °C/min.[1] The amount of mass lost is expressed as mass percent loss and can be used to correct the mass of sample used in techniques such as VSM where the mass of the magnetic material is critical to determine magnetization in terms of emu/g.

A Q5000 TGA instrument (TA Instruments) was used to perform TGA and mass correct samples of FeOx nanoparticles. The platinum TGA pans were loaded with 5-50 mg of dry FeOx nanoparticles, under a nitrogen flow rate of 25 mL/min, and the temperature was ramped at 10 °C/min from room temperature to 150°C and held isothermal for 15 minutes. This was followed

by additional temperature increase to 400°C at 10 °C/min and held isothermal for 60 minutes.

3.2.5 Transmission Electron Microscopy (TEM)

Direct imaging of nanoparticles with atomic scale resolution can be performed with transmission electron microscopy (TEM) which uses a beam of electrons to acquire the image.[192,193] TEM uses an electron beam gun to produce a beam of electrons that will probe a sample.[193] The transmitted electron beam is dependent upon the amount of diffraction, the atomic number of the material, and phase contrast.[193] To enhance the contrast and gain higher resolution images the sample stage should have different properties than the sample being analyzed.[192,193]

A Zeiss LIBRA® 120 PLUS TEM was used to acquire bright field TEM images of the FeOx nanoparticles. Sample preparation was done by drying a drop of dilute FeOx nanoparticles (20 mg/mL) in 0.25% TMAOH solution on copper TEM grids (Ted Pella Inc., 200 mesh Formvar carbon type B). For CMPVA-FeOx the cleanup, desalting, and centrifuge filters were all done as described above prior to TEM sample preparation. Image J software was used to analyze the TEM images and calculate the nanoparticle size.

3.2.6 Radiofrequency Heating

FeOx nanoparticle heating characteristics were investigated with a 1.2-2.4 kW EasyHeat induction heating system with a coil designed at a set point of 200 Ampere (A) to run at 1222 watt (W) and frequency (f) of 269 kHz to produce an alternating magnetic field with a magnetic field strength (H) of 37.4 kA/m at 175.4 A. Other magnetic field strengths were used for small time length investigations of heating nanoparticles in cells. Ampere's law can be used to calculate the magnetic field strength (H) (**Equation 14**) produced by a coil with length (L), and

number of turns (N), in a magnetic field (B), current (I) and using the permeability of free space(μ_o.).[194]

$$BL = \mu_o N I_o \quad (14)$$

The magnetic field strength is related to the magnetic field as shown in **Equation 15**.[189] By substituting **Equation 14** into **Equation 15** we can approximate the magnetic field strength produced inside the coil (**Equation 16**). The coil used in these studies had 8 turns (N=8) and a length of 0.0375 m (L=0.0375 m) which corresponds to H= 37.4 kA/m at 175.4 A.

$$B = \mu_o H \quad (15)$$

$$H = \frac{N}{L} I_o \quad (16)$$

An OpSens fiber optic temperature sensor measured the *in situ* nanoparticle solution temperature when RF AC magnetic fields were applied. SoftSens software was used to record temperature every 1.4 seconds. The RF heating of 3 mL of 0.25% TMAOH aqueous FeOx nanoparticle (20 mg/mL) solution was used to compare the RF heating rates of samples at 175.4 A and H=37.4 kA/m over 600 seconds. All solutions were corrected for potential convective heating by measuring a control 3 mL sample of water under identical conditions. The initial linear increase of temperature per unit time (dT/dt) of the water control (0.549°C/min) was subtracted from the initial linear increase of all TMAOH nanoparticle samples tested.

The RF heating data collected must be corrected based on iron concentration to more accurately compare samples. The iron concentration was determined using a Prussian blue assay. A serial dilution of Fe inductively coupled plasma (ICP) standard (Alfa Aesar, Iron, plasma standard solution, Specpure®, Fe 1000 µg/mL) was used to build a standard curve as measured by UV-Vis absorbance assay (λ=685 nm) using a Nanoquant plate reader (Tecan). As prepared RF heating FeOx TMAOH nanoparticle solutions were diluted 1:100 and 2.14 µL of 70% nitric

acid (BDH Chemicals) was added to 30 μL of the diluted sample. This sample was heated at 90°C for 1 hour. The dissolved FeOx sample (10 μL) was added to 1 μL of 20% potassium ferrocyanide (Prussian blue) aqueous solution (Electron Microscopy Sciences, 20%) and 0.5 μL of 20% HCl solution (Electron Microscopy Sciences, 20%). After 15 minutes of incubation at room temperature the UV-Vis absorbance was measured at λ=685 nm.

3.3 Results and Discussions

3.3.1 Investigation of Synthesis Parameters

Magnetic fluid hyperthermia requires a specific crystallite size with minimal size distribution to obtain the most efficient nanoparticle heating effect. To improve and optimize the benzyl alcohol synthesis of FeOx nanoparticles several reaction parameters were investigated. The parameters of interest are concentration, temperature, and addition of extra iron precursor (modified seed growth). The reaction concentration was modulated by concentration of iron precursor in a constant 20 mL volume of benzyl alcohol. The reaction parameters and nanoparticle properties were analyzed using JMP software's effect screening to ascertain trends of reaction parameters upon the resultant nanoparticle properties.

A naming system was used to track of the large number of reaction conditions performed. The first and second additions of $Fe(acac)_3$ are denoted as "A" and "B" and separated with an underscore. The gram amount of $Fe(acac)_3$ added to the 20 mL of benzyl alcohol are listed immediately following A and B. The length of time, in hours, the reaction was carried out is listed as "-X" for both A and B additions. Temperature is listed in parenthesis for reactions where precise control of temperature was investigated. When temperature is not listed the reaction was heated to reflux using a heating mantle that was shown to have similar temperatures

and rate of reflux. For example a reaction carried out in 20 mL of benzyl alcohol with 2 g of $Fe(acac)_3$ added initially and heated at 175°C for 24 hours and followed by an addition of 2 g of $Fe(acac)_3$ and heated at 175°C for an additional 24 hours is named A2-24(175)_B2-24(175). For reactions that were carried out under nitrogen flow the reaction name begins with a "N_2". A reaction of 20 mL of benzyl alcohol with 2g of $Fe(acac)_3$ added initially and reacted at 205°C for 24 hours is named N_2-A2-24(205).

Characterization of nanoparticles was done using XRD, DLS, VSM corrected by TGA, and RF heating measurements to identify their crystallite size, hydrodynamic diameter and PDI values, saturation magnetization, and RF heating capabilities for internal comparisons. Nanoparticles were first characterized by XRD to verify the nanoparticles are indeed FeOx and to calculate the crystallite size. The XRD patterns for FeOx nanoparticles produced by reactions N_2-A2-24, A2-24, and A2-24_B2-24 are displayed in **Figure 3.1**. It is not necessary to show all of the XRD patterns as they all indicate FeOx. It is important to reiterate that XRD cannot distinguish between magnetite and maghemite.

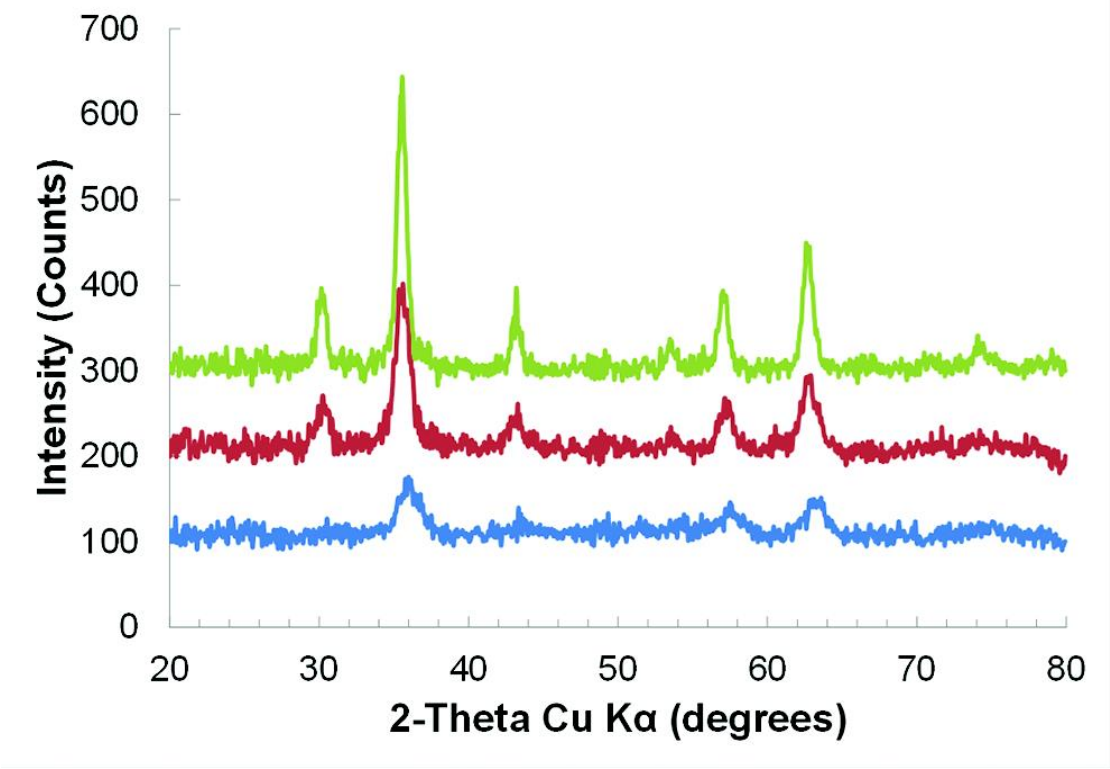

Figure 3.1. XRD peaks of samples: N_2-A2-24 (blue), A2-24 (red), and A2-24_B2-24 (green). An offset of 100 count increments was used to clearly show each reactions pattern.

Next, it is important to examine the hydrodynamic diameter and determine the size distribution in terms of PDI values with DLS. These measurements are very useful in determining how the reaction conditions affected the resultant nanoparticle. **Figure 3.2** and **Table 3.2** respectively show the DLS determined hydrodynamic diameter and peak data for reaction A4-24(195)_B4-24(195). **Figure 3.2** displays the DLS pattern based on percent intensity and percent volume to show that intensity results are biased towards larger sizes. It is important to note that the results based on intensity are biased towards larger sized nanoparticles as they will more intensely scatter the light. Therefore, the results based on volume were used when reporting the hydrodynamic diameter as it more accurately represents the total population of nanoparticles.

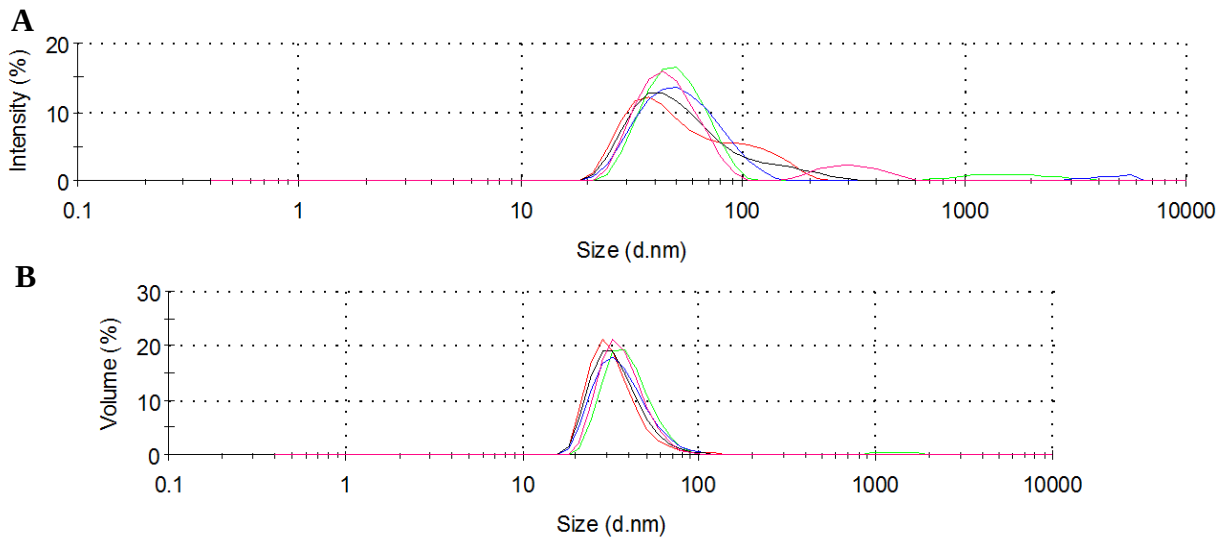

Figure 3.2. The DLS hydrodynamic size measurements displayed in terms of percent intensity (A) and percent volume (B) for reaction A2-24(195)_B2-24(195). The Z-average hydrodynamic diameter was equal to 47.75 nm and the PDI was equal to 0.219.

Table 3.2. The DLS determine hydrodynamic size, percent composition, and width of each peak for the size distribution by percent intensity and size distribution by percent volume for reaction A2-24(195)_B2-24(195).

Size Distribution by Percent Intensity			
	Hydrodynamic Diameter (nm)	**% Intensity**	**Width (nm)**
Peak 1	47.08	86.8	14.31
Peak 2	313.3	13.2	95.5
Peak 3	0	0	0
Size Distribution by Percent Volume			
	Hydrodynamic Diameter (nm)	**% Volume**	**Width (nm)**
Peak 1	37.52	99.3	11.26
Peak 2	328.1	0.7	109.5
Peak 3	0	0	0

The magnetic properties of the nanoparticles were next investigated with VSM and weight corrected using TGA. The hysteresis curve from VSM and mass percent loss over time from

TGA is shown in **Figure 3.3** and **Figure 3.4** respectively. The TGA determined weight loss was between 94.6% and 85.9% for all samples. The VSM determined M_S values were between 48.54 and 57.69 emu/g for samples synthesized under nitrogen and were between 55.5 and 84.57 emu/g for samples synthesized under atmospheric conditions.

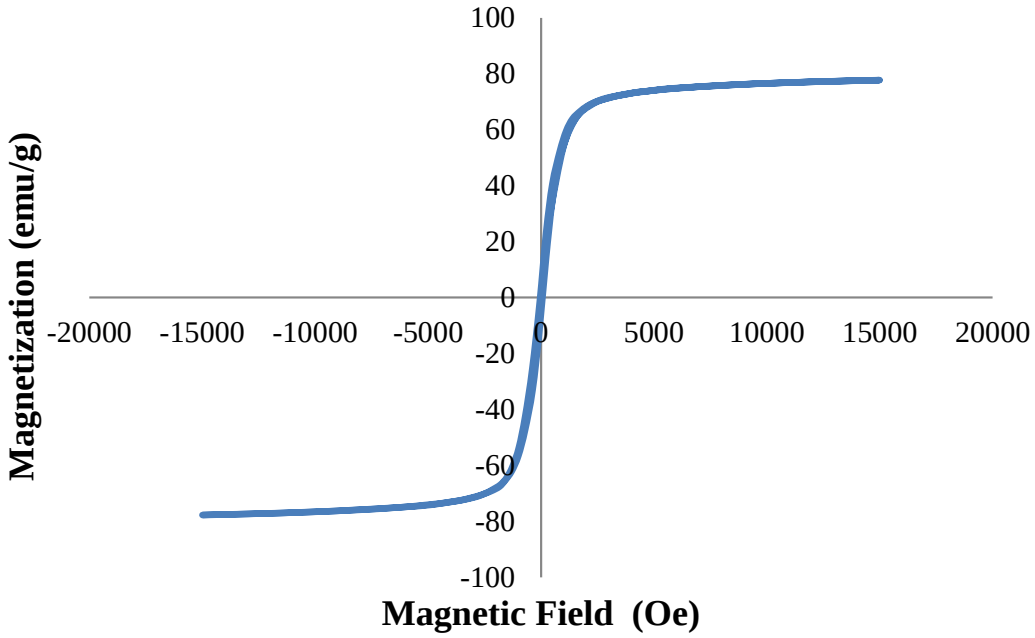

Figure 3.3. VSM measured hysteresis loop of TGA mass corrected (10.901 mg * 0.945164 = 10.303 mg) A2-24(195)_B2-24(195) nanoparticles.

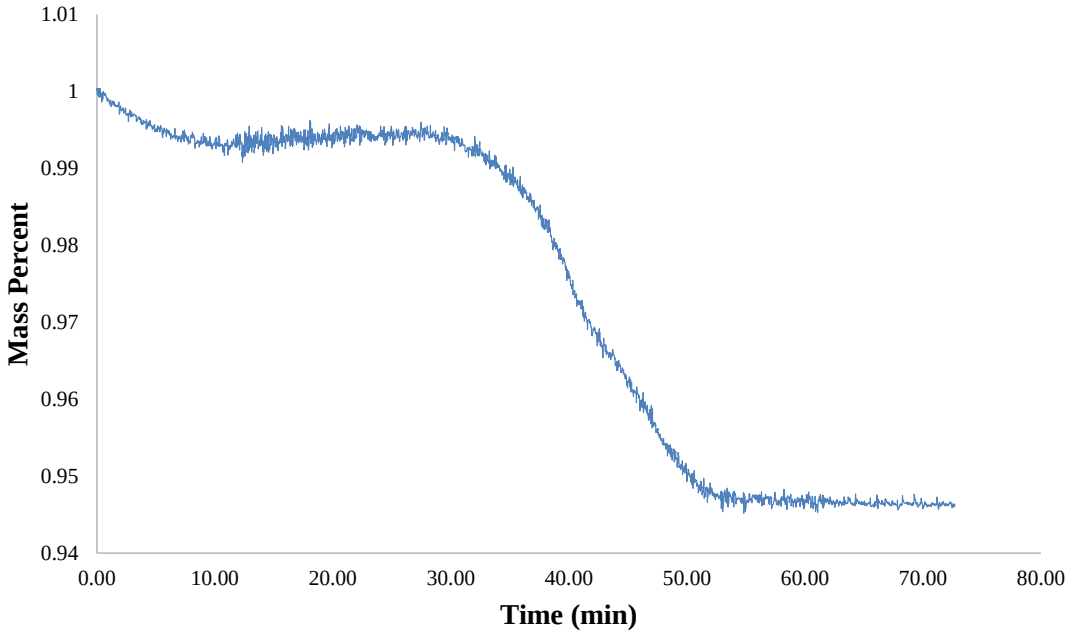

Figure 3.4. TGA of A2-24(195)_B2-24(195) nanoparticles revealing a final mass percent of 0.945164 at 400°C.

RF heating measurements were calculated from fiber optic temperature collected data for concentration matched TMAOH FeOx nanoparticle solutions. Sample heating curves for deionized water, N_2-A2-24, A2-24, A2-24_B2-24, and A2-24(195)_B2-24(195) reactions are shown in **Figure 3.5**. Prussian blue assay was used to normalize the concentrations of iron for internal comparisons. Altering the synthetic parameters we were able to obtain RF heating measurement between 0.01 and 5.55 [°C/min]/mg.

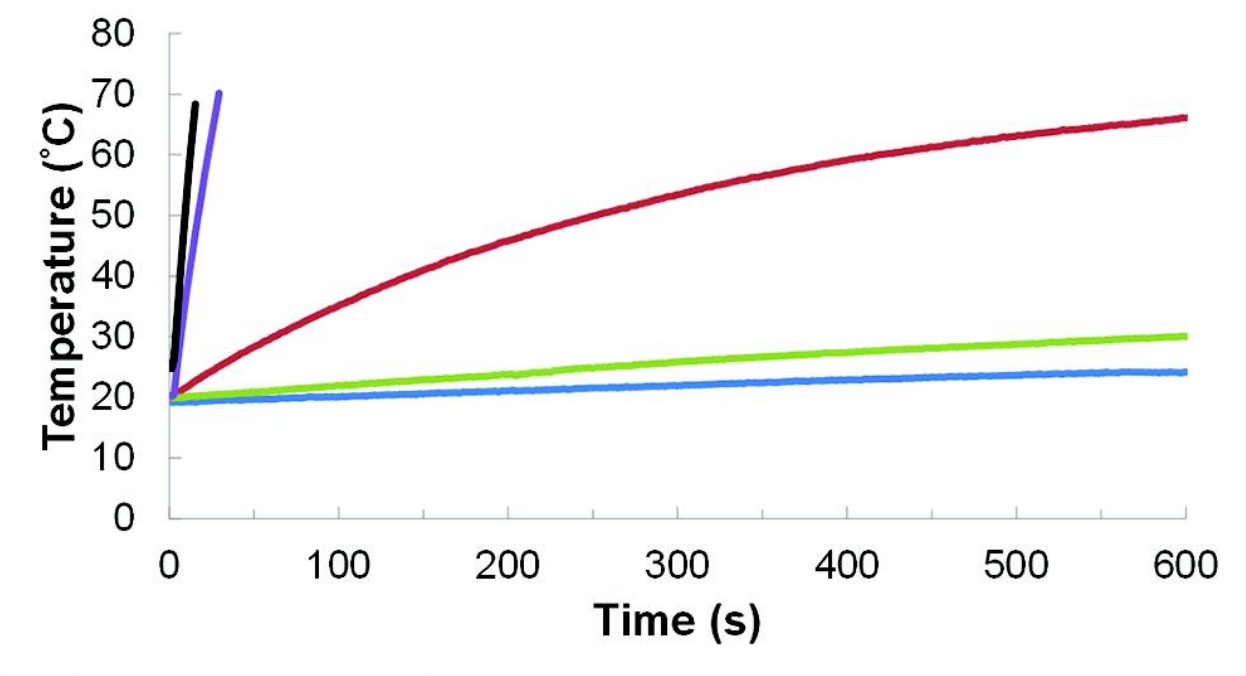

Figure 3.5. RF heating curves of water and FeOx samples dispersed in 0.25% TMAOH. Prussian Blue assay determined the iron concentrations for deionized water (blue), A2-24 under nitrogen (green), A2-24 (red), A2-24_B2-24 (purple), and A2-24(195)_B2-24(195) (black) to be 0, 14.48, 15.40, 14.00, and 15.36 mg/mL respectively. Temperature was recorded every 1.4 seconds in an alternating magnetic field set at 175.4 A for 600 seconds or until reaching approximately 70°C.

3.3.2 Effect of Reaction Environment

Initial benzyl alcohol synthesis reactions were carried out under nitrogen flow. Thermal decomposition of $Fe(acac)_3$ or iron carboxylate salts are most commonly reported in literature as using nitrogen or argon flow.[51,131,143,144,195-198] The reaction N_2-A2-24 produced nanoparticles with 6.5 ± 1.2 nm crystallite sizes based on the Scherrer formula for calculating crystallite sizes from line broadening of peaks in the XRD pattern shown in **Figure 3.1**. Characterization with VSM and corrected by TGA revealed the M_s= 53.39 emu/g. DLS revealed a hydrodynamic

diameter of 23.23 nm and a PDI of 0.351. This crystallite size is well below the desired 15-16 nm crystallite of ideal FeOx nanoparticles for RF induced hyperthermia. It should be noted that there is not a clear relationship between crystallite and hydrodynamic sizes, but the primary goal was to produce nanoparticles with the ideal crystallite size and low size distribution for maximum RF heating. Benzyl alcohol can be oxidized to benzaldehyde and further oxidized to benzoic acid at temperatures below the thermal decomposition temperatures as seen in glycol syntheses of metal and metal oxide nanoparticles.[53,120-122,199] Based on this information our hypothesis was that by running the reaction open to air we could facilitate the production of larger crystallite sizes. To investigate formation of nanoparticles at lower temperatures based on the added oxidation mechanism, the reactions were monitored every minute while the reaction was heated to its final temperature. This revealed that reactions open to air had reflux drips starting at approximately 178°C and increasing as the temperature approached 205°C indicating the formation of benzaldehyde (boiling point = 178.1°C).[200] The oxidation of benzyl alcohol to benzaldehyde suggests that a reduction of $Fe(acac)_3$ may also be occurring at these temperatures. The addition of a second mechanism of formation of monomers and nuclei starting at temperatures below thermal decomposition could allow for better separation of nucleation and growth phases leading to larger crystallite sizes.[37] Additionally, the formation of monomers and nuclei occurring at the lower temperatures due to an oxidation reduction mechanism occur when the temperature ramp rate is still high which would also lead to larger separation of nucleation and growth leading to larger crystallite sizes.[37] Carrying out the reaction open to air (A2-24) resulted in FeOx nanoparticles with 8.33 ± 0.393 nm crystallite sizes (**Figure 3.1**), M_s of 70.839 emu/g, hydrodynamic diameter of 13.64 and PDI of 0.703. This reaction is crucial as it demonstrates the ability to produce larger crystallite sizes and more crystalline nanoparticles by

only changing the reaction environment. The PDI value suggests a broad size distribution which may be narrowed by altering the other reaction parameters. In an attempt to elucidate why larger crystallites were formed the reaction color changes and corresponding temperatures were recorded every minute as the temperature was initially increased. The thermal decomposition of $Fe(acac)_3$ depends on the solvent it is dissolved in, but is generally reported to occur around 170-180°C.[201] As seen in **Figure 3.6** the color change from dark red to black indicating nanoparticle formation occurred at lower temperatures and earlier in the reaction when the reaction was carried out under air (**Figure 3.6B**). The solution for reaction under nitrogen remained dark red until 31 minutes in to the reaction at a temperature of 174.4°C and turned completely black at 40 minutes. The solution for reaction open to air, however first started to change colors after only 20 minutes at 169.4°C and became completely black after 30 minutes of reaction. This corroborates the hypothesis that the presence of oxygen allows for the generation of monomers and nuclei at lower temperatures and earlier in the reaction due to a possible oxidation reduction mechanism.

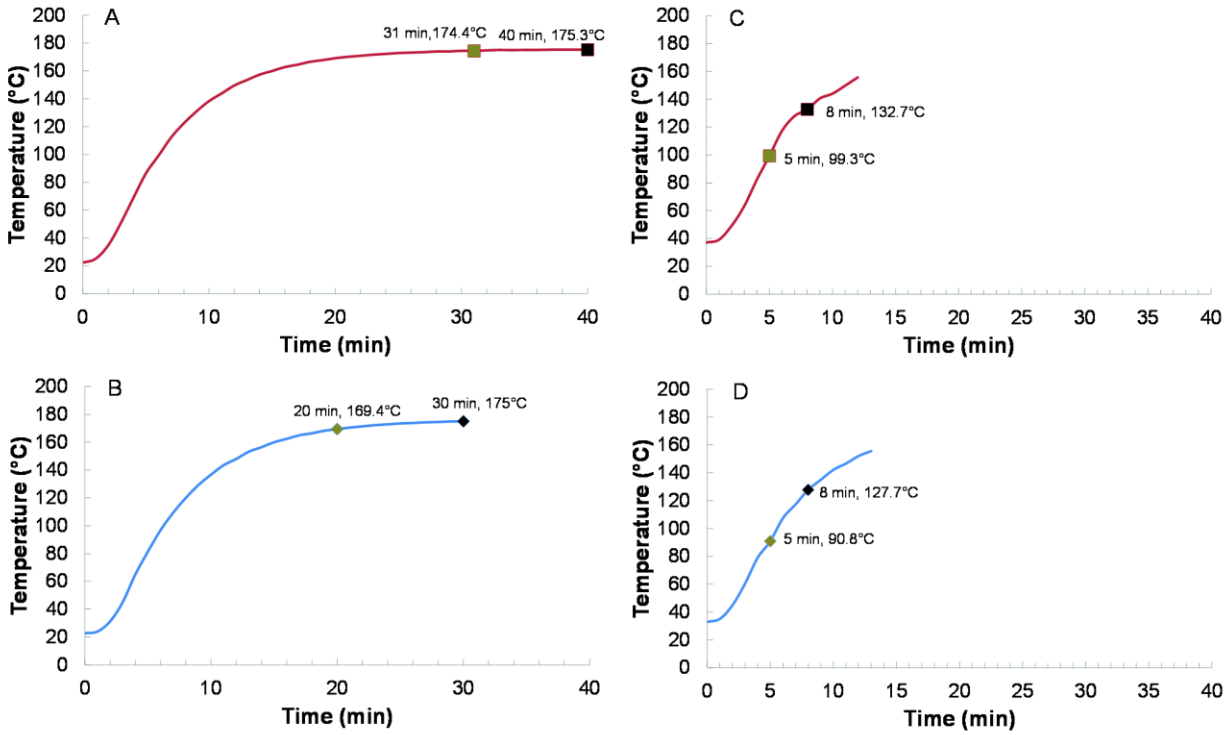

Figure 3.6. Heating curves for reaction of $Fe(acac)_3$ in Benzyl Alcohol heated to 175°C under nitrogen (A), and air (B). Heating curves for reaction containing $FeCl_2$, NaOH, and Benzyl Alcohol heated to 150°C under nitrogen flow (C), and air (D). For reactions under nitrogen the initial and final color changes are indicated with a gold and black square. Likewise, the color changes are indicated with a gold and black diamond for reactions open to air.

To verify that benzyl alcohol is reducing the iron precursor, $Fe(acac)_3$ was replaced with glycol reagents, $FeCl_2$ and sodium hydroxide (NaOH).[53,120,122,199] XRD confirmed that these reactions carried out under nitrogen and air still produced FeOx (**Figure 3.7**) and further indicated that an additional mechanism is responsible for the formation of FeOx nanoparticles in benzyl alcohol since thermal decomposition did not occur in the $FeCl_2$, NaOH, and benzyl alcohol reaction.

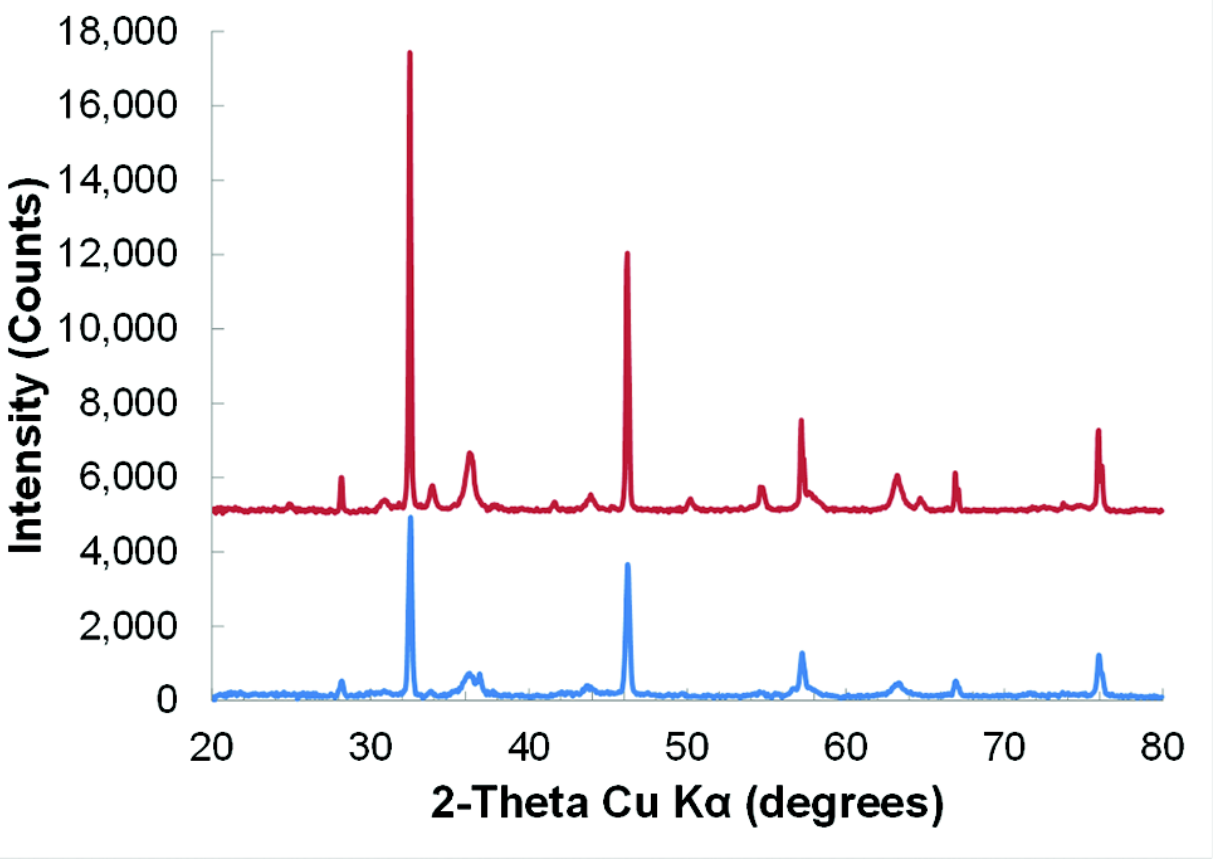

Figure 3.7. XRD peak patterns for benzyl alcohol, $FeCl_2$, and NaOH under nitrogen flow (blue), and open to air (red) offset by 5000 intensity counts. NaCl was indicated by peaks at 32.5 and 46.2 angles. It was determined that the reaction under nitrogen and open to air contained 71% and 77% NaCl respectively.

The reaction color and temperatures were also recorded for the $FeCl_2$, NaOH, and benzyl alcohol reactions carried out open to air and under nitrogen flow (**Figure 3.6C and D).** Reaction under nitrogen flow first changed colors at 99.3°C and was completely black at 132.7°C, while the reaction open to air had an initial color change at 90.8°C and was completely black at 127.7°C. This further corroborates the hypothesis that the benzyl alcohol synthesis open to air produces larger crystallite sizes by facilitating earlier generation of monomers and nuclei and thus a better separation of nucleation and growth. Based on this mechanistic insight, the remaining synthesis

reactions were primarily run open to air and reaction parameters were changed to gain larger crystallite sizes and smaller size distributions.

3.3.3 Effect of Reaction Temperature

Increasing temperature of the reaction was hypothesized to further increase the crystallite size based on recent reports that higher temperatures were required for sustained crystallite growth.[121,202] The heating mantle was replaced with a silicon oil bath to more efficiently control the temperature. Additionally, the reflux of the benzyl alcohol solution was shown to start as low as 178°C as benzaldehyde was most likely formed. Therefore, using the heating mantle to reach reflux temperatures in air was most likely occurring at approximately 178°C and not at the boiling point of benzyl alcohol (205°C).[200] Increasing the temperature to 205°C was hypothesized to further increase the crystallite size. Nitrogen reactions with varying reaction temperatures were used as comparisons to reactions open to air to further elucidate the reaction mechanisms occurring and to better determine other effects such as magnetization saturation changes.

Nitrogen synthesis reaction temperatures were varied between 150-205°C and the resultant nanoparticle properties are shown in **Table 3.3**. In addition to the reaction changing color at later time points and at higher temperatures when compared to reactions open to air, the nitrogen reaction did not contain reflux drips at 205°C. The absence of reflux drips suggests that the oxidation and reduction of benzyl alcohol and $Fe(acac)_3$ is not occurring when reacted under nitrogen flow. Furthermore, this confirms that the primary mechanism of generation of monomers and nuclei is due to thermal decomposition. Without reduction of Fe^{3+} to Fe^{2+} the magnetite crystal structure is unlikely to form. This is validated by the lower magnetization

saturation values of 48.54-57.69 emu/g exhibited by nanoparticles produced under nitrogen flow. This result is in accordance with the lower magnetization saturation values of maghemite as compared to magnetite in bulk and nanomaterials.[203]

Table 3.3. Effect of various temperatures in reactions under nitrogen flow on nanoparticle properties.

Reaction	Magnetization (emu/g)[a]	RF Heating ([°C/min]/mg)[b]	Crystallite size (nm)	Hydrodynamic Diameter (nm)	PDI[c]
N_2-A2-24	53.39		6.47 ± 1.17	23.23	0.351
N_2-A2-24(150)	48.54*	0.01	5.65 ± 0.76	13.02	0.372
N_2-A2-24(175)	57.69	0.04	6.06 ± 0.52	11.51	0.306
N_2-A2-24(195)	57.09*	0.02	6.3 ± 0.89		
N_2-A2-24(205)	57.56*	0.05	11.3 ± 0.73	38.48	0.152

[a]mass unit indicates grams of FeOx nanoparticles corrected by TGA.
[b]mass unit indicates milligrams of Fe determined by Prussian blue assay.
[c]Polydispersity Index (PDI) determined by DLS.
*VSM data was corrected using 0.88 percent weight of sample

For the nitrogen syntheses the crystallite size only changed when the reaction reached 205°C, however the magnetization was only 57.56 emu/g suggesting that mainly maghemite was present. While larger nanoparticle sizes were obtainable by the nitrogen synthesis the nanoparticles most likely consisted of the less magnetic maghemite crystal structure.

Higher magnetization saturation values and crystallite sizes were obtainable at lower temperatures with the reactions open to air, as seen in **Table 3.4**. The larger magnetization saturation values at lower temperatures strongly suggests the presence of magnetite and offers additional evidence that a redox mechanism plays a significant role in the production of FeOx nanoparticles. The size distribution as indicated by PDI was much lower for reactions at 205°C. The trend of decreasing PDI as temperature increased was also seen for reactions under nitrogen

flow; however the larger magnetization saturation values and crystallite sizes make the FeOx nanoparticles synthesized open to air much more advantageous.

Table 3.4. Effect of various temperatures in reactions open to air on nanoparticle properties.

Reaction	Magnetization (emu/g)[a]	RF Heating ([°C/min]/mg)[b]	Crystallite size (nm)	Hydrodynamic Diameter (nm)	PDI[c]
A2-24	70.839	0.17	8.8 ± 0.61	13.64	0.703
A2-24(125)	-	-	-	-	-
A2-24(150)	55.50	0.06	6.2	13.58	0.589
A2-24(175)	70.91	0.14	8.9 ±1.39	12.45	0.61
A2-24(195)	74.32	0.18	8.1 ± 0.59	13.3	0.65
A2-24(205)	73.36*	2.76	14.1 ± 0.80	24.53	0.275

[a]mass unit indicates grams of FeOx nanoparticles corrected by TGA.
[b]mass unit indicates milligrams of Fe determined by Prussian blue assay.
[c]Polydispersity Index (PDI) determined by DLS.
*VSM data was corrected using 0.925 percent weight of sample

It should be noted that reaction A2-24 was most comparable to reactions A2-24(175) and A2-24(195) confirming that the heating mantle had inefficient control of temperature that may have fluctuated between these temperatures. The larger PDI values of these reactions were attributed to an overlap between thermal decomposition and redox of benzyl alcohol and $Fe(acac)_3$. Comparing the RF heating capabilities of FeOx nanoparticles produced by reactions under nitrogen flow or open to air reveals drastically higher heating capabilities. This is attributed to the larger crystallite sizes; however the RF heating may be limited by the lower magnetization saturation values for nitrogen reactions. More specifically, the reaction open to air with M_S=70.91 emu/g had an RF heating rate almost three times as high as the largest crystallite FeOx achieved with nitrogen reactions. The larger crystallite sizes for reactions open to air is explained by the LaMer growth model, where reduction of Fe^{3+} to Fe^{2+} produces the first nuclei at lower temperatures and then the reaction exhibits a large influx of new monomers as the reaction

reaches higher temperatures where both thermal decomposition and redox reactions occur. This large influx of monomers leads to a burst nucleation even and is quickly depleted to begin growth on the nuclei. Since there are two "stages" where monomers and nuclei are formed there is also a higher resultant size distribution, but this also leads to larger crystallite sizes. At 205°C the temperature ramp rate is very high and passes through the beginning of the redox and thermal decomposition mechanisms creating a large number of monomers which in turn causes a quicker burst nucleation leading to smaller size distributions.

The effect of temperature on nanoparticle characteristics revealed several interesting conclusions. Reactions open to air produce larger crystallite sizes at lower temperatures due to the added redox mechanisms and lower temperature refluxing due to the formation of benzaldehyde. Through modulation of the temperature the added redox mechanism of reactions open to air can be taken exploited to more efficiently tune the crystallite size and size distribution of nanoparticles. This is possible due to the better separation of nucleation and growth and burst nucleation process that occurs in the reactions open to air.

3.3.4 Effect of Reaction Concentration

According to LaMer growth methodology the iron precursor concentration can also be modulated to increase the production of monomers and further shorten the burst nucleation event leading to larger crystallite sizes. Increasing reactant precursor concentrations has been reported to increase the overall particle size.[204] The LaMer growth model (**Figure 3.8**) is useful in interpreting results of changing reaction parameters. The production of nanoparticles can be split into three main sections including generation of monomers, self-nucleation, and growth. In the benzyl alcohol reaction the monomers are generated from thermal decomposition and reduction

of $Fe(acac)_3$. When the concentration of monomers is sufficiently high, termed the concentration minimum for nucleation (C_{min}^{nu}), self-nucleation will begin. In the self-nucleation phase the concentration of monomers will be rapidly depleted and will switch to the growth phase when the concentration is decreased below the C_{min}^{nu}.[3,205] Theoretically the concentration of monomers can approach but never reach the critical limiting supersaturation or the concentration maximum of nucleation (C_{max}^{nu}). This is because as the critical limiting supersaturation is approached the rate of nucleation exponentially increases and will overcome even the largest rate of generation of monomers.[3,205,206] The rate of generation of monomers controls the maximum monomer concentration that can be reached or how quickly the nucleation step will occur, since the nucleation rate increases exponentially until it becomes effectively

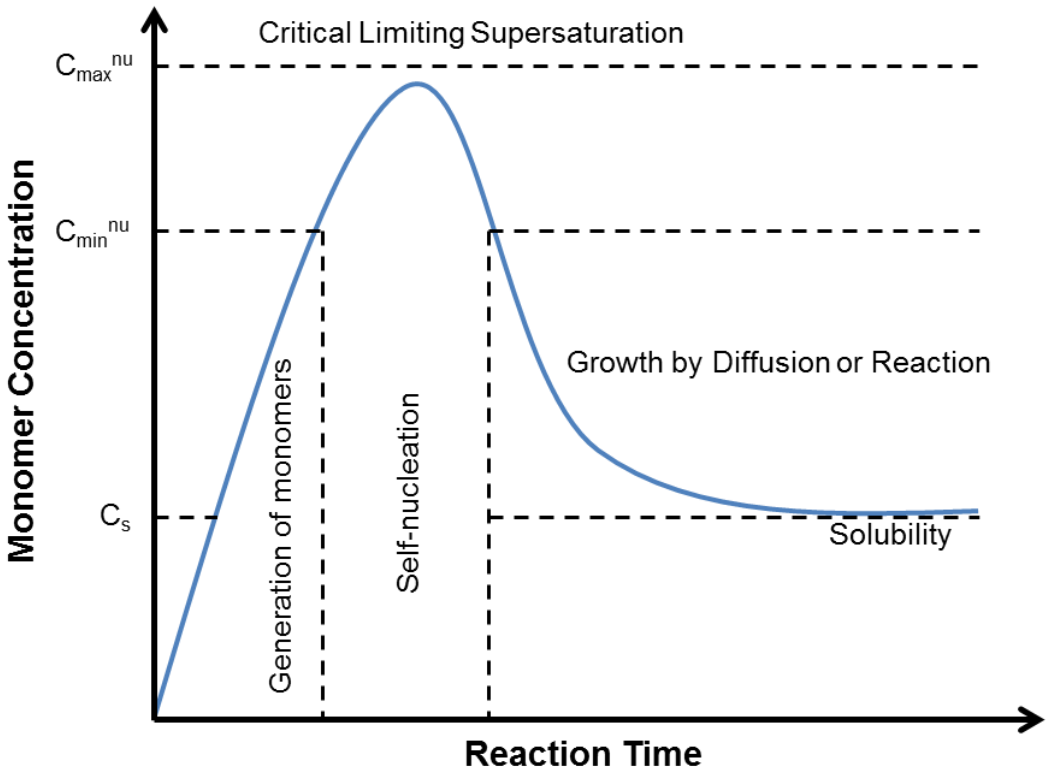

Figure 3.8. LaMer growth model scheme, displaying the generation of monomers, self-nucleation, and growth phases. Adapted from [3].

infinite at the critical limiting supersaturation concentration.[3] The ramification of this is that faster generation of monomers will lead to quicker "burst" nucleation events which will decrease the size distribution of nuclei leading into the growth phase.[3,205] The growth phase is controlled by either diffusion of monomers to the surface of nuclei or reaction rate of monomers onto the surface of nuclei depending on which process is rate limiting.[207] Growth will continue until the monomer concentration is depleted to the solubility concentration of monomers (C_S).[3,205] At this point Ostwald ripening will occur where smaller nanoparticles are dissolved to grow on the energetically favored larger nanoparticles.[208,209] If the nanoparticles are monodisperse when Ostwald ripening begins more polydisperse nanoparticles will be created. Alternatively if the nanoparticles are polydisperse they will become more monodisperse by Ostwald ripening.

The effect of reaction concentration was investigated to further increase the crystallite size of the FeOx nanoparticles. To investigate this parameter the $Fe(acac)_3$ was increased from 2 grams to 4 and 6 grams in reactions (A2-24, A4-24 A6-24). However, this resulted in no significant change in crystallite size for these reactions (**Table 3.5**).

Table 3.5. Effect of various concentrations of $Fe(acac)_3$ on nanoparticle properties.

Reaction	Magnetization (emu/g)[a]	RF Heating ([°C/min]/mg)[b]	Crystallite size (nm)	Hydrodynamic Diameter (nm)	PDI[c]
A2-24	70.84	0.17	8.8 ± 0.61	13.64	0.703
A4-24	68.99	0.13	8.3	14.68	0.2
A6-24	68.25	0.22	7.9	16.5	0.164
A2-24(205)	73.36*	2.76	14.1 ± 0.80	24.53	0.275
A4-24(205)	73.07*	1.86	11.7 ± 0.73	22.85	0.269
A6-24(205)	69.93*	0.85	8.2 ± 1.56	23.9	0.512

[a]mass unit indicates grams of FeOx nanoparticles corrected by TGA.
[b]mass unit indicates milligrams of Fe determined by Prussian blue assay.
[c]Polydispersity Index (PDI) determined by DLS.
*VSM data was corrected using 0.925 percent weight of sample

Interestingly, the hydrodynamic diameter increased (13.64 nm, 14.68 nm, and 16.5 nm) and the size distribution decreased (PDI= 0.703, 0.2, 0.164) when the reactant concentration was increased in agreement with the reported LaMer growth model.[3,205,206] More specifically the hydrodynamic size increased due to the growth phase switching from being limited by diffusion to limited by reaction. When growth is limited by diffusion the monomers will have sufficient time to react in the proper orientation which results in crystalline growth. However, when growth is limited by reaction the monomers will not always orient in a way suitable for crystalline growth, thus more amorphous growth will occur. With more amorphous growth the nanoparticles will have larger nanoparticle sizes and smaller crystallite sizes. At these temperatures the increase of concentration increases the generation of monomers resulting in more monodisperse nanoparticles.

The same set of reactions was also investigated at 205°C to determine if the same trend occurred when more precise temperature control was present. The higher temperature greatly increases the generation of monomers leading to larger crystallite sizes as seen in the previous section. Increased temperatures will also increase the rate of nucleation and the diffusion/reaction growth mechanisms. **Figure 3.9** depicts the theorized effect of increasing both temperature and concentration on the LaMer growth model. It was thought that the combined increase in temperature and concentration would result in even faster generation of monomers. This is represented by a steeper slope in the generation of monomers phase. Interestingly, increased concentration of $Fe(acac)_3$ at 205°C resulted in a decreasing crystallite size (14.1 ± 0.80 nm to 11.7 ± 0.73 nm to 8.2 ± 1.56 nm) while the hydrodynamic diameter was constant. The PDI was only increased when the concentration was increased to 6 g and is consistent with growth limited by reaction leading to larger size distributions.[207]

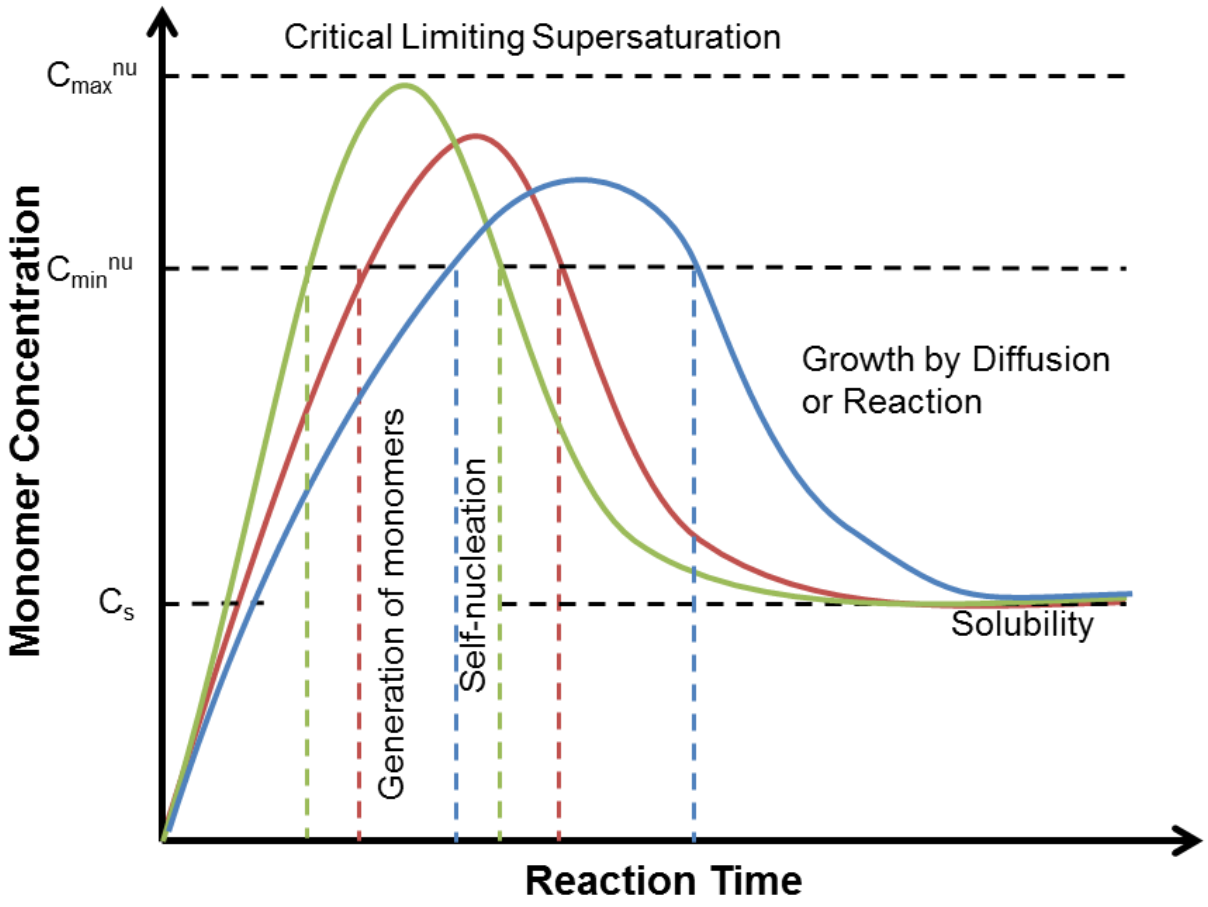

Figure 3.9. Proposed effect of increasing temperature and concentrations of precursor on LaMer growth model (blue). The red curve represents the proposed effects of increasing either temperature or concentration. The green curve represents the proposed effect of increasing both temperature and concentration.

Based on the results of A6-24(205) an alternative explanation using LaMer growth method was rationalized. In this reaction, the generation of monomers may have reached a limit where further increases in temperature or precursor concentrations may not increase the rate of monomer generation. Instead the nucleation event could possibly be prolonged if the rate of

monomer generation has indeed reached a maximum. This theorized effect is shown in **Figure 3.10** (green curve).

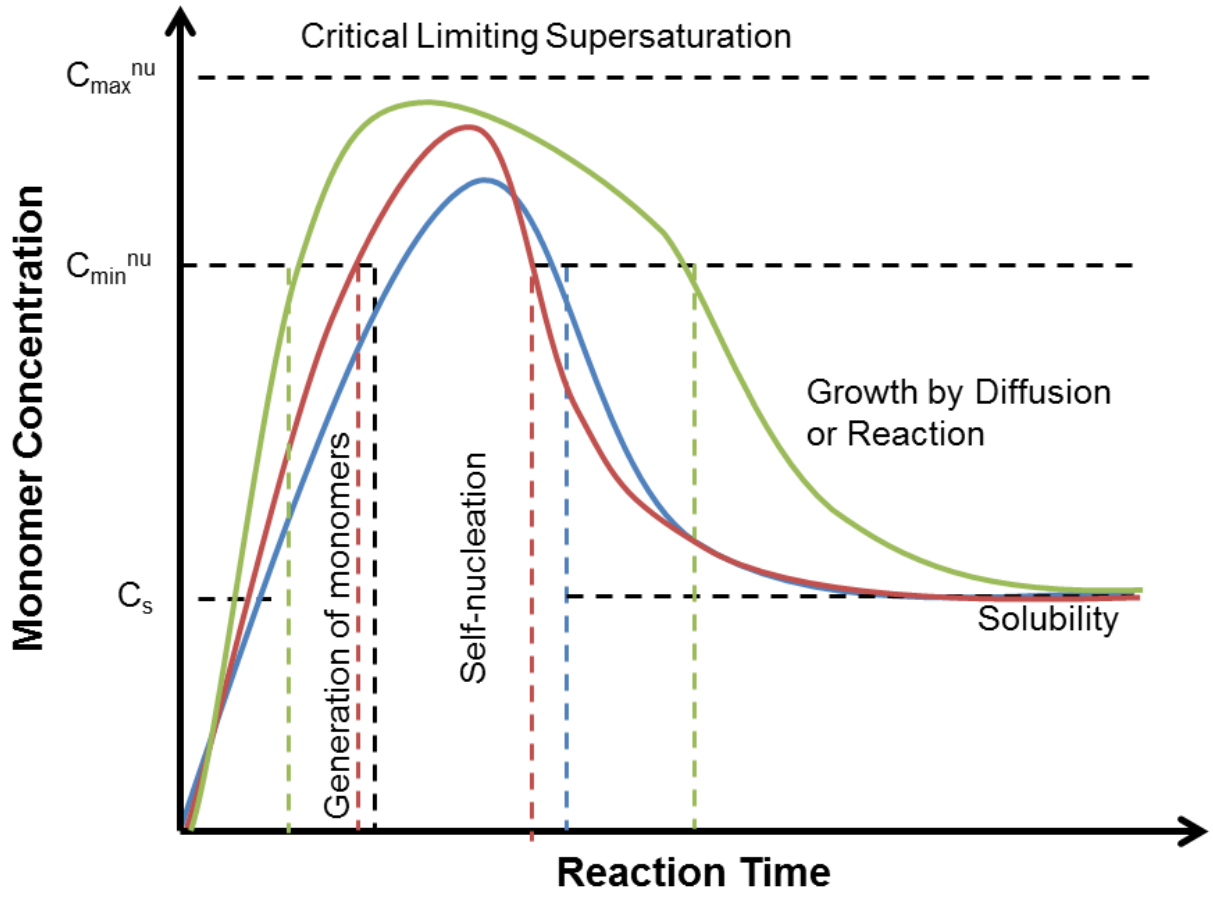

Figure 3.10. Proposed effect of increasing temperature and concentrations of precursor on LaMer growth model (blue). The red curve represents the proposed effects of increasing both temperature and concentration. The green curve represents the proposed effect of increasing both temperature and concentration when a maximum generation of monomers has been reached resulting in prolonged nucleation.

Prolonging the nucleation event would lead to broader size distributions, more nuclei, and smaller particle sizes. More nuclei with a large concentration of monomers would lead to

increased amorphous growth due to growth limited by reaction. This theory is in accordance with the results observed for A6-24(205) which has approximately the same hydrodynamic size (23.9 nm), but a much smaller crystallite size (8.2 ± 1.56 nm) and larger size distribution (PDI= 0.512).

Based on these results of increasing concentration of $Fe(acac)_3$ and temperature, the optimum starting amount of $Fe(acac)_3$ for achieving the largest crystallite sizes is 2 g. The combined increase in reaction temperature and iron precursor for benzyl alcohol synthesis can be rationalized by the LaMer growth model where increasing temperature and/or precursor concentration increases the rate of monomer generation. The largest crystallite size of 14.1 ± 0.80 was achieved in reaction A2-24(205). Since a potential limit was reached for rate of monomer generation at these conditions a modified seed growth method was used in attempts to further increase the crystallite size and decrease size distribution for maximum RF heating potential.

3.3.5 Effect of Parameters: Modified Seed Growth

Seed growth methods have been used to further increase the size of nanoparticles, but often require cooling or aging steps followed by washing and drying the nanoparticles to produce a powder often referred to as "seeds".[129,210,211] Next, the seeds are re-dispersed in the solvent with additional iron precursor prior to carrying out the reaction. A modified seed growth method was developed in attempts to increase the crystallite size and decrease the size distribution to produce optimum nanoparticle properties for RF hyperthermia. Instead of following traditional seed growth methods the nanoparticle "seeds" are not washed and dried to a powder, but are kept at elevated reaction temperatures and additional iron precursor (second addition) is added as a

dry powder. This was done to keep the reaction at suitable temperatures for high rates of monomer generation that will then nucleate and grow on the seeds.

The A2-24 reaction was used as the first half of the modified seed reaction to discern how different temperatures and concentrations of second additions affect the resultant nanoparticle properties. These reactions are listed in **Table 3.6.**

Table 3.6. Effect of various temperatures in the modified seed growth on nanoparticle properties.

Reaction	Magnetization (emu/g)[a]	RF Heating ([°C/min]/mg)[b]	Crystallite size (nm)	Hydrodynamic Diameter (nm)	PDI[c]
A2-24	70.839	0.170	8.8 ± 0.61	13.64	0.703
A2-24(175)	70.91	0.14	8.9 ± 1.39	12.45	0.61
A2-24(195)	74.32	0.18	8.1 ± 0.59	13.3	0.65
A2-24(205)	73.36	2.76	14.1 ± 0.80	24.53	0.275
A2-24_B2-24	75.7	2.536	14.4 ± 2.42	28.93	0.148
A2-24_B2[cool addition]-24	72.488	0.670	9.5 ± 0.71	20.76	0.252
A2-24(175)_B2-24(175)	77.89	1.004	11.6 ± 1.01	24.53	0.404
A2-24(185)_B2-24(185)	77.249	1.068	11.2 ± 0.94	23.11	0.395
A2-24(195)_B2-24(195)	78.202	4.041	14.9 ± 0.74	37.52	0.219
A2-24(205)_B2-24(205)	77.77	5.55	19.5 ± 1.06	44.63	0.265

[a]mass unit indicates grams of FeOx nanoparticles corrected by TGA.

[b]mass unit indicates milligrams of Fe determined by Prussian blue assay.

[c]Polydispersity Index (PDI) determined by DLS.

*VSM data was corrected using 0.925 percent weight of sample

The modified seed growth using the heating mantle (A2-24 and A2-24_B2-24) resulted in larger crystallite size (8.8 ± 0.61 vs. 14.4 ± 2.42) and drastically reduced PDI values (0.703 vs. 0.148). Transmission electron microscopy (TEM) was used to directly image the morphology of the FeOx nanoparticles (**Figure 3.11**).

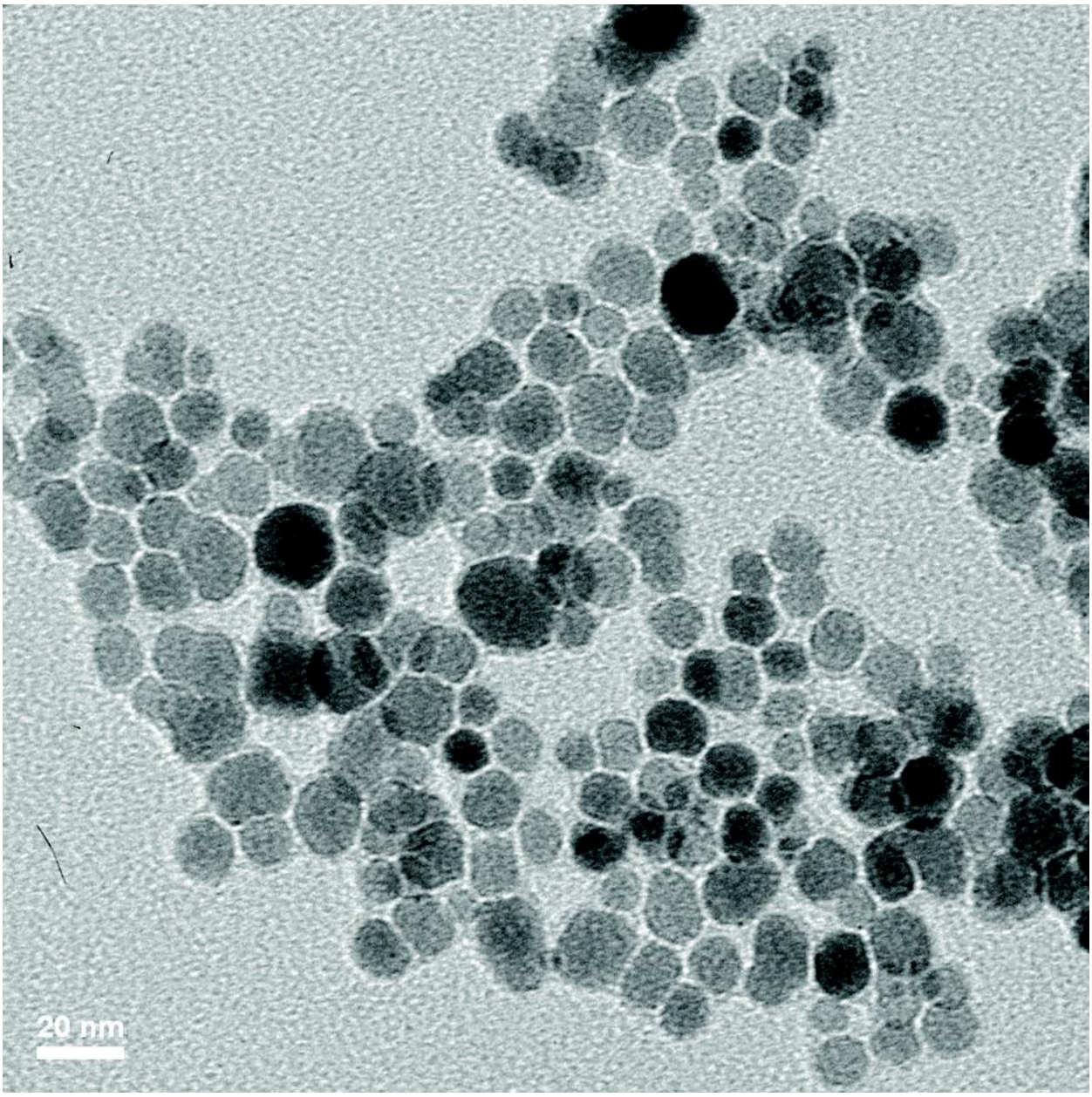

Figure 3.11. TEM bright field image A2-24_B2-24 nanoparticles dispersed with TMAOH. Image J software determined an average particle diameter of 15.28 ± 2.21 nm.

The "hot" addition of iron precursor at the second addition step provides a burst nucleation event producing nuclei that will be dissolved to grow on the thermodynamically favored larger seed nanoparticles. This is also in accordance with Ostwald ripening resulting in a decrease in size

distribution.[208,209] Reaction A2-24_B2$_{[cool\ addition]}$-24 was used to corroborate the "hot" addition effect of lower size distribution by reducing the temperature to 30°C prior to the second addition of $Fe(acac)_3$. Indeed, the hot addition facilitates larger crystallite growth (14.4 ± 2.42 vs. 9.5 ± 0.71 nm) with lower size distribution (PDI= 0.148 vs. 0.252). More specifically, the hot addition facilitates a faster generation rate of monomers.

Temperature was shown to play a significant role in increasing the crystallite size and decreasing polydispersity for reactions without a seed growth step. Temperature was therefore investigated to determine the effect in the modified seed growth. Reactions A2-24(175)_B2-24(175), A2-24(185)_B2-24(185), A2-24(195)_B2-24(195), and A2-24(205)_B2-24(205) were carried out and their characteristics are shown in **Table 3.6**. A2-24(175)_B2-24(175) reaction was used as the starting comparison point for temperature investigation. The crystallite size changed from 11.6 ± 1.01 nm in reaction A2-24(175)_B2-24(175) to 11.2 ± 0.94 at 185°C, 14.9 ± 0.74 at 195°C and 19.5 ± 1.06 at 205°C. The temperature at 185°C did not change the crystallite size which is thought to be explained by insufficient increase in temperature to cause a significant change in the nucleation event. The decrease in size distribution for the modified seed growth at their respective temperatures was thought to be facilitated by the second addition of iron precursor resulting in Ostwald ripening focusing the size distribution. Interestingly, the modified seed growth reaction at 205°C had a crystallite size of 19.5 ± 1.06 and the highest RF heating value 5.55 [oC/min]/mg even though the RF heating capabilities are theorized to exponentially decay above 15-16 nm. The theoretic decrease in RF heating above 15-16 nm is for superparamagnetic nanoparticles only, therefore the theoretic RF heating decrease may not be seen as the nanoparticles above 15-16 nm are most likely switching to single domain particles.

Further analysis of the VSM hysteresis curve for A2-24(205)_B2-24(205) (**Figure 3.12**) reveals some remnant magnetization indicating presence of single domain particles.

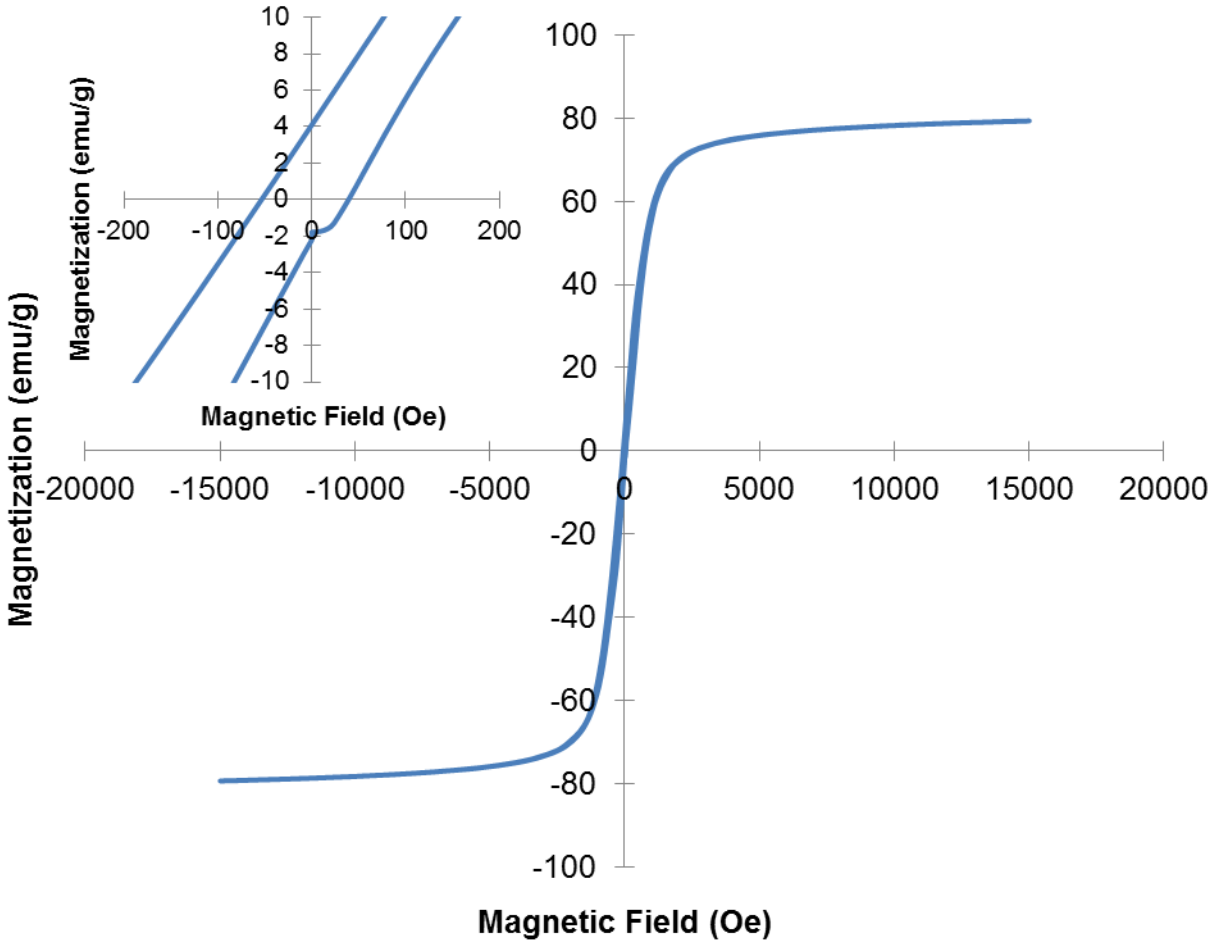

Figure 3.12. Hysteresis curve for reaction A2-24(205)_B2-24(205). Inset shows the remnant magnetization and coercivity is non-zero.

Since the crystallite size determined by XRD is biased towards larger sizes, it is entirely possible that the majority number population of nanoparticles have crystallite sizes closer to 15-16 nm. Using the specific heat of water c_{H2O} = 4.18 $\frac{Ws}{gK}$ as a close approximation of the true specific heat

of the nanoparticle solution, the SAR value was calculated to be 1,175.56 $\frac{W}{g}$. The SAR value was normalized using the H = 37.4 $\frac{kA}{m}$ and f = 270 kHz of the coil used to calculate the ILP value of 3.1127 $\frac{nHm^2}{kg}$. Commercially available synthetic ferrofluids are reported to have ILP values of 0.15-3.12 $\frac{nHm^2}{kg}$.[23]

Next, changes in iron precursor concentration effect in the modified seed growth method were investigated. To do this both first and second additions of $Fe(acac)_3$ were increased. It was thought that the size distribution could be lowered while maintaining the larger crystallite sizes achieved by increasing the temperature. **Table 3.7** lists the reactions where concentration and temperature were changed for the modified seed growth reactions.

Table 3.7. Effect of various $Fe(acac)_3$ concentrations in the modified seed growth on nanoparticle properties.

Reaction	Magnetization (emu/g)[a]	RF Heating ([°C/min]/mg)[b]	Crystallite size (nm)	Hydrodynamic Diameter (nm)	PDI[c]
A2-24(195)_B2-24(195)	78.202	4.04	14.9 ± 0.74	37.52	0.219
A2-24(205)_B2-24(205)	77.77	5.55	19.5 ± 1.06	44.63	0.265
A4-24(195)_B2-24(195)	75.12*	3.13	14.95 ± 2.03	29.5	0.36
A4-24(195)_B4-24(195)	76.56*	4.48	13.4 ±1.61	31.94	0.121
A4-24(205)_B4-24(205)	73.76	2.74	12.4 ± 1.11	26.67	0.146
A4-24(195)_B6-24(195)	76.09	3.43	15.2 ± 1.50	26.6	0.112
A4-24(205)_B6-24(205)	84.57	3.14	15.3 ± 2.45	28.2	0.14
A6-24(195)_B2-24(195)	72.27	2.71	11.4 ± 1.25	43.89	0.305
A6-24(195)_B4-24(195)	73.29	2.88	12.9 ± 0.92	23.5	0.176
A6-24(195)_B6-24(195)	75.1*	2.58	14.1 ±0.98	26.19	0.231

[a]mass unit indicates grams of FeOx nanoparticles corrected by TGA.
[b]mass unit indicates milligrams of Fe determined by Prussian blue assay.
[c]Polydispersity Index (PDI) determined by DLS.
*VSM data was corrected using 0.925 percent weight of sample

Increasing the concentration of the first addition, A4-24(195)_B2-24(195), produced nanoparticles with similar crystallite sizes of 14.95 ± 2.03 nm, but with a higher PDI value of 0.36. This is an important reaction as the RF heating rate was decreased even though the crystallite size was very similar. This is most likely due to the larger PDI value. Increasing the concentration at the second addition was thought to be crucial to utilize Ostwald ripening to minimize the size distribution.[208,209] When the second addition is lower than the first addition there may not be sufficient added monomers to facilitate size distribution focusing and/or retain crystalline growth. This can be seen when comparing reactions A4-24(195)_B2-24(195) and A4-24(195)_B4-24(195). In reaction A4-24(195)_B2-24(195) the second addition of only 2 g resulted in more crystalline growth (14.95 ± 2.03 crystallite size and 29.5 nm hydrodynamic size) compared to reaction A4-24(195)_B4-24(195) having more amorphous growth (13.4 ±1.61 crystallite size and 31.94 nm hydrodynamic size). The more amorphous growth is consistent with the theory of growth limited by reaction. The lower PDI value of 0.121 for reaction A4-24(195)_B4-24(195) (compared to 0.36) most likely explains the higher measured RF heating rate of 4.48 [oC/min]/mg. Size distribution narrowing by increasing the second addition concentration can be explained by having a sufficiently high concentration of monomers where both seeds and newly formed nanoparticles will have an equal number of monomers in their diffusion layer.[212] When this happens the smaller nanoparticles will grow at a faster rate and "catch up" to the larger seed nanoparticles that are growing; this process reduces the surface energy which is energetically favored.[212,213] This means that when larger nanoparticles are produced after the first addition a higher concentration of monomers is required to maintain crystal growth and to reduce the size distribution. Even further reduction in size distribution with more crystalline growth was observed for reaction A4-24(195)_B6-24(195). Similar trend is seen

for reactions A6-24(195)_B4-24(195), and A6-24(195)_B6-24(195) when comparing to reaction A6-24(195)_B2-24(195).

3.3.6 Examination of Radiofrequency Induced Heating Properties

All of the benzyl alcohol reactions were compiled into **Table 3.8** to assess the effects of nanoparticle characteristics and synthetic parameters on RF heating rate. **Table 3.8** was sub categorized by color with nitrogen reactions listed in blue and reactions open to air in green. This color scheme coincides with the colors used in **Figure 3.13 A-F** to graphically compare the nanoparticle characteristics. Several interesting trends can be seen in these comparisons.

First, the reactions open to air all had higher M_s values between 70-85 emu/g except for reaction A2-24(150), whereas the nitrogen reactions were in the range of 48-58 emu/g, (**Figure 3.13 A,C,E**). Thus, the presence of air during the reaction leads to higher magnetization saturation values and possibly magnetite instead of maghemite crystal structures. It is important to point out the M_s value differences as the RF heating is highest for reactions open to air as seen in **Figure 3.13 E**.

Table 3.8. Effect of various $Fe(acac)_3$ concentrations, temperatures, and reaction environment on nanoparticle properties. Reactions are grouped by their reaction environment: nitrogen (blue) and open to air (green).

Reaction	Magnetization (emu/g)[a]	RF Heating ([°C/min]/mg)[b]	Crystallite size (nm)	Hydrodynamic Diameter (nm)	PDI[c]
N_2-A2-24	53.39		6.47 ± 1.17	23.23	0.351
N_2-A2-24(150)	48.54*	0.01	5.65 ± 0.76	13.02	0.372
N_2-A2-24(175)	57.69	0.04	6.06 ± 0.52	11.51	0.306
N_2-A2-24(195)	57.09*	0.02	6.3 ± 0.89		
N_2-A2-24(205)	57.56*	0.05	11.3 ± 0.73	38.48	0.152
A2-24	70.839	0.170	8.8 ±0.61	13.64	0.703
A2-24(125)	-	-	-	-	-
A2-24(150)	55.50	0.06	6.2	13.58	0.589
A2-24(175)	70.91	0.689	8.9 ±1.39	12.45	0.61
A2-24(195)	74.322	0.175	8.1 ± 0.59	13.3	0.65
A4-24	68.99	0.134	8.3	14.68	0.2
A6-24	68.25	0.219	7.9	16.5	0.164
A2-24(205)	73.09	2.76	14.1 ± 0.80	24.53	0.275
A4-24(205)	73.79	1.86	11.7 ± 0.73	22.85	0.269
A6-24(205)	71.19	0.85	8.2 ± 1.56	23.9	0.512
A2-24_B2-24	75.7	2.536	14.4 ± 2.42	28.93	0.148
A2-24_B2[cool addition]-24	72.488	0.670	9.5 ± 0.71	20.76	0.252
A2-24(175)_B2-24(175)	77.89	1.004	11.6 ± 1.01	24.53	0.404
A2-24(185)_B2-24(185)	77.249	1.068	11.2 ± 0.94	23.11	0.395
A2-24(195)_B2-24(195)	78.202	4.041	14.9 ± 0.74	37.52	0.219
A2-24(205)_B2-24(205)	77.77	5.55	19.5 ± 1.06	44.63	0.265
A4-24(195)_B2-24(195)	75.12*	3.13	14.95 ± 2.03	29.5	0.36
A4-24(195)_B4-24(195)	76.56*	4.48	13.4 ±1.61	31.94	0.121
A4-24(205)_B4-24(205)	73.76	2.74	12.4 ± 1.11	26.67	0.146
A4-24(195)_B6-24(195)	76.09	3.43	15.2 ± 1.50	26.6	0.112
A4-24(205)_B6-24(205)	84.57	3.14	15.3 ± 2.45	28.2	0.14
A6-24(195)_B2-24(195)	72.27	2.71	11.4 ± 1.25	43.89	0.305
A6-24(195)_B4-24(195)	73.29	2.88	12.9 ± 0.92	23.5	0.176
A6-24(195)_B6-24(195)	75.1*	2.58	14.1 ±0.98	26.19	0.231
A2-2_B2-24	76.1	0.211	9.3 ± 0.45	20.07	0.373
A2-2_B4-24	72.18	0.212	9.8 ± 1.33	17.72	0.304
A2-2_B6-24	75.56	0.639	10.5 ± 1.02	19.42	0.368

[a]mass unit indicates grams of FeOx nanoparticles corrected by TGA.

[b]mass unit indicates milligrams of Fe determined by Prussian blue assay.

[c]Polydispersity Index (PDI) determined by DLS.

*VSM data was corrected using 0.925 and 0.88 percent weight of samples in air and under nitrogen respectively

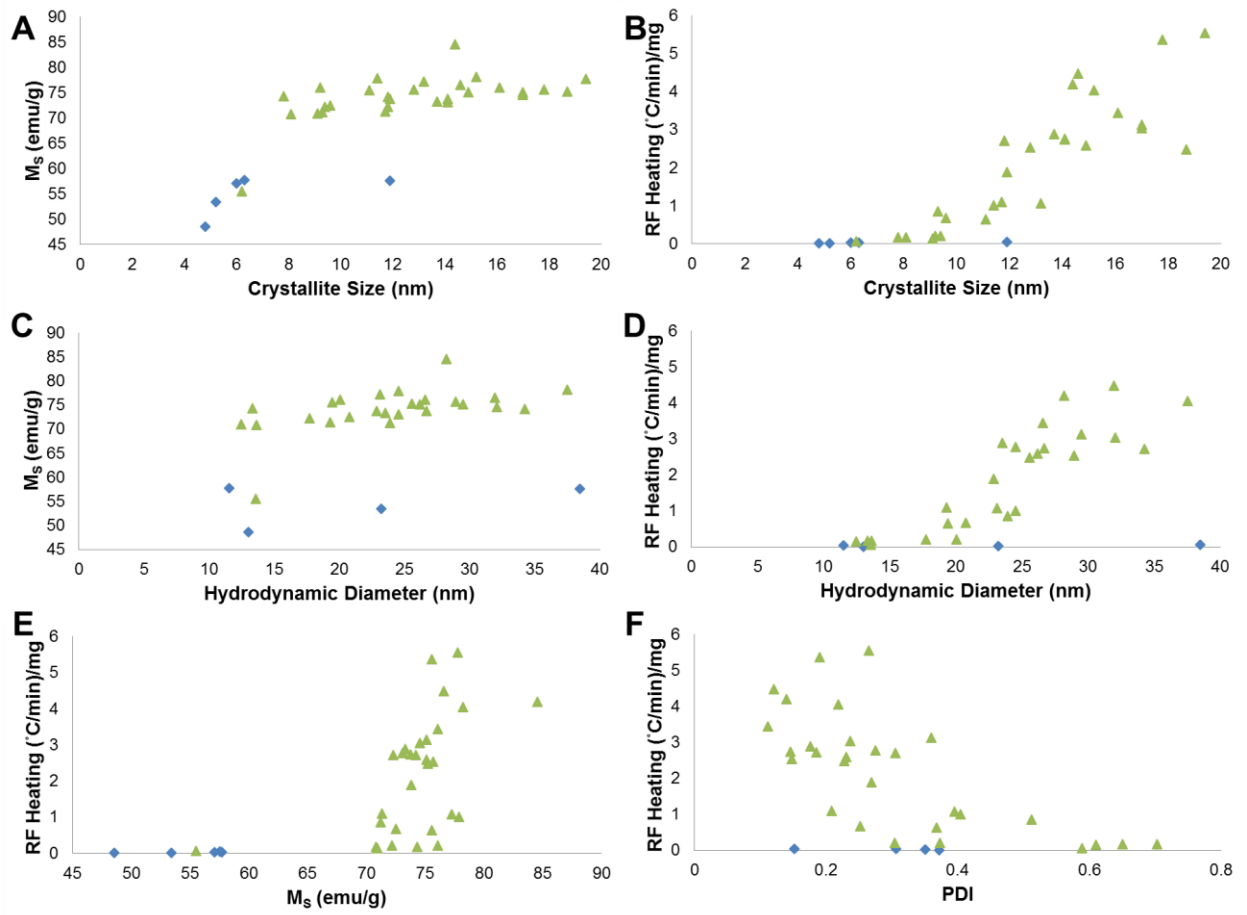

Figure 3.13. Plots comparing nanoparticle properties with reactions under nitrogen and open to air indicated by blue diamonds and green triangles respectively. (A, B) Plots of crystallite size versus M_s and RF heating. (C, D) Plots of hydrodynamic diameter versus M_s and RF heating. (E) Plot showing M_s versus RF heating. (F) Plot of polydispersity index versus RF heating.

Next, there is a strong trend between crystallite size and RF heating. This was expected based on previously reported literature. Similarly there is a correlation between hydrodynamic diameter and RF heating, however it is hard to determine if this is a real trend or just due to the hydrodynamic diameter increasing as crystallite size increases. The linear correlation between hydrodynamic diameter and crystallite size can be seen in **Figure 3.14 B.** There potentially exists

an optimal crystallite to hydrodynamic size ratio for RF heating based on being able to provide maximum heat loss to surrounding solution. **Figure 3.14 A** indicates no clear correlation between crystallite size and size distribution. Therefore, the trend of increasing RF heating as size distribution decreases is most likely real. Overall, the effect of crystallite size, hydrodynamic diameter, and size distribution appear to have the most impact on RF heating.

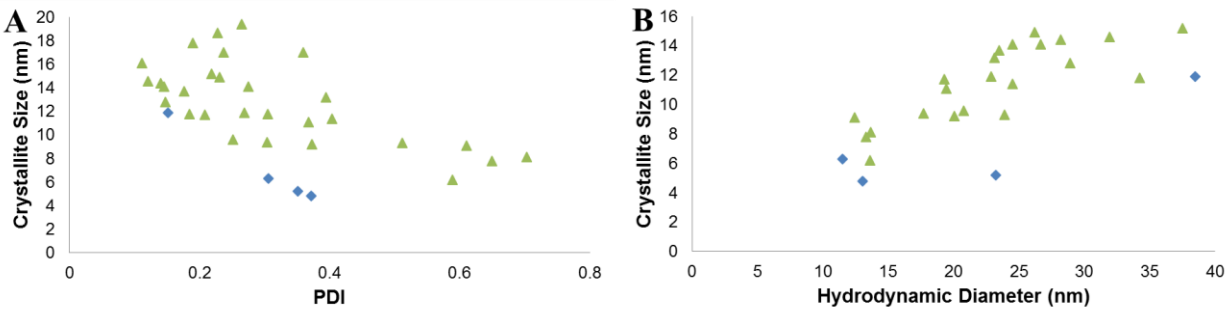

Figure 3.14. Plots comparing PDI versus crystallite size (A) and hydrodynamic diameter versus crystallite size (B) for reactions under nitrogen and open to air indicated by blue diamonds and green triangles respectively.

Based on these initial comparisons JMP software was used to screen the effects and determine which nanoparticle properties are significantly affecting RF heating. JMP software was also used to further elucidate the reaction parameters that significantly affect nanoparticle properties. All of the reactions open to air were used for effect screening. After determining which nanoparticle properties significantly affect the RF heating rates, a model was created and tested to determine its effectiveness in predicting RF heating based on nanoparticle properties. Likewise, models were created to determine nanoparticle properties based on reaction parameters.

The effects of crystallite size, hydrodynamic diameter, PDI, magnetization saturation, and ratio of crystallite size to hydrodynamic diameter determined by volume (Volume CS/HS) on RF heating were analyzed for the seed growth syntheses listed in **Table 3.9**. The effect screening table is shown in **Figure 3.9**. Analysis of variance determined that crystallite size, PDI, and volume CS/HS were all significant (**Table 3.11**). Crystallite size had the most significant effect on RF heating. A model was created using least squares and emphasis on effect leverage of the significant nanoparticle properties to estimate the resultant RF heating. The ANOVA had a significance of <0.0001 indicating that the 3 nanoparticle properties did have a significant effect on the RF heating. The actual predicted fit plot is shown in **Figure 3.15** and has an R^2 value of 0.95. The parameter estimates (**Table 3.12**) were used to formulate **Equation 17** to predict RF heating, where CS and HD are crystallite size and hydrodynamic diameter. Crystallite size, volume CS/HS, and PDI had prob>t values of <0.0001, 0.0002, and 0.0002 respectively.

Table 3.9. List of seed growth syntheses and nanoparticle properties used in the effect screening and predicted model.

	Crystallite Size	Hydrodynamic Diameter	PDI	Ms	RF Heating	CS/HS	Volume CS/HS
A2-24(175)_B2-24(175)	11.4	24.53	0.404	77.89	1.00	0.46	0.1
A2-24(185)_B2-24(185)	13.2	23.11	0.395	77.249	1.07	0.57	0.19
A2-24(195)_B2-24(195)	15.2	37.52	0.219	78.202	4.04	0.41	0.07
A6-24(195)_B2-24(195)	11.8	43.89	0.305	72.27	2.71	0.27	0.02
A2-24(205)_B2-24(205)	19.4	44.63	0.265	77.77	5.55	0.43	0.08
A6-24(195)_B4-24(195)	13.7	23.5	0.176	73.29	2.88	0.58	0.2
A6-24(195)_B6-24(195)	14.9	26.19	0.231	75.10	2.58	0.57	0.18
A4-24(195)_B2-24(195)	17	29.5	0.36	75.12	3.13	0.58	0.19
A4-24(195)_B4-24(195)	14.6	31.94	0.121	76.56	4.48	0.46	0.1
A4-24(195)_B6-24(195)	16.1	26.6	0.112	76.09	3.43	0.61	0.22
A4-24(205)_B6-24(205)	14.4	28.2	0.14	84.57	4.19	0.51	0.13
A4-24(205)_B4-24(205)	14.1	26.67	0.146	73.76	2.74	0.53	0.15
A2-24(205)_B2-24(205)	17.8	43.92	0.19	75.59	5.36	0.41	0.07

Table 3.10. Effect screening of crystallite size, hydrodynamic diameter, PDI, magnetization saturation, and volume CS/HS on RF heating.

Term	Contrast		Lenth t-Ratio	Individual p-Value	Simultaneous p-Value
Crystallite Size	1.05604		8.76	0.0006*	0.0044*
VOLUME CS/HS	-0.54518		-4.52	0.0071*	0.0488*
PDI	-0.57009		-4.73	0.0057*	0.0428*
Ms	0.10951		0.91	0.3305	0.9955
CS/HS	-0.07613		-0.63	0.5582	1.0000
Hydrodynamic Diameter	-0.00486		-0.04	0.9704	1.0000
Crystallite Size*Crystallite Size	-0.00493	*	-0.04	0.9702	1.0000
Crystallite Size*VOLUME CS/HS	-0.04050	*	-0.34	0.7665	1.0000
VOLUME CS/HS*VOLUME CS/HS	-0.08034	*	-0.67	0.5120	1.0000
Crystallite Size*PDI	0.12447	*	1.03	0.2736	0.9790
VOLUME CS/HS*PDI	0.17518	*	1.45	0.1426	0.7691
PDI*PDI	0.10654	*	0.88	0.3445	0.9972

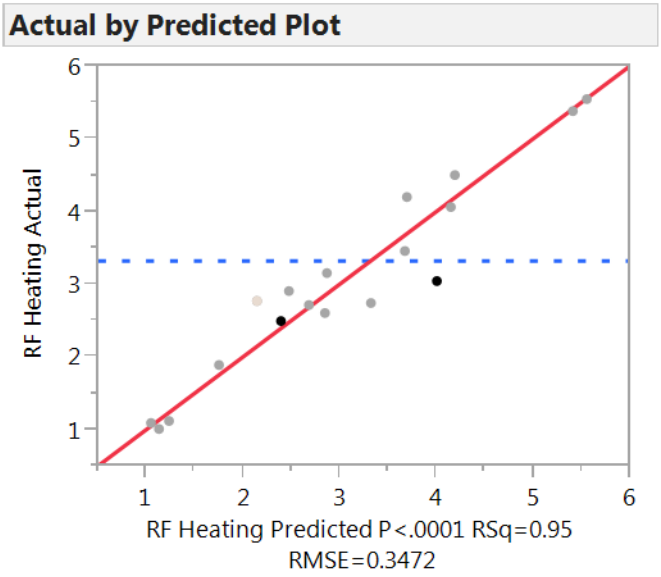

Figure 3.15. The actual vs predicted RF heating fit of the model of crystallite size, PDI, and volume CS/HS on RF heating.

Table 3.11. ANOVA results for the predicted model effect of significant nanoparticle properties on RF heating.

Source	DF	Sum of Squares	Mean Square	F Ratio
Model	3	22.58684	7.52895	62.4514
Error	9	1.085012	0.12056	**Prob > F**
C. Total	12	23.67185		<.0001

Table 3.12. Parameter estimates for the model fit least squares of significant nanoparticle properties effecting RF heating.

Term	Estimate	Std Error	t Ratio	Prob>|t|
Intercept	-0.26799	0.816764	-0.33	0.7503
Crystallite Size	0.423428	0.04583	9.24	<.0001
VOLUME CS/HS	-9.93554	1.614326	-6.15	0.0002
PDI	-6.01891	1.016722	-5.92	0.0002

$$RF=-0.26799+(0.423428*CS)+(-9.93554*\text{Volume CS/HS})+(-6.01891*PDI) \quad (17)$$

Table 3.13. Predicted and actual RF heating values.

	RF Heating	
Synthesis	**Predicted**	**Actual**
A3-24(205)_B3-24(205)	4.025245	3.037383
A2.5-24(205)_B2.5-24(205)	2.387036	2.481686
A2-24_B2-24	1.224124	1.092966

Using the properties of reactions A3-24(205)_B3-24(205), A2.5-24(205)_B2.5-24(205), and A2-24_B2-24 the RF heating values were predicted using **Equation 17** as shown in **Table 3.13**. The predicted RF heating values were in close agreement with measured RF heating values for reactions A2.5-24(205)_B2.5-24(205), and A2-24_B2-24. The A3-24(205)_B3-24(205)

predicted RF heating values were larger than the actual RF heating values (4.025245 (oC/min)/mg vs. 3.037383 (oC/min)/mg). It is speculated that the model is a good predictor of the actual measured RF heating considering the large amount of compounding measurement errors. Further reactions would increase the validity of the model and increase the efficiency in predicting RF heating values.

Next, the reaction pararmeters of temperature, first addition, and second addition were investigated to screen for effects on resulting nanoparticle properties. Only crystallite size, PDI, and volume CS/HS were investigated as they were found to be the only significant predictors of RF heating. The effect screening was unable to predict crystallite size, PDI, or volume CS/HS with an acceptable R^2 value. The effect screening identified a 'null term' indicating that there is some additional factor influencing the nanoparticle properties besides temperature, first addition amount, and second addition amount. Further investigation is needed to determine this additional effect. However, it is speculated that this could be due to the reaction concentration affecting the heating rate. Another possible explanation is that there is insufficient data regarding the nanoparticle properties at 24 hours after the first addition to accurately determine how the second addition affects the final resulting properties. Further analysis using the nanoparticle properties after 24 hours of reaction as a starting point for predicting increase in crystallite size could reveal the important parameter.

Chapter 4: Surface Functionalization of Benzyl Alcohol Synthesized Iron Oxide Nanoparticles

4.1 Experimental Section

4.1.1 Reagents, Materials, and Equipment

All chemicals and materials were used as received. Water (H_2O) (Fisher Scientific, Optima ® LC/MS grade), Tetramethylammonium hydroxide (TMAOH) solution (Alfa Aesar, 25% w/w aq.), poly (vinyl alcohol) (Polysciences, Inc., MW ~6000, 80 mol% hydrolyzed), bromoacetic acid (Alfa Aesar, 98+%), sodium hydroxide (NaOH) (Alfa Aesar, pearl, 97%), 70% ethanol (EtOH) (Sigma Aldrich, 200 proof for molecular biology), ethanol (Pharmco-AAPER, 190 proof ACS/USP grade), (3-Aminopropyl)trimethoxysilane (APTS) (Alfa Aesar, 97%), (3-aminominopropyl)triethoxysilane (APTES) (Alfa Aesar, 98%), (3-Glycidyloxypropyl) trimethoxysilane (GLYMO) (Acros Organics,98%), L-cysteine (Cys) (Alfa Aesar, 98+%), DL-serine (Ser) (Alfa Aesar, 99%), DL-arginine (Arg) (Alfa Aesar, 98%), DL-lysine monohydrochloride (Lys) (Alfa Aesar, 99%), DL-Threonine (Thr) (Alfa Aesar, 99%), glycine (Gly) (Alfa Aesar, 99%), L-glutamine (Gln) (Sigma, ≥99%), L-(+)-asparagine (Asn) (Alfa Aesar, 99%), hydroxylamine HCl, citric acid, anhydrous (BDH, 99.5-100.5%), (S)-(-)-4-Amino-2-

hydroxybutyric acid (SAHBA) (Aldrich Chemistry, 96%), γ-aminobutryic acid (ABA) (Sigma Life Science ≥99%), ethylenediamine (EDA) (Acros Organics, 99+%, extra pure), tetraethylenepentamine (TEPA) (Acros Organics, technical grade), hydrochloric acid (HCl) (Fischer, Optima™, 32-35%), 0.2 µm filter (PALL Life Sciences, Acrodisc® Syringe Filter 0.2 µm Supor® Membrane Low Protein Binding), 30k, and 100k molecular weight cutoff (MWCO) centrifuge filter (PALL Life Sciences, Macrosep® Advance Device), PD-10 desalting column (GE Healthcare, Sephadex® G-25 medium), Fe inductively coupled plasma (ICP) standard (Alfa Aesar, Iron, plasma standard solution, Specpure®, Fe 1000 µg/mL), hydrochloric acid solution (HCl) (Electron Microscopy Sciences, 20%), potassium ferrocyanide aqueous solution (Prussian Blue) (Electron Microscopy Sciences, 20%), S-2-(4-Aminobenzyl)-1,4,7,10-tetraazacyclododecane tetraacetic acid (DOTA) (Macrocyclics), $^{177}LuCl_3$ (Perkin Elmer), 1-Ethyl-3-(3-dimethylaminopropyl)carbodiimide (EDC) (Thermo Scientific), N-hydroxysulfosuccinimide (S-NHS) (Thermo Scientific), β–mercaptoethanol (Sigma Aldrich), ammonium hydroxide (Fisher Scientific, Optima grade), 0.25 M ammonium acetate , and 0.1 M 2-(*N*-morpholino)ethanesulfonic acid (MES) buffer containing 0.9% NaCl (Optima grade NH_4OH adjusted pH =6.4).

4.1.2 Synthesis of Carboxymethylated Polyvinyl Alcohol (CMPVA)

Polyvinyl alcohol (PVA) can be reacted with bromoacetic acid and base to synthesize carboxymethylated polyvinyl alcohol (CMPVA) as previously reported.[94,130] First, three different solutions were made including: Solution A – 5 g of PVA dissolved in 50 mL of H_2O, Solution B – 5.324 g of sodium hydroxide (NaOH) dissolved in 25 mL of H_2O, and Solution C – 11.575 g of bromoacetic acid dissolved in 200 mL of 70% ethanol (EtOH). To Solution C 3.33 g of NaOH

was added slowly and stirred to dissolve. Solution A was set on a stirring hot plate and heated to 50°C with constant stirring prior to slow addition of Solution B. Next, a drop wise addition of Solution C, to the mixed Solution A and B was carried out and reacted under a reflux condenser for five hours to carboxymethylate the PVA. After carboxymethylation, the pH of the CMPVA was measured and adjusted to approximately 6.0 with a 1 M solution of hydrochloric acid. The CMPVA was then precipitated out of solution by addition of cold EtOH. The precipitated CMPVA in cold EtOH was centrifuged at 3,000×g for 15 minutes (Thermo Scientific, Sorvall Legend X1R centrifuge) to remove any unreacted chemicals. This process was repeated 3-6 times to fully wash the CMPVA. The washed CMPVA was then dried using a vacuum oven set at 50°C for one week.

4.1.3 Surface Functionalization with CMPVA

To modify the surface with CMPVA, 40 mg of dry FeOx nanoparticles were sonicated for 180 minutes in 2 mL of 0.0625%, 0.125%, 0.25%, or 0.5% w/w aqueous tetramethyl ammonium hydroxide (TMAOH) solution. Dispersing the nanoparticles prior to addition of surface functionalization ligands is crucial to efficiently surface functionalize individual nanoparticles. During the entire surface functionalization procedure the nanoparticles were not magnetically stirred to prevent possible aggregation due to magnetic fields causing additional interparticle attraction. A 40 mg/mL CMPVA solution was made by dissolving dry CMPVA in water with low heating and stirring. Next, 10 mL of the 40 mg/mL CMPVA solution was diluted with 9.5 mL of H_2O immediately prior to addition of 0.5 mL of the nanoparticle TMAOH solution. This solution was sonicated for 180 minutes. The initial dilution of CMPVA was found to aid in the nanoparticle surface functionalization. It is thought that surface functionalization is

more efficient at lower concentrations of nanoparticles, which reduces the distance between nanoparticles during CMPVA surface functionalization. The nanoparticle CMPVA solution was allowed to sit for one week. In first attempts at surface functionalization with CMPVA the nanoparticle CMPVA solution was allowed to sit for 2 weeks, however the particles initially became clear at 1 week. Therefore, 1 week was chosen as the minimal amount of time, since nanoparticles in CMPVA were still turbid at 24-48 hours.

Next, CMPVA-FeOx nanoparticles were washed using a 30k molecular weight cut-off (MWCO) centrifugal filter spun at 4,000×g to remove excess CMPVA and any residual TMAOH. This centrifuge process also concentrated the nanoparticle solution. This concentrated solution was transferred to a clean vial and sonicated briefly (15 minutes) to aid in proper re-dispersion. Further clean-up was carried out using a disposable PD-10 desalting column that was equilibrated with H_2O. This step was used to remove non-functionalized or aggregated nanoparticles as well as any remaining TMAOH. The desalting column diluted the sample slightly, so an additional 30k centrifuge filter was spun at 4,000×g for one hour. A 0.2 µm sterile filter was used in a biosafety laminar flow hood to sterilize the CMPVA-FeOx nanoparticles and remove any CMPVA-FeOx clusters larger than 200 nm.

4.1.4 Surface Functionalization with APTS or APTES

Surface functionalization with APTS or APTES was performed by adding 10 mg of dry FeOx nanoparticles to a 0.125% TMAOH solution. This was sonicated for 30 minutes to disperse the nanoparticles. Prior to addition of APTS or APTES the nanoparticle TMAOH solution was diluted with 8 mL of H_2O and vortexed briefly (10 seconds). Immediately after dilution, either 1.78 mL of (3-Aminopropyl)trimethoxysilane (APTS) or 2.38 mL (3-

aminominopropyl)triethoxysilane (APTES) was added dropwise followed by a quick 10 second vortex spin. The surface modification reaction was magnetically stirred at 60°C for one hour. The solution pH was adjusted to about 7.4 with 32-35% hydrochloric acid (HCl) solution. Magnetic separation for 1 hour was used to pull out partially, incompletely, or aggregated surface functionalized nanoparticles. The remaining clear honey colored top solution was 0.2 μm filtered to remove any large APTS or APTES nanoparticles as well as any excess reacted APTS or APTES that may clog up the centrifuge filter. This solution was then washed 3-5 times with H_2O in a 30k MWCO centrifuge filter spun at 4,000rpm for 10 minutes in a swing bucket centrifuge. In the final wash step the solution was concentrated to 1.5 mL and the pH was readjusted to about 7.4. Sterile filtration with a 0.2 μm filter in a biosafety laminar flow hood was used to obtain the final sterile surface functionalized product.

4.1.5 Surface Functionalization with GLYMO and Base Catalyzed Epoxide Ring Opening with Nucleophiles

The surface functionalization process with GLYMO started with adding 10 mg of dry FeOx nanoparticles to 10 mL of 0.125% TMAOH solution. The nanoparticle TMAOH solution was sonicated for 30 minutes to fully disperse the nanoparticles. This solution was then further diluted upon addition of 8 mL of H_2O prior to addition of 2.25 mL of 3-Glycidyloxypropyl trimethoxysilane (GLYMO) (0.0114 mol). It is essential that the GLYMO be added all at once rather than dropwise to facilitate efficient surface modification. Following the GLYMO addition, the solution was vortexed for 10 seconds and then magnetically stirred and heated at 60°C for 1 hour. After approximately 15 minutes of reaction the solution changed colors from a clear brown solution to a muddy brown solution. This indicated surface modification with GLYMO, as the

terminal epoxy groups should render the nanoparticles unstable at the high pH. The three membered epoxy ring was opened through a base catalyzed reaction with addition of a nucleophile. This reaction could have been acid-catalyzed, but this was not done as low pH could start to dissolve the surface of the FeOx nanoparticles. Additional base (1.6 mL of 25% TMAOH) was added immediately prior to addition of 1:1 molar ratio of the following nucleophiles: glycine (Gly) (0.86 g), DL-serine (Ser) (1.2g), γ-aminobutyric acid (ABA) (1.18 g), or (S)-(-)-4-amino-2hydroxybutyric acid (SAHBA) (1.36 g), L-cysteine (Cys) (1.38 g), DL-lysine-monohydrochloride (Lys) (2.08 g), L-glutamine (Gln) (1.67 g), DL-arginine (Arg) (1.86 g), L-(+)-asparagine (Asn) (1.51 g), DL-Threonine (Thr) (1.36 g), hydroxylamine (0.79 g) or citric acid, anhydrous (2.19 g). Ethylenediamine (EDA) (0.763 mL) or tetraethylenepentamine (TEPA) (2.18 mL) were also used, but no additional TMAOH base was added as these chemical compounds are inherently basic. The reaction was continued at 60°C with magnetic stirring for 1 hour. At this point the reaction was removed from heat and the pH was adjusted with 32-35% HCl to a pH of about 7.4. As a first cleanup step any nanoparticles that were not stable were magnetically separated for 1 hour. Only the top clear honey colored stable solution of nanoparticles was removed and subjected to a 0.2 μm filter. Next, the particles were washed with water 3-5 times in a 30k molecular weight cutoff (MWCO) centrifuge filter spinning at 4,000 rpm for 10 minutes. The final wash was spun down to approximately 3 mL and the solution was then subjected to a disposable PD-10 desalting column equilibrated with water or PBS. As a final step the nanoparticles pH was checked and adjusted to 7.4 and then sterilized with a 0.2 μm filter in a biosafety laminar flow hood to obtain the final product.

4.1.6 EDC Coupling DOTA Chelate and Radiolabeling

The SAHBA-FeOx and CMPVA-FeOx nanoparticles were linked to DOTA metal chelate by EDC coupling reaction. First, 500 µL of SAHBA-FeOx or CMPVA-FeOx were mixed with 500 µL of 0.1 M MES buffer (NH_4OH adjusted pH=6.4). Next, 100 mg of EDC was dissolved in 500 µL Ultra H_2O and 100 mg of S-NHS was dissolved in 500 µL Ultra H_2O. Activation of the carboxyl groups was performed by addition of 100 µL of EDC solution. The activated carboxyl groups were stabilized by addition of 100 µL of the S-NHS solution. After 10 mins 2 µL of β–mercaptoethanol was added. In 100 µL of Ultra grade H_2O 2 mg of DOTA was dissolved and then added to the FeOx in MES buffer to form an amide bond between the terminal amine on the DOTA chelate and the activated carboxyl groups of SAHBA-FeOx or CMPVA-FeOx. The reaction was allowed to react for 1.5 hours, before quenching with 100 µL of 0.275 M hydroxylamine. The resultant DOTA-SAHBA-FeOx or DOTA-CMPVA-FeOx were buffered exchange with a PD-10 column equilibrated with ammonium acetate.

Radiolabeling with ^{177}Lu was performed by adding 40 µL of $^{177}LuCl_3$ (~10 mCi) and 20 µL of NH_4OH to the DOTA-SAHBA-FeOx or DOTA-CMPVA-FeOx in ammonium acetate. The maximum beta energy of ^{177}Lu is 0.497 MeV (79%), but the average beta energy is 0.13 MeV. The ^{177}Lu also has two gamma energies at 208 keV (11%) and 113 keV (6.4%). The chelation of ^{177}Lu by DOTA was carried out at 40°C in a silicon oil bath overnight. The silicon oil bath was magnetically stirred. An MCX column was used to remove any free ^{177}Lu from ^{177}Lu-DOTA-SAHBA-FeOx or ^{177}Lu-DOTA-CMPVA-FeOx. A PD-10 column was used to buffer exchange ^{177}Lu-DOTA-SAHBA-FeOx or ^{177}Lu-DOTA-CMPVA-FeOx into non-sterile DPBS and to remove any free ^{177}Lu-DOTA or DOTA chelate. The 'washed' ^{177}Lu-DOTA-SAHBA-FeOx or ^{177}Lu-DOTA-CMPVA-FeOx were then concentrated using a 3k MWCO

centrifuge filter spinning at 4,000 rpm in a swing bucket centrifuge for 10 minutes. The final product was obtained by 0.2 µm filtering in a sterile laminar flow hood.

4.2 Characterization Techniques

4.2.1 Fourier Transform Infrared (FTIR) Attenuated Total Reflectance (ATR) Spectroscopy

Fourier transform infrared (FTIR) attenuated total reflectance (ATR) spectroscopy is paramount when analyzing the chemistry of colloid surfaces such as surface functionalized FeOx nanoparticles.[214] The ability to analyze the surface functionalization in the aqueous environment is advantageous as it prevents the possibility of altering the surface functionalization during drying steps or removal from the aqueous environment.[214] The attenuated total reflectance utilizes the properties of an internal reflectance element (IRE) with a high refractive index. These properties allow for the interface between the IRE and sample to be probed with infrared radiation. When the infrared radiation interacts with the interface an evanescent wave will penetrate slightly into the sample and absorb resulting in an absorption spectrum.[214] The depth of penetration (d_p) depends on the incident wavelength (λ), refractive index of IRE (n_1), refractive index of sample (n_2), and angle of incidence (θ) (**Equation 18**).[214]

$$d_p = \frac{\lambda}{2\pi n_1 \sqrt{\sin^2\theta - \left(\frac{n_2}{n_1}\right)^2}} \quad (18)$$

When the infrared light interacts with the surface of the sample, after passing through the IRE, the created perpendicular standing wave becomes 'attenuated' if the sample absorbs the infrared light.[214] The refractive wave will lose some energy and is termed 'attenuated total reflectance'.[214]

FTIR-ATR spectroscopy was performed on a Thermo Scientific Nicolet 6700 equipped with a smart iTR for ATR to analyze liquid or dry samples. Single bounce ATR was used to examine all samples placed on the diamond crystal. The ATR system used has a penetration depth of 2.03 μm at an incident wavelength of 1000 cm^{-1}, an incident wavelength angle of 42º, and a refractive index of 2.4.

4.2.2 X-ray Photoelectron Spectroscopy (XPS)

X-ray photoelectron spectroscopy (XPS) was performed on a Thermo Scientific ESCALAB 250 spectrometer using a monochromatic Al Kα X-ray source (1486.6 eV). External and internal flood guns were utilized to account for the organic coatings with charge composition. Sample preparation involved pressing nitrogen dried samples onto a strip of indium foil and attachment to the sample holder with double-sided adhesive carbon tape. CasaXPS software was used to analyze all data. Adventitious carbon at 284.8 eV was used to correct the observed binding energies.

4.2.3 High-Performance Liquid Chromatography (HPLC)

High-performance liquid chromatography (HPLC) was performed using a Waters isocratic HPLC system, equipped with UV-VIS absorbance and radioactivity (Bioscan) detectors to determine the radiochemical purity of radiolabeled FeOx nanoparticles eluted from a size exclusion-gel permeation chromatography column. The buffer used was 90% 50 mM ammonium acetate and 10% methanol. Aqueous samples were loaded before DOTA coupling to FeOx, after radiolabeling and MCX column, and after PD-10 column wash steps.

4.3 CMPVA Discussion

4.3.1 Surface Functionalization and Optimization for Biostability

The following naming system was used to keep track of the different types of surface functionalizations. The abbreviation of the respective surface functionalization precedes 'FeOx' and is separated by a hyphen. For example, carboxymethylated polyvinyl alcohol surface functionalized FeOx nanoparticles are referred to as 'CMPVA-FeOx'. Any additional modifications to the surface functionalization will precede the surface functionalization abbreviation and will also be separated by a hyphen.

Carboxymethylated polyvinyl alcohol (CMPVA) was used to provide colloidal and biological stability as well as providing terminal carboxyl groups for future conjugation. Optimization of this process is beneficial to facilitate higher yield, better biological stability, and increased biofunctionalization potential. The carboxyl groups on CMPVA polymer interact strongly with the surface iron atoms of FeOx nanoparticles and create a hydrophilic surface due to terminal carboxyl and hydroxyl groups.[94] Therefore, it is important to optimize the surface functionalization process to ensure that an adequate number of carboxyl groups interact with the FeOx surface and a sufficient number of carboxyl groups are oriented outward to provide solution stability and sites for further conjugation. Optimization is especially important to determine how to effectively surface functionalize differently sized nanoparticles as even small changes in nanoparticle size will have drastic differences in surface area to volume ratio for a given gram amount of material. Several parameters were investigated to determine how to best adjust reaction parameters to functionalize varying nanoparticle sizes.

First, the carboxymethylation of polyvinyl alcohol was confirmed by FTIR-ATR spectroscopy of CMPVA. The spectrum from FTIR-ATR of CMPVA is shown in **Figure 4.1**.

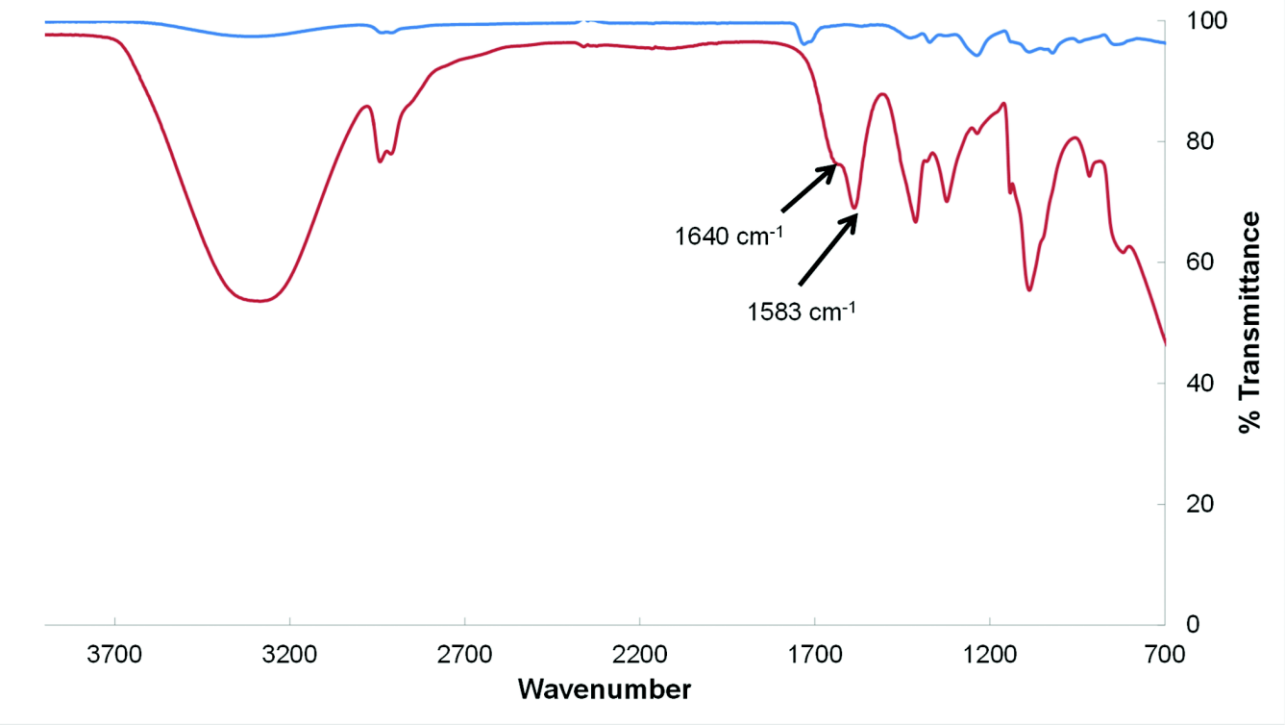

Figure 4.1. The FTIR spectra shown as % transmittance vs wavenumber is shown with polyvinyl alcohol in blue, and carboxymethylated polyvinyl alcohol in red. Peaks at 1640, 1583 and 1417 indicate the presence of carboxylate anion and the peak at 1089 cm^{-1} indicates the ether group. Polyvinyl acetate presence was indicated by peak at 1730 cm^{-1}. The disappearance of the 1730 cm^{-1} peak and appearance of peaks at 1600 and 1417 cm^{-1} are indicative of acetate groups being replaced by carboxylate ion groups in CMPVA.

Peaks at 1640 and 1417 cm^{-1} are indicative of asymmetrical C=O stretching mode for carboxylate ion and the peak at 1089 cm^{-1} indicates asymmetrical stretching of C-O-C respectively.[215] Typically the surface functionalization of FeOx nanoparticles with CMPVA involves a difficult phase transfer process to establish aqueous colloidal stability. The as synthesized nanoparticles were stable in organic solutions such as chloroform and were transferred to an aqueous 1.5% TMAOH solution by mixing overnight. The dry FeOx

nanoparticles produced by the modified seed growth method in benzyl alcohol were uniquely able to be dispersed in TMAOH directly and without the use of organic solutions such as chloroform. This is one large advantage to using the benzyl alcohol synthesized nanoparticles. The previously reported CMPVA surface functionalization methods did not provide long term colloidal stability in PBS, tissue culture medium, or other biologically relevant medium. It was thought that the previous methods had been optimized for their particular FeOx nanoparticle synthesis and certain factors may influence the efficiency of surface modification including pH, nanoparticle diameter, base concentration, and number of polymer per nanoparticle. These factors were investigated in an attempt to improve surface functionalization efficiency.

The concentration of TMAOH used was first investigated as the initial step is to disperse the nanoparticles in a TMAOH solution. It is advantageous to have well dispersed nanoparticles to properly surface functionalize individual nanoparticles and thus limit the amount of bridging or coating of aggregated nanoparticles. Low and high concentrations of base can lead to insufficient nanoparticle separation. Several concentrations (0.0625%, 0.125%, 0.25%, and 0.5% w/w TMAOH) were used to disperse the nanoparticles (20 mg/mL; 40:1 CMPVA to FeOx mass ratio). FeOx nanoparticles in these TMAOH solutions were analyzed with DLS to determine differences in hydrodynamic diameter and dispersion of nanoparticles. The hydrodynamic diameters were similar (26.42 ± 1.31 nm) as well as the PDI values throughout the different TMAOH concentrations as shown in **Table 4.1.** At each step in the surface functionalization procedure and wash steps DLS was performed. This provided an easy way to analyze the initial base concentration effect on efficiency of surface functionalization.

Table 4.1. Initial hydrodynamic diameters and PDI values for various v/v % concentration of TMAOH.

% TMAOH	Hydrodynamic Diameter (nm)	PDI[a]
0.0625	25.99	0.38
0.125	29.96	0.363
0.25	23.61	0.39
0.5	26.12	0.41

[a]Polydispersity Index (PDI) determined by DLS.

The results from the DLS investigation are shown in **Figure 4.2**. Aliquots were taken from four time points throughout the surface functionalization procedure and were labelled steps 1-4. Aliquots were taken before 30k MWCO centrifuge filter (step 1), after 30k MWCO centrifuge filter (step 2), and first (step 3) and second (step 4) fractions of elution from disposable PD-10 desalting column. Large hydrodynamic diameters indicate possible bridging between nanoparticles and/or functionalizing an aggregation of nanoparticles. Large PDI values indicate large size distributions which are indicative of multiple size populations and/or aggregation. As can be seen with the 0.0625% TMAOH nanoparticle solution the PDI value was 0.51 and only 5% of nanoparticles were not above 1000 nm (**Figure 4.2 A**). This is in accordance with the visual observation that the solution became turbid and had visible aggregation and precipitation after CMPVA was introduced. It was not surprising that subsequent steps 2-4 also contained large hydrodynamic diameters and PDI values.

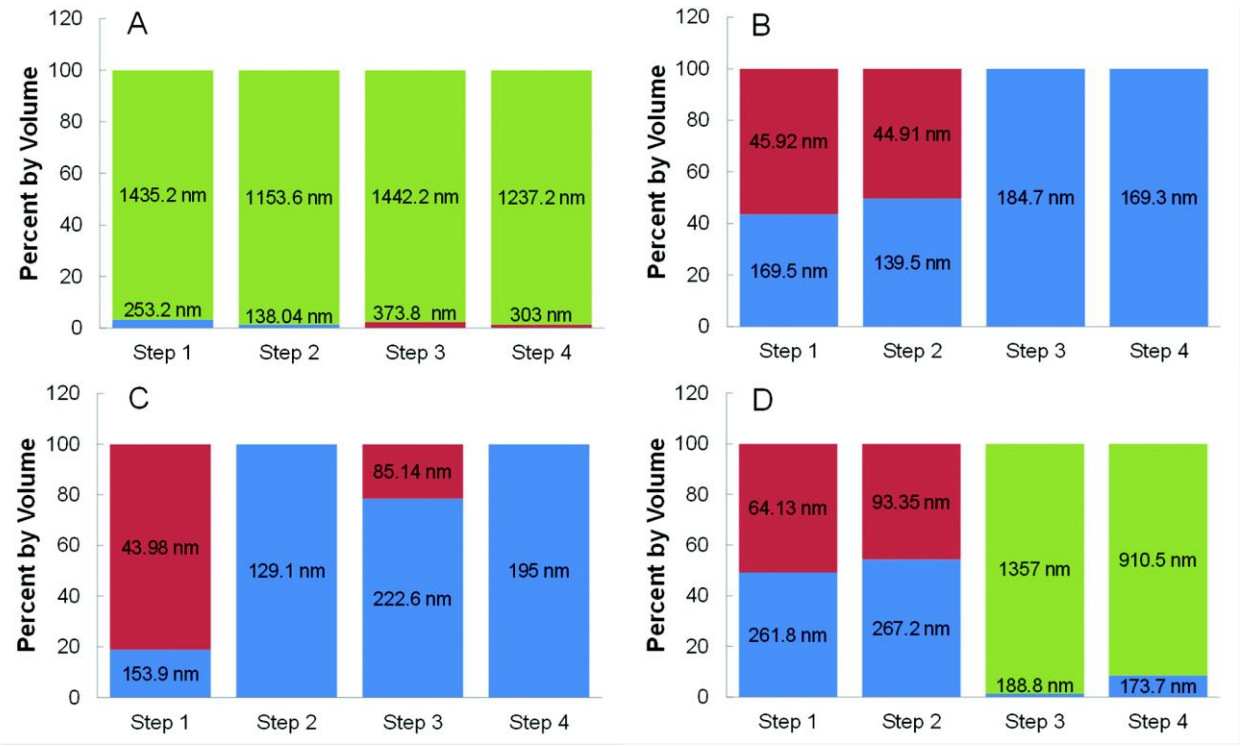

Figure 4.2. DLS hydrodynamic size measurements at 4 steps throughout the surface functionalization process with CMPVA based on several TMAOH concentrations. The concentrations of TMAOH used were (A) 0.0625% TMAOH, (B) 0.125% TMAOH, (C) 0.25% TMAOH, and (D) 0.5%. The four steps when aliquots were taken are listed in order: before and after a 30k MWCO centrifuge filter and 1st and 2nd elution fractions from a PD-10 desalting column. Small, medium, and large hydrodynamic diameters correspond to inadequately functionalized (red), adequately functionalized (blue), or aggregated nanoparticles (green).

To investigate if the pH after addition of CMPVA was sufficient in maintaining dispersion, samples of CMPVA only and FeOx nanoparticles containing CMPVA were titrated with TMAOH. The pH changes upon addition of 6.25% TMAOH to solutions of CMPVA only and

FeOx nanoparticles containing CMPVA are shown in **Figure 4.3.** Identical reaction concentrations of CMPVA and nanoparticles were used when titrating with 6.25% TMAOH.

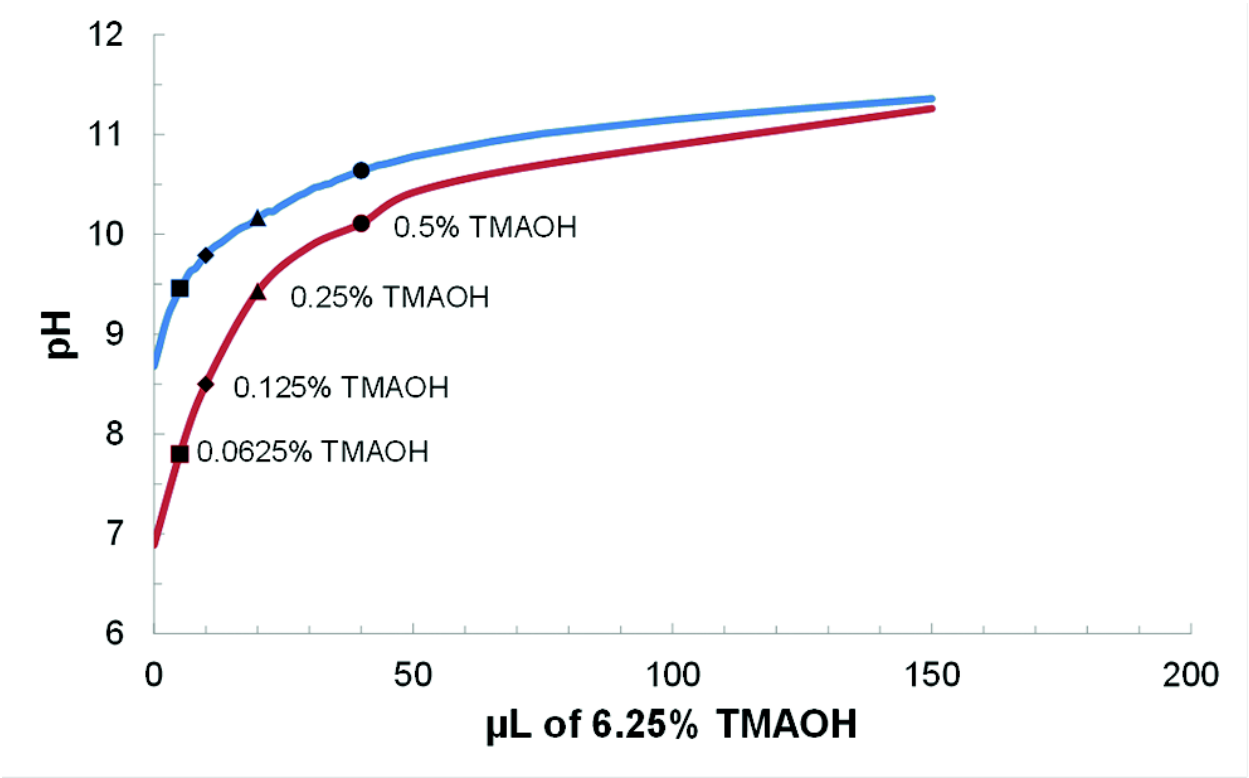

Figure 4.3. Solutions of CMPVA (blue) and FeOx nanoparticles with CMPVA (red) titrated with 6.25% TMAOH. Several markers indicate solution pH when TMAOH concentrations used in the DLS study were reached.

A pH above 8.5 was deemed necessary to maintain a dispersion of nanoparticles for efficient surface functionalization with CMPVA. It was concluded that 0.0625% TMAOH offered a sufficiently high pH to initially disperse the nanoparticles, but the nanoparticles quickly aggregated due to a pH drop upon addition of CMPVA. As can be seen in **Figure 4.3** the pH of nanoparticles with CMPVA at 0.0625% drops below 8.5 to a pH of 6.89. Next, the pH changes at

the 0.5% TMAOH solution in **Figure 4.3** revealed that the 0.5% TMAOH concentration provided dispersion for the functionalization with CMPVA (steps 1 and 2 in **Figure 4.2 D**), however after elution from the PD-10 desalting column (steps 3 and 4 in **Figure 4.2 D**) it is apparent that removal of TMAOH by the desalting column resulted in the nanoparticles aggregating and crashing out of solution. This instability was further confirmed by a large amount of crashed nanoparticles on the PD-10 column and the large percentage by volume (>90%) with hydrodynamic diameters exceeding 1000 nm. The crashed nanoparticles on the PD-10 column were most likely stabilized by TMAOH only since nanoparticles dispersed in TMAOH only completely crashed when loaded on to a PD-10 desalting column. All of these observations and results leads to the interpretation that the high concentration of TMAOH prevented an adequate exchange of TMAOH with CMPVA. A high concentration gradient of TMAOH results in retention of more TMAOH than CMPVA resulting in TMAOH molecules being more likely to re-interact with the FeOx surface. While the 0.5% TMAOH solution resulted in mainly unstable nanoparticles there was a small population of 188.8 and 173.7 nm hydrodynamic diameter nanoparticles that were attributed to 'inadequately functionalized' CMPVA surface functionalized nanoparticles. They were termed this because they displayed aggregation and loss of colloidal stability over time. It is thought that the removal of TMAOH led to reordering of the CMPVA on FeOx nanoparticles leading to bridging and aggregation. This exemplifies the importance of the PD-10 desalting column step to increase the long term stability and separate a stable population. While the 0.5% TMAOH solution resulted in surface functionalization of a small population of nanoparticles, this concentration did not produce the desired long term stability.

The 0.125% and 0.25% TMAOH FeOx nanoparticle solutions resulted in stable CMPVA surface functionalized nanoparticles. There were crucial differences that can be seen after elution from the PD-10 desalting column (step 3- **Figure 4.2 C**). It can be seen that 20% of the population of the 0.25% TMAOH nanoparticle solution is inadequately functionalized. Similar to the 0.5% TMAOH step 3 and 4, the removal of TMAOH from the 0.25% TMAOH nanoparticle solution revealed that there was a population that was not fully functionalized and would lead to aggregation through bridging and/or reordering of CMPVA polymers. Interestingly, when the TMAOH was removed in steps 3 and 4 for the 0.125% TMAOH nanoparticles solution the population shifted from a 50:50 population of adequately to inadequately functionalized nanoparticles to 100% adequately surface functionalized nanoparticles. Additionally, the PDI values for 0.125% and 0.25% TMAOH nanoparticles solutions were 0.169 and 0.163 respectively indicating small size distributions and minimal aggregation or crashing. Since, 0.125% TMAOH nanoparticle solution had a larger initial population of adequately CMPVA surface functionalized nanoparticles (step 1) it resulted in a higher overall yield. Of the four TMAOH concentrations tested the 0.125% was chosen as the best concentration for CMPVA surface functionalization.

Subsequently, the above conditions were tested on a different size of nanoparticles to determine the methods applicability. Reaction A2-24_B2-24 nanoparticles (used in TMAOH concentration study) had a crystallite size of 12.8 nm and a hydrodynamic diameter of 28.9 nm. Nanoparticles produced by reaction A2-24(195)_B2-24(195) were chosen as they had a crystallite size of 15.2 nm and a hydrodynamic diameter of 37.5 nm. First, the same surface functionalization conditions and methods as above were tested on the larger nanoparticles (20 mg/mL CMPVA, 0.125% TMAOH, and same mass ratio of CMPVA to nanoparticles). This

method did indeed functionalize the surface with CMPVA; however the final product's hydrodynamic size was 310.97 ± 51 nm which resulted in aggregation and precipitation. Additionally, this size is too large to be sterile filtered and is therefore less applicable regardless of stability. The large resultant hydrodynamic diameter was thought to be a result of excessive CMPVA concentration leading to higher chances of crosslinking or bridging of multiple nanoparticles. The same mass amount of smaller nanoparticles contains a greater number of total nanoparticles and a larger total surface area which greatly offsets the ratio of CMPVA to nanoparticles. An approximate ratio of number of CMPVA molecules to number of FeOx nanoparticles or total surface area was calculated. The nanoparticles were treated as spheres as TEM confirmed spherical nanoparticle morphology. The surface area and volume of a sphere were used to simplify the calculations. The density of magnetite (5.17 g/cm^3) was used when determining the number of nanoparticles in 10 mg of sample by mass. The total number of nanoparticles and surface area of one nanoparticle were used to determine the total surface area of 10 mg of nanoparticles. The 400 mg of CMPVA, used to functionalize the surface of A2-24_B2-24 nanoparticles, equates to 66.67 μmoles or 4.015×10^{19} of 6,000 molecular weight CMPVA. The surface area, volume and mass of one nanoparticle are shown in **Table 4.2** to illustrate the large differences of particle properties with small changes in the diameter of nanoparticles.

Table 4.2. Values of nanoparticle properties calculated using crystallite and hydrodynamic diameter.

Crystallite diameter (nm)	Volume (m^3)	SA (m^2)	SA/V	Mass of 1 NP (g)
12.8	1.10E-24	5.15E-16	0.47	5.68E-18
15.2	1.84E-24	7.26E-16	0.39	9.51E-18
Hydrodynamic Diameter (nm)				
28.9	1.26E-23	2.62E-15	0.21	6.53E-17
37.5	2.76E-23	4.42E-15	0.16	1.43E-16

The total number and total surface area of nanoparticles in 10 mg sample are shown in **Table 4.3**. These ratios were used to determine the amount of CMPVA to use for the investigation of surface functionalizing larger nanoparticles by matching the ratios used in the TMAOH optimization for CMPVA surface functionalization.

Table 4.3. Total number and surface area of nanoparticles in 10 mg are shown based on different crystallite and hydrodynamic diameters. The ratio of the number of CMPVA molecules to both nanoparticles and total surface area are also shown.

Crystallite diameter (nm)	# of NP in 10 mg	SA in 10 mg (m^2)	#of CMPVA:NP	# of CMPVA:SA
12.8	1.76E+15	9.07E-01	2.28E+04	4.43E+19
15.2	1.05E+15	7.64E-01	3.82E+04	5.26E+19
Hydrodynamic Diameter (nm)				
28.9	1.53E+14	4.02E-01	2.62E+05	1.00E+20
37.5	7.01E+13	3.09E-01	5.73E+05	1.30E+20

Based on the ratios calculated it was determined that when the crystallite size increased from 12.8 to 15.2 nm the CMPVA concentration should be 11.9 mg/mL. Likewise, based on hydrodynamic diameter increase from 28.9 to 37.5 nm the CMPVA concentration should be 9.15

mg/mL. When the CMPVA concentration was adjusted based on surface area it was determined that 16.8 mg/mL and 15.4 mg/mL be used respective of calculations using crystallite or hydrodynamic diameter. It should be noted that the original article[94] used slightly different crystallite (15 nm instead of 15.2 nm) and hydrodynamic diameter (30 nm instead of 28.9 nm and 37 nm instead of 37.5 nm) values which resulted in calculating 12.4 mg/mL and 10.7 mg/mL CMPVA concentration based on total number of particles for crystallite and hydrodynamic size respectively and 17.1 mg/mL and 16.2 mg/mL based on total surface area for crystallite and hydrodynamic size respectively. Since, hydrodynamic diameter is larger than the particle size and crystallite size is smaller than the particle size the values were averaged. Optimally 2.28×10^{4} CMPVA molecules should be used for every one nanoparticle or 4.43×10^{19} CMPVA molecules should be used based on the total surface area of 10 mg. Using the same mass amount of A2-24(195)_B2-24(195) nanoparticles the above averaged values were used to determine if calculations based on total number or total surface area is more accurate. Two surface functionalization attempts with 11.6 mg/mL and 16.7 mg/mL of CMPVA (values from original article that were tested) were used in place of 20 mg/mL CMPVA originally used. Aliquots of the two surface functionalizations were taken before and after a 30k MWCO centrifuge filter and from 3 elution fractions from a PD-10 desalting column to compare the efficiency (**Figure 4.4**). It was determined that adjusting the CMPVA concentration based on number of nanoparticles (11.6 mg/mL of CMPVA) lead to more efficient functionalization of nanoparticles.

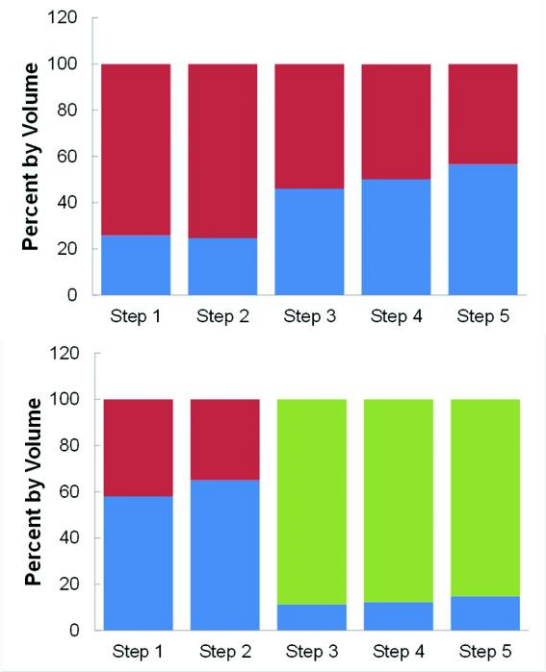

Figure 4.4. DLS hydrodynamic size measurements based on volume for different CMPVA concentrations based on total number of nanoparticles (A) (11.5 mg/mL CMPVA) or surface area (B) (16.6 mg/mL) in 10 mg of FeOx nanoparticles at various steps in the clean-up process. Depending on the hydrodynamic size the volume population of nanoparticles was labelled as either functionalized (blue), partially functionalized (red), or aggregated (green) nanoparticles. The four steps when aliquots were taken are listed in order: before and after a 30k MWCO centrifuge filter and 1st and 2nd elution fractions from a PD-10 desalting column.

The resultant CMPVA nanoparticles had an average hydrodynamic size of 199.97 ± 34.04 nm (50%) and 54.79 ± 24.53 nm (50%) with a PDI of 0.206 (**Figure 4.4**). The hydrodynamic size of A2-24(195)_B2-24(195) CMPVA nanoparticles is slightly larger than the A2-24_B2-24 CMPVA nanoparticles, but they were stable in various media. This was expected since A2-24(195)_B2-24(195) nanoparticles had a larger crystallite and hydrodynamic size before CMPVA surface functionalization. The CMPVA surface functionalization based on surface area

had a majority of nanoparticles with large hydrodynamic diameters (approaching 1000 nm). This suggests that the nanoparticles were aggregating due to a high concentration of CMPVA.

CMPVA surface functionalization of A4-24(195)_B6-24(195) nanoparticles for broad stability assessment was carried out with some minor modifications to the CMPVA surface functionalization method. These modifications were used as they more closely resemble the surface modification procedure of APTS, APTES, and GLYMO that were used in the stability assessment. The initial dispersion of nanoparticles in TMAOH solution was only sonicated for 30 minutes prior to addition of CMPVA solution. The time allotted for CMPVA modification of the surface was 24 hours instead of 1 week. FTIR-ATR was used to confirm successful surface functionalization with CMPVA. **Figure 4.5** displays the FTIR-ATR spectra of bare FeOx nanoparticles and water. The normalized FTIR-ATR spectra of CMPVA nanoparticles with water subtracted out is shown in **Figure 4.6**. FTIR-ATR was carried out on CMPVA-FeOx in solution to discern the functional groups without potentially altering the functional groups which may have occurred by drying nanoparticles to a fine powder prior to FTIR characterization. In **Figure 4.6** the C-H stretching vibrations, asymmetrical C=O stretching mode for dimerized saturated carboxylic acids, and asymmetrical stretching of C-O-C are indicated respectively by the existence of peaks at 2940, 1716, and 1092 cm^{-1}. The 2940 cm^{-1} peak can be attributed to C-H stretching vibrations of the carbon chain in CMPVA instead of the very strong and broad O-H stretching vibrations due to subtraction of water from the spectra.

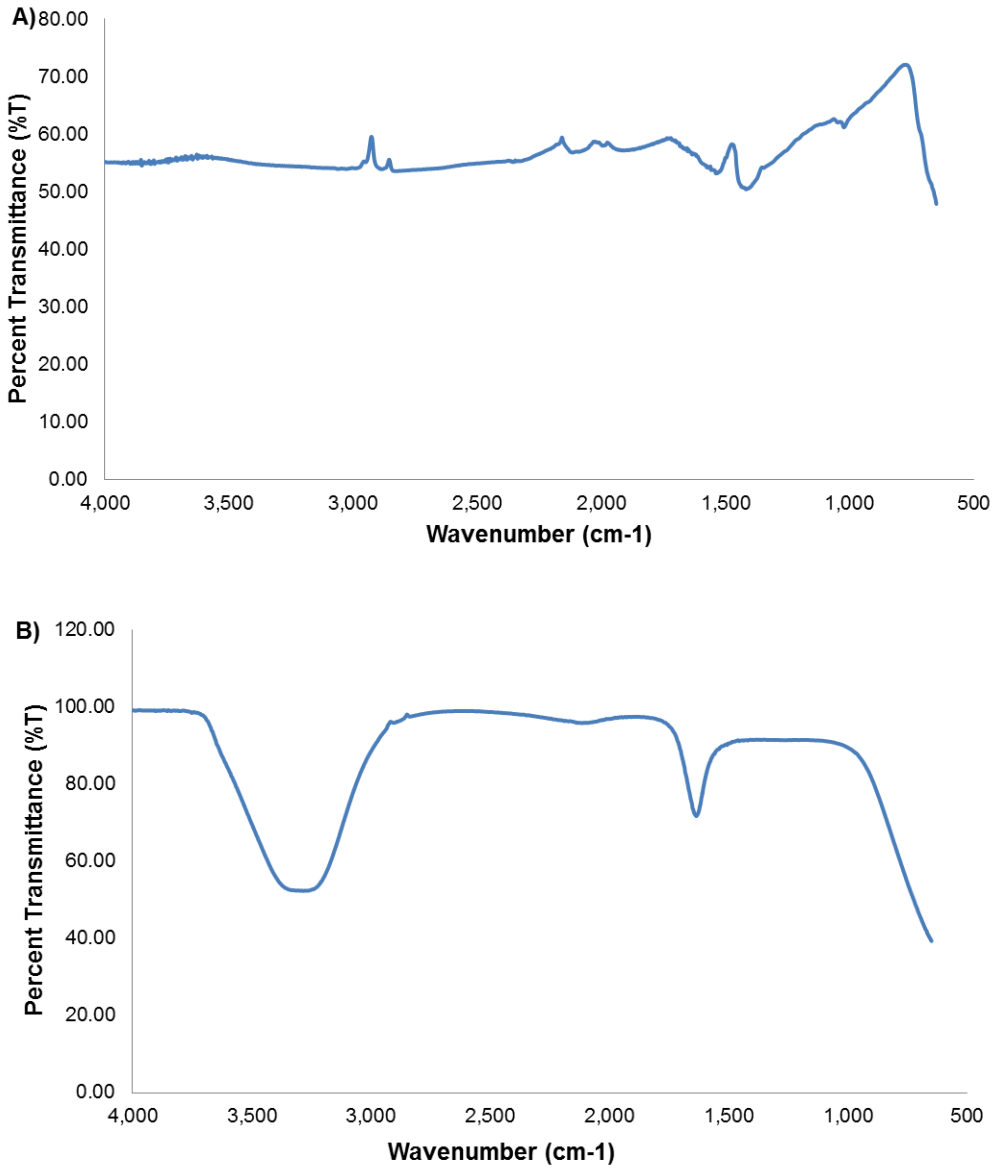

Figure 4.5. FTIR-ATR spectra of A) FeOx nanoparticles and B) water.

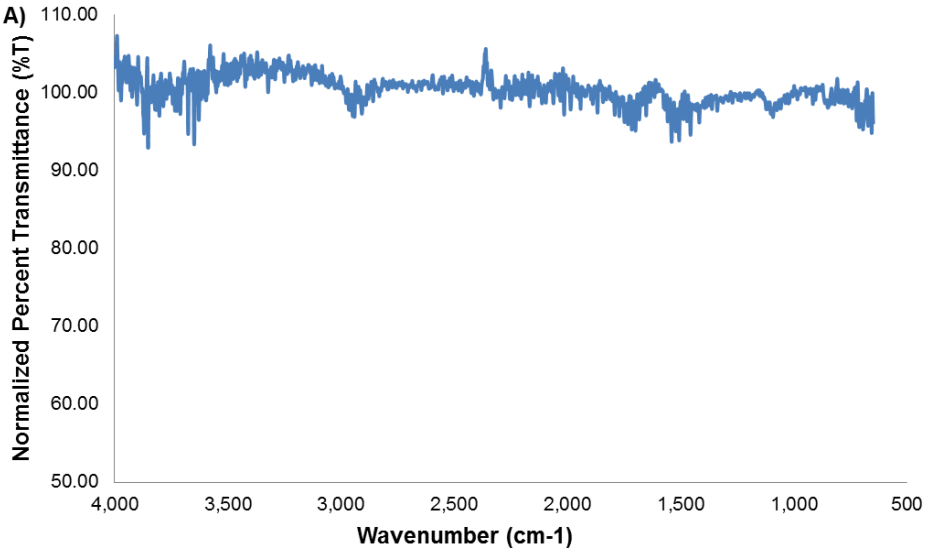

Figure 4.6. Normalized FTIR-ATR spectra of CMPVA-FeOx aqueous solution with water subtracted.

DLS was also used to confirm modification of FeOx nanoparticles with CMPVA (**Figure 4.7**). Interestingly, the shorter sonication time used to disperse nanoparticles and shorter CMPVA reaction time reduced the resultant hydrodynamic size to 91.6±20.53 (100%) with a PDI value of 0.148±0.015. This is important as this is the upper limit of the "optimal size" of nanoparticles to avoid opsoinzation and clearance from the body, and to facilitate more passive targeting. Zeta potential further corroborated the presence of CMPVA on FeOx nanoparticles. A negative zeta potential indicated carboxylic acid groups at pH=7.4 (**Figure 4.8**).

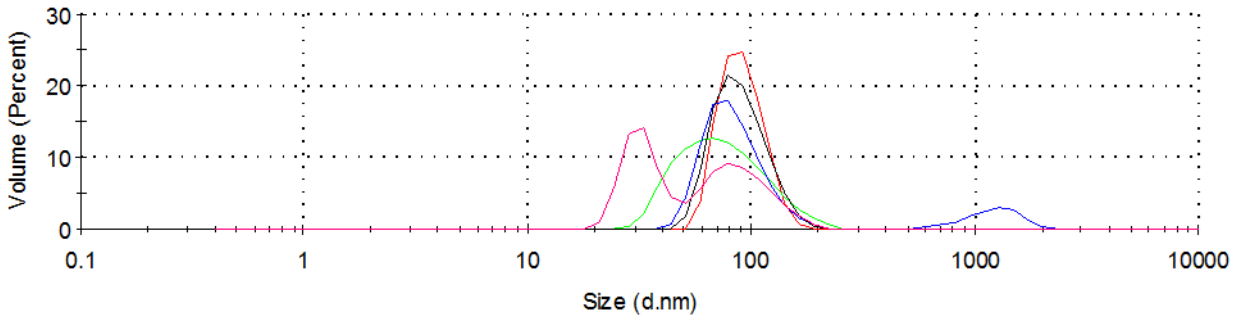

Figure 4.7. DLS hydrodynamic diameter by volume percentage for CMPVA-FeOx.

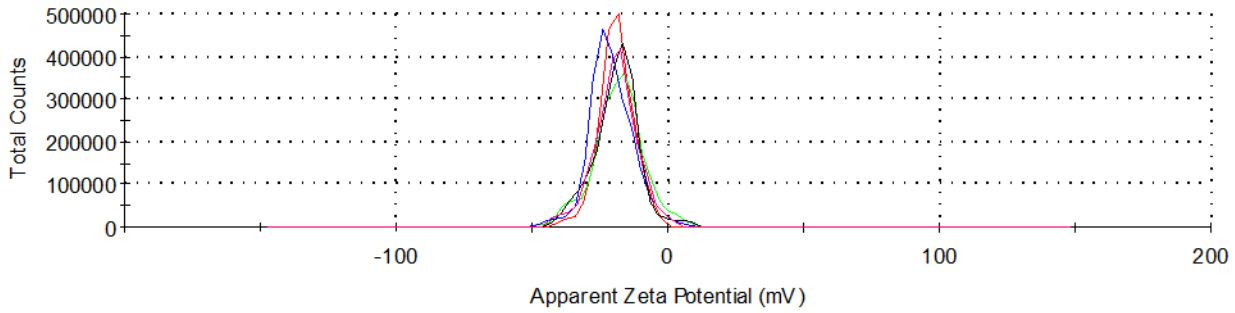

Figure 4.8. Zeta potential measurement of CMPVA -FeOx.

4.4 Silane Surface Functionalization of Iron Oxide Nanoparticles

FeOx nanoparticles (A4-24(195)_B6-24(195)) were surface functionalized with three silane ligands including GLYMO, APTS, and APTES. These silane surface functionalizations are used in many applications including corrosion protection,[216-218] adhesive durability,[219] semiconductor coatings,[220-223] and surface passivation[224] and are well characterized and understood for bulk materials. GLYMO was chosen because the epoxy ring can be easily opened with a base catalyzed reaction involving nucleophilic ligands to provide a multitude of surface functionalizations with different properties. This epoxy ring opening can be base or acid catalyzed allowing for rapid alterations in the surface chemistry such as charge and terminal functional groups present. These alterations however will have significant effects on the stability in different buffers and medium. Therefore investigate how different ligands affect the stability in different aqueous stability will provide a better understanding of how the stability can be tailored by choice of ligands. APTS-FeOx and APTES-FeOx were used as comparison surface functionalizations in the stability assessment as they are a commonly used in literature to surface functionalize nanoparticles for aqueous stability.[225,226] Hydrolysis and condensation of APTS,

APTES, and GLYMO to the surface of FeOx nanoparticle results in a silica-like shell or network surrounding the FeOx nanoparticle. However, the inherent solubility and rate of hydrolysis of each silane notably affects the resultant surface functionalization efficiency.[150] The solubility difference of APTS and APTES compared to GLYMO determined how the silanes were added to the nanoparticle solution. A slow drop-wise addition of APTS and APTES was required for efficient surface functionalization. APTS and APTES are most soluble at pH~10 in water. Therefore when adding these silanes to the TMAOH nanoparticle solution (high pH), a quick addition could lead to a high local concentration of the silanes and a nucleation event preventing efficient condensation on the surface of the FeOx nanoparticles. Upon titration to pH 7.4 with HCl the terminal amine groups of APTS-FeOx and APTES-FeOx provided sufficient colloidal stability and were ready for subsequent wash and purification steps.

In contrast, GLYMO is highly soluble at pH=5.3. The complete and rapid addition of GLYMO facilitates the generation of an emulsion-like suspension where the GLYMO ligands will interact with the FeOx and condense to the surface in the proper orientation. The condensation can be visibly seen as the clear brown TMAOH nanoparticle solution changes to a "muddy brown" color after 10-15 minutes of reaction. This color change is the result of the alteration of solubility of the nanoparticles due to the terminal epoxy groups of the GLYMO shifting the nanoparticle stability to lower pH. At this point addition of extra TMAOH base and nucleophiles were used to open the epoxy ring to provide aqueous stability. Addition of a nucleophile at the high pH resulted in an immediate color change from "muddy brown" to clear brown indicating the successful base-catalyzed epoxy ring opening. This color change was not always indicative of aqueous stability as the addition of Lys, Arg, Cys, Thr, Asn, Gln, hydroxylamine, or citric acid did not result in colloidal stability once the pH was adjusted to 7.4.

Only Gly, Ser, EDA, TEPA, ABA or SAHBA proved to provide sufficient colloidal stability at pH=7.4. **Figure 4.9** is a visual comparison of sufficient colloidal stability provided by Gly and Ser at pH=7.4, even in the presence of a rare earth magnet, and the unstable and precipitated solutions of Lys, Gln, Arg, and Cys.

Figure 4.9. Visual aqueous stability assessment at pH=7.4 in presence of a magnet of several nucleophilic ligands used to open the GLYMO epoxy ring. Aqueous stability was indicated by a clear brown top solution as seen in Gly-FeOx and Ser-FeOx. From left to right: Lys-FeOx, Gln-FeOx, Gly-FeOx, Ser-FeOx, Arg-FeOx, and Cys-FeOx.

The instability in a magnetic field is critical in identifying unstable nanoparticles and is used as the first step in the washing and purification process. Bridging and aggregation due to inefficient electrostatic repulsion or steric hindrance is the most likely cause of the aggregation seen in GLYMO-FeOx nanoparticles modified with Lys, Arg, Cys, Thr, Asn, Gln, hydroxylamine, or citric acid.

The APTS-FeOx, APTES-FeOx, and GLYMO-FeOx nanoparticles were all washed, purified, and sterilized after pH titration and magnetic separation of unstable nanoparticles. This process was also used for CMPVA nanoparticles used in the stability investigation. The PD-10 desalting column was not used for additional cleanup of APTS-FeOx or APTES-FeOx nanoparticles as these nanoparticles crashed on the column during the elution step. The reasoning behind this is that APTS and APTES surface functionalizations require specific counter-ion salts for stability and the size exclusion PD-10 column swiftly separates the ions from the much larger nanoparticles. The rapid removal of the counter-ions required for stability results in aggregation and instability as the nanoparticles move through the PD-10 column. Additional 30k MWCO centrifuge filter wash steps were applied in lieu of the PD-10 column to further remove excess APTS and APTES and as a buffer exchange step. The sterilization with a 0.2 μm sterile filter in a sterile bio-safety laminar flow hood was the last step of the wash, purification, and sterilization process.

Characterization with FTIR, XPS, and DLS was used to confirm the addition of APTS, APTES, and GLYMO to the surface of FeOx nanoparticles. The normalized FTIR-ATR spectra for APTS-FeOx and APTES-FeOx with water removed are displayed in **Figure 4.10.** The normalized FTIR-ATR spectra for GLYMO-FeOx and further modified with Gly, Ser, EDA, TEPA, ABA, and SAHBA with water removed are shown in **Figure 4.11-13.** When the

GLYMO-FeOx terminal epoxy ring is opened and modified with a nucleophile the nanoparticle is named without the GLYMO. For example, 'Ser-FeOx' refers to the terminal epoxy ring opening of GLYMO-FeOx with Ser. The primary identifying peaks of respective surface functionalizations are listed in **Table 4.4**. There are several silane containing peaks corresponding to SiO-H, Si-O-Si, and Si-O-H stretches that were present at approximately 1100 cm-1, 1058 cm-1, and 918 cm-1 respectively.[227-230] Each of the silanes contained a C-H stretching doublet from the propyl group that absorbs at 2930 cm^{-1} and 2860 cm^{-1}.[227,228] The terminal amine group of APTS-FeOx and APTES-FeOx nanoparticles had peaks indicative of N-H stretching vibration, weak asymmetrical NH_3^+ bending, and symmetrical NH_3^+ bending at 3420 cm^{-1}, 1660-1610 and 1550-1485 cm^{-1} respectively.[215,227,228] A combined asymmetric NH^{3+} bending vibration and torsional oscillation was present in APTS-FeOx, APTES-FeOx, EDA-FeOx, and TEPA-FeOx nanoparticles at peaks of 2222-2000 cm^{-1}.[215]

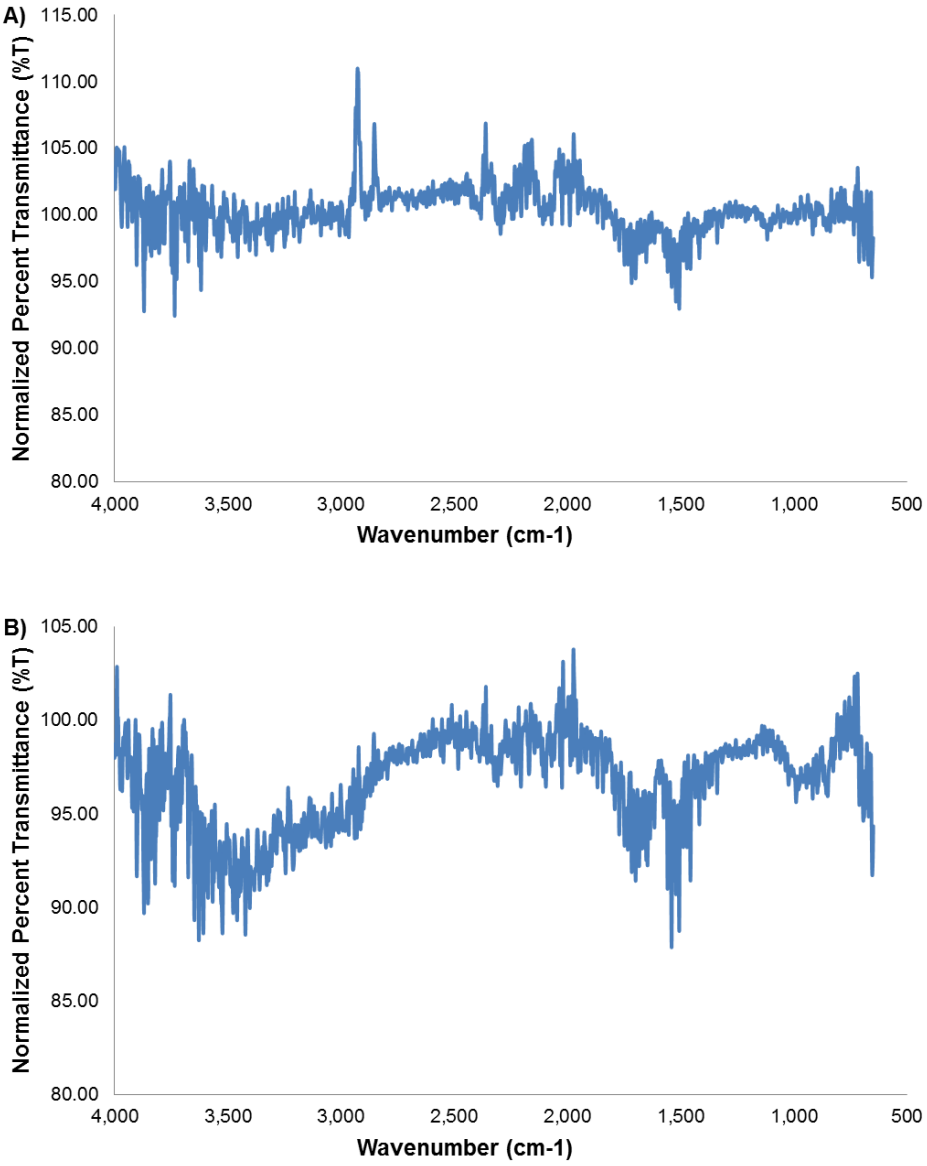

Figure 4.10. FTIR-ATR spectra with normalized percent transmittance for A) APTS-FeOx and B) APTES-FeOx with water subtracted.

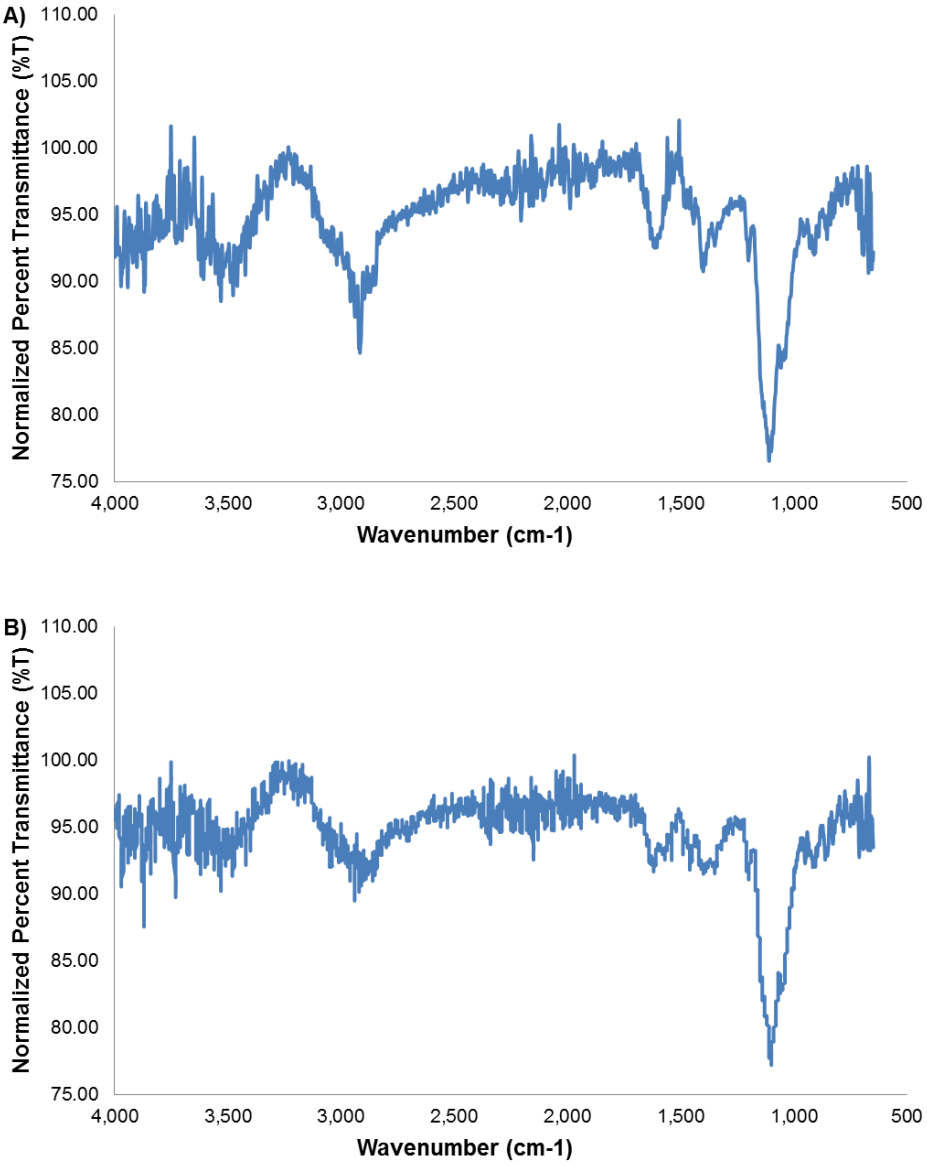

Figure 4.11. FTIR-ATR spectra with normalized percent transmittance for A) Gly-FeOx and B) Ser-FeOx with water subtracted.

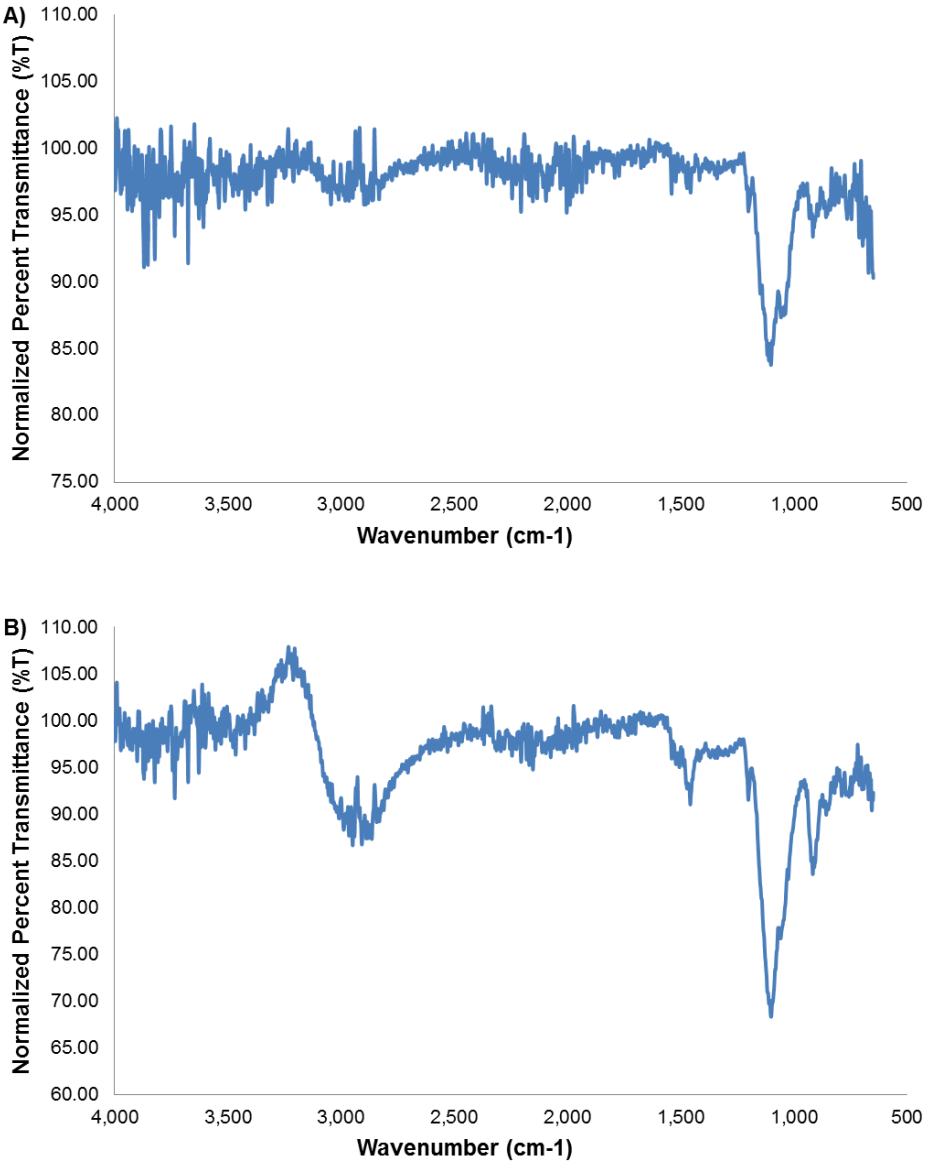

Figure 4.12. FTIR-ATR spectra with normalized percent transmittance for A) EDA-FeOx and B) TEPA-FeOx with water subtracted.

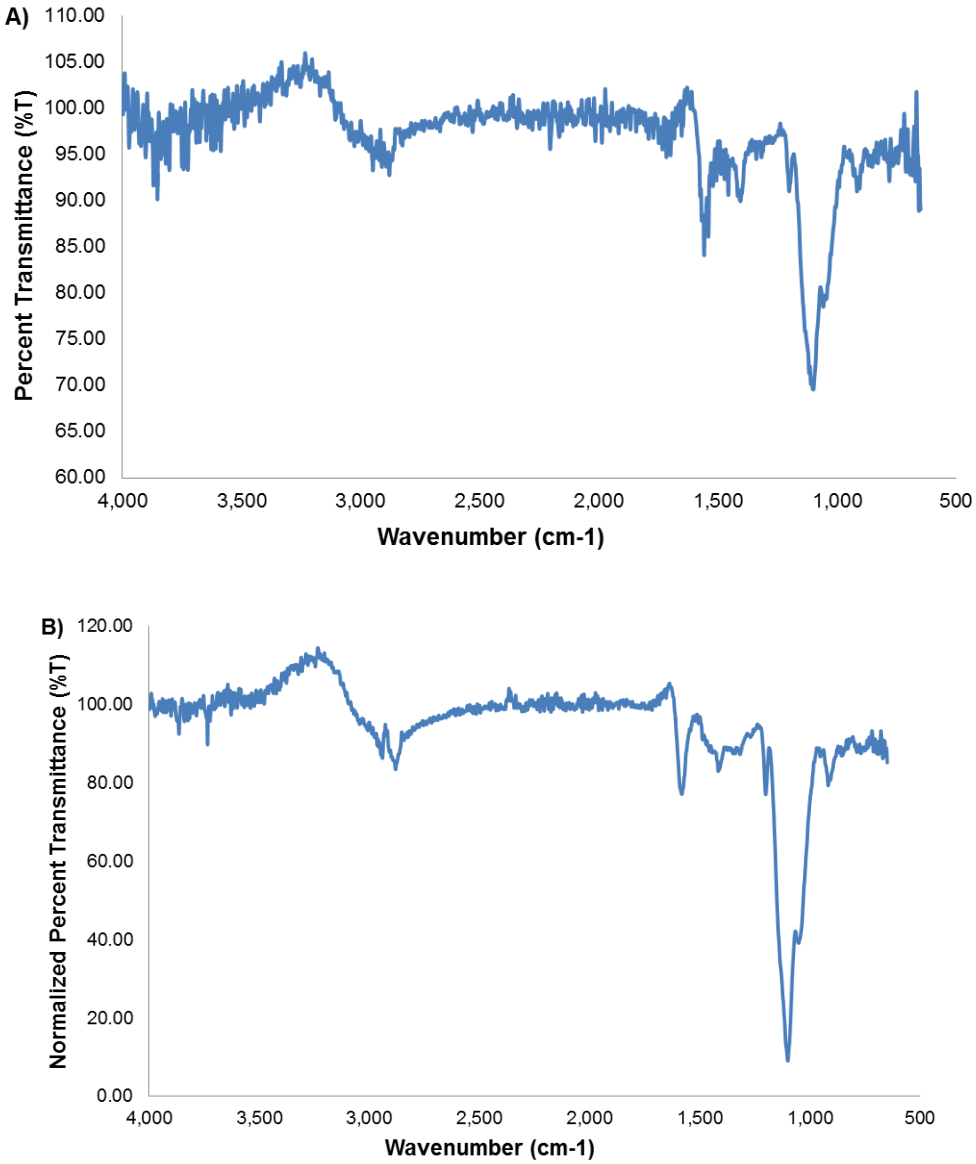

Figure 4.13. FTIR-ATR spectra with normalized percent transmittance for A) ABA-FeOx and B) SAHBA-FeOx with water subtracted.

Epoxy ring opening by respective nucleophiles was confirmed by the absence of the "12 micron band" peak at 750-840 cm^{-1} and ring breathing frequency for the epoxide group at 1250 cm^{-1}.[215] FTIR-ATR spectra comparison of GLYMO-FeOx and SAHBA-FeOx demonstrate the epoxy ring opening (**Figure 4.14)**. The epoxy ring peaks are absence in all GLYMO nanoparticle

functionalizations after the addition of the nucleophilic ligand (**Figure 4.11-13 and Table 4.4**). In **Figure 4.14** it is important to note the appearance of peaks at 1581 and 1416 cm^{-1} corresponding to the terminal carboxylate anion which indicates that the amine group of SAHBA opened the epoxy ring.[215]

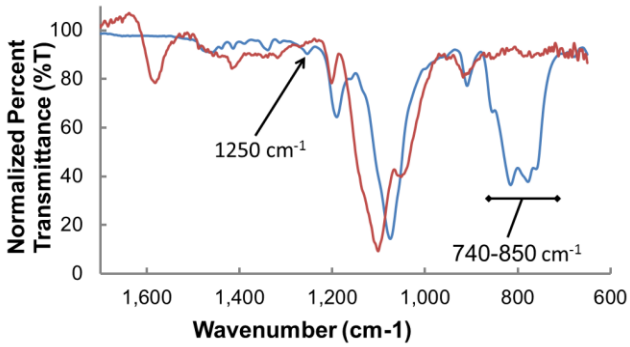

Figure 4.14. Normalized FTIR-ATR spectrum of GLYMO-FeOx (blue line) and SAHBA-FeOx (red line). Epoxy ring opening with SAHBA is indicated by disappearance of peaks at 1250 and 740-850 cm^{-1} and appearance of peaks at 1581 and 1416 cm^{-1}.

Table 4.4. List of identifying FTIR-ATR peaks surface functionalized FeOx nanoparticles.

Peak Description and Wavenumber (cm^{-1})		**APTS-FeOx**	**APTES-FeOx**	**EDA-FeOx**	**TEPA-FeOx**	**Gly-FeOx**	**Ser-FeOx**	**ABA-FeOx**	**SAHBA-FeOx**
N-H stretching	3420	3455	3422	3422	3421	3422	3421	3422	3421
C-H stretching doublet, propyl group	2930 2860	2965 2892	2930 2846	2964 2898	2964 2864	2916 2870	2939 2858	2920 2879	2941 2880
Asymmetric NH_3^+ bending vibration and torsional oscillation	2222-2000	2100	2095	2205	2152				
Carboxylate Anion	1650-1550 1400					1614 1400	1616 1400	1558 1405	1581 1416
Epoxy Ring Breathing Frequency	1250								
CO_2 stretching/ C-O stretch	1320-1000			1201	1201	1201	1201	1201	1201
SiO-H	1100	1118		1101	1101	1110	1100	1100	1101
Si-O-Si	1058			1057	1057	1057	1058	1058	1060
Si-O-H	918	917	917	916	917	911	916	916	917
12 micron band	840-750								

XPS was first used to characterize the non-surface functionalized nanoparticles. High-resolution Fe 3p XPS characterization of A4-24(195)_B6-24(195) nanoparticles (**Figure 4.15**) was used to determine the amount of magnetite and maghemite present. High-resolution Fe 2p XPS spectrum is not suitable to distinguish between magnetite and maghemite crystal structures due to multiple satellite peaks and broad line widths.[231,232] The Fe 3p peak was deconvoluted into three peaks at 53.119 eV, 55.195 eV, and 56.279 eV. The 53.119 eV peak was attributed to Fe^{2+} ions.[232] The 55.195 and 56.279 eV were attributed to Fe^{3+} ions.[231,232] Pure magnetite will consist of a 1:2 Fe^{2+} to Fe^{3+} ratio, but experimentally it was determined to be 0.52.[231,232] Since the ratio of Fe^{2+} to Fe^{3+} was 3:96 it was concluded that the sample contained a mixture of magnetite and maghemite as maghemite contains no Fe^{2+} ions. Using the experimentally determined Fe^{2+} to Fe^{3+} ratio of 0.52 for pure magnetite it was estimated that the sample with a ratio of 3:96 contained approximately 8.86% magnetite and 91.14% maghemite.

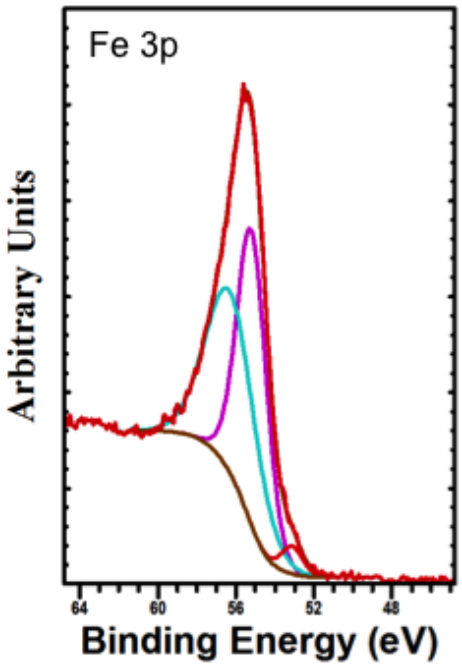

Figure 4.15. High-resolution Fe 3p XPS spectrum of FeOx nanoparticles without surface modification.

XPS was also used to further verify surface functionalization and confirm epoxy ring opening. Non-surface functionalized FeOx nanoparticles are shown in **Figure 4.16**.The FeOx nanoparticles XPS N 1s and Si 2p spectra (not shown) revealed no peaks were present providing confirmation that peaks in these spectra of APTS-FeOx, Gly-FeOx, and Ser-FeOx are due to their respective surface functionalization's.

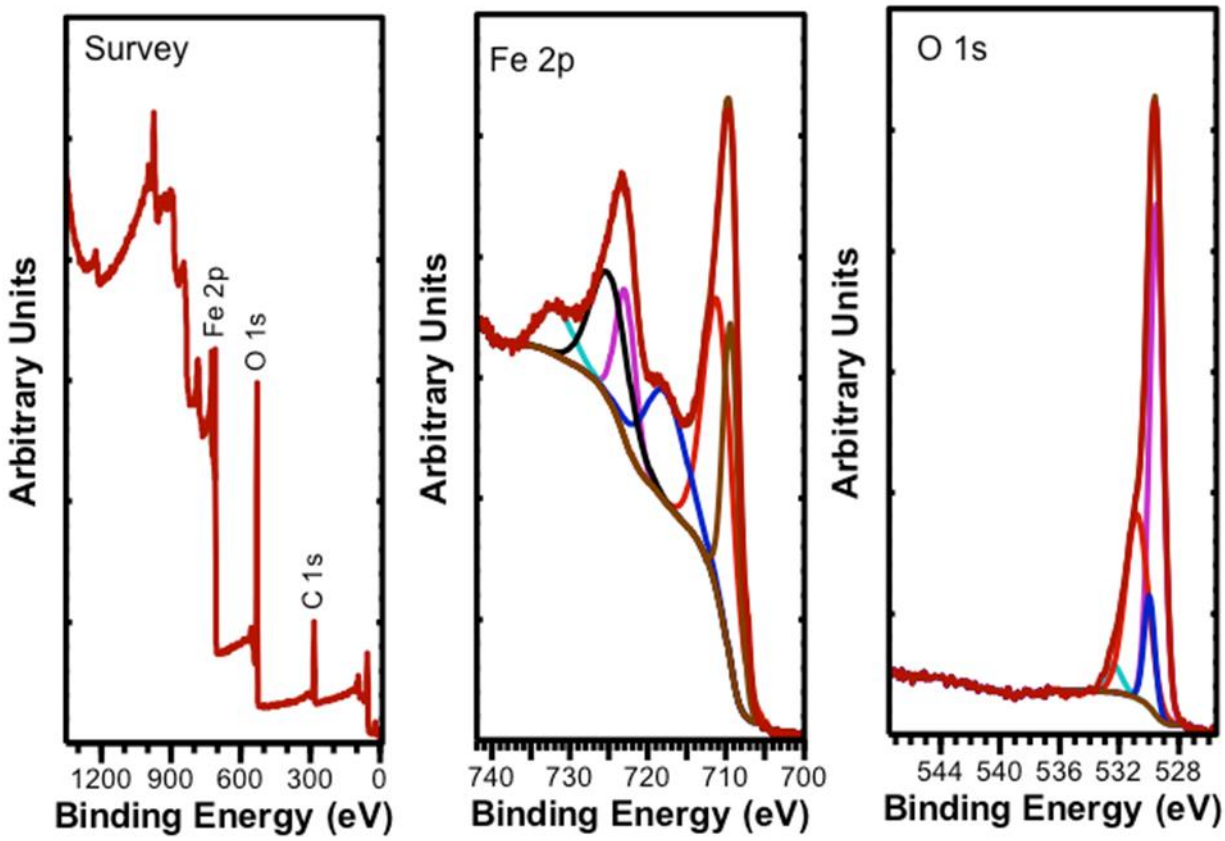

Figure 4.16. XPS survey spectrum, and high resolution Fe 2p, and O 1s spectra of FeOx nanoparticles without surface modification.

Analyzing the XPS survey scan of the APTS-FeOx (**Figure 4.17**) revealed presence of iron, oxygen, carbon, silicon, and nitrogen as expected for successful surface functionalization.

Further analysis of the high-resolution Si 2p spectrum revealed the presence of Si-C and Si-O bonds from the deconvulted peaks positioned at 102.038 eV, and 104.732 eV.[233] This confirms the presence of the APTS and the successful hydrolysis of the silane. However, to confirm successful silanization with the FeOx nanoparticles analysis of the high-resolution O 1s spectrum is required. The O 1s peak was deconvulted into four peaks at 529.803 eV, 530.424 eV, 531.573 eV, and 532.573 eV binding energies. The peaks at 530.424 eV, 531.573 eV are most likely due to impurities from benzyl alcohol, benzaldehyde, or even acetylacetonate. The peaks at 529.803 eV and 532.573 eV correspond to Fe-O and Si-O binding energies.[231,234] These peaks confirm the successful silanization of APTS to FeOx nanoparticles. The high-resolution N 1s spectrum was next analyzed to further determine the APTS is modifying the surface as expected. Indeed, the N 1s doublet peak was deconvulted into three peaks at 399.323 eV, 400.245 eV, and 401.328 eV binding energies indicating N-C, $-NH_2$, and $-NH_3^+$ respectively.[234] The high-resolution C 1s spectrum was used to further confirm that the attachment of the APTS to FeOx is occurring through the Si-O-Fe rather than a NHCO bond. A NHCO bond would appear in the C 1s spectrum with binding energy of 292 eV.[233] The only peaks deconvulted from the C 1s spectrum were 284.988 eV, 286.197 eV, and 288.291 eV corresponding to C-C/C-H bonds, C-O/C-N, and carbon impurities.[233,235]

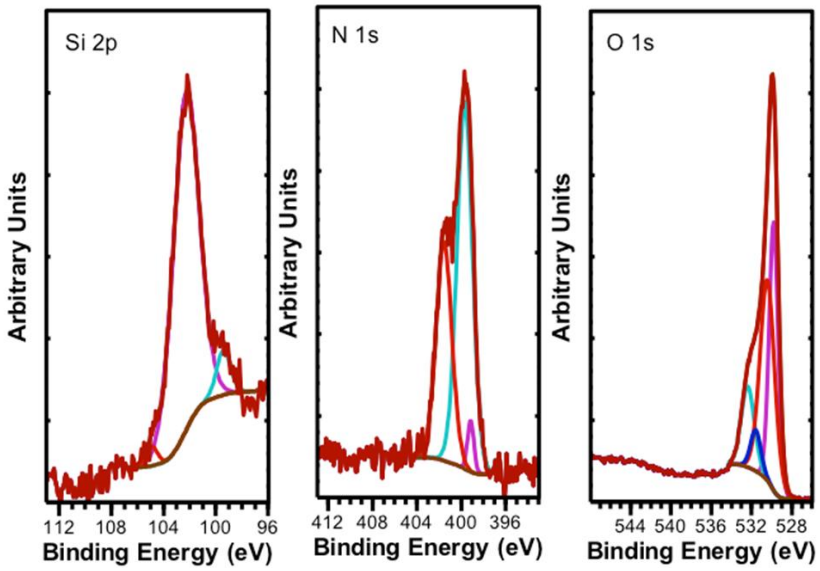

Figure 4.17. XPS high-resolution Si 2p, N 1s, and O 1s spectra of APTS-FeOx nanoparticles.

Gly-FeOx and Ser-FeOx were investigated with XPS to confirm successful GLYMO silanization and attachment to FeOx and successful epoxy ring opening by the amine in Gly and Ser. Ser-FeOx had similar silane peaks to APTS as expected and are shown in the high-resolution Si 2p, N 1s, and O 1s spectra (**Figure 4.18**). In the high-resolution Si 2p spectrum the peak can be deconvulted into 102.484 and 103.1781 eV binding energy peaks corresponding to Si-C and Si-O bonds in GLYMO. Next, the O 1s spectrum was analyzed and the main peak deconvoluted into four peaks at 529.617, 530.987, 532.067, and 532.651 eV binding energies. The 529.617 eV binding energy peak is attributed to the oxygen in Fe_3O_4.[231] The 530.987 and 532.651 eV binding energies are attributed to the carboxylic acid of Ser. The epoxy ring opening with Ser through the amine rather than the carboxylic acid is confirmed by absence of a 533.13 eV binding energy peak.[236] Analysis of the high-resolution N 1s spectrum revealed three deconvulted peaks at binding energies of 399.589 eV, 401.354 eV, and 402.851 eV

corresponding to N-C, NH_2, and NH_2^+, respectively.[237] The N 1s spectrum further corroborates the amine opening of the epoxide ring as expected.

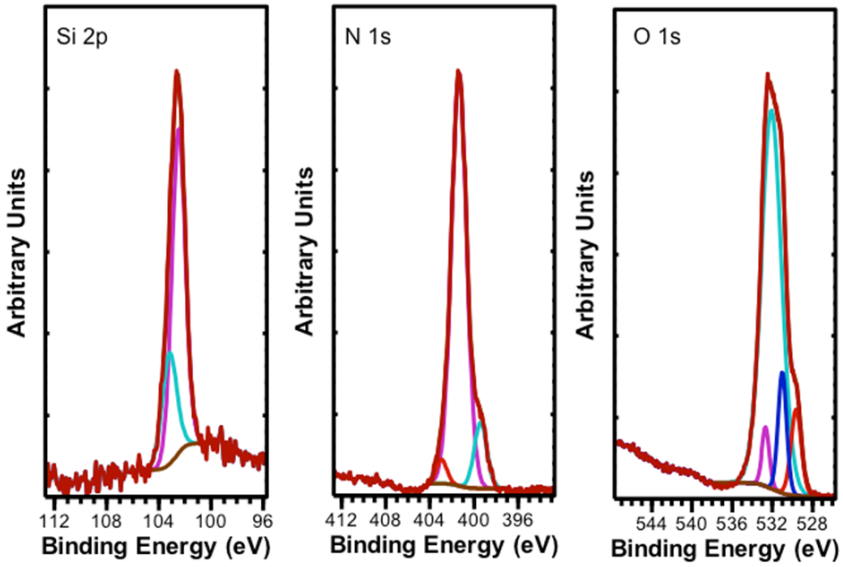

Figure 4.18. XPS high-resolution Si 2p, N 1s, and O 1s spectra of Ser-FeOx nanoparticles.

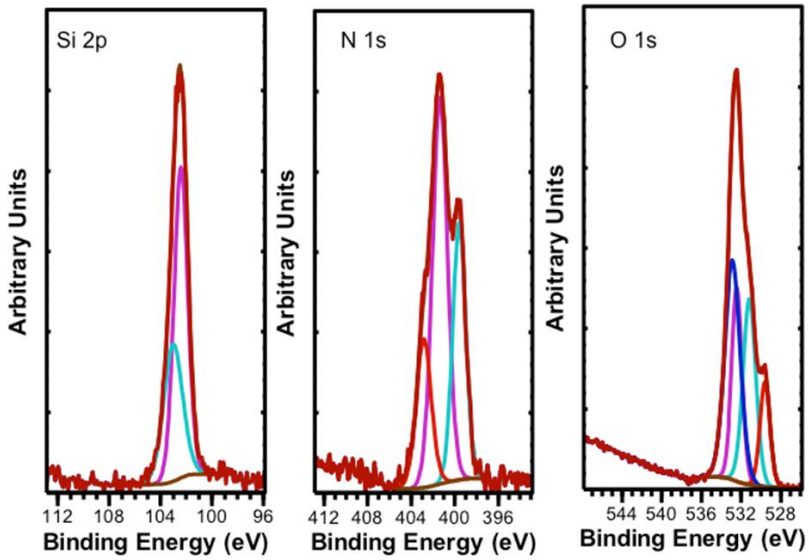

Figure 4.19. XPS high-resolution Si 2p, N 1s, and O 1s spectra of Ser-FeOx nanoparticles.

The Gly-FeOx high resolution XPS spectra (**Figure 4.19**) was in close agreement with the Ser-FeOx XPS spectra as expected. The high-resolution Si 2p spectrum revealed Si-O and SiO_2 peaks at 102.412 and 102.98 eV binding energies from the GLYMO. The high-resolution O 1s spectrum also revealed a Fe-O bond at 529.591 eV. The Si-O, and carboxylic acid oxygen bonds from glycine were observed at 532.42 eV, and 531.148 eV and 532.682 eV respectively.[238] The high-resolution N 1s spectrum further established the amine group opened the GLYMO epoxy ring, indicated by 399.589, 401.354, and 402.851 eV binding energy corresponding to N-C, NH_2, and NH_2^+.[237]

DLS is an invaluable characterization technique to determine the properties of the surface modified nanoparticles in solution. The efficiency of surface functionalization was assessed by hydrodynamic diameter, polydispersity index (PDI), and zeta potential (ζ), listed in **Table 4.5**. The DLS size measurements and zeta potential measurements for each surface functionalization are shown in **Figures 4.21-23**. The hydrodynamic diameter change for each surface functionalization as compared to TMAOH nanoparticles depends on the surface functionalization. Possible aggregation was revealed in some of the surface functionalizations which contained a small volume fraction of larger hydrodynamic diameters. The small hydrodynamic diameter of APTS-FeOx (17.83±7.628 (99.9%)) compared to the hydrodynamic diameters of APTES-FeOx (92.15±17.77 (71.4%) and 332.5±58.37 (28.6%)) suggests that APTS is most likely more stable than APTES. APTES has a 7 fold slower hydrolysis rate than APTS which most likely resulted in some incomplete or insufficient surface functionalization; this is supported by the second larger hydrodynamic diameter population for APTES. [150]

Table 4.5. DLS measurements of hydrodynamic diameter, polydispersity index, and Zeta potential for surface functionalized FeOx nanoparticles.

Surface Functionalization	Hydrodynamic Diameter (nm)	Polydispersity Index (PDI)	Zeta Potential (ζ) (mV)
TMAOH-FeOx	26.6±7.795 (100%)	0.112	
APTS-FeOx	17.83±7.628 (99.9%)	0.317	21.5±1.33
APTES-FeOx	92.15±17.77 (71.4%) 332.5±58.37 (28.6%)	0.386	21.1±1.94
EDA-FeOx	35.56±11.09 (99.9%) 193.2±41.47 (0.1%)	0.221	46.4±13.1
TEPA-FeOx	38.12±9.959 (100%)	0.150	41.2±19.7
Gly-FeOx	29.13±12.67 (100%)	0.228	-22.4±5.8
Ser-FeOx	34.63±6.5 (82.3%) 110.3±32.88 (17.7%)	0.219	-20.2±11.2
ABA-FeOx	29.56±5.713 (93) 114.2±37.97 (7%)	0.372	-21.8±5.09
SAHBA-FeOx	25.59±6.269 (99.2%) 126.7±36.98 (0.8%)	0.269	-29.2±14
CMPVA-FeOx	91.6±20.53 (100%)	0.148	-19.2±0.936

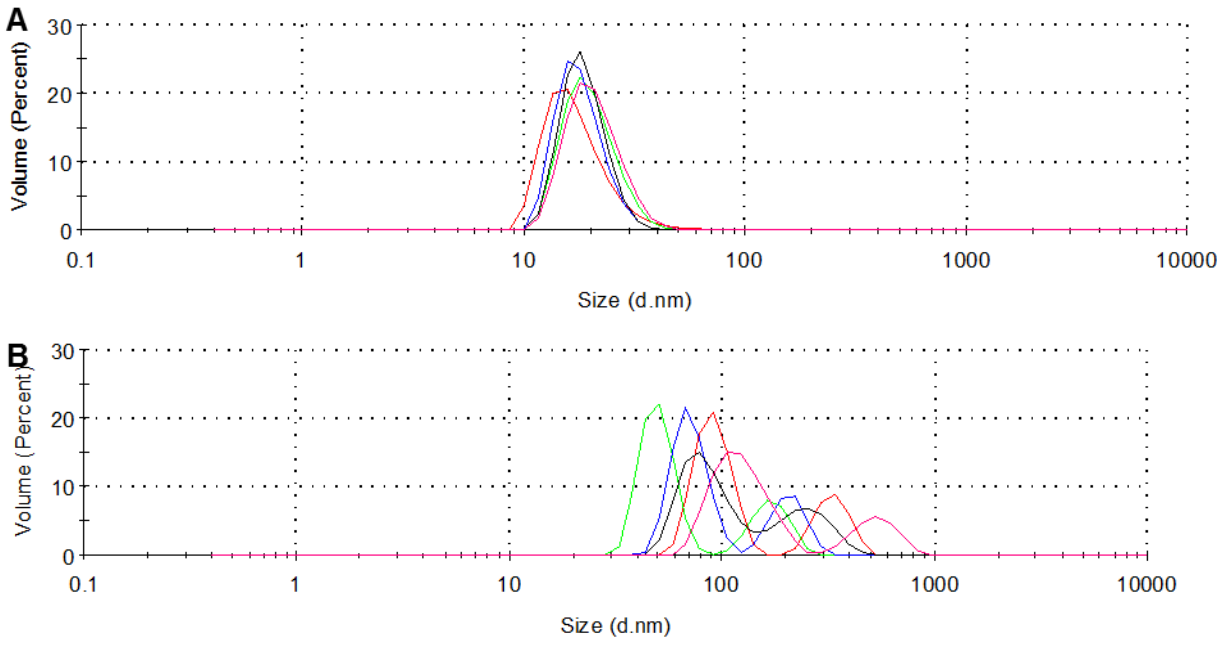

Figure 4.20. DLS measurements based on volume percent for A) APTS-FeOx and B) APTES-FeOx.

Remarkably, there was a range of hydrodynamic diameters and PDI values for GLYMO nanoparticles. While the differences are subtle they are more than likely due to small changes in size of the added nucleophile, formation of differing water solvation shell sizes, and/or magnetic separation selecting a particular size. Despite the differences in hydrodynamic size and PDI values these GLYMO functionalized nanoparticles produced a stable colloid at biologically relevant pH.

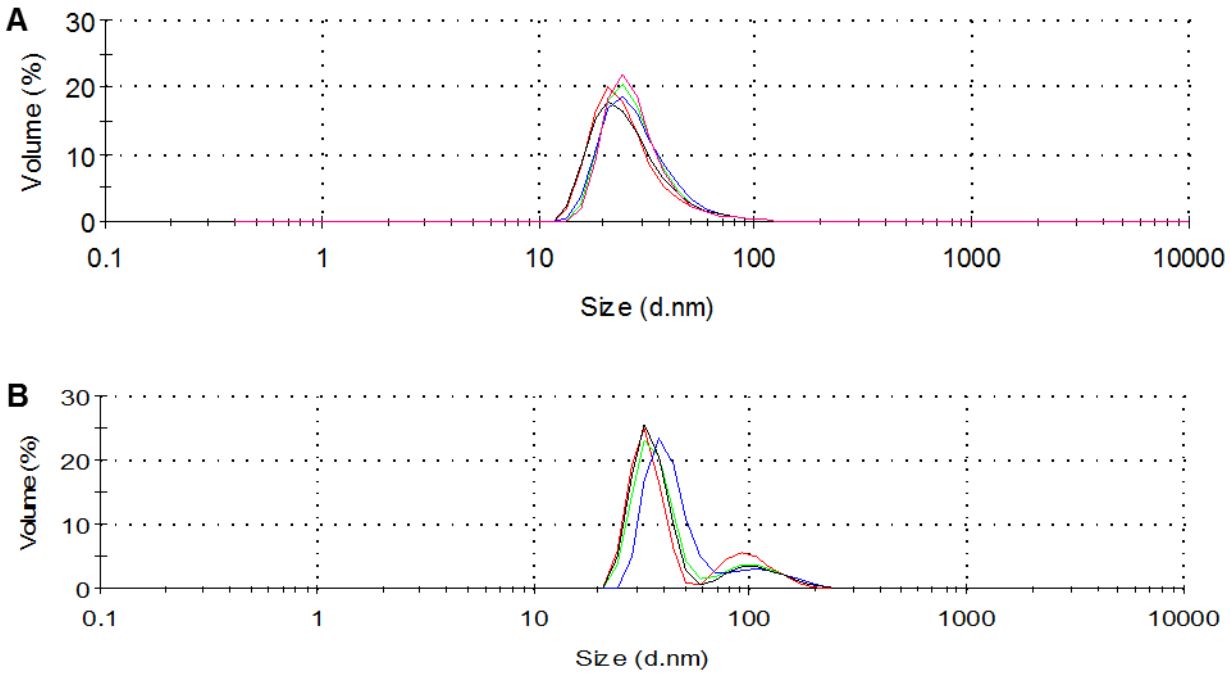

Figure 4.21. DLS measurements based on volume percent for A) Gly-FeOx and B) Ser-FeOx.

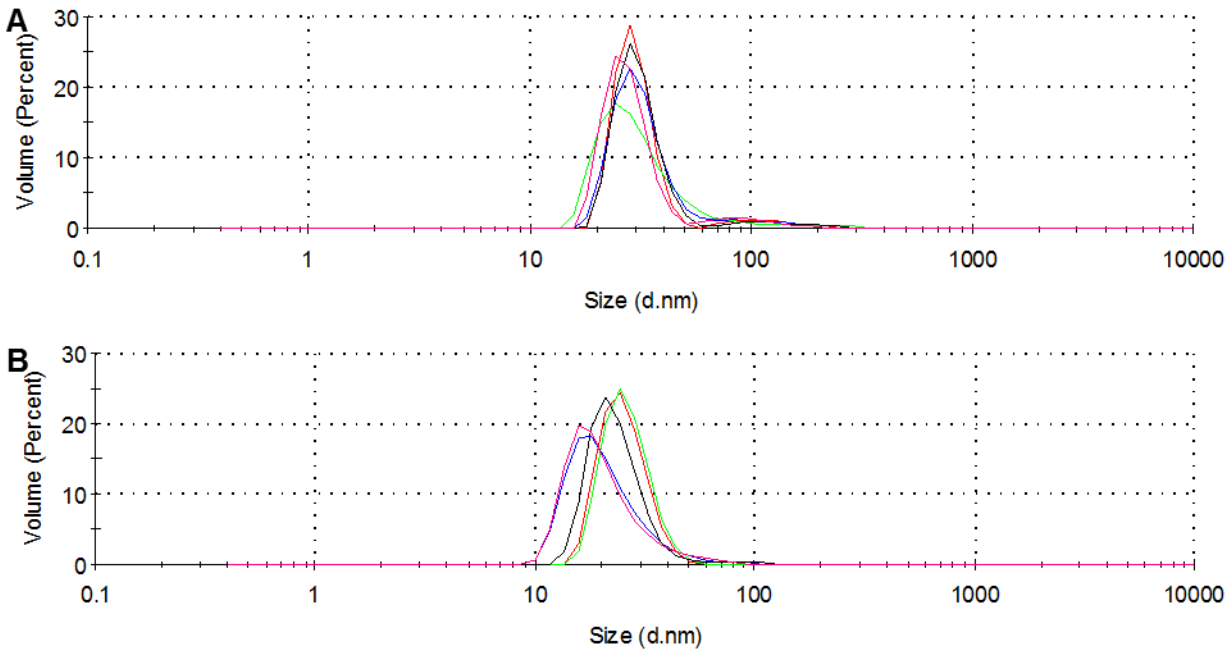

Figure 4.22. DLS measurements based on volume percent for A) ABA-FeOx and B) SAHBA-FeOx.

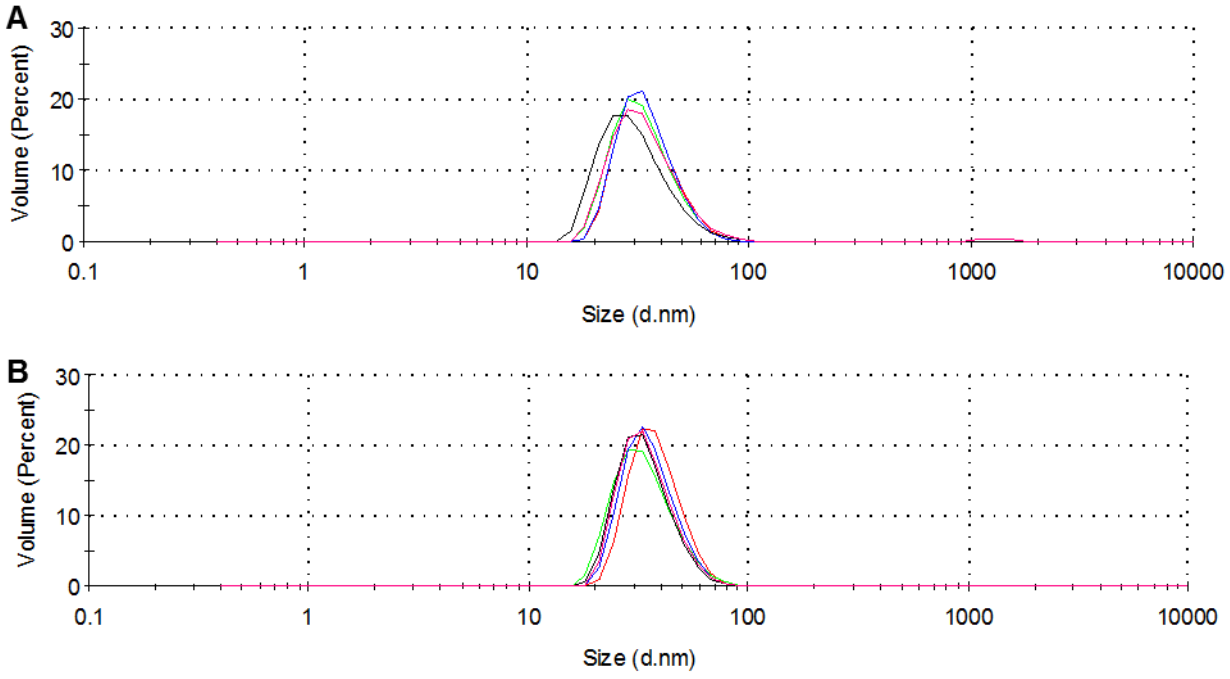

Figure 4.23. DLS measurements based on volume percent for A) EDA-FeOx and B) TEPA-FeOx.

DLS was next used to measure the zeta potential which can be useful in predicting cellular interactions. The zeta potential measurements are shown in **Figures 4.24-27**. The presence of terminal carboxylate groups in Gly-FeOx, Ser-FeOx, ABA-FeOx, SAHBA-FeOx and CMPVA nanoparticles resulted in negative zeta potentials. The negative zeta potentials due to terminal carboxyl groups is expected as the amine groups of these molecules are much better nucleophiles than alcohol groups or water and will open the epoxy ring much more efficiently.[239] SAHBA-FeOx had the most negative zeta potential of -29.2 mV. The chemically similar ligands SAHBA and Ser differ in the carbon chain length and position of the alcohol group in relation to the carboxylic acid group. This is important as the OH group in SAHBA is closer to the electron withdrawing group of the carboxylic acid thus lowering the pKa resulting in a more negative zeta potential at pH of 7.4. Large negative or positive zeta potentials have been reported as an indicator of colloidal stability, but may not always indicate stability in biologically relevant medium that cannot be easily measured using DLS.

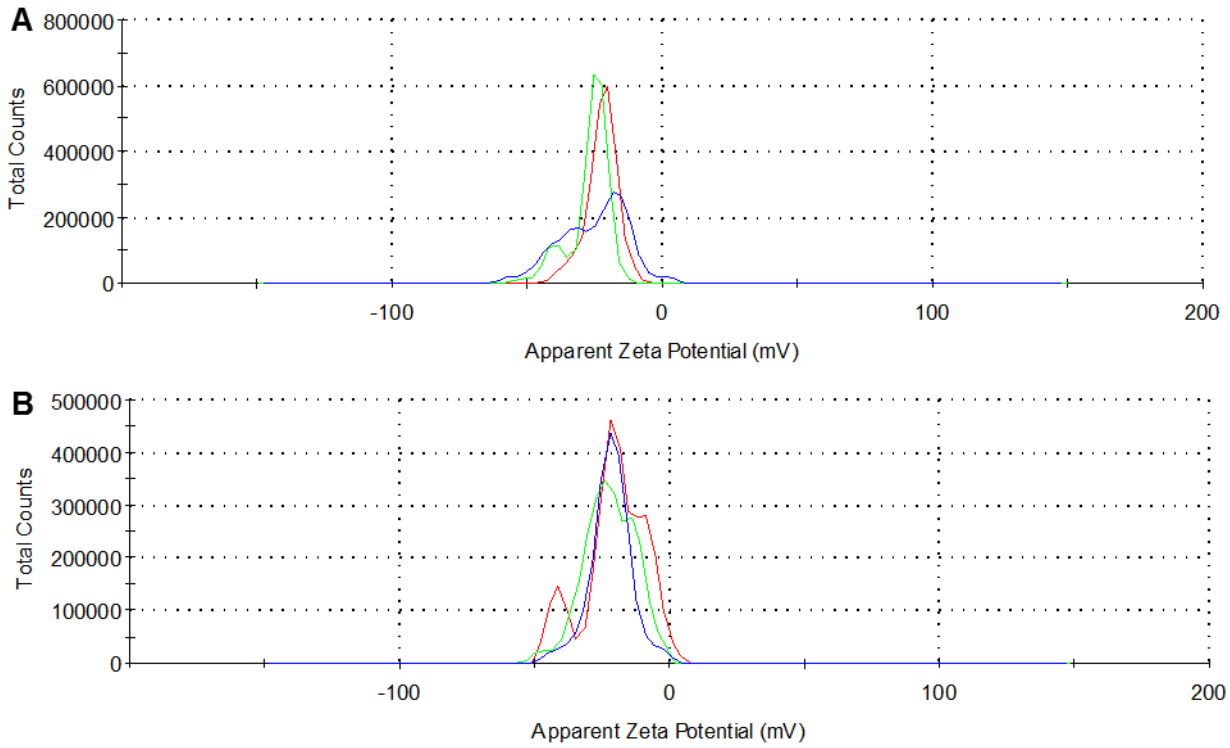

Figure 4.24. Zeta potential measurement of A) Gly-FeOx and B) Ser-FeOx nanoparticles.

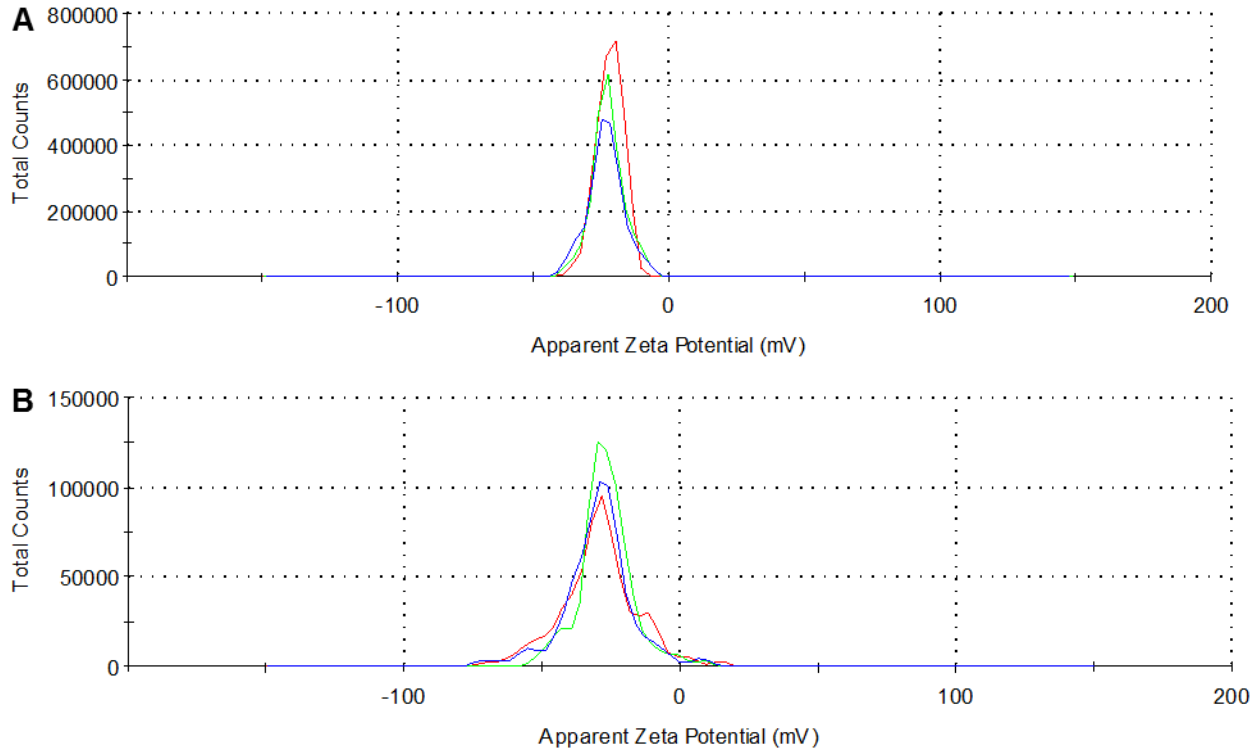

Figure 4.25. Zeta potential measurement of A) ABA-FeOx and B) SAHBA-FeOx nanoparticles.

The APTS-FeOx, APTES-FeOx, EDA-FeOx, and TEPA-FeOx nanoparticles all had positive zeta potentials as expected (**Figure 4.26 and 4.27**). This was due to the terminal protonated amine groups at pH of 7.4. The APTS-FeOx and APTES-FeOx nanoparticles were expected to have the same final surface functionalization despite different starting ligands. This was further corroborated by the similar zeta potentials measured. The EDA-FeOx and TEPA-FeOx nanoparticles had zeta potentials twice as large as APTS-FeOx /APTES-FeOx which resulted from the larger amount of primary and secondary amines present in EDA-FeOx and TEPA-FeOx nanoparticles as compared to APTS-FeOx and APTES-FeOx nanoparticles. Additionally, the pH titration to 7.4 for EDA-FeOx and TEPA-FeOx nanoparticles required more HCl than the APTS-FeOx and APTES-FeOx nanoparticles, further substantiating the zeta potential differences.

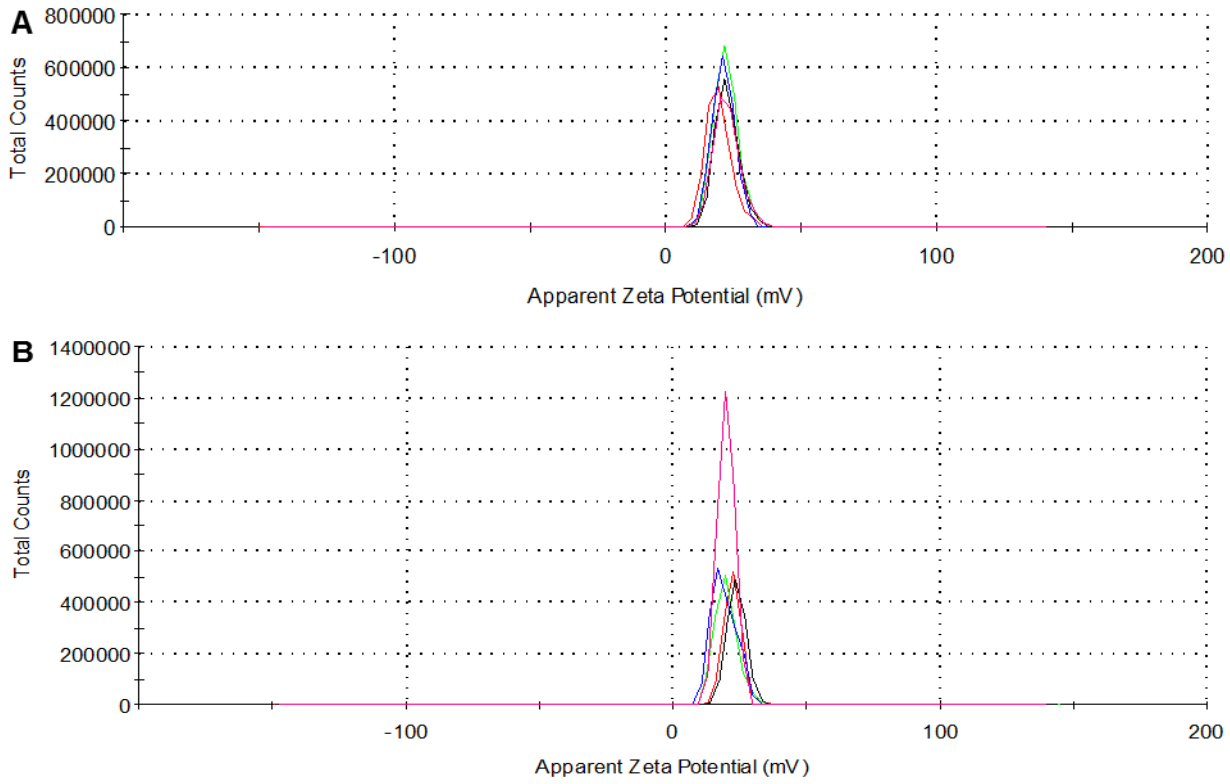

Figure 4.26. Zeta potential measurement of A) APTS-FeOx and B) APTES-FeOx.

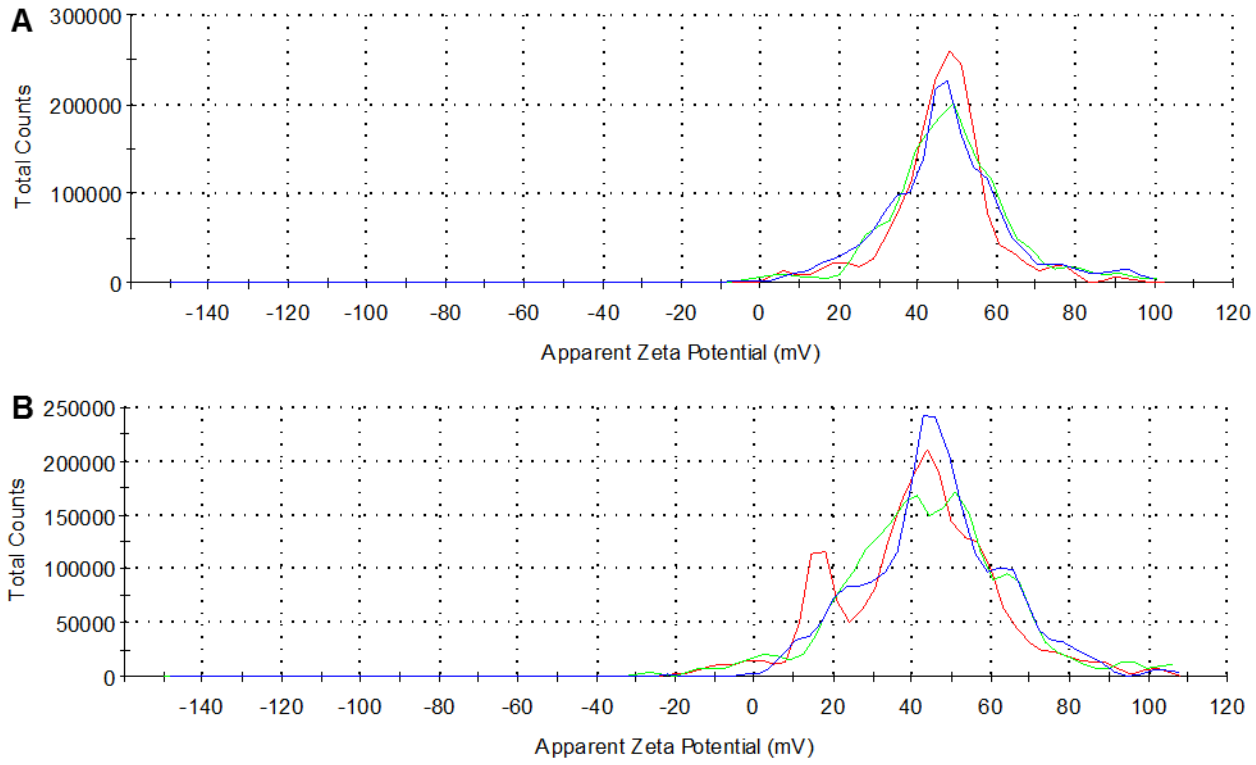

Figure 4.27. Zeta potential measurement of A) EDA-FeOx and B) TEPA-FeOx.

4.5 Stability Assessment in Different Biologically Relevant Medium

The stability assessment of the surface functionalized FeOx nanoparticles is vital in predicting how efficiently they can be used in biological applications. By testing the stability in several biologically relevant medium a better understanding of biological effects such as cellular uptake, biodistribution, and retention can be accomplished. The surface functionalization methods were chosen to provide biological stability and allow for further conjugation potential via 1-Ethyl-3-(3-dimethylaminopropyl)carbodiimide (EDC) coupling. More specifically, APTS and APTES were chosen as they are commonly used surface functionalizations with reported aqueous stability provided by terminal amines. The CMPVA surface functionalization was used as it was shown to have stability in a wide range of biological media. GLYMO surface functionalizations were chosen as they provided a convenient and rapid way to modify the

surface with a nucleophile. The benefit of the GLYMO method is that a variety of nucleophiles can be used to tailor the stability to specific applications. Several amino acids were used in attempts to provide a variety of terminal groups granting a "bio-stealth" like property and EDA and TEPA were chosen to produce an amine terminal functionalization that would be a good comparison to APTS and APTES functionalizations. While a variety of tested amino acids and compounds were unsuccessful in providing stability after magnetic extraction and purification steps, Gly-FeOx and Ser-FeOx had very promising initial stabilities. Thus, ABA and SAHBA were chosen as they are chemically and structurally similar to Gly and Ser respectively. In a recent study increasing chain length of multidentate block copolymers were shown to positively affect the stability of FeOx nanoparticles in PBS.[240] ABA contains a slightly longer carbon chain than glycine. SAHBA differs from Ser as it contains a slightly longer carbon chain and the alcohol group is closer in proximity to the carboxylic acid group. With the alcohol closer to the carboxylic acid it is thought that stability would be improved by increasing the electrostatic repulsion between nanoparticles by producing a more negative zeta potential.

Water, 1x PBS, 0.5x PBS, 0.9% NaCl, CSF, CM, and HS were used to determine the stability and investigate potential causes of instability of the different surface functionalizations. Visual assessment of the surface functionalized FeOx nanoparticles at various time points were used in place of DLS measurements as not all solutions can be easily measured using DLS techniques. Visual assessment was broken into three categories: clear solution, cloudy solution, and precipitated/crashed solution representing stability, partial stability, and complete instability respectively. The stability was monitored at several time points from initial dispersion to 2 weeks in test medium. **Table 4.6** summarizes the times at which each surface functionalized nanoparticle first showed signs of instability (cloudy or precipitation). Upon initial inspection all

surface functionalized nanoparticles were stable in all media except EDA-FeOx and TEPA-FeOx. Both of these became cloudy in cell medium and HS immediately.

Table 4.6. List of first signs of instability of various surface functionalized FeOx nanoparticles; indicated by a cloudy or precipitated solution.

	H_2O	1x PBS	0.5x PBS	0.9% NaCl	CSF	CM	HS
APTS-FeOx		2 hours	2 hours		2 hours	48 hours	
APTES-FeOx		2 hours	2 hours	2 hours	2 hours	24 hours	24 hours
EDA-FeOx						2 hours	24 hours
TEPA-FeOx					1 week	2 hours	2 hours
Gly-FeOx						2 weeks*	24 hours
Ser-FeOx						2 weeks**	2 weeks
ABA-FeOx						2 weeks*	2 weeks
SAHBA-FeOx						2 weeks**	
CMPVA-FeOx						2 weeks**	

*Small amount of precipitation may be due to cell medium sitting at room temperature

**Very small amount of precipitation which may be due to cell medium sitting at room temperature

Visual inspection of nanoparticles in water revealed that even at 1 month time (**Figure 4.28**) all surface functionalizations were clear and stable. This is important to note as stability in water does not necessarily indicate stability in the biological media of interest. PBS was investigated as it is a very commonly used biological buffer. All nanoparticles except APTS-FeOx and APTES-FeOx were soluble in 1x PBS at 2 weeks. APTS-FeOx and APTES-FeOx showed initial aggregation at 2 hours and were completely precipitated out of solution at 24 hours.

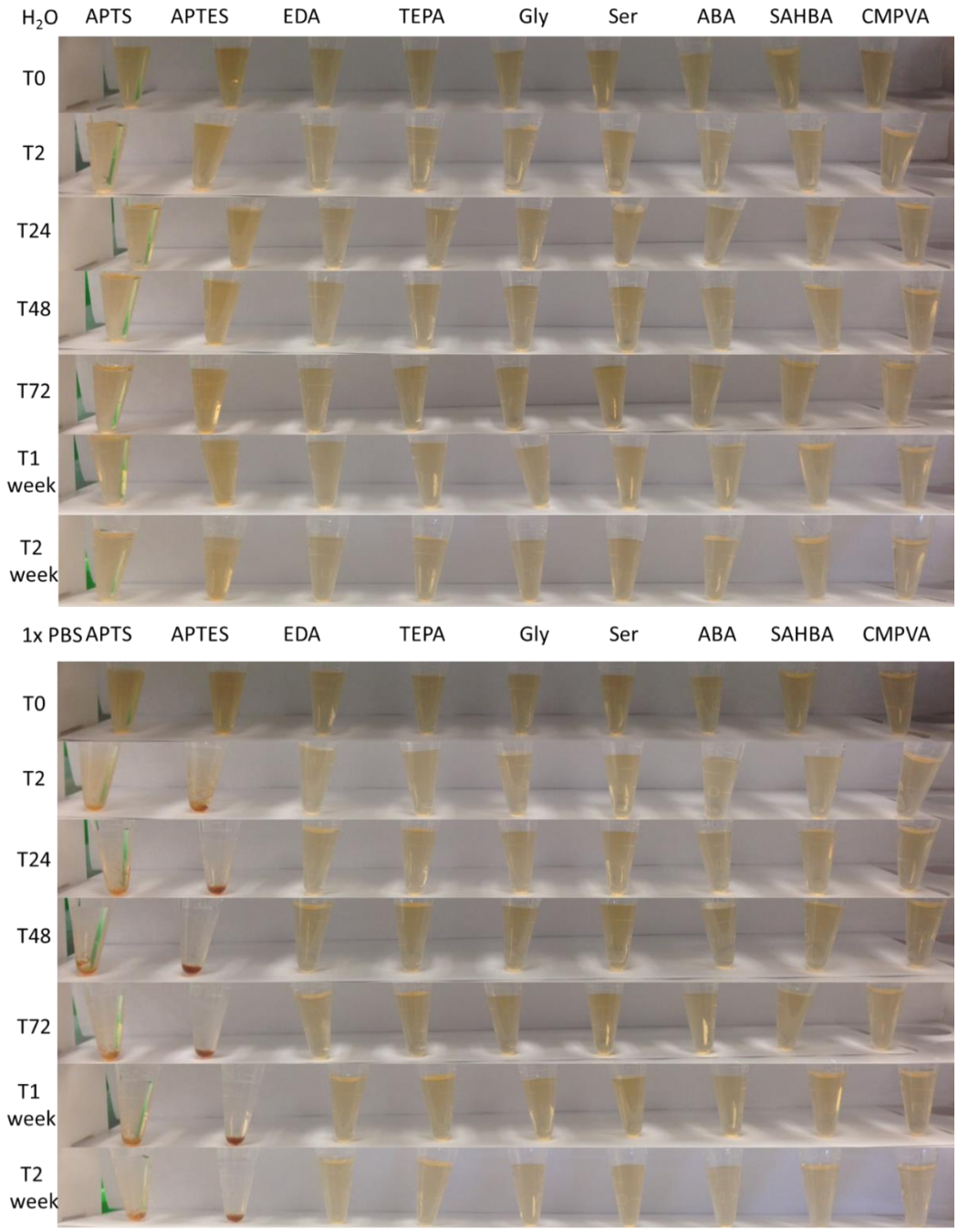

Figure 4.28. Time study of surface functionalized FeOx nanoparticle stability in water (H_2O) and 1x phosphate buffered saline (PBS). Clear, cloudy, or aggregated precipitations indicate stable, partially stable, or complete instability respectively.

Assessment of stability in 0.5x PBS and 0.9% NaCl (**Figure 4.29**) solutions were chosen to ascertain if the phosphate ions or concentration of sodium and chloride counter ions caused the instability in 1x PBS for APTS-FeOx and APTES-FeOx. Interestingly, APTS-FeOx and APTES-FeOx had the same stability in 0.5x PBS, but APTES-FeOx was instable in 0.9% NaCl. This suggests that the phosphate ions are causing instability in APTS-FeOx. Analysis of the DLS data (**Table 4.5**) shows that APTES-FeOx has a much larger hydrodynamic size (92.15±17.77 nm (71.4%) and 332.5±58.37 nm (28.6%)) as compared to APTS-FeOx (17.83±7.628 nm (99.9%)). This difference in size and the inability to 0.2 μm sterile filter APTS-FeOx or APTES-FeOx solutions after several days prompted further investigation. To further investigate the difference in stability the hydrodynamic size was analyzed in water at two time points. The data **(Figure 4.30)** shows a hydrodynamic diameter increase over time for both APTS-FeOx and APTES-FeOx, but the extent of increase suggests that APTES-FeOx aggregates at a much faster rate than APTS-FeOx. This suggests that the APTES-FeOx may not have completely formed a silane shell and may be reorienting and forming a silane shell around multiple nanoparticles. Alternatively, a re-hydrolyzation process leading to improper silane shell reforming could also be occurring leading to larger hydrodynamic sizes and instability. The APTES-FeOx is able to maintain stability in water even with changes in hydrodynamic size, but the addition of salts causes complete precipitation. These results suggests that APTS-FeOx and APTES-FeOx may appear clear and stable in some solutions, but are susceptible to re-hydrolysis and aggregation over time.

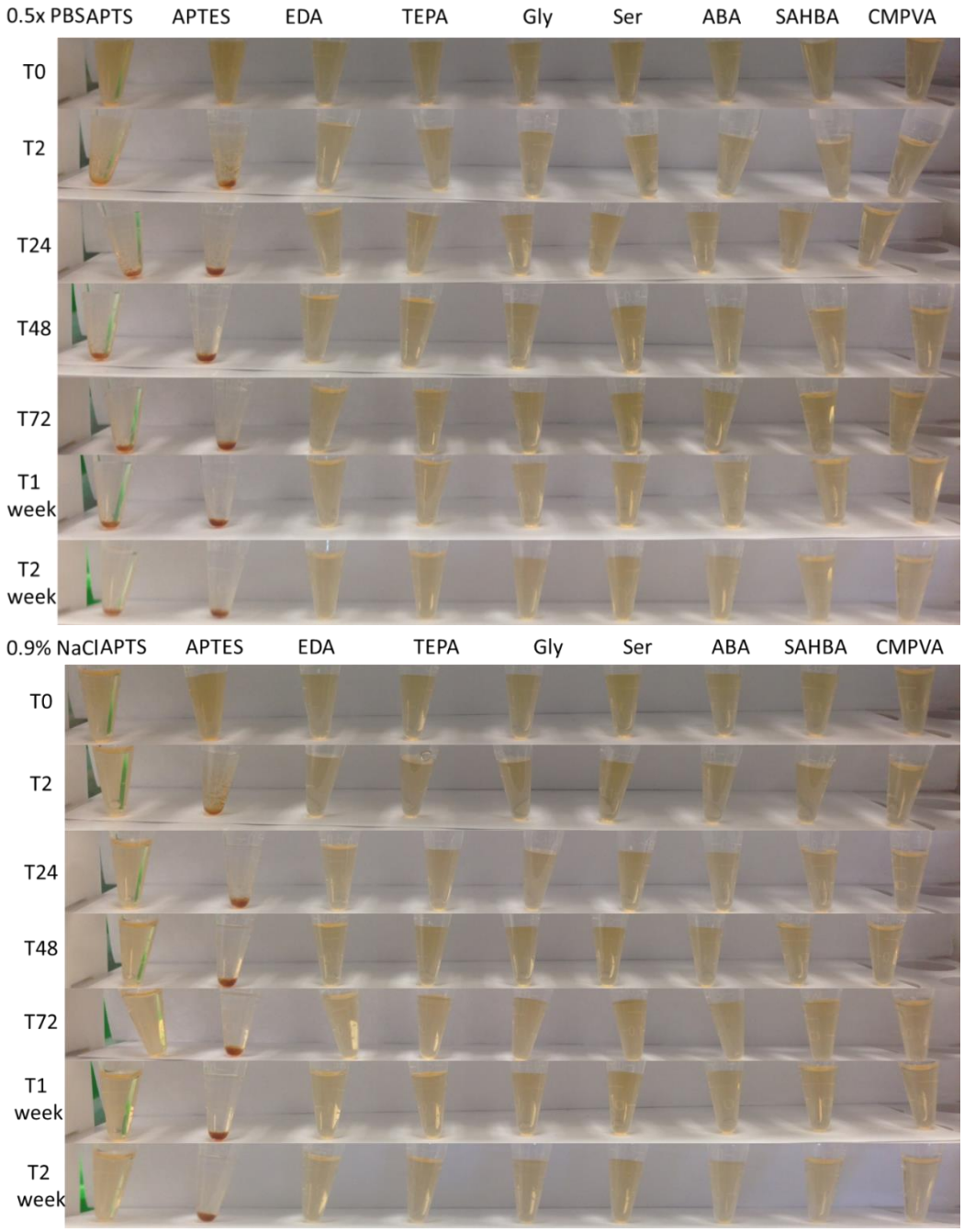

Figure 4.29. Time study of surface functionalized FeOx nanoparticle stability in 0.5x PBS and 0.9% sodium chloride (saline). Clear, cloudy, or aggregated precipitations indicate stable, partially stable, or complete instability respectively.

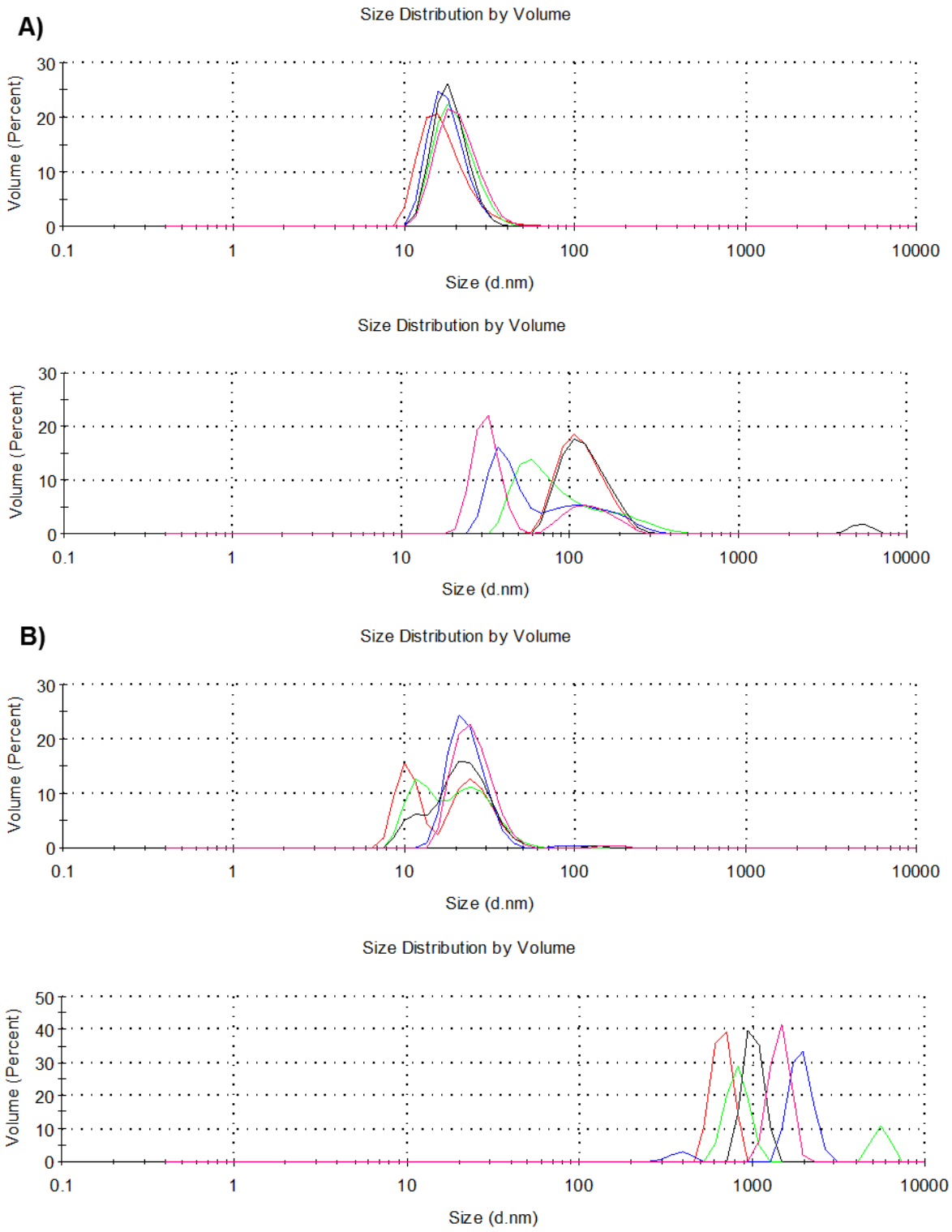

Figure 4.30. DLS hydrodynamic size measurements of APTS-FeOx (A) or APTES-FeOx (B) after 1 (Top) and 12 days (Bottom).

CSF stability is important to investigate for the application of FeOx nanoparticles for the treatment of glioblastoma multiforme (GBM). CSF is a close representation of the environment that the nanoparticles would be subjected to in treatment of brain tumors. In **Figure 4.31** it can be seen that APTS-FeOx and APTES-FeOx first show signs of instability at 2 hours and at 24 hours are completely crashed out of solution. TEPA-FeOx showed a small amount of precipitation at 1 week indicating partial instability. Instability at these short time periods limits their applicability in delivering time sensitive brachytherapy. Additionally, the instability could prohibit blood circulation and/or uptake.

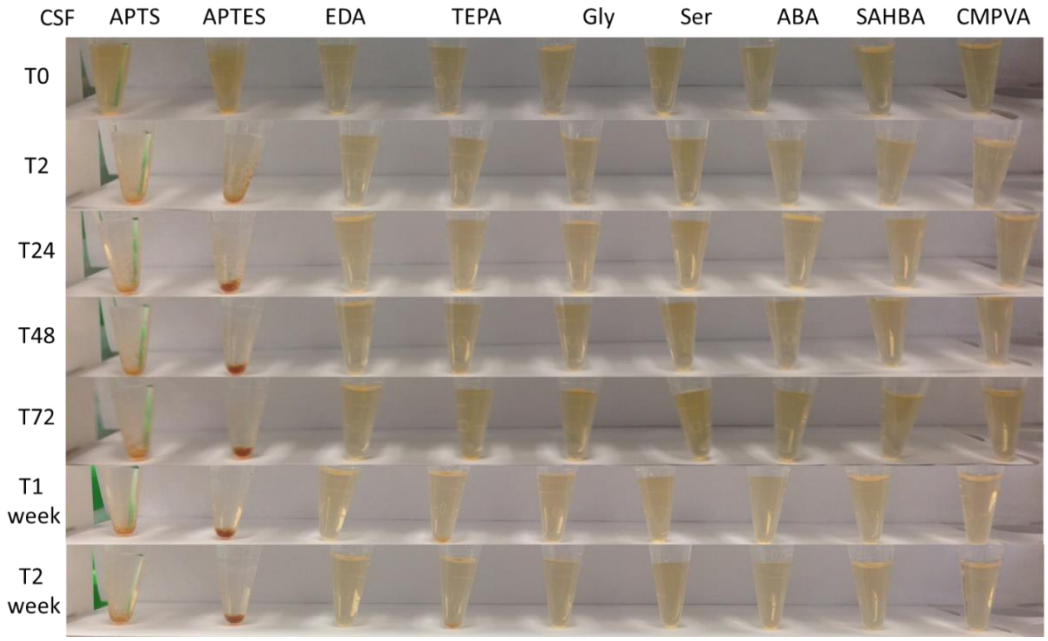

Figure 4.31. Time study of surface functionalized FeOx nanoparticle stability in artificial cerebral spinal fluid (CSF). Clear, cloudy, or aggregated precipitations indicate stable, partially stable, or complete instability respectively.

In vitro investigations of FeOx nanoparticles are often performed using complete cell medium containing FBS. Similarly, *in* vivo administered FeOx nanoparticles in humans will

have some degree of interaction with HS. The proteins contained in the respective serum can have varying degrees of interaction with the nanoparticles and therefore affect the stability. Thus, stability assessments in these media are imperative and are shown in **Figure 4.32**. Protein coronas can form around nanoparticles when introduced to media containing serum which will directly and substantially affect cellular interactions.[241] Interestingly, EDA-FeOx and TEPA-FeOx nanoparticles instantaneously became cloudy upon introduction to CM or HS and were approaching complete precipitation at 2 hours. The other positive zeta potential surface functionalizations, APTS-FeOx and APTES-FeOx, also displayed aggregation signs early. At 48 hours for APTS-FeOx and 24 hours for APTES-FeOx aggregation and precipitation began. The negative surface functionalized nanoparticles showed small amounts of precipitation for Gly-FeOx and Ser-FeOx and very small amounts of precipitation for ABA-FeOx, SAHBA-FeOx, and FeOx at 2 weeks. Analyzing the HS stability revealed that only APTS-FeOx, SAHBA-FeOx, and CMPVA-FeOx retained stability at 2 weeks. The stability was very similar in CM and HS for APTES-FeOx, EDA-FeOx, TEPA-FeOx, and Ser-FeOx suggesting that the FBS in CM was the cause of instability. Gly-FeOx was instable at 24 hours in HS and only showed small amounts of instability at 2 weeks in CM suggesting that the higher concentration of serum in HS as compared to CM resulted in the different stabilities.

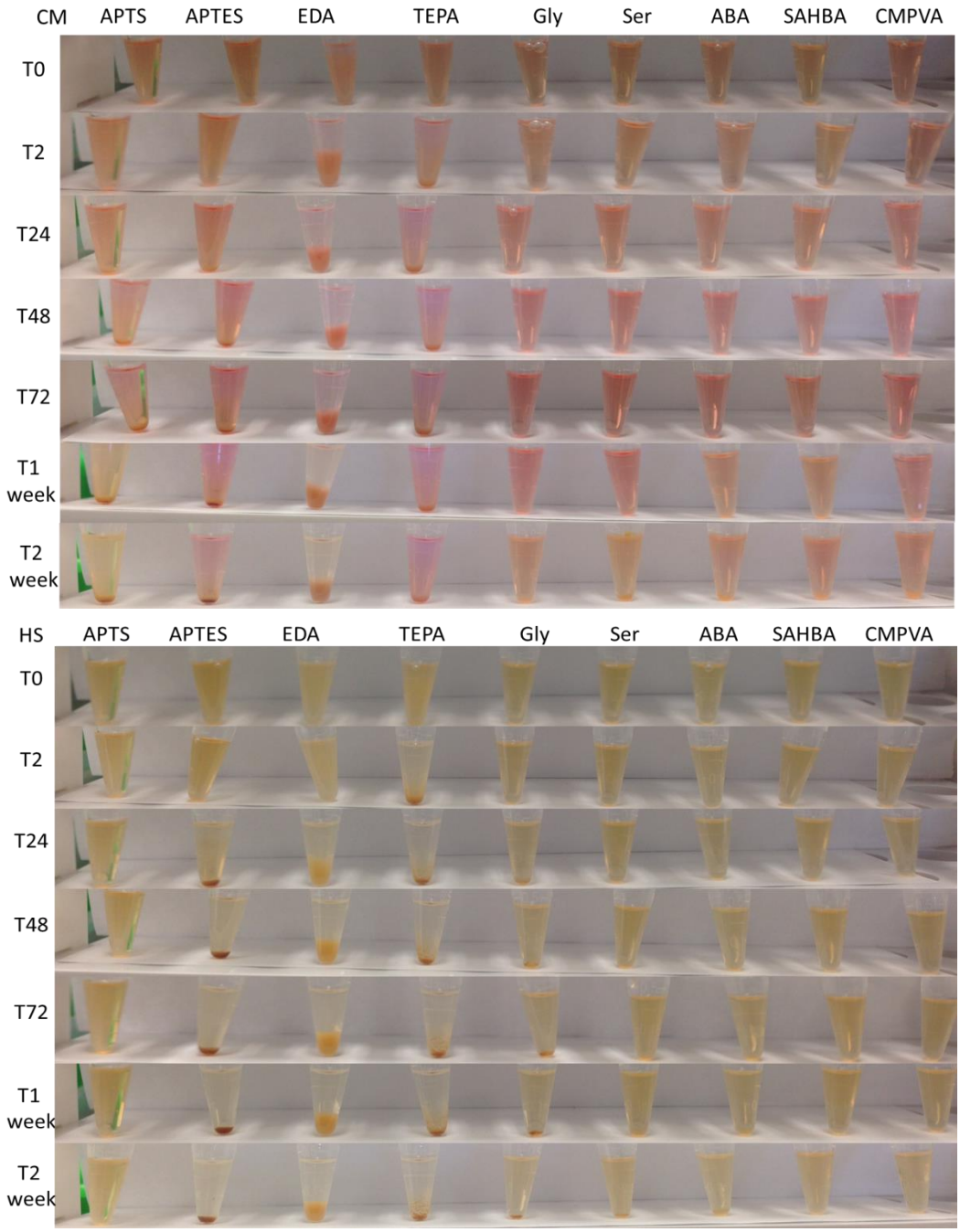

Figure 4.32. Time study of surface functionalized FeOx nanoparticle stability in cell medium (CM) and human serum (HS). Clear, cloudy, or aggregated precipitations indicate stable, partially stable, or complete instability respectively.

Interesting stability information can be established when comparing the differences of stability in PBS, CM, and HS. With regards to APTS-FeOx the instability can be attributed to phosphate ions rather than serum proteins as the APTS-FeOx nanoparticles remained stable in HS at 2 weeks. The differences between positive and negative zeta potential surface functionalizations are striking. The larger degree of instability of positive surface functionalizations as compared to negative surface functionalizations seen in CM and HS offers some substantiation to claims of higher cellular uptake values recorded for cationic amine group functionalizations. However, the increased uptake recorded may be due to crashed cationic surface functionalizations and not true uptake or internalization.

DLS investigation of APTS-FeOx, APTES-FeOx, EDA-FeOx, and TEPA-FeOx in water was assessed after 12 days to determine if any changes were occurring that were not visually seen. The hydrodynamic size after twelve days in water for APTS-FeOx and APTES-FeOx is shown in **Figures 4.30;** EDA-FeOx and TEPA-FeOx is shown in **Figure 4.33 and 4.34**. APTS-FeOx nanoparticles increased from 17.83±7.628 nm (99.9%) to 122.1±37.45 nm (95.7%) and 5326±699.2 nm (4.3%) where APTES increased to 674.7±85.2 nm (100%) (**Figure 4.30**). EDA-FeOx and TEPA-FeOx surface functionalized nanoparticles measured hydrodynamic diameters were 35.56 ±11.09 nm (99.9%) and 38.12±9.959 nm (100%) respectively. After 12 days EDA-FeOx and TEPA-FeOx surface functionalized nanoparticles measured hydrodynamic diameters were 27.82±11.01 nm (100%) and 29.52±9.047nm (100%). This is crucial as it clearly shows that the silane on the EDA-FeOx and TEPA-FeOx nanoparticles does not alter overtime whereas the APTS silane does alter over time resulting in larger hydrodynamic diameters.

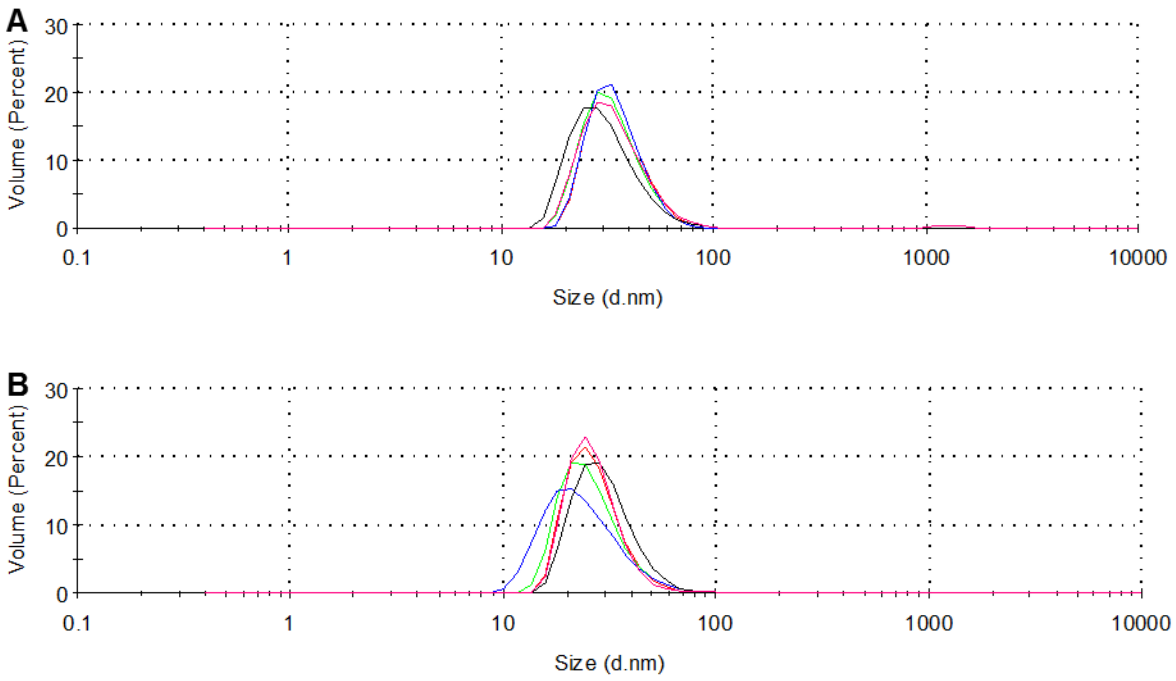

Figure 4.33. Dynamic light scattering hydrodynamic diameter measurement by volume for EDA-FeOx nanoparticles (A) and EDA-FeOx nanoparticles 12 days later (B).

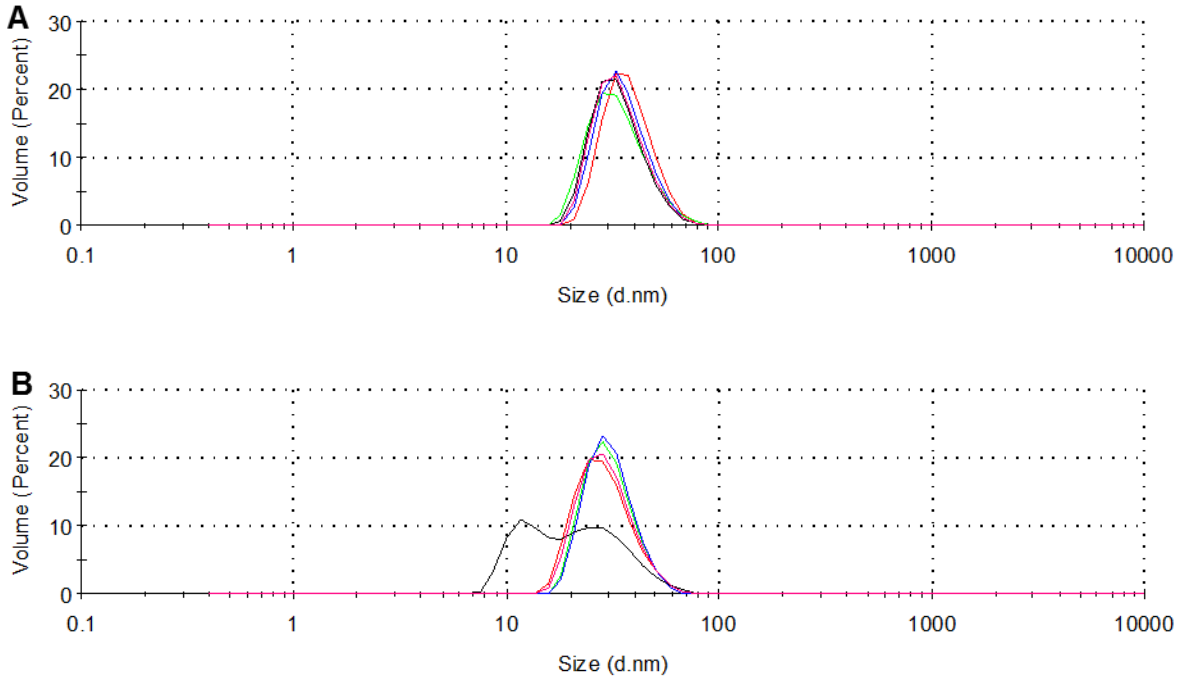

Figure 4.34. Dynamic light scattering hydrodynamic diameter measurement by volume for TEPA-FeOx nanoparticles (A) and TEPA-FeOx nanoparticles 12 days later (B).

The long term stability was analyzed at 3 weeks, 1 month and 5 months (**Figure 4.35 and 4.36**). The stability at 1 month was deemed sufficient for initial stability assessment. The 5 month time point may not be an accurate representation of long term stability as there was some volume changes observed in a few of the microcentrifuge tubes most likely due to evaporation. The volume changes do not seem to be related to media and are considered an effect of random inefficient sealing of microcentrifuge tubes which resulted in only some of the samples evaporating. Regardless, the 5 month analysis is helpful in visualizing instability that may have been present and unseen at earlier time points. For water the first signs of instability were seen at 5 months for APTES-FeOx and very small amounts of precipitation in Gly-FeOx, and Ser-FeOx. There was some small amount of precipitation at 5 months in 1x PBS for Gly-FeOx, and Ser-FeOx, but not 0.5x PBS. At 5 months the first and small signs of instability in CSF were observed for Gly-FeOx, Ser-FeOx, ABA-FeOx, and CMPVA-FeOx.

In conclusion, CMPVA-FeOx, Ser-FeOx, ABA-FeOx, and SAHBA-FeOx demonstrated broad stability at 1 week. The CMPVA-FeOx and SAHBA-FeOx nanoparticles only had minimal precipitation in CM at 2 weeks, but were otherwise stable up to 5 months with the exception of some CMPVA-FeOx precipitation in CSF. Overall, SAHBA-FeOx had the best and broadest solution stability even at 5 months. It is thought that the longer carbon chain and the alcohol being in closer proximity to the carboxylate group in SAHBA provided the best electrosteric stability of the surface functionalizations tested. Furthermore, this investigation suggests that the presence of both hydroxyl and carboxyl groups appear to provide the best and broadest stability as seen in CMPVA-FeOx and SAHBA-FeOx. The different media revealed that the concentration of salt, sugar, and protein can have dramatic effects on the stability. More specifically, water or PBS stability is not indicative of stability in all biologically relevant media.

These two surface functionalizations have relatively large differences in hydrodynamic size, but similar broad stability and zeta potentials. They will potentially be very useful in determining differences in biological effects based on size.

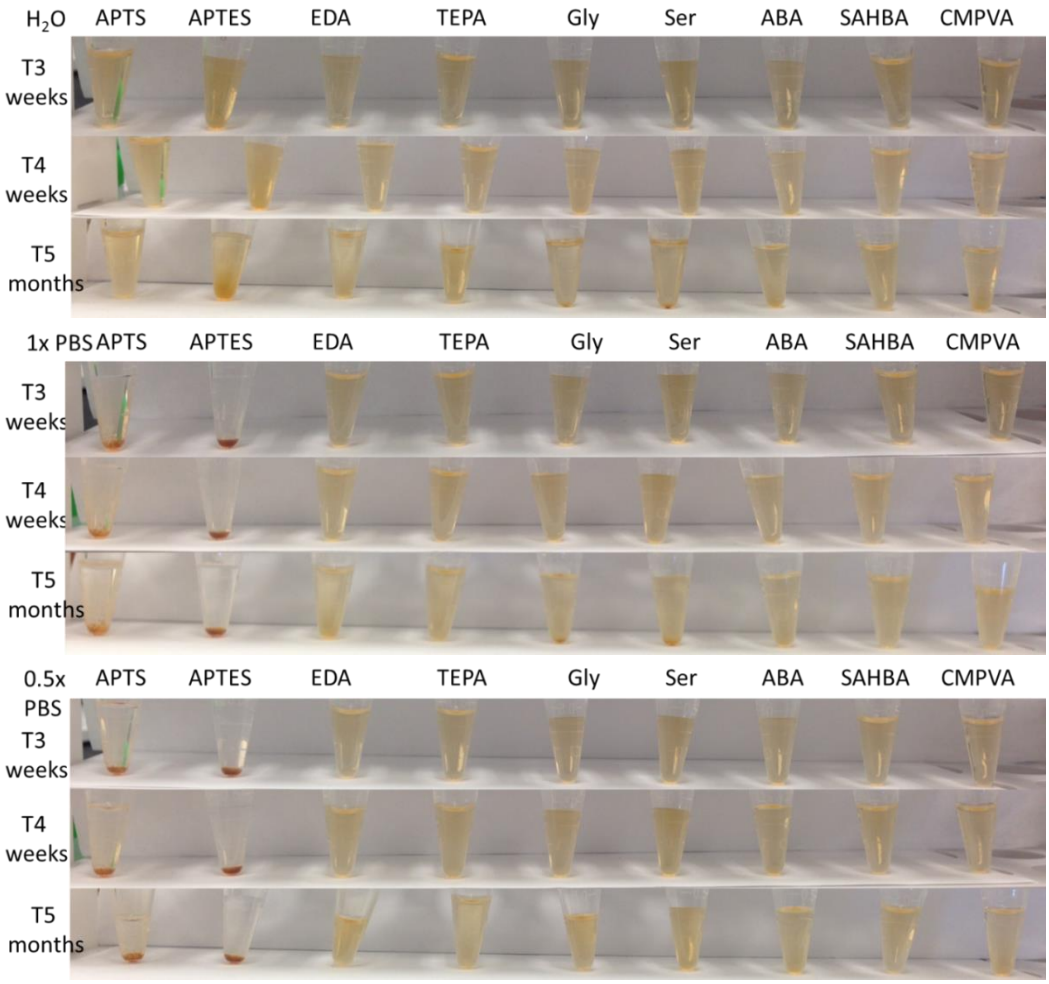

Figure 4.35. Time study of surface functionalized FeOx nanoparticle stability in water, 1x PBS, and 0.5x PBS at 3 weeks, 4 weeks, and 5 months. Clear, cloudy, or aggregated precipitations indicate stable, partially stable, or complete instability respectively.

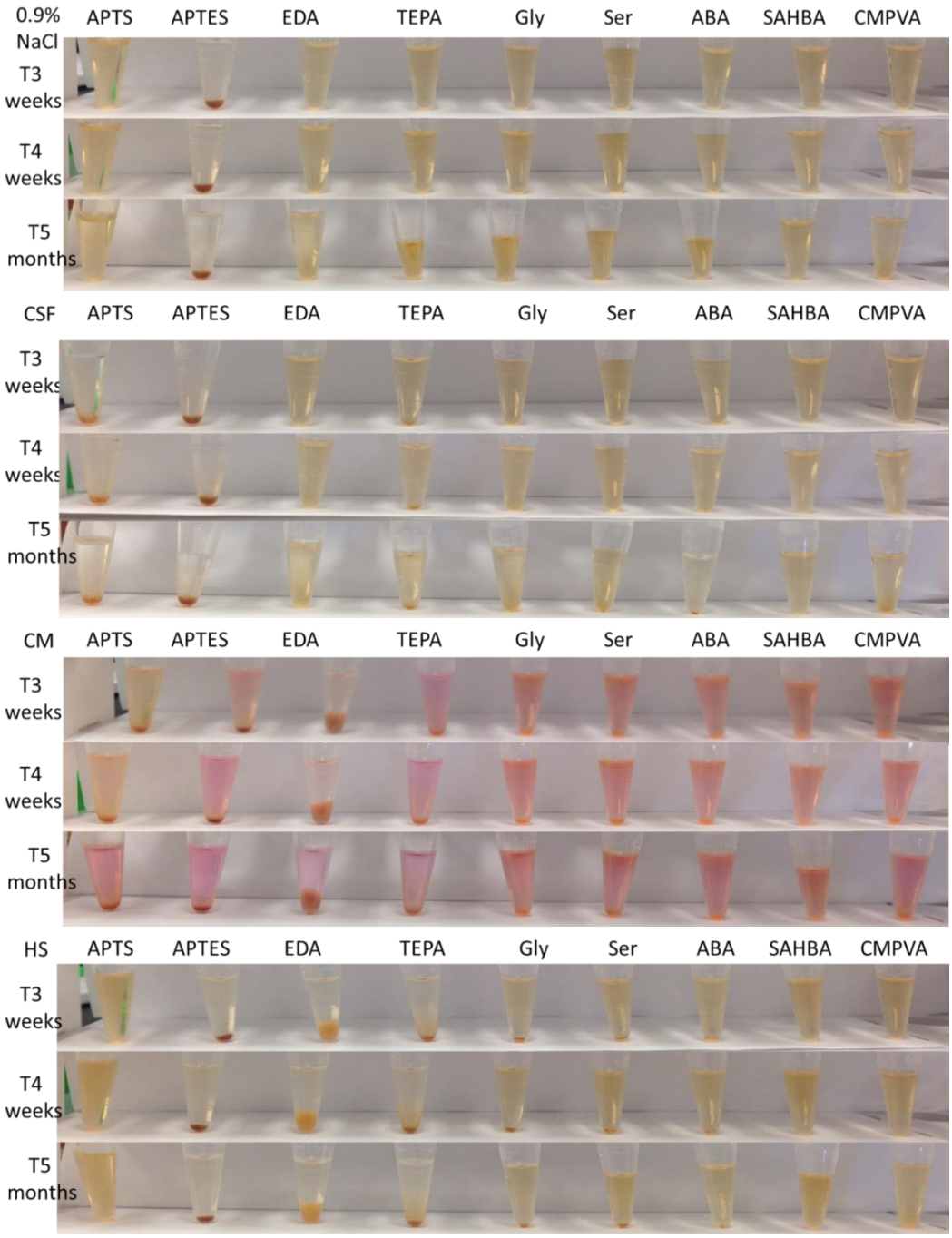

Figure 4.36. Time study of surface functionalized FeOx nanoparticle stability in 0.9% NaCl, CSF, CM, and HS at 3 weeks, 4 weeks, and 5 months. Clear, cloudy, or aggregated precipitations indicate stable, partially stable, or complete instability respectively.

4.6 Iron Oxide Nanoplatform: Confirming Conjugation Potential with a Radiotherapeutic

The surface functionalizations were chosen not only to provide biological stability, but to also provide additional conjugation potential. To demonstrate their conjugation potential a metal chelate, DOTA, was conjugated to SAHBA-FeOx and CMPVA-FeOx nanoparticles. DOTA can chelate Lutetium-177 (^{177}Lu), primarily a beta emitter that has been used to treat GBM in preclinical murine orthotopic xenograft models.[48] It can also be easily monitored due to a relatively small amount of gamma emmision.[48] Successful attachment of the DOTA chelate and radiolabeling with ^{177}Lu will demonstrate these FeOx surface functionalized nanoparticles ability to act as a nanoplatform for additional radiotherapeutics. SAHBA-FeOx and CMPVA-FeOx were chosen as they showed the best stability results. 1-Ethyl-3-(3-dimethylaminopropyl)carbodiimide (EDC) is a water soluble carbodiimide used for the coupling reaction of carboxyl and amine groups to form an amide bond.[93] N-hydroxysulfosuccinimide (S-NHS) is used to increase the efficiency of the carboxyl and primary amine coupling reaction.[93]

High-performance liquid chromatography (HPLC) was used to confirm successful EDC coupling of the DOTA chelate and determine the radiochemical purity of radiolabeled ^{177}Lu-DOTA-SAHBA-FeOx. The HPLC elution profiles of SAHBA-FeOx measured by UV-VIS absorbance at 254 nm and radioactivity detectors are shown in **Figure 4.37**. This was done to establish the time at which SAHBA-FeOx nanoparticles elute and confirm no radioactivity is present. Next, EDC coupling of the DOTA chelate to the SAHBA-FeOx was performed and then radiolabeled with ^{177}Lu. HPLC was used after removal of free metal cations with an MCX column, specifically ^{177}Lu. Dose calibrator measurements of ^{177}Lu-DOTA-SAHBA-FeOx after MCX column indicated a 52.4% chelation yield. The absorbance results in **Figure 4.38** show

additional peaks at approximately 12.05 and 21.9 mins corresponding to free ^{177}Lu-DOTA, and ammonium hydroxide buffer, respectively. The radioactivity peak (**Figure 4.38**) centered at approximately 9.18 mins overlaps with the absorbance at 254 nm peak (~8.49 mins) indicating successful radiolabeling of DOTA-SAHBA-FeOx nanoparticles with ^{177}Lu. It should be noted that the HPLC radioactivity elution time is slightly delayed due to the time required for the elution to reach the radioactivity counter. The radioactivity peak at 12.33 mins represents free ^{177}Lu-DOTA.

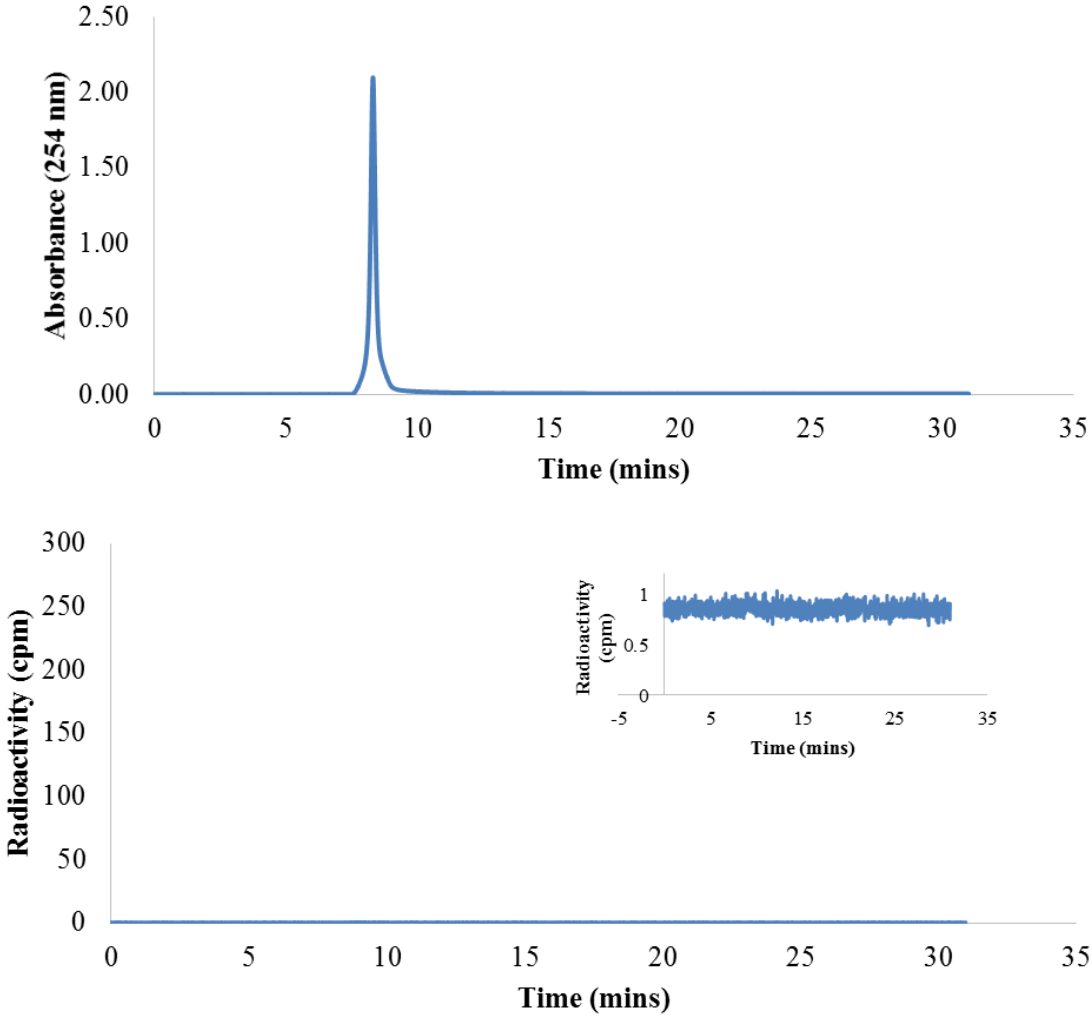

Figure 4.37. HPLC elution profiles of SAHBA-FeOx nanoparticles. The absorbance at 254 nm (top) and radioactivity counts (bottom) are shown.

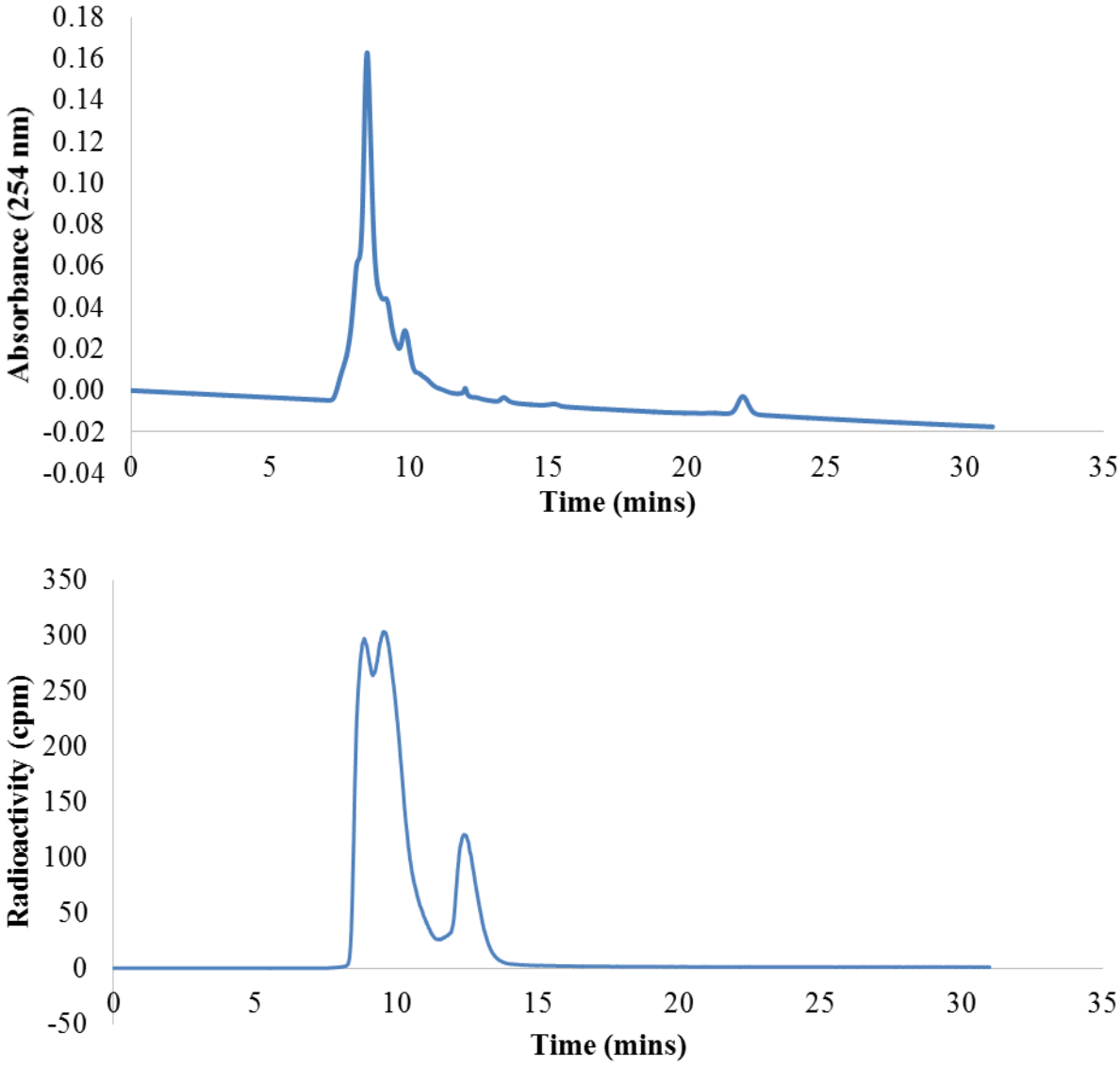

Figure 4.38. HPLC elution profiles of ^{177}Lu-DOTA-SAHBA-FeOx post MCX column elution. The normalized absorbance at 254 nm (top) and radioactivity counts (bottom) are shown.

To remove the remaining free ^{177}Lu-DOTA, and DOTA, a PD-10 size exclusion column was used. Dose calibrator measurements of ^{177}Lu-DOTA-SAHBA-FeOx after PD-10 column indicated a 14.5% synthetic radiochemical yield. The absorbance at 254 nm in **Figure 4.39** only contains one peak centered at approximately 8.6 mins confirming the successful removal of

remaining free ^{177}Lu-DOTA, and DOTA chelate by the PD-10 column. Furthermore, the presence of only one radioactivity peak at 8.79 mins confirms the removal of free ^{177}Lu-DOTA.

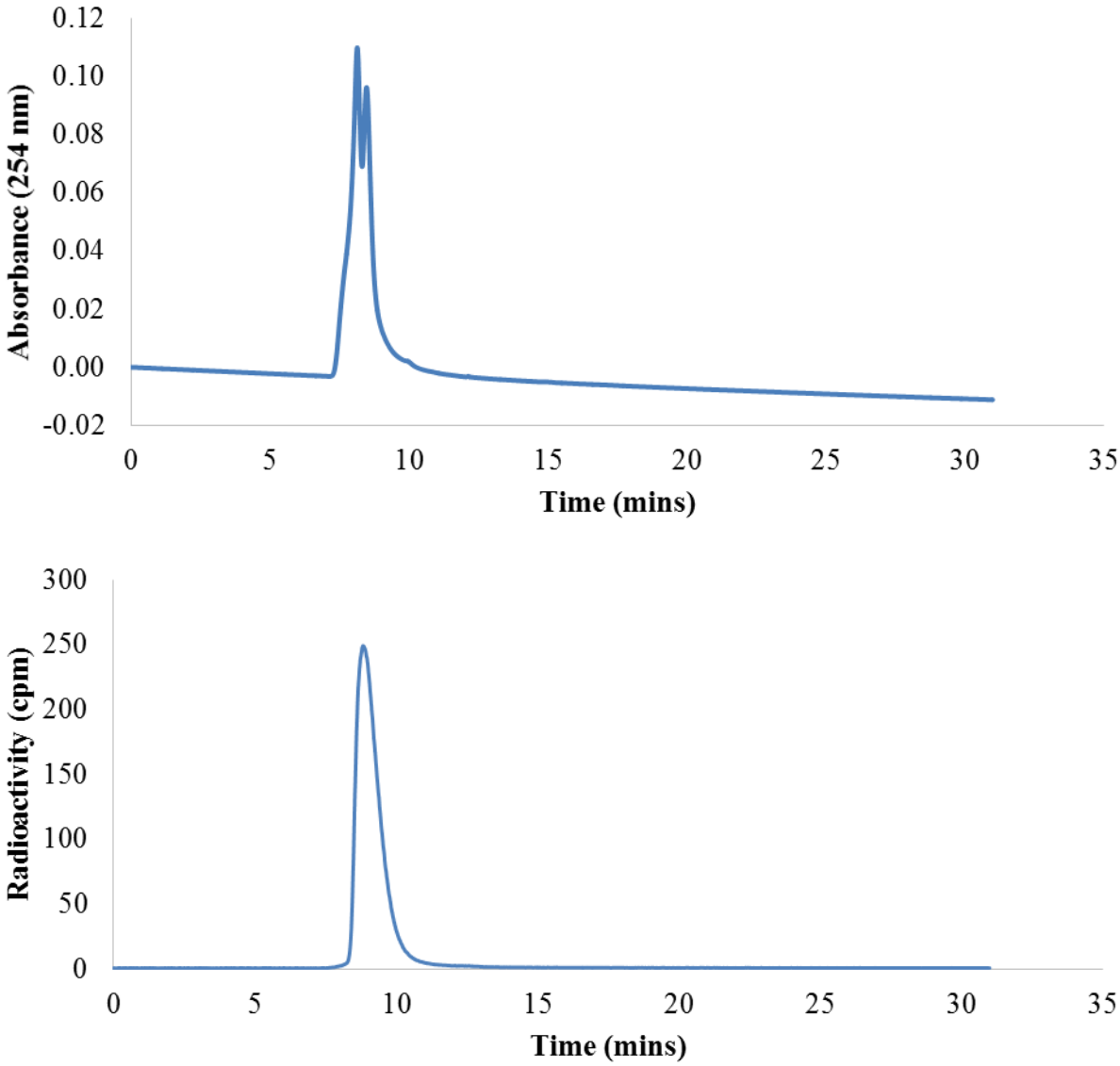

Figure 4.39. HPLC elution profiles of ^{177}Lu-DOTA-SAHBA-FeOx post MCX and PD-10 column elution. The absorbance at 254 nm (top) and radioactivity counts (bottom) are shown.

Next, an HPLC study was used to determine the radiochemical stability of the nanoplatform when subjected to RF hyperthermia. This investigation is essential in determining

the ability of the nanoparticles to deliver both hyperthermia and brachytherapy. The radiochemical stability was assessed for ^{177}Lu-DOTA-SAHBA-FeOx after 0, 15, and 45 minutes of RF heating. If the ^{177}Lu is released from the DOTA chelate or ^{177}Lu-DOTA is released from the nanoparticle after RF heating there could be a reduction in the treatment dose in the region of interest and potential radiation damage to normal tissue in other regions. Additionally, free ^{177}Lu has been shown to incorporate in bone which could limit the amount of activity that can be safely used in treatment, due to radiation sensitivity of bone marrow.[242,243] The HPLC separated absorbance spectrum for 0, 10, and 15 minutes of RF heating is shown in **Figure 4.40**. The HPLC integrated peak areas at approximately 8.3-11.4 mins and 12.03-14.01 mins correspond to ^{177}Lu-DOTA-SAHBA-FeOx and ^{177}Lu-DOTA respectively. Changes in integrated peak areas were used to assess the heat stability after 15 and 45 minutes of RF heating (**Figure 4.41**). The integrated peak ratios of ^{177}Lu-DOTA-SAHBA-FeOx to ^{177}Lu-DOTA were 97.2% to 2.8%, 97.2% to 2.8%, and 97.6% to 2.4% for 0, 10 and 15 minutes of RF heating. No significant increases in integrated peak areas for radioactivity were observed after 15 or 45 minutes of RF heating, confirming the heat stability of ^{177}Lu-DOTA-SAHBA-FeOx.

Furthermore, gamma counting was used to determine if any ^{177}Lu was released after heating. To accomplish this, the ^{177}Lu-DOTA-SAHBA-FeOx nanoparticles were passed through a MCX column after RF heating and the MCX column was gamma counted after elution of the ^{177}Lu-DOTA-SAHBA-FeOx. The gamma counts per minute of the MCX columns for RF heating ^{177}Lu-DOTA-SAHBA-FeOx 0, 10, and 15 mins were 120,686 cpm, 117,373 cpm, and 118,275 cpm respectively. The MCX column can remove ^{177}Lu from the stable ^{177}Lu-DOTA-SAHBA-FeOx as the MCX column more strongly binds ^{177}Lu. This result shows clearly that no significant amount of ^{177}Lu was released upon RF heating.

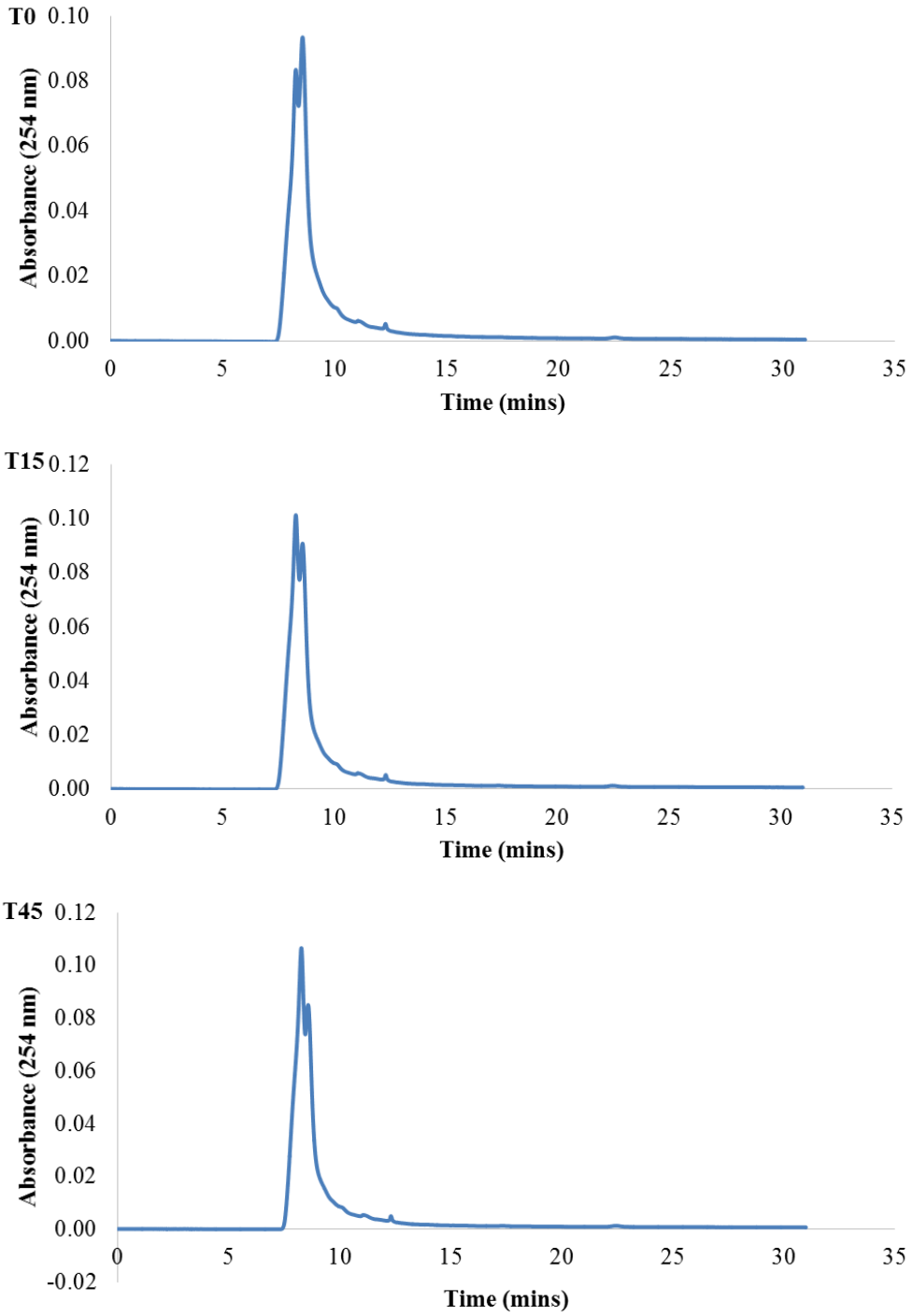

Figure 4.40. HPLC elution profiles absorbance at 245 nm of ^{177}Lu-DOTA-SAHBA-FeOx final product after T0, T15, and T45 minutes of RF heating.

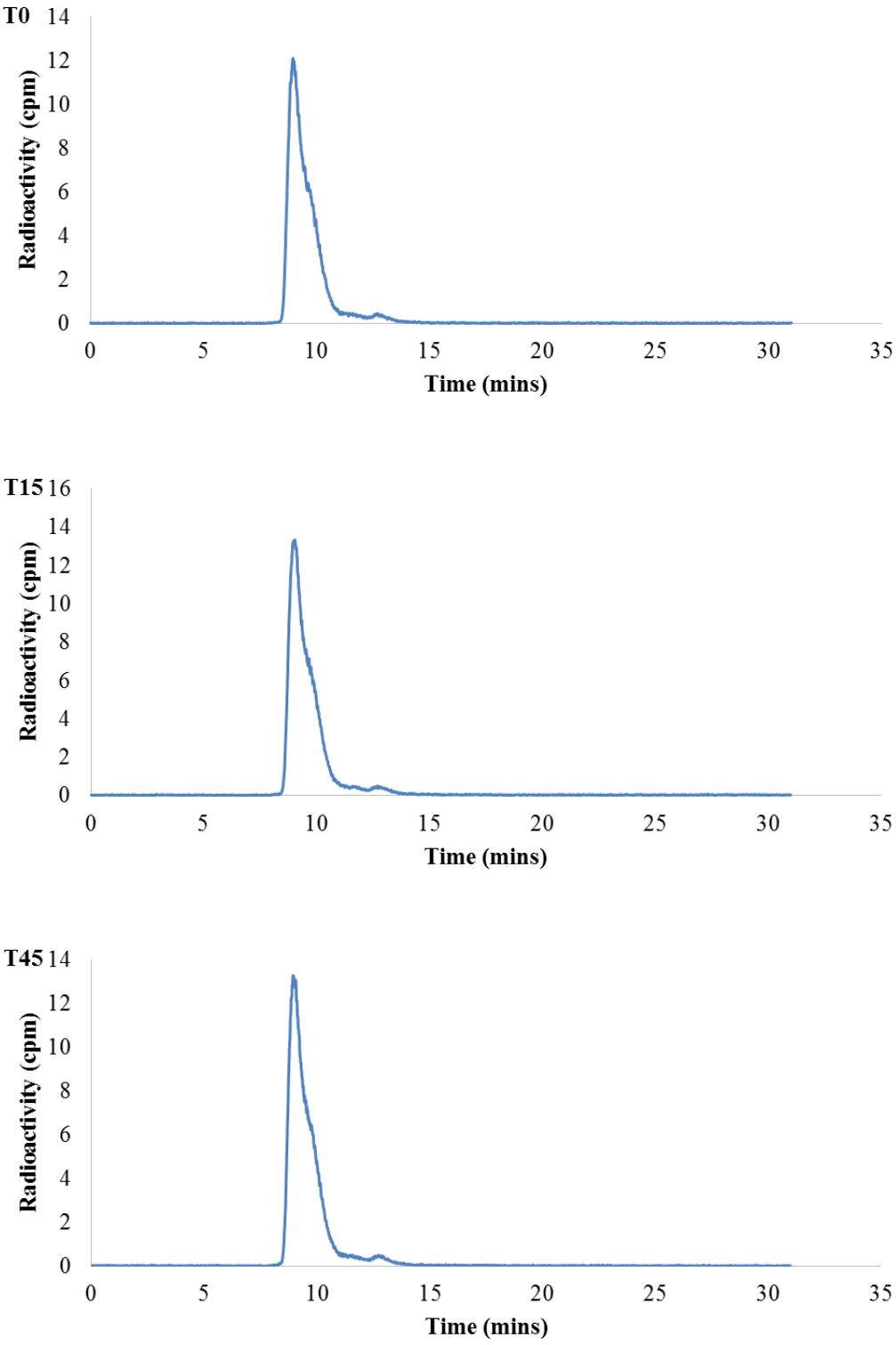

Figure 4.41. HPLC elution profiles radioactivity counts of ^{177}Lu-DOTA-SAHBA-FeOx final product after T0, T15, and T45 minutes of RF heating.

HPLC absorbance and radioactivity analysis confirmed the successful conjugation of DOTA metal chelate and radiolabeling with ^{177}Lu to SAHBA-FeOx and CMPVA-FeOx. Greater than 97% radiochemical purity was obtainable with the cleanup methods used. Additionally, no significant amount of ^{177}Lu or ^{177}Lu-DOTA was released from ^{177}Lu-DOTA-SAHBA-FeOx nanoparticles after RF heating. These results demonstrate the possibility of expanding the conjugation to include combinations of other radiotherapeutics, chemotherapeutics, and/or diagnostic agents by utilizing EDC coupling.

In this chapter the synthesized nanoparticles were easily surface functionalized without the need for difficult phase transfer methods. For surface functionalization with CMPVA, an optimal 0.125% TMAOH concentration was determined. Furthermore, it was determined that for different nanoparticle sizes the methods are best modified by changing the amount of surface functionalization ligand relative to the number of nanoparticles. The CMPVA surface functionalization methods were successfully used to produce APTS-FeOx, APTES-FeOx, and GLYMO-FeOx. The GLYMO-FeOx nanoparticles proved to be very beneficial as the terminal epoxy ring could be modified with a variety of nucleophiles to provide different biological stability properties. FeOx nanoparticle surface functionalizations were verified through FTIR-ATR, XPS, and/or DLS characterization. Stability investigations revealed that SAHBA-FeOx had the best and broadest stability in different biologically relevant media. The SAHBA-FeOx and CMPVA-FeOx demonstrated further conjugation potential via the EDC coupling of DOTA metal chelate and radiolabeling with ^{177}Lu. This produces a theranostic FeOx nanoparticle that can potentially provide radiotherapy and hyperthermia, with MRI capability.

Chapter 5: Biological Testing of Surface Functionalized Iron Oxide Nanoparticles

5.1 Experimental Section

5.1.1 Reagents, Materials, and Equipment

T75 flask (Greiner Bio-One, CELLSTAR®, red filter cap, sterile), Dulbecco's phosphate buffered saline (DPBS) (Corning, cellgro, without calcium and magnesium, sterile), 0.25% trypsin solution (Hyclone), handheld automated cell counter (Millipore, Scepter™), 6-well plate (Greiner Gio-One, Cellstar®), 96-well plates (Greiner Bio-One, Cellstar®), artificial cerebral spinal fluid (CSF) (Harvard Apparatus, artificial), human serum (HS) (Bioreclamation, LLC), modified DMEM/F-12 medium (Hyclone, 0.1 µm sterile filtered) containing 10% fetal bovine serum (FBS) (Seradigm, ultimate grade, triple 0.1 µm sterile filtered), 1% antibiotic/antimycotic solution (Hyclone, 10,000 U/mL Penicillin G, 10,000 µg/mL Streptomycin, 25 µg/mL Amphotericin B, 0.2 µm filtered), Cell Lytic^{TM} M lysis buffer (Sigma), cell proliferation reagent WST-1 (Roche)

5.1.2 Tissue Culture and Cellular Uptake Studies

For biological testing, M059K, GBM-6, or U87MG (AmericanType Culture Collection) cell lines were incubated at 37°C and 5% CO_2 in either T75 or T25 flasks containing complete cell medium. Upon reaching ~80% confluence the cells were washed with Dulbecco's phosphate buffered saline (DPBS) and trypsinised with 0.25% trypsin solution to passage or split the cells into additional culture flasks. A handheld automated cell counter was used to determine the concentration of cells. Cells were diluted to a concentration of 75,000 cells/mL of culture medium prior to plating 2 mL in each well of a 6-well plate. The cells were allowed to attach overnight (~16 hours). Cellular uptake was determined by adding 200 µL of surface functionalized nanoparticles (250 µg/mL). After 4 hours of uptake the cell medium was aliquoted (500 µL), followed by aspiration of the remaining medium. Next, cells were washed three times with DPBS. Cells were lifted in approximately 1.5 mL of DPBS and transferred to a microcentrifuge tube. Cells were centrifuged at 13,000 rpm for 7 minutes to pellet the cells. The supernatant was discarded and 30 µL of Cell Lytic™ M lysis buffer was added and sonicated for 15 minutes. To dissolve the nanoparticles and cells 2.14 µL of 70% nitric acid was added and heated in a heat block at 90°C for 1 hour. A 30 µL aliquot of the collected cell media with 2.14 µL of 70% nitric acid was also heated at 90°C for 1 hour. Prussian blue assay was used to determine the amount of iron. The concentration of cells and amount of iron were used to calculate the cell uptake in units of iron per cell.

5.1.3 WST-1 Cell Proliferation Assays

Cytotoxicity was assessed by a WST-1 cell proliferation assay in a 96-well format. The cells were diluted to a concentration of 25,000 cells/mL of cell medium and 100 µL (2,500 cells)

were plated in each well (n=7). After attaching overnight, 10 µL of PBS control or surface functionalized nanoparticles (250 µg/mL) was added to each well on two 96-wells plates to assess proliferation at 24 and 48 hours. Cell medium was aspirated at 24 or 48 hours and 110 µL of cell proliferation reagent WST-1 in cell medium (500 µL in 5 mL of cell media) was added to each well. The cells were incubated at 37°C and 5% CO_2. At 30, 60, 90, and 120 minutes the 96-well plate was shaken for 60 seconds in a plate reader equipped with UV-VIS. UV-VIS was measured at 440 nm with a reference at 620 nm.

A half maximal inhibitory concentration (IC_{50}) was also determined using a WST-1 assay similar to the cytotoxicity methods above. A 10x DMEM-FBS solution was created by dissolving 1.56 g of DMEM powder (HyClone Laboratories Inc., DME/F -12 1:1+2.5 mM L glutamine, +15 mM HEPES buffer, -sodium bicarbonate) and 0.2438 g of sodium bicarbonate ($NaHCO_3$) (Sigma, 99.5%) in 10 mL of Ultra H_2O. This solution was 0.1 µm sterile filtered in a sterile biological laminar flow hood. Next, 9 mL of the 10x DMEM solution was mixed with 9 mL of sterile 10x FBS to obtain a 5x DMEM-FBS solution. To 120 µL of the 5x DMEM-FBS solution a total of 540 µL of SAHBA-FeOx nanoparticles (~2,200 µg of Fe/mL) and water was added to create 81.81%, 75%, 65.909%, 50%,40%, 20%, 10%, and 0% (1769, 1555, 1179, 944, 472, and 236 µg of Fe/mL) treatment concentrations. After plating 2,500 cells in 100 µL in each well of a 96-well plate the cells were allowed to attach overnight, the medium was then aspirated and then treated with 110 µL of SAHBA-FeOx DMEM-FBS solutions. After 24 hours of treatment, the WST-1 cell proliferation assay was completed as stated above. The resulting cell proliferation values were analyzed in Microsoft Excel with Solver add-in to fit a non-linear IC_{50} curve. Solver was used to minimize the sum of squares of the predicted y-values from **Equation 19**, where A, B, C and D constants are the maximum point, slope of the middle section of the

curve, point of inflection, and minimum point respectively. The IC_{50} was determined by rearranging **Equation 19** to formulate **Equation 20**.

$$y = D + \frac{(A-D)}{1+\left(\frac{x}{C}\right)^{B}} \tag{19}$$

$$x = C \times \left[\frac{(A-y)}{(y-D)}\right]^{\left(\frac{1}{B}\right)} \tag{20}$$

5.1.4 Colony Forming Cell Assay of RF Hyperthermia treated M059K Cells

M059K cells were harvested from a T75 culture flask and counted. Next, 800,000 cells were transferred to a 15 mL conical tube and centrifuged at 1,500 rpm for 5 minutes to pellet the cells. The cells were re-dispersed in 1 mL of cell medium and added to 4 mL of cell medium in a T25 culture flask. Overnight incubation allowed time for the cells to attach. CMPVA nanoparticle treatment or PBS control (250 µL) was added to respective T25 flask and placed back in the incubator for 24 hours. After 24 hour incubation the cells were harvested with 1 mL of trypsin and quenching with 3 mL of cell medium. Next, three 500 µL aliquots of PBS control and six 500 µL CMPVA nanoparticle treatments were added to microcentrifuge tubes. For the PBS control an additional 150 µL of cell medium was added (no particle control group). Three of the CMPVA nanoparticle treatment aliquots received 150 µL of cell medium (particle group) and three received 150 µL of extra CMPVA nanoparticles (~325 µg of iron) in cell medium (extra particle group). Each treatment group was then heated in a water bath at 37°C for one minute prior to RF heating for 0, 10 or 15 minutes at 200.2 A, and 1287 W, in a coil tuned to ~270 kHz. The colony assay performed by diluting each treatment to 150 cells/mL and plating 300 cells (2 mL) on 6-well plates in triplicate. Cell colonies were stained with crystal violet dye and counted at 2 weeks.

5.1.5 U87MG Glioblastoma Tumor Implantation

The *in* vivo mice investigations were conducted according to protocols sanctioned by the McGuire VAMC institutional animal care and use committee (IACUC# 01748). For tumor implantation, female athymic nude-Foxn1nu mice (Harlan Laboratories) were first anesthetized with isoflurane (3% knockdown, 2% maintenance in oxygen). Next, the mice were positioned in a stereotactic frame (David Kopf Instruments). A drill was positioned after a midline incision to drill a 0.7 mm burr hole at a position 0.5 mm anterior to the bregma and 2 mm laterally to the right. Next, a microinjection pump (Bioanalytical Systems) equipped with a 25 µL Hamilton syringe and a 28 gauge removable needle was positioned at a depth of 4.0 mm into the brain (measured from the surface of the skull). The syringe was loaded with 5 µL of PBS containing 5 x 10^4 U87MG cells per µL. The cell suspension was infused at a constant rate of 0.2 µL per minute for a period of 10 minutes resulting in deposition of 1 x 10^5 cells. After infusion, sterile bone wax was utilized to seal the burr hole and the midline incision was sutured. After sufficient recovery time, the animals were returned to the vivarium.

5.1.6 Radioactivity Dose Preparation and Survival Study

CMPVA-FeOx or SAHBA-FeOx were further conjugated to DOTA chelate via EDC coupling, radiolabeled with ^{177}Lu, washed, purified, and sterilized as described in **section 4.1.6**. Additionally, DOTA chelate only was also radiolabeled to serve as a treatment group. The radioactivity was measured by gamma well counting and dose calibrator. The radioactivity was matched for ^{177}Lu-DOTA, ^{177}Lu-DOTA-SAHBA-FeOx, and ^{177}Lu-DOTA-CMPVA-FeOx by dilution with PBS, SAHBA-FeOx, and CMPVA-FeOx respectively. SAHBA-FeOx and CMPVA-FeOx nanoparticles were used for dilution in order to retain a similar concentration of

nanoparticles to the SAHBA-FeOx treatment group. Additionally, three radioactivity concentrations were prepared for each treatment in sterile microcentrifgue tubes to account for ^{177}Lu radioactive decay (half-life= 6.7 days) over the three days required for surgical procedures and infusion of 40 mice (15, 15, 10 mice for days 1, 2, and 3 respectively). More specifically, the three concentrations were required to allow for a constant infusion volume of 10 µL in order to deliver the same radioactive dosage to the mice. The U87MG survival study consisted of 40 mice randomized into five treatment groups (n=8) including PBS control, SAHBA FeOx, ^{177}Lu-DOTA, ^{177}Lu-DOTA-SAHBA-FeOx, and ^{177}Lu-DOTA-CMPVA-FeOx. All radiolabeled treatment groups were planned to receive approximately 10 µCi of ^{177}Lu-DOTA, ^{177}Lu-DOTA-SAHBA-FeOx, or ^{177}Lu-DOTA-CMPVA-FeOx. For CED the mice were placed into a stereotactic frame and a midline incision was made to reveal the burr hole. After removal of bone wax the microinjection needle was centered stereotactically on the burr hole and lowered to a depth of 4 mm to hit the center of the tumor. Next, CED of the treatment groups was performed at 0.2 µL/min flow rate for 50 minutes to deliver a total volume of 10 µL. A rodent study of CED with aqueous infusion using a 28-gauge needle was proven to provide effective CED.[244] For further verification a 0.6% agarose gel (1.5 mL in microcentrifuge tube) was also infused with 10 µL of each treatment to determine average activity delivered at time of infusion. Survival studies were conducted by weight measurements of mice daily in order to follow the disease progression. Mice were weighed on the day of infusion and a loss of body weight was used as a surrogate end point for death. Mice were euthanized when body weight was reduced to 80% of maximum weight. Euthanasia was performed by CO_2 asphyxiation.

5.1.7 Statistical Analysis

Where appropriate, values are mean ± standard error. Cell survival and cell uptake treatment groups are compared to the control group using analysis of variance (ANOVA) and Dunnett two-sided post hoc test with a 0.05 significance level. ANOVA Tukey honest significant difference (HSD) post hoc test with a 0.05 significance level was used to compare between individual treatment groups. The *in vivo* survival study data was analyzed using a Mantel-Cox log rank test for pair-wise comparisons. IBM SPSS Statistics 22 software was used to perform all statistical analysis.

5.2 Cellular Uptake, Proliferation, and IC_{50} Investigations

The cellular uptake of APTS-FeOx, APTES-FeOx, CMPVA-FeOx, and Gly-FeOx, Ser-FeOx, EDA-FeOx, TEPA-FeOx, ABA-FeOx, and SAHBA-FeOx at 4 hours is shown in **Figure 5.1** as percent uptake and picograms (pg) of iron per cell. The cellular uptake method used in this study was not able to discern between internalized nanoparticles or surface adsorbed nanoparticles, but did allow for comparison between differences in surface functionalized nanoparticles. Upon first analysis the uptake of EDA-FeOx and TEPA-FeOx appear to have by far the best cellular uptake with uptake calculated to be 96.2 ± 8.8 pg of iron/cell and 71.7 ± 20.6 % uptake for EDA-FeOx and 99.2 ± 32.7 pg of iron/cell and 41.3 ± 9.0 % uptake for TEPA-FeOx. ANOVA Tukey HDC post-hoc test revealed that both EDA-FeOx and TEPA-FeOx were statistically different than the PBS control ($p<0.001$) (**Appendix - Tables A1-5**). Positive zeta charge may indeed increase interaction with the surface of the cells, but it was determined that the high cellular uptake is a false indication of the true cellular uptake for two reasons. First, there is a known cell medium instability that could lead to precipitation on the surface of cells.

Second, visual clumping of EDA-FeOx and TEPA-FeOx could be seen during incubation with cells in the cell uptake study. This result is important as it illustrates, rather dramatically, the potential for artificially high cellular uptake due to instability upon introduction into cell medium. Both of these GLYMO surface functionalizations appeared stable in water, 1x PBS, 0.5x PBS, and 0.9% NaCl for more than 2 weeks, but were significantly precipitated after only 2 hours in cell medium. Therefore, the stability of nanoparticles to be used in biological applications must be carefully evaluated and considered when reporting high cell uptake. The other positive zeta potential surface functionalizations, APTS-FeOx and APTES-FeOx, resulted in higher cell uptake values compared to the negative surface functionalizations. However, ANOVA Tukey HSD post hoc test revealed only significant differences between APTS-FeOx or APTES-FeOx and either EDA-FeOx or TEPA-FeOx.

Cellular uptake studies with APTS-FeOx or APTES-FeOx that was not prepared immediately prior to testing resulted in larger cellular uptakes further corroborating the connection between instability/size and cellular uptake seen in EDA-FeOx and TEPA-FeOx uptake. More specifically given time the APTS-FeOx and APTES-FeOx formed larger aggregates due to rehydrolyzing or restructuring causing increased instability and cellular uptake. Examining the negative zeta potential surface functionalizations reveals similar uptake values within the range of 0.19-0.46% uptake or 0.65-1.41 pg of iron per cell. All five of the tested anionic surface functionalizations had strikingly similar stabilities. The similar stability and terminal group chemistry results in similar measured cellular uptake values. Remarkably, the SAHBA-FeOx nanoparticles, which were stable in a wide array of media, had the lowest uptake (0.65±0.06 pg of iron per cell, 0.19±0.03% uptake). However, ANOVA Tukey HSD post-hoc tests (**Appendix – Tables 1-5**) CMPVA-FeOx, Gly-FeOx, Ser-FeOx, ABA-FeOx, and SAHBA-

FeOx SAHBA-FeOx were only statistically different when compared to EDA-FeOx or TEPA-FeOx. More studies may reveal a significant link between better stability and lower cellular uptake. Future reports linking only positive zeta potential to higher cellular uptake may need to be reported as lower stability resulting in higher cell uptake.

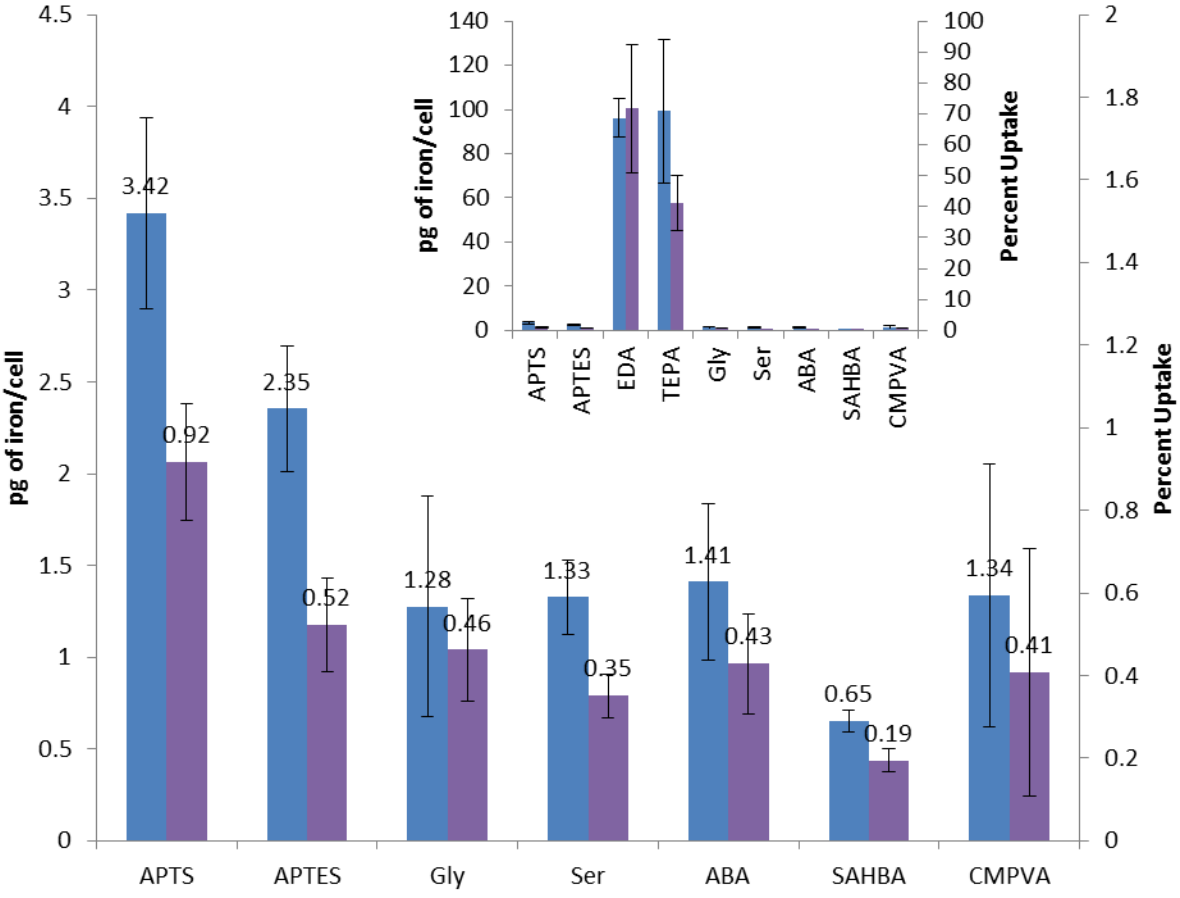

Figure 5.1. GBM-6 cellular uptake results for surface functionalized FeOx nanoparticles; reported in units of percent uptake (purple) or pg of iron/cell (blue). EDA-FeOx and TEPA-FeOx uptake values are included in the inset figure with a larger y-axis.

Initial toxicity was investigated in terms of proliferation using a WST-1 cell proliferation assay at 24 and 48 hours. The results are shown in **Figure 5.2**. TEPA-FeOx had significant

(ANOVA Tukey HSD post-hoc test) difference in proliferation as compared to the control at both 24 and 48 hours (**Appendix – Tables A6-12**). This was expected due to the high degree of instability in cell medium at short time points and the large amount of cell uptake. Larger amounts of cell uptake may be preventing essential cellular processes leading to the observed toxicity and decreased proliferation rates. Interestingly the EDA-FeOx only showed decreases in cell proliferation at 48 hours even though the nanoparticles were instable in cell medium and had large amounts of cell uptake. Further analysis of WST-1 with ANOVA Tukey and Dunnett two-sided post-hoc tests (**Appendix – Table A6-12**) only indicated a significant reduction in cell proliferation, compared to the PBS control, at 24 hours for TEPA-FeOx nanoparticles and at 48 hours for EDA-FeOx and TEPA-FeOx nanoparticles.

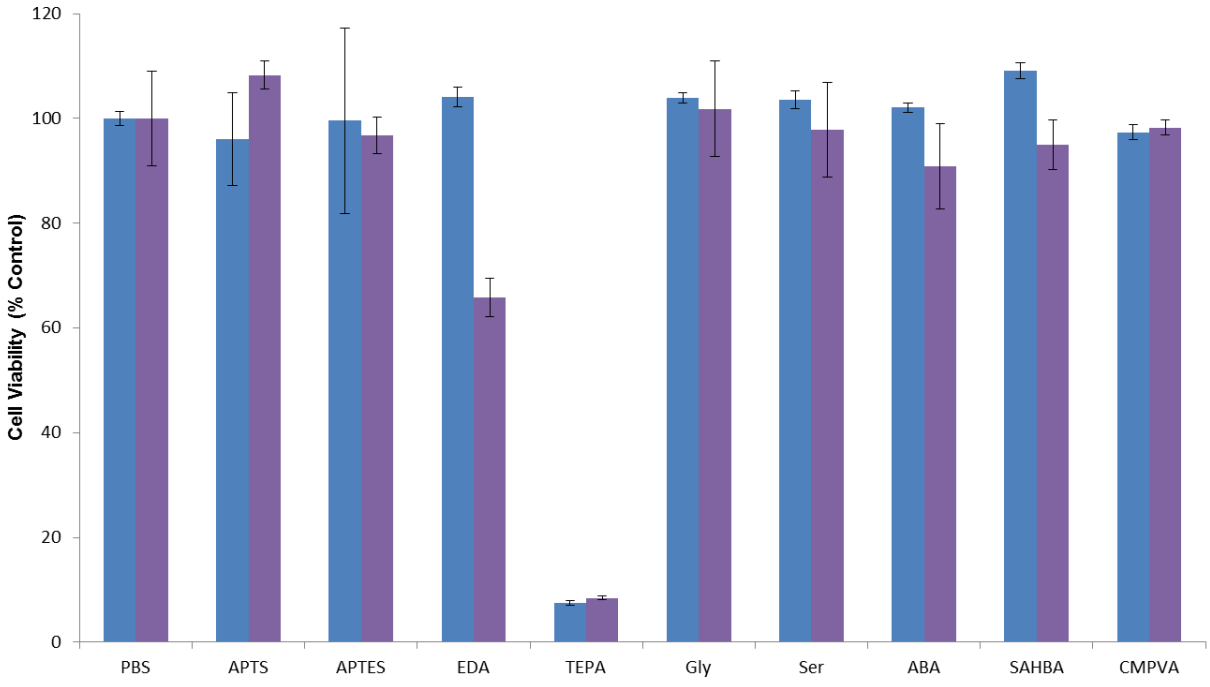

Figure 5.2. Effect of surface functionalized nanoparticles on cell proliferation at 24 (blue) and 48 (purple) hours.

The half maximal inhibitory concentration (IC_{50}) of SAHBA-FeOx was determined by WST-1 and cell titer blue cell proliferation assays at 24 hours using several concentrations of SAHBA-FeOx in U87 cells. The results from both assays are shown in **Figure 5.3**. The non-linear curve was fitted using Microsoft Excel Solver add-in by minimizing the sum of squares of **Equation 19** predicted y-values. Due to increased cell proliferation at the lowest concentration of SAHBA-FeOx the curve was solved without the 0 SAHBA-FeOx concentration data point. The A, B, C, and D constant values were found to be 120.0642, 5.838533, 53.19202, and 24.84344 respectively when minimizing the sum of squares. The sum of squares was minimized to 12.59 or 112.77 for WST-1 and cell titer blue respectively. Using **Equation 20** it was found that the IC_{50} at 24 hours of treatment with SAHBA-FeOx was 1495.91 or 1320.38 µg/mL for 2,500 U87 cells plated 24 hours prior to treatment based on WST-1 and cell titer blue respectively. The difference in percent control of cell viability for the two cell proliferation assays is thought to be due to determination via absorbance (WST-1) or fluorescence (cell titer blue) measurements. Due to the color of the iron oxide solutions it is thought that there could be some overlap in the WST-1 UV-VIS absorbance measurements resulting in higher cell viability as compared to the PBS control. Therefore, the cell titer blue fluorescent based assay is more likely indicative of the true cell viability. However, we also see an increase in cell viability as compared to the PBS control for both assays at low concentrations suggesting that the FeOx nanoparticle treatment may be increasing cell viability. Further investigation is needed to comment further.

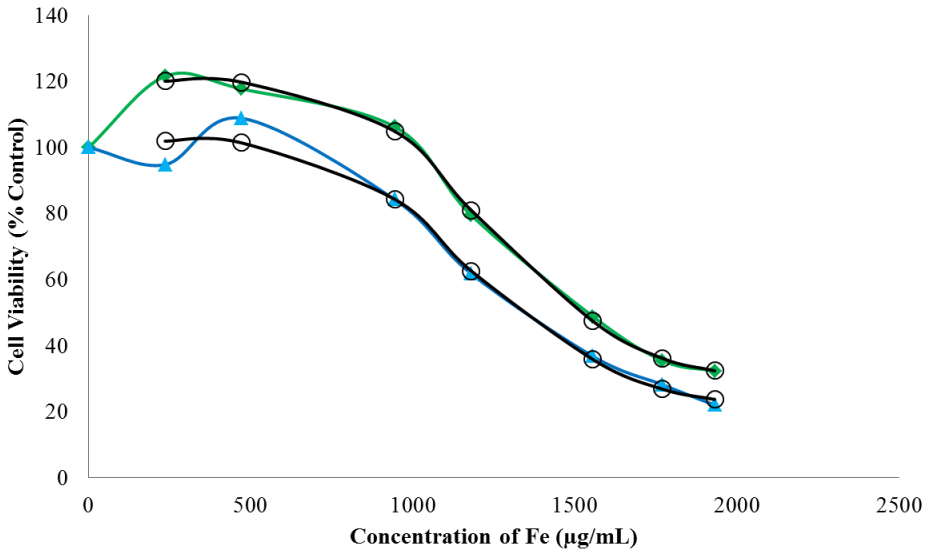

Figure 5.3. Effect of varying concentrations of SAHBA-FeOx on cell proliferation at 24 hours based on WST-1 (green) and cell titer blue (blue) assays used to determine IC_{50}. The IC_{50} trend line is shown in black with open circles representing estimated y-values.

5.3 Effect of Hyperthermia on Cell Proliferation

WST-1 cell proliferation assay was also used to investigate potential differences of RF induced hyperthermia. M059K glioblastoma cells were selected for initial *in vitro* hyperthermia studies to verify the FeOx nanoparticles could be used to kill glioblastoma cells by delivering sufficient hyperthermia. The CMPVA surface functionalized A2-24_B2-24 nanoparticles were used due to their well-studied surface functionalization and low polydispersity. The cellular uptake (**Figure 5.4**) revealed that the M059K cells had an uptake value of 0.2 µg of Fe per 100,000 cells when treated with 2.18 mg/mL iron concentration of CMPVA nanoparticles. Extra CMPVA nanoparticles were added after 24 hours of uptake prior to cell heating as a positive control and to ensure an adequate concentration of nanoparticles to demonstrate RF hyperthermia. An additional ~325 µg of iron was added for the extra nanoparticles group

resulting in 99.94% of 'external' and 0.06% 'internal' nanoparticles (0.2 µg/325.2 µg). With such a large excess of 'external' nanoparticles the extra nanoparticles group was considered a mixture with a dominant percent of 'external' heating and the particle group was considered only 'internal' heating.[245,246]

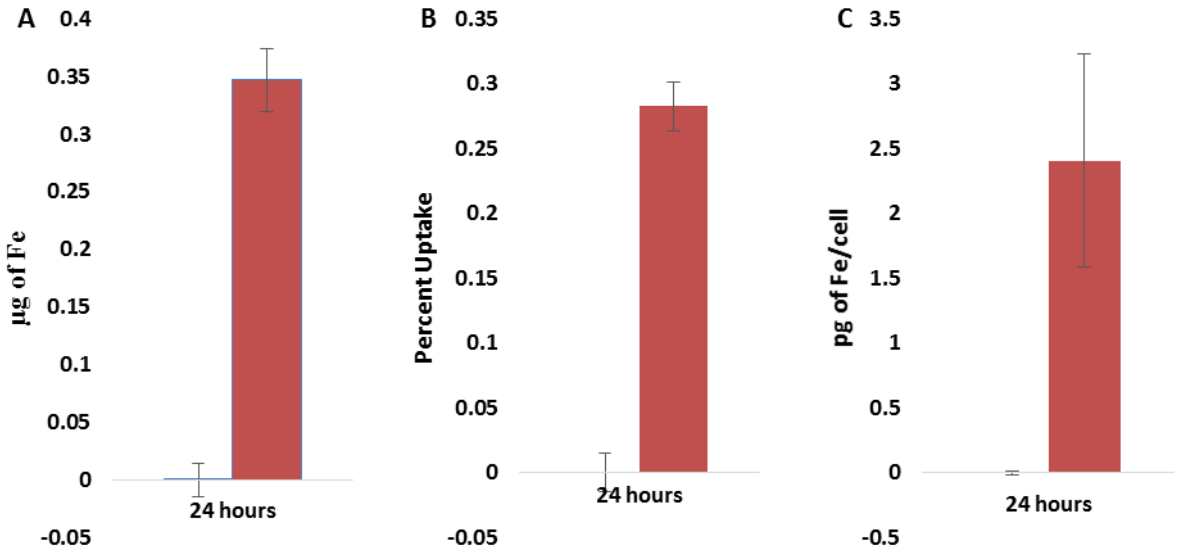

Figure 5.4. M059J cell uptake of CMPVA-FeOx (red) and PBS control (Blue) at 24 hours in terms of µg of iron (A), percent uptake (B), and pg of Fe/cell (C).

The results of the *in vitro* hyperthermia experiment are shown in **Figure 5.5**. Analysis of the 'no heat' treatment (**Figure 5.5.** top (blue)) for PBS control, nanoparticles, and extra nanoparticles, revealed no significant differences in cell proliferation further corroborating no significant toxicity of CMPVA nanoparticles (**Appendix –Tables A13-16** statistical analysis results).

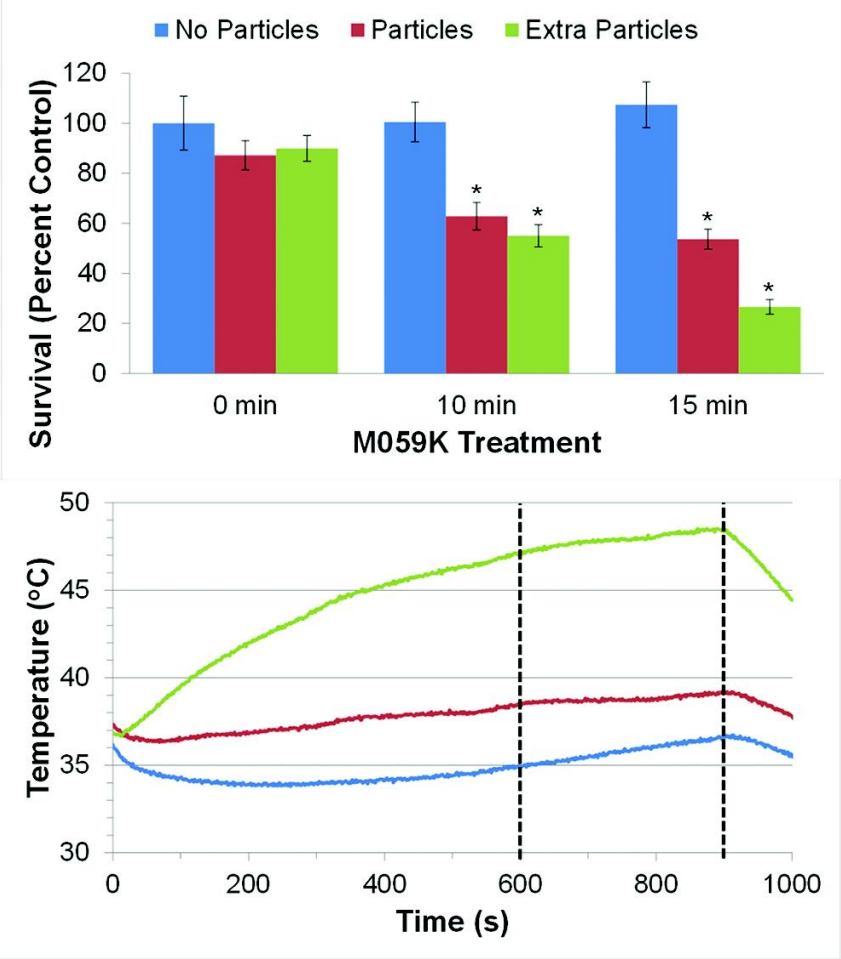

Figure 5.5. RF hyperthermia effect on M059K survival as determined by colony assay. (Top) No particle (blue), particle (red), and extra particle (green) treatment groups survival are shown at 0, 10 and 15 minutes with a * indicating a significant difference determined by ANOVA and Dunnett two-sided post-hoc tests with a 0.05 significance level. (Bottom) The corresponding treatments measured RF hyperthermia over 15 minutes with dashed lines indicating 10 and 15 minutes of heating.

The PBS control showed no changes in cell proliferation after exposure to RF AC magnetic field for 10 and 15 minutes. The RF heating of the PBS control (**Figure 5.5.** bottom, blue line) was measured and did not have significant deviation from 37°C. The RF hyperthermia of the

nanoparticle and extra nanoparticle treatments had measurable and significant lowering of cell proliferation at 10 minutes. Interestingly, the decreases of cell proliferation were seen in both treatments with different temperature measurements (**Figure 5.5**, bottom). Even though the temperature only reached 38.5°C after ten minutes of RF heating (red line) it had similar cell killing as compared to the extra particle group (green line) with a temperature increase to 47.1°C. Analyzing the 15 minutes heating revealed that both nanoparticle and extra nanoparticle treatments had significant cell killing when compared to the PBS control treatment. At first glance, the extra nanoparticle group at 15 minutes appears to have additional cell killing, but was not found to be significant based on ANOVA Tukey HSD post hoc test (**Appendix – Tables A13-16**). At 15 minutes the extra nanoparticle group temperatures entered the thermal ablation range at 48.4°C, where the nanoparticle group only reached 39.1°C. It should be noted that repeating the experiment with additional replicates (higher N) could elucidate significant differences that is expected for the larger temperature differences. However, these results were sufficient to demonstrate glioblastoma cell killing via RF induced hyperthermia and revealed potential vast differences based on 'internal' and 'external' hyperthermia.

5.4 Survival Study- Iron Oxide nanoparticle ^{177}Lu Brachytherapy Investigation

The efficacy of FeOx nanoparticles in providing brachytherapy was investigated for ^{177}Lu-DOTA-SAHBA-FeOx and ^{177}Lu-DOTA-CMPVA-FeOx nanoparticles. These two surface functionalized nanoparticles were chosen due to their similar broad and long term stability characteristics, and differences in surface functionalization size. It was hypothesized that the smaller size of ^{177}Lu-DOTA-SAHBA-FeOx could facilitate better distribution within the tumor.

In order to test this hypothesis an *in vivo* survival study using a murine orthotopic xenograft model of glioblastoma multiforme (U87MG) was used. Radiolabeling SAHBA-FeOx and CMPVA-FeOx nanoparticles with ^{177}Lu was confirmed with HPLC absorbance and radioactivity measurements (**Figures 5.6 and 5.7**). The overlap of peaks in the 254 nm absorbance and radioactivity spectra at the same elution time confirms the successful radiolabel chelation product for both ^{177}Lu-DOTA-SAHBA-FeOx and ^{177}Lu-DOTA-CMPVA-FeOx nanoparticles. The radioactivity counts are shifted slightly to longer elution times due to delay in time required to travel from elution to the eSatin radioactivity counter. Dose calibrator measurements were used to determine the chelation yield, and synthetic radiochemical yield. After washing with the MCX column the chelation yield was estimated to be 64%, 54.9%, and 83.6% yield for ^{177}Lu-DOTA-SAHBA-FeOx, ^{177}Lu-DOTA-CMPVA-FeOx, and ^{177}Lu-DOTA respectively. The synthetic radiochemical yield, after PD-10 wash, was estimated to be 23.6% for ^{177}Lu-DOTA-SAHBA-FeOx and 14.2% for ^{177}Lu-DOTA-CMPVA-FeOx. The ^{177}Lu-DOTA was not run on the PD-10 column due to inability to visualize the progression through the PD-10 column and collect only the ^{177}Lu-DOTA.

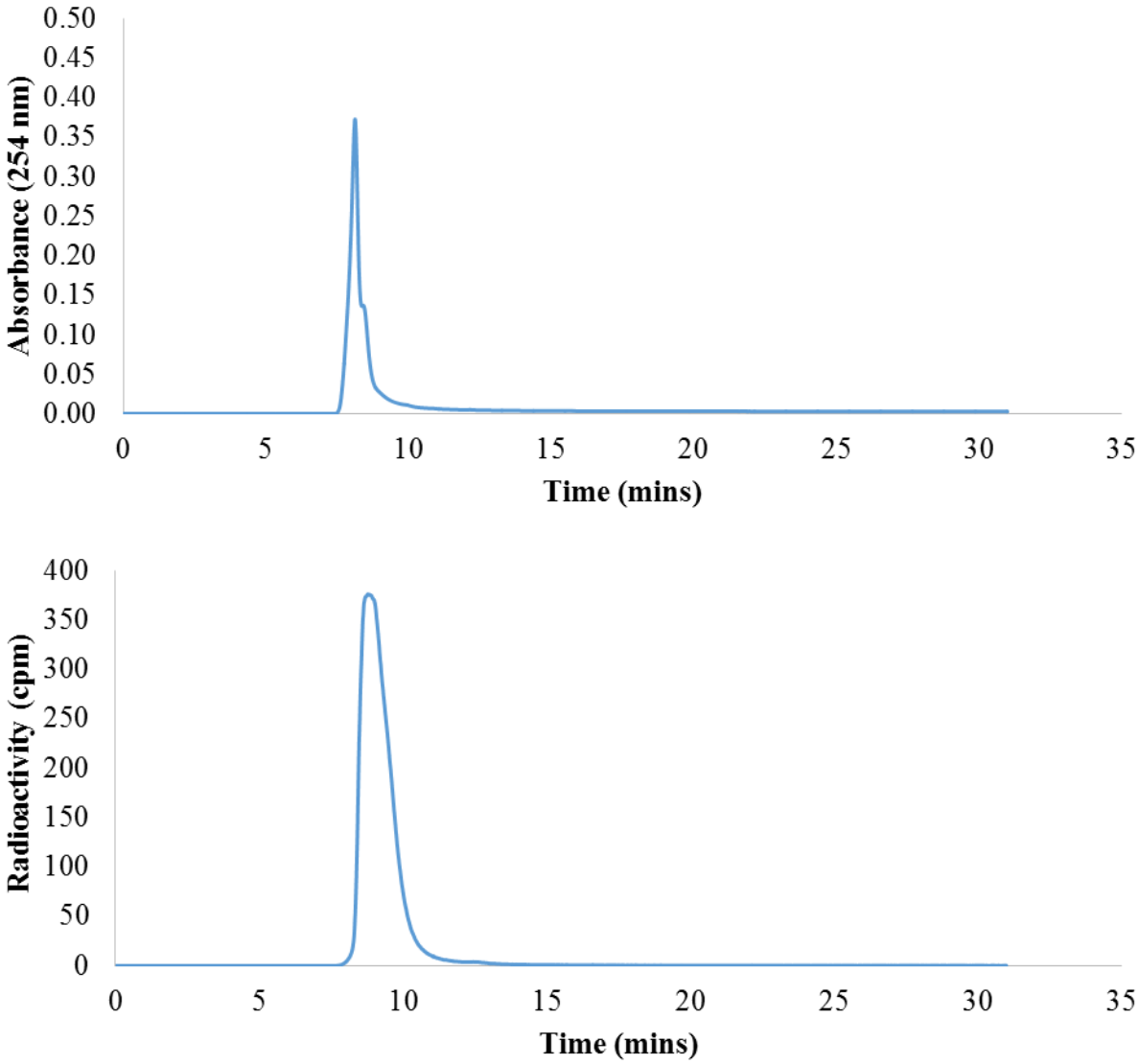

Figure 5.6. HPLC of ^{177}Lu-DOTA-SAHBA-FeOx final product. The absorbance at 254 nm (top) and radioactivity counts (bottom) are shown.

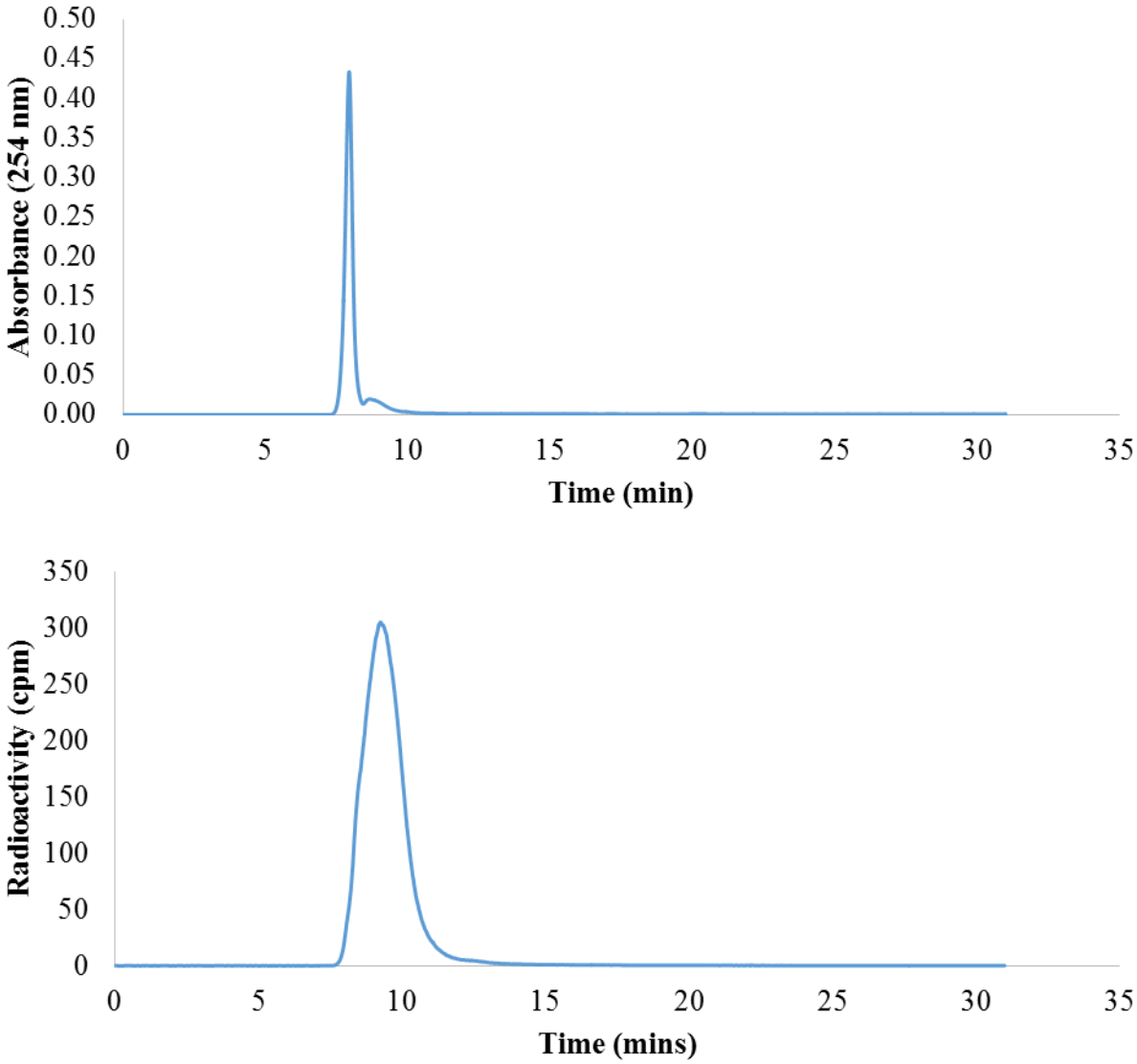

Figure 5.7. HPLC of ^{177}Lu-DOTA-CMPVA-FeOx final product. The absorbance at 254 nm (top) and radioactivity counts (bottom) are shown.

Agarose gels were also infused with ^{177}Lu-DOTA, ^{177}Lu-DOTA-SAHBA-FeOx, or ^{177}Lu-DOTA-CMPVA-FeOx in order to determine the average infused ^{177}Lu activity. Gamma well counting and back decaying of agarose gels revealed an average infused ^{177}Lu activity of 9.72 ± 0.03, 8.59 ± 0.20, and 9.10 ± 0.37 µCi for ^{177}Lu-DOTA, ^{177}Lu-DOTA-SAHBA-FeOx, or ^{177}Lu-

DOTA-CMPVA-FeOx respectively. The survival curves for PBS, SAHBA-FeOx, ^{177}Lu-DOTA, ^{177}Lu-DOTA-SAHBA-FeOx and ^{177}Lu-DOTA-CMPVA-FeOx *in vivo* treatments are shown in **Figure 5.8**. The pair-wise comparison of a log rank Mantel-Cox test revealed differences in survival between the five treatment groups (**Appendix - Tables A17 and A18**). The FeOx control treatment was significantly different than ^{177}Lu-DOTA control (significance = 0.000), but was not significantly different from the PBS control (significance = 0.058). A larger survival study may elucidate a significant difference between the SAHBA-FeOx and PBS and ^{177}Lu-DOTA control groups. The difference between SAHBA-FeOx and ^{177}Lu-DOTA is speculated to be a combination of two factors. First, there is evidence from WST-1 cell proliferation assays that SAHBA-FeOx may potentially increase cell proliferation which could translate to increased tumor growth rate and reduced survival time. Second, ^{177}Lu-DOTA may possibly have a small positive effect on survival, however no significant difference was found between ^{177}Lu-DOTA and PBS treatment at this dose level. A significant difference was revealed between the three controls and ^{177}Lu-DOTA-SAHBA-FeOx (significance 0.000), as well as between the three controls and ^{177}Lu-DOTA-CMPVA-FeOx (significance 0.000). These results confirm the effective brachytherapy deliver by ^{177}Lu-DOTA-SAHBA-FeOx and ^{177}Lu-DOTA-CMPVA-FeOx. There was no significant difference between ^{177}Lu-DOTA-SAHBA-FeOx and ^{177}Lu-DOTA-SAHBA-FeOx. This is not surprising as only one mouse in the ^{177}Lu-DOTA-SAHBA-FeOx lived 37 more days than the last surviving ^{177}Lu-DOTA-CMPVA-FeOx mouse. Since one mouse is representative of 12.5% of the population, a larger study will be necessary to determine if this is a real effect on number of long term survivors between ^{177}Lu-DOTA-SAHBA-FeOx and ^{177}Lu-DOTA-CMPVA-FeOx nanoparticle treatments due to differences in hydrodynamic diameters or surface chemistry. Additionally, further studies such as biodistribution and retention

investigations are needed to confirm no biological differences between ^{177}Lu-DOTA-SAHBA-FeOx and ^{177}Lu-DOTA-CMPVA-FeOx.

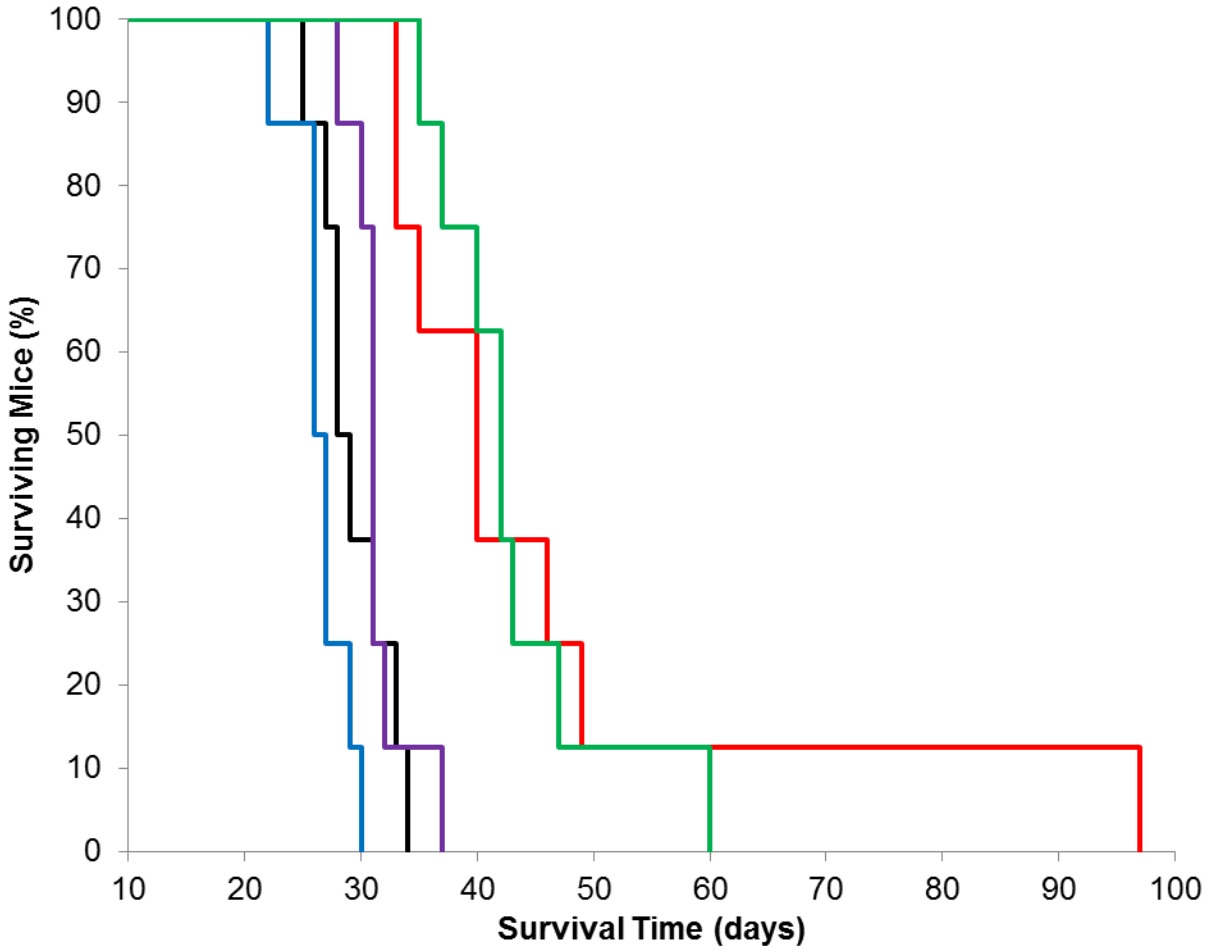

Figure 5.8. Survival study using murine orthotopic xenograft model of glioblastoma multiforme (U87MG) treated with PBS (Black), FeOx (Blue), ^{177}Lu-DOTA (Purple), ^{177}Lu-DOTA-SAHBA-FeOx (Red), and ^{177}Lu-DOTA-CMPVA-FeOx (Green). Significantly different treatment groups from control are indicated by a * as determined by ANOVA and Dunnett two-sided post hoc test at a 0.05 significance level.

Chapter 6: Conclusion

6.1 Conclusion

The first goal of this dissertation was to synthesize FeOx nanoparticles via an innovative and optimizable benzyl alcohol modified seed growth to obtain ideal nanoparticle properties for increased RF induced magnetic hyperthermia treatment of cancer. This was achieved by investigating reaction environment, precursor concentration, and temperature effects on resultant nanoparticle properties.

1. Carrying out the reaction in the presence of air instead of under nitrogen flow provided an additional mechanism of nucleation and growth besides the thermal decomposition. This added oxidation of benzyl alcohol to benzaldehyde mechanism allowed for reduction of $Fe(acac)_3$ facilitating possible synthesis of magnetite and synthesizing nanoparticles with larger crystallite sizes by better separation of nucleation and growth. This was in accordance with reflux occurring just above benzaldehyde's boiling point (178.1°C).
2. Increasing the $Fe(acac)_3$ concentration and/or temperature results were explained by the LaMer growth and Ostwald ripening methods. These increases result in increased monomer generation leading to faster burst nucleation events (reaching higher rates of

nucleation) and a better separation of nucleation and growth leading to larger crystallite sizes and smaller size distributions. The mixed reaction-diffusion limited growth processes and Ostwald ripening were used to explain the differences in amorphous vs. crystallite growth and increasing or decreasing size distributions respectively. There appears to be a limit of monomer generation based on increasing concentration and temperature that result in a prolonged nucleation event leading to larger size distributions, amorphous growth, and smaller crystallite sizes.

3. The modified seed growth aided in obtaining larger crystallite sizes that were more crystalline and had a lower size distribution. Nanoparticles produced by the modified seed growth methods resulted in some of the largest RF heating values.
4. The best RF magnetic heating values were obtained for reaction A2-24(205)_B2-24(205) which has a crystallite size of 19.5 ± 1.06 nm and a PDI of 0.265. The SAR and ILP values (SAR = 1,175.56 W/g and ILP = 3.113 $\frac{nHm^2}{kg}$) are comparable to some of the best commercially available ferrofluids.
5. JMP software was able to model the nanoparticle properties effect on RF heating. The determined equation for predicting RF heating could reasonably predict the RF heating properties based on the significant nanoparticle properties of crystallite size, PDI, and volume CS/HS.

The second goal was to design a surface functionalization method that can provide true colloidal and biological stability and is easily conjugated with additional targeting ligands, chemotherapeutics, or radiotherapeutics.

1. The GLYMO surface functionalization process provided a simple method that could be tuned with a wide array of nucleophiles to obtain broad biological stability.
2. SAHBA-FeOx and CMPVA-FeOx had the best and broadest stability of the surface functionalizations tested. Both surface functionalizations proved stable in water, PBS, saline, CSF, complete cell medium, and human serum. SAHBA-FeOx had the best overall stability even at 5 months.
3. Further conjugation potential was proven by EDC coupling a DOTA chelate and radiolabeling with ^{177}Lu. HPLC verified the EDC coupling and radiolabeling process was successful. The EDC coupling can be used to attach chemotherapeutics, radiotherapeutics, and/or diagnostics containing a primary amine or carboxyl group.

The final goal was to initially investigate biological effects of iron oxide nanoparticles on cell proliferation and uptake, as well as investigate initial *in vitro* effect of hyperthermia and *in vivo* brachytherapy delivery.

1. The surface functionalized iron oxide nanoparticles, with the exception of EDA-FeOx and TEPA-FeOx, were shown to not significantly affect the cell proliferation indicating no toxicity.
2. Cellular uptake measurements revealed that proper stability in water or PBS and cell medium or other relevant medium is essential to measuring accurate cellular uptake. The EDA-FeOx and TEPA-FeOx nanoparticles were not stable in cell medium which resulted in false indication of high cellular uptake values. Furthermore, statistical analysis between positive (APTS-FeOx and APTES-FeOx) and negative (CMPVA-FeOx, Gly-FeOx, Ser-FeOx, ABA-FeOx, and SAHBA-FeOx) nanoparticles revealed no statistically

significant differences in cellular uptake. This finding is not in agreement with literature reporting's of increased cellular uptake for positive surface charged nanoparticles.

3. Cell colony assay revealed that RF heating with surface functionalized FeOx nanoparticles could be used to effectively kill cells. Furthermore, there is evidence suggesting that cell killing can be obtained without large increases in solution temperature which would be highly beneficial for RF hyperthermia applications.
4. Survival studies of murine orthotopic xenograft model of glioblastoma multiforme (U87MG) treated with PBS, FeOx, ^{177}Lu-DOTA, ^{177}Lu-DOTA-SAHBA-FeOx, and ^{177}Lu-DOTA-CMPVA-FeOx showed that SAHBA-FeOx and CMPVA-FeOx nanoparticles can be effectively used to delivery brachytherapy via CED.

The investigation into the benzyl alcohol modified seed growth synthetic parameters and JMP analysis revealed important nucleation and growth mechanism. This lead to the ability to optimize synthesis to produce optimal nanoparticle characteristics for RF induced magnetic hyperthermia. The GLYMO surface functionalization process proved to be a facile method with tunable colloidal/biological stability and is directly applicable to biomedical applications including hyperthermia and brachytherapy delivery. Researching the material synthesis, surface functionalization, and biological testing proved to be a more directly applicable approach to furthering iron oxide nanoparticles to the clinic for RF induced magnetic hyperthermia.

References

References

1. Cornell, R. M.; Schwertmann, U. *The Iron Oxides: Structure, Properties, Reactions, Occurences and Uses, Second Edition;* Wiley-VCH: Weinhiem, 2004; .

2. Ketteler, G.; Weiss, W.; Ranke, W.; Schlogl, R. Bulk and surface phases of iron oxides in an oxygen and water atmosphere at low pressure. *Phys. Chem. Chem. Phys.* **2001**, *3*, 1114-1122.

3. LaMer, V. K.; Dinegar, R. H. Theory, Production and Mechanism of Formation of Monodispersed Hydrosols. *J. Am. Chem. Soc.* **1950**, *72*, 4847-4854.

4. Gilchrist, R. K.; Medal, R.; Shorey, W. D.; Hanselman, R. C.; Parrott, J. C.; Taylor, C. B. Selective Inductive Heating of Lymph Nodes. *Ann. Surg.* **1957**, *146*, 596-606.

5. Gazeau, F.; Lévy, M.; Wilhelm, C. Optimizing magnetic nanoparticle design for nanothermotherapy. *Nanomedicine* **2008**, *3*, 831-844.

6. Song, C.; Park, H.; Griffin, R. Improvement of tumor oxygenation by mild hyperthermia. *Radiat. Res.* **2001**, *155*, 515-528.

7. Peer, A. J.; Grimm, M. J.; Zynda, E. R.; Repasky, E. A. Diverse immune mechanisms may contribute to the survival benefit seen in cancer patients receiving hyperthermia. *Immunol. Res.* **2010**, *46*, 137-154.

8. Spiro, I.; McPherson, S.; Cook, J.; Ling, C.; DeGraff, W.; Mitchell, J. Sensitization of Low-Dose-Rate Irradiation by Nonlethal Hyperthermia. *Radiat. Res.* **1991**, *127*, 111-114.

9. Kumar, C. S. S. R.; Mohammad, F. Magnetic nanomaterials for hyperthermia-based therapy and controlled drug delivery. *Adv. Drug Deliv. Rev.* **2011**, *63*, 789-808.

10. Goldstein, L.; Dewhirst, M.; Repacholi, M.; Kheifets, L. Summary, conclusions and recommendations: adverse temperature levels in the human body. *Int. J. Hyperthermia* **2003**, *19*, 373-384.

11. Beachy, S. H.; Repasky, E. A. Toward establishment of temperature thresholds for immunological impact of heat exposure in humans. *Int. J. Hyperthermia* **2011**, *27*, 344-352.

12. Jordan, A.; Scholz, R.; Wust, P.; Fahling, H.; Felix, R. Magnetic fluid hyperthermia (MFH): Cancer treatment with AC magnetic field induced excitation of biocompatible superparamagnetic nanoparticles. *J. Magn. Magn. Mater.* **1999**, *201*, 413-419.

13. Mornet, S.; Vasseur, S.; Grasset, F.; Duguet, E. Magnetic nanoparticle design for medical diagnosis and therapy. *J. Mater. Chem.* **2004**, *14*, 2161-2175.

14. Krishnan, S.; Diagaradjane, P.; Cho, S. H. Nanoparticle-mediated thermal therapy: Evolving strategies for prostate cancer therapy. *Int. J. Hyperthermia* **2010**, *26*, 775-789.

15. van der Zee, J. Heating the patient: a promising approach? *Annals of Oncology* **2002**, *13*, 1173-1184.

16. Reinhold, H. S.; Endrich, B. Tumour microcirculation as a target for hyperthermia. *Int. J. Hyperthermia* **1986**, *2*, 111-137.

17. Jordan, A.; Wust, P.; Fahling, H.; John, W.; Hinz, A.; Felix, R. Inductive Heating of Ferrimagnetic Particles and Magnetic Fluids - Physical Evaluation of their Potential for Hyperthermia. *Int. J. Hyperthermia* **1993**, *9*, 51-68.

18. Rosensweig, R. Heating magnetic fluid with alternating magnetic field. *J. Magn. Magn. Mater.* **2002**, *252*, 370-374.

19. Ma, M.; Wu, Y.; Zhou, H.; Sun, Y.; Zhang, Y.; Gu, N. Size dependence of specific power absorption of Fe3O4 particles in AC magnetic field. *J. Magn. Magn. Mater.* **2004**, *268*, 33-39.

20. Lee, J.; Jang, J.; Choi, J.; Moon, S. H.; Noh, S.; Kim, J.; Kim, J.; Kim, I.; Park, K. I.; Cheon, J. Exchange-coupled magnetic nanoparticles for efficient heat induction. *Nat. Nanotechnol.* **2011**, *6*, 418-422.

21. Roschmann, P. Radiofrequency Penetration and Absorption in the Human-Body - Limitations to High-Field Whole-Body Nuclear-Magnetic-Resonance Imaging. *Med. Phys.* **1987**, *14*, 922-931.

22. Hergt, R.; Dutz, S. Magnetic particle hyperthermia—biophysical limitations of a visionary tumour therapy. *J. Magn. Magn. Mater.* **2007**, *311*, 187-192.

23. Kallumadil, M.; Tada, M.; Nakagawa, T.; Abe, M.; Southern, P.; Pankhurst, Q. A. Suitability of commercial colloids for magnetic hyperthermia. *J. Magn. Magn. Mater.* **2009**, *321*, 1509-1513.

24. Singh, D.; McMillan, J. M.; Kabanov, A. V.; Sokolsky-Papkov, M.; Gendelman, H. E. Bench-to-bedside translation of magnetic nanoparticles. *Nanomedicine* **2014**, *9*, 501-516.

25. Torres-Lugo, M.; Rinaldi, C. Thermal potentiation of chemotherapy by magnetic nanoparticles. *Nanomedicine* **2013**, *8*, 1689-1707.

26. Jeyadevan, B. Present status and prospects of magnetite nanoparticles-based hyperthermia. *J. Ceram. Soc. Jpn.* **2010**, *118*, 391-401.

27. Laurent, S.; Forge, D.; Port, M.; Roch, A.; Robic, C.; Elst, L. V.; Muller, R. N. Magnetic iron oxide nanoparticles: Synthesis, stabilization, vectorization, physicochemical characterizations, and biological applications. *Chem. Rev.* **2008**, *108*, 2064-2110.

28. Issa, B.; Obaidat, I. M.; Albiss, B. A.; Haik, Y. Magnetic Nanoparticles: Surface Effects and Properties Related to Biomedicine Applications. *Int. J. Mol. Sci.* **2013**, *14*, 21266-21305.

29. Deatsch, A. E.; Evans, B. A. Heating efficiency in magnetic nanoparticle hyperthermia. *J. Magn. Magn. Mater.* **2014**, *354*, 163-172.

30. Huang, S.; Wang, S.; Gupta, A.; Borca-Tasciuc, D.; Salon, S. J. On the measurement technique for specific absorption rate of nanoparticles in an alternating electromagnetic field. *Meas. Sci. Technol.* **2012**, *23*, 035701.

31. Suto, M.; Hirota, Y.; Mamiya, H.; Fujita, A.; Kasuya, R.; Tohji, K.; Jeyadevan, B. Heat dissipation mechanism of magnetite nanoparticles in magnetic fluid hyperthermia. *J. Magn. Magn. Mater.* **2009**, *321*, 1493-1496.

32. Hanson, M. The Frequency-Dependence of the Complex Susceptibility of Magnetic Liquids. *J. Magn. Magn. Mater.* **1991**, *96*, 105-113.

33. Shliomis, M. I.; Pshenichnikov, A. F.; Morozov, K. I.; Shurubor, I. Y. Magnetic properties of ferrocolloids. *J. Magn. Magn. Mater.* **1990**, *85*, 40-46.

34. Brown, W. F. Thermal Fluctuations of a Single-Domain Particle. *Phys. Rev.* **1963**, *130*, 1677-1686.

35. Lemine, O. M.; Omri, K.; Iglesias, M.; Velasco, V.; Crespo, P.; de la Presa, P.; El Mir, L.; Bouzid, H.; Yousif, A.; Al-Hajry, A. gamma-Fe2O3 by sol-gel with large nanoparticles size for magnetic hyperthermia application. *J. Alloys Compounds* **2014**, *607*, 125-131.

36. Yuan, Y.; Tasciuc, D. B. Comparison between experimental and predicted specific absorption rate of functionalized iron oxide nanoparticle suspensions. *J. Magn. Magn. Mater.* **2011**, *323*, 2463-2469.

37. Hergt, R.; Dutz, S.; Mueller, R.; Zeisberger, M. Magnetic particle hyperthermia: nanoparticle magnetism and materials development for cancer therapy. *J. Phys. Condens. Matter.* **2006**, *18*, S2919-S2934.

38. Karimi, Z.; Karimi, L.; Shokrollahi, H. Nano-magnetic particles used in biomedicine: Core and coating materials. *Materials Science & Engineering C-Materials for Biological Applications* **2013**, *33*, 2465-2475.

39. Shenoi, M. M.; Shah, N. B.; Griffin, R. J.; Vercellotti, G. M.; Bischof, J. C. Nanoparticle preconditioning for enhanced thermal therapies in cancer. *Nanomedicine* **2011**, *6*, 545-563.

40. Fillmore, H. L.; Shultz, M. D.; Henderson, S. C.; Cooper, P.; Broaddus, W. C.; Chen, Z. J.; Shu, C.; Zhang, J.; Ge, J.; Dorn, H. C.; Corwin, F.; Hirsch, J. I.; Wilson, J.; Fatouros, P. P. Conjugation of functionalized gadolinium metallofullerenes with IL-13 peptides for targeting and imaging glial tumors. *Nanomedicine* **2011**, *6*, 449-458.

41. Hergt, R.; Hiergeist, R.; Hilger, I.; Kaiser, W.; Lapatnikov, Y.; Margel, S.; Richter, U. Maghemite nanoparticles with very high AC-losses for application in RF-magnetic hyperthermia. *J. Magn. Magn. Mater.* **2004**, *270*, 345-357.

42. Creixell, M.; Bohorquez, A. C.; Torres-Lugo, M.; Rinaldi, C. EGFR-Targeted Magnetic Nanoparticle Heaters Kill Cancer Cells without a Perceptible Temperature Rise. *ACS Nano* **2011**, *5*, 7124-7129.

43. Domenech, M.; Marrero-Berrios, I.; Torres-Lugo, M.; Rinaldi, C. Lysosomal Membrane Permeabilization by Targeted Magnetic Nanoparticles in Alternating Magnetic Fields. *ACS Nano* **2013**, *7*, 5091-5101.

44. Sun, C.; Lee, J. S. H.; Zhang, M. Magnetic nanoparticles in MR imaging and drug delivery. *Adv. Drug Deliv. Rev.* **2008**, *60*, 1252-1265.

45. Weissleder, R.; Stark, D.; Engelstad, B.; Bacon, B.; Compton, C.; White, D.; Jacobs, P.; Lewis, J. Superparamagnetic Iron-Oxide - Pharmacokinetics and Toxicity. *Am. J. Roentgenol.* **1989**, *152*, 167-173.

46. Owens, D.; Peppas, N. Opsonization, biodistribution, and pharmacokinetics of polymeric nanoparticles. *Int. J. Pharm.* **2006**, *307*, 93-102.

47. Shultz, M. D.; Wilson, J. D.; Fuller, C. E.; Zhang, J.; Dorn, H. C.; Fatouros, P. P. Metallofullerene-based Nanoplatform for Brain Tumor Brachytherapy and Longitudinal Imaging in a Murine Orthotopic Xenograft Model. *Radiology* **2011**, *261*, 136-143.

48. Wilson, J. D.; Broaddus, W. C.; Dorn, H. C.; Fatouros, P. P.; Chalfant, C. E.; Shultz, M. D. Metallofullerene-Nanoplatform-Delivered Interstitial Brachytherapy Improved Survival in a Murine Model of Glioblastoma Multiforme. *Bioconjug. Chem.* **2012**, *23*, 1873-1880.

49. Fatouros, P. P.; Shultz, M. D. Metallofullerenes: a new class of MRI agents and more? *Nanomedicine* **2013**, *8*, 1853-1864.

50. Kelkar, S. S.; Reineke, T. M. Theranostics: Combining Imaging and Therapy. *Bioconjug. Chem.* **2011**, *22*, 1879-1903.

51. Gupta, A.; Gupta, M. Synthesis and surface engineering of iron oxide nanoparticles for biomedical applications. *Biomaterials* **2005**, *26*, 3995-4021.

52. Johannsen, M.; Gneveckow, U.; Taymoorian, K.; Thiesen, B.; Waldoefner, N.; Scholz, R.; Jung, K.; Jordan, A.; Wust, P.; Loening, S. A. Morbidity and quality of life during

thermotherapy using magnetic nanoparticles in locally recurrent prostate cancer: Results of a prospective phase I trial. *Int. J. Hyperthermia* **2007**, *23*, 315-323.

53. Carroll, K. J.; Shultz, M. D.; Fatouros, P. P.; Carpenter, E. E. High magnetization aqueous ferrofluid: A simple one-pot synthesis. *J. Appl. Phys.* **2010**, *107*, 09B304.

54. Reimer, P.; Balzer, T. Ferucarbotran (Resovist): a new clinically approved RES-specific contrast agent for contrast-enhanced MRI of the liver: properties, clinical development, and applications. *Eur. Radiol.* **2003**, *13*, 1266-1276.

55. Singh, A.; Patel, T.; Hertel, J.; Bernardo, M.; Kausz, A.; Brenner, L. Safety of Ferumoxytol in Patients With Anemia and CKD. *Am. J. Kidney Dis.* **2008**, *52*, 907-915.

56. Auerbach, M. Ferumoxytol as a New, Safer, Easier-to-Ad minister Intravenous Iron: Yes or No? *Am. J. Kidney Dis.* **2008**, *52*, 826-829.

57. Spinowitz, B. S.; Kausz, A. T.; Baptista, J.; Noble, S. D.; Sothinathan, R.; Bernardo, M. V.; Brenner, L.; Pereira, B. J. G. Ferumoxytol for Treating Iron Deficiency Anemia in CKD. *J. Am. Soc. Nephrol.* **2008**, *19*, 1599-1605.

58. Maier-Hauff, K.; Rothe, R.; Scholz, R.; Gneveckow, U.; Wust, P.; Thiesen, B.; Feussner, A.; von Deimling, A.; Waldoefner, N.; Felix, R.; Jordan, A. Intracranial thermotherapy using magnetic nanoparticles combined with external beam radiotherapy: Results of a feasibility study on patients with glioblastoma multiforme. *J. Neurooncol.* **2007**, *81*, 53-60.

59. Pradhan, P.; Giri, J.; Samanta, G.; Sarma, H. D.; Mishra, K. P.; Bellare, J.; Banerjee, R.; Bahadur, D. Comparative evaluation of heating ability and biocompatibility of different ferrite-based magnetic fluids for hyperthermia application. *J. Biomed. Mater. Res. Part B Appl. Biomater.* **2007**, *81B*, 12-22.

60. Pennacchioli, E.; Fiore, M.; Gronchi, A. Hyperthermia as an adjunctive treatment for soft-tissue sarcoma. *Expert Rev. Anticancer Ther.* **2009**, *9*, 199-210.

61. Emerich, D. F.; Thanos, C. G. The pinpoint promise of nanoparticle-based drug delivery and molecular diagnosis. *Biomol. Eng.* **2006**, *23*, 171-184.

62. Hillyer, J.; Albrecht, R. Gastrointestinal persorption and tissue distribution of differently sized colloidal gold nanoparticles. *J. Pharm. Sci.* **2001**, *90*, 1927-1936.

63. Thorley, A. J.; Tetley, T. D. New perspectives in nanomedicine. *Pharmacol. Ther.* **2013**, *140*, 176-185.

64. Weissleder, R.; Kelly, K.; Sun, E.; Shtatland, T.; Josephson, L. Cell-specific targeting of nanoparticles by multivalent attachment of small molecules. *Nat. Biotechnol.* **2005**, *23*, 1418-1423.

65. Silva, G. Neuroscience nanotechnology: Progress, opportunities and challenges. *Nat. Rev. Neurosci.* **2006**, *7*, 65-74.

66. Ruenraroengsak, P.; Cook, J. M.; Florence, A. T. Nanosystem drug targeting: Facing up to complex realities. *J. Controlled Release* **2010**, *141*, 265-276.

67. Maeda, H. The enhanced permeability and retention (EPR) effect in tumor vasculature: The key role of tumor-selective macromolecular drug targeting. *Adv. Enzyme Regul.* **2001**, *41*, 189-207.

68. Lazzari, S.; Moscatelli, D.; Codari, F.; Salmona, M.; Morbidelli, M.; Diomede, L. Colloidal stability of polymeric nanoparticles in biological fluids. *J. Nanopart. Res.* **2012**, *14*, 920-920.

69. Kamiya, H.; Iijima, M. Surface modification and characterization for dispersion stability of inorganic nanometer-scaled particles in liquid media. *Sci. Tech. Adv. Mater.* **2010**, *11*, 044304.

70. Mout, R.; Moyano, D. F.; Rana, S.; Rotello, V. M. Surface functionalization of nanoparticles for nanomedicine. *Chem. Soc. Rev.* **2012**, *41*, 2539-2544.

71. Boisselier, E.; Astruc, D. Gold nanoparticles in nanomedicine: preparations, imaging, diagnostics, therapies and toxicity. *Chem. Soc. Rev.* **2009**, *38*, 1759-1782.

72. Zhao, W.; Brook, M. A.; Li, Y. Design of Gold Nanoparticle-Based Colorimetric Biosensing Assays. *Chembiochem* **2008**, *9*, 2363-2371.

73. de Vasconcelos, C.; Pereira, M.; Fonseca, J. Polyelectrolytes in solution and the stabilization of colloids. *J. Dispersion Sci. Technol.* **2005**, *26*, 59-70.

74. Yang, M.; Neubauer, C.; Jennings, H. Interparticle potential and sedimentation behavior of cement suspensions - Review and results from paste. *Adv. Cem. Based Mater.* **1997**, *5*, 1-7.

75. Dupont, J.; Scholten, J. D. On the structural and surface properties of transition-metal nanoparticles in ionic liquids. *Chem. Soc. Rev.* **2010**, *39*, 1780-1804.

76. Wang, Z.; Yi, X.; Li, G.; Guan, D.; Lou, A. A functional theoretical approach to the electrical double layer of a spherical colloid particle. *Chem. Phys.* **2001**, *274*, 57-69.

77. Derjaguin, B. On the repulsive forces between charged colloid particles and on the theory of slow coagulation and stability of lyophobe sols. *J. Chem. Soc. Faraday Trans.* **1940**, *35*, 0203-0214.

78. Verwey, E. Theory of the Stability of Lyophobic Colloids. *J. Phys. Colloid Chem.* **1947**, *51*, 631-636.

79. Quesada-Perez, M.; Callejas-Fernandez, J.; Hidalgo-Alvarez, R. Interaction potentials, structural ordering and effective charges in dispersions of charged colloidal particles. *Adv. Colloid Interface Sci.* **2002**, *95*, 295-315.

80. HidalgoAlvarez, R.; Martin, A.; Fernandez, A.; Bastos, D.; Martinez, F.; delasNieves, F. Electrokinetic properties, colloidal stability and aggregation kinetics of polymer colloids. *Adv. Colloid Interface Sci.* **1996**, *67*, 1-118.

81. Moghimi, S. M.; Szebeni, J. Stealth liposomes and long circulating nanoparticles: critical issues in pharmacokinetics, opsonization and protein-binding properties. *Prog. Lipid Res.* **2003**, *42*, 463-478.

82. Moghimi, S. M.; Muir, I. S.; Illum, L.; Davis, S. S.; Kolb-Bachofen, V. Coating particles with a block co-polymer (poloxamine-908) suppresses opsonization but permits the activity of dysopsonins in the serum. *Biochim. Biophys. Acta* **1993**, *1179*, 157-165.

83. Lasic, D. D.; Martin, F. J.; Gabizon, A.; Huang, S. K.; Papahadjopoulos, D. Sterically stabilized liposomes: a hypothesis on the molecular origin of the extended circulation times. *Biochimica et Biophysica Acta (BBA) - Biomembranes* **1991**, *1070*, 187-192.

84. de Gennes, P. G. Polymers at an interface; a simplified view. *Adv. Colloid Interface Sci.* **1987**, *27*, 189-209.

85. Koo, O. M.; Rubinstein, I.; Onyuksel, H. Role of nanotechnology in targeted drug delivery and imaging: a concise review. *Nanomedicine* **2005**, *1*, 193-212.

86. Winter, P.; Caruthers, S.; Kassner, A.; Harris, T.; Chinen, L.; Allen, J.; Lacy, E.; Zhang, H.; Robertson, J.; Wickline, S.; Lanza, G. Molecular Imaging of angiogenesis in nascent vx-2 rabbit tumors using a novel alpha(v)beta(3)-targeted nanoparticle and 1.5 tesla magnetic resonance imaging. *Cancer Res.* **2003**, *63*, 5838-5843.

87. Moghimi, S. M. Modulation of lymphatic distribution of subcutaneously injected poloxamer 407-coated nanospheres: the effect of the ethylene oxide chain configuration. *FEBS Lett.* **2003**, *540*, 241-244.

88. Labhasetwar, V. Nanotechnology for drug and gene therapy: the importance of understanding molecular mechanisms of delivery. *Curr. Opin. Biotechnol.* **2005**, *16*, 674-680.

89. Hashizume, H.; Baluk, P.; Morikawa, S.; McLean, J. W.; Thurston, G.; Roberge, S.; Jain, R. K.; McDonald, D. M. Openings between Defective Endothelial Cells Explain Tumor Vessel Leakiness. *Am. J. Pathol.* **2000**, *156*, 1363-1380.

90. Yuan, F.; Dellian, M.; Fukumura, D.; Leunig, M.; Berk, D.; Torchilin, V.; Jain, R. Vascular-Permeability in a Human Tumor Xenograft - Molecular-Size Dependence and Cutoff Size. *Cancer Res.* **1995**, *55*, 3752-3756.

91. Bandyopadhyay, A.; Raghavan, S. Defining the Role of Integrin alpha v beta 6 in Cancer. *Curr. Drug Targets* **2009**, *10*, 645-652.

92. Dai, W.; Yang, T.; Wang, Y.; Wang, X.; Wang, J.; Zhang, X.; Zhang, Q. Peptide PHSCNK as an integrin α5β1 antagonist targets stealth liposomes to integrin-overexpressing melanoma. *Nanomedicine* **2012**, *8*, 1152-1161.

93. Sehgal, D.; Vijay, I. A Method for the High-Efficiency of Water-Soluble Carbodiimide-Mediated Amidation. *Anal. Biochem.* **1994**, *218*, 87-91.

94. Gilliland, S. E.; Carpenter, E. E.; Shultz, M. D. Modified Seed Growth of Iron Oxide Nanoparticles in Benzyl Alcohol â€“ Optimization for Heating and Broad Stability in Biomedical Applications. *Nanobiomedicine* **2014**, *1*.

95. Asati, A.; Santra, S.; Kaittanis, C.; Perez, J. M. Surface-Charge-Dependent Cell Localization and Cytotoxicity of Cerium Oxide Nanoparticles. *ACS Nano* **2010**, *4*, 5321-5331.

96. Nagy, A.; Steinbrueck, A.; Gao, J.; Doggett, N.; Hollingsworth, J. A.; Iyer, R. Comprehensive Analysis of the Effects of CdSe Quantum Dot Size, Surface Charge, and Functionalization on Primary Human Lung Cells. *ACS Nano* **2012**, *6*, 4748-4762.

97. Nasu, T.; Tokumitsu, K.; Konno, T.; Suzuki, K. Reduction of iron-oxide by ball-milling with hydrogen gas flow. *Mater. Sci. Forum* **2000**, *343-3*, 435-440.

98. Tokumitsu, K.; Nasu, T.; Suzuki, K.; Greer, A. Deoxidation of iron oxide by ball-milling. *Mater. Sci. Forum* **1998**, *269-2*, 181-186.

99. Suryanarayana, C. Mechanical alloying and milling. *Prog. Mater Sci.* **2001**, *46*, 1-184.

100. Rishton, S.; Lu, Y.; Altman, R.; Marley, A.; Bian, X.; Jahnes, C.; Viswanathan, R.; Xiao, G.; Gallagher, W.; Parkin, S. Magnetic tunnel junctions fabricated at tenth-micron dimensions by electron beam lithography. *Microelectron. Eng.* **1997**, *35*, 249-252.

101. Morjan, I.; Alexandrescu, R.; Dumitrache, F.; Birjega, R.; Fleaca, C.; Soare, I.; Luculescu, C. R.; Filoti, G.; Kuncer, V.; Vekas, L.; Popa, N. C.; Prodan, G.; Ciupina, V. Iron Oxide-Based Nanoparticles with Different Mean Sizes Obtained by the Laser Pyrolysis: Structural and Magnetic Properties. *J. Nanosci. Nanotechnol.* **2010**, *10*, 1223-1234.

102. Popovici, E.; Dumitrache, F.; Morjan, I.; Alexandrescu, R.; Ciupina, V.; Prodan, G.; Vekas, L.; Bica, D.; Marinica, O.; Vasile, E. Iron/iron oxides core-shell nanoparticles by laser pyrolysis: Structural characterization and enhanced particle dispersion. *Appl. Surf. Sci.* **2007**, *254*, 1048-1052.

103. Alexandrescu, R.; Morjan, I.; Voicu, I.; Dumitrache, F.; Albu, L.; Soare, I.; Prodan, G. Combining resonant/non-resonant processes: Nanometer-scale iron-based material preparation via CO2 laser pyrolysis. *Appl. Surf. Sci.* **2005**, *248*, 138-146.

104. Dumitrache, F.; Morjan, I.; Alexandrescu, R.; Ciupina, V.; Prodan, G.; Voicu, I.; Fleaca, C.; Albu, L.; Savoiu, M.; Sandu, I.; Popovici, E.; Soare, I. Iron-iron oxide core-shell nanoparticles synthesized by laser pyrolysis followed by superficial oxidation. *Appl. Surf. Sci.* **2005**, *247*, 25-31.

105. Martelli, S.; Mancini, A.; Giorgi, R.; Alexandrescu, R.; Cojocaru, S.; Crunteanu, A.; Voicu, I.; Balu, M.; Morjan, I. Production of iron-oxide nanoparticles by laser-induced pyrolysis of gaseous precursors. *Appl. Surf. Sci.* **2000**, *154*, 353-359.

106. Basak, S.; Chen, D.; Biswas, P. Electrospray of ionic precursor solutions to synthesize iron oxide nanoparticles: Modified scaling law. *Chem. Eng. Sci.***2007**, *62*, 1263-1268.

107. Gurav, A.; Kodas, T.; Pluym, T.; Xiong, Y. Aerosol Processing of Materials. *Aerosol Sci. Technol.* **1993**, *19*, 411-452.

108. Kaushika, A.; Khan, R.; Solanki, P. R.; Pandey, P.; Alam, J.; Ahmad, S.; Malhotra, B. D. Iron oxide nanoparticles-chitosan composite based glucose biosensor. *Biosens. Bioelectron.* **2008**, *24*, 676-683.

109. Kim, D.; Zhang, Y.; Voit, W.; Rao, K.; Muhammed, M. Synthesis and characterization of surfactant-coated superparamagnetic monodispersed iron oxide nanoparticles. *J. Magn. Magn. Mater.* **2001**, *225*, 30-36.

110. Massart, R.; Cabuil, V. Effect of some Parameters on the Formation of Colloidal Magnetite in Alkaline-Medium - Yield and Particle-Size Control. *J. Chim. Phys. Phys. -Chim. Biol.* **1987**, *84*, 967-973.

111. Lee, J.; Isobe, T.; Senna, M. Preparation of ultrafine Fe3O4 particles by precipitation in the presence of PVA at high pH. *J. Colloid Interface Sci.* **1996**, *177*, 490-494.

112. Massart, R.; Dubois, E.; Cabuil, V.; Hasmonay, E. Preparation and Properties of Monodisperse Magnetic Fluids. *J. Magn. Magn. Mater.* **1995**, *149*, 1-5.

113. Sugimoto, T.; Matijevic, E. Formation of Uniform Spherical Magnetite Particles by Crystallization from Ferrous Hydroxide Gels. *J. Colloid Interface Sci.* **1980**, *74*, 227-243.

114. Albornoz, C.; Jacobo, S. Preparation of a biocompatible magnetic film from an aqueous ferrofluid. *J. Magn. Magn. Mater.* **2006**, *305*, 12-15.

115. Wan, J.; Chen, X.; Wang, Z.; Yang, X.; Qian, Y. A soft-template-assisted hydrothermal approach to single-crystal Fe3O4 nanorods. *J. Cryst. Growth* **2005**, *276*, 571-576.

116. Salazar-Alvarez, G.; Muhammed, M.; Zagorodni, A. Novel flow injection synthesis of iron oxide nanoparticles with narrow size distribution. *Chem. Eng. Sci.***2006**, *61*, 4625-4633.

117. Chin, A. B.; Yaacob, I. I. Synthesis and characterization of magnetic iron oxide nanoparticles via w/o microemulsion and Massart's procedure. *J. Mater. Process. Technol.* **2007**, *191*, 235-237.

118. Lim, B.; Rahtu, A.; Gordon, R. Atomic layer deposition of transition metals. *Nat. Mater.* **2003**, *2*, 749-754.

119. Teja, A. S.; Koh, P. Synthesis, properties, and applications of magnetic iron oxide nanoparticles. *Progress in Crystal Growth and Characterization of Materials* **2009**, *55*, 22-45.

120. Carroll, K. J.; Reveles, J. U.; Shultz, M. D.; Khanna, S. N.; Carpenter, E. E. Preparation of Elemental Cu and Ni Nanoparticles by the Polyol Method: An Experimental and Theoretical Approach. *J. Phys. Chem. C* **2011**, *115*, 2656-2664.

121. Miguel-Sancho, N.; Bomati-Miguel, O.; Roca, A. G.; Martinez, G.; Arruebo, M.; Santamaria, J. Synthesis of Magnetic Nanocrystals by Thermal Decomposition in Glycol Media: Effect of Process Variables and Mechanistic Study. *Ind. Eng. Chem. Res.* **2012**, *51*, 8348-8357.

122. Fievet, F.; Fievet-Vincent, F.; Lagier, J.; Dumont, B.; Figlarz, M. Controlled Nucleation and Growth of Micrometer-Size Copper Particles Prepared by the Polyol Process. *J. Mater. Chem.* **1993**, *3*, 627-632.

123. Kim, E.; Lee, H.; Kwak, B.; Kim, B. Synthesis of ferrofluid with magnetic nanoparticles by sonochemical method for MRI contrast agent. *J. Magn. Magn. Mater.* **2005**, *289*, 328-330.

124. Lu, A.; Salabas, E. L.; Schueth, F. Magnetic nanoparticles: Synthesis, protection, functionalization, and application. *Angew. Chem. Int. Ed.* **2007**, *46*, 1222-1244.

125. Kharisov, B. I.; Dias, H. V. R.; Kharissova, O. V.; Manuel Jimenez-Perez, V.; Olvera Perez, B.; Munoz Flores, B. Iron-containing nanomaterials: synthesis, properties, and environmental applications. *RSC Advances* **2012**, *2*, 9325-9358.

126. Hao, R.; Xing, R.; Xu, Z.; Hou, Y.; Gao, S.; Sun, S. Synthesis, Functionalization, and Biomedical Applications of Multifunctional Magnetic Nanoparticles. *Adv. Mater.* **2010**, *22*, 2729-2742.

127. Sato, S.; Murakata, T.; Yanagi, H.; Miyasaka, F.; Iwaya, S. Hydrothermal Synthesis of Fine Perovskite Pbtio3 Powders with a Simple Mode of Size Distribution. *J. Mater. Sci.* **1994**, *29*, 5657-5663.

128. Zhang, L.; He, R.; Gu, H. Oleic acid coating on the monodisperse magnetite nanoparticles. *Appl. Surf. Sci.* **2006**, *253*, 2611-2617.

129. Sun, S.; Zeng, H.; Robinson, D.; Raoux, S.; Rice, P.; Wang, S.; Li, G. Monodisperse MFe2O4 (M = Fe, Co, Mn) nanoparticles. *J. Am. Chem. Soc.* **2004**, *126*, 273-279.

130. Liong, M.; Shao, H.; Haun, J. B.; Lee, H.; Weissleder, R. Carboxymethylated Polyvinyl Alcohol Stabilizes Doped Ferrofluids for Biological Applications. *Adv. Mater.* **2010**, *22*, 5168-+.

131. Qiao, R.; Yang, C.; Gao, M. Superparamagnetic iron oxide nanoparticles: from preparations to in vivo MRI applications. *J. Mater. Chem.* **2009**, *19*, 6274-6293.

132. Niederberger, M.; Bartl, M.; Stucky, G. Benzyl alcohol and titanium tetrachloride - A versatile reaction system for the nonaqueous and low-temperature preparation of crystalline and luminescent titania nanoparticles. *Chem. Mater.* **2002**, *14*, 4364-4370.

133. Niederberger, M.; Bartl, M. H.; Stucky, G. D. Benzyl Alcohol and Transition Metal Chlorides as a Versatile Reaction System for the Nonaqueous and Low-Temperature Synthesis of Crystalline Nano-Objects with Controlled Dimensionality. *J. Am. Chem. Soc.* **2002**, *124*, 13642-13643.

134. Sudareva, N.; Chubarova, E. Time-dependent conversion of benzyl alcohol to benzaldehyde and benzoic acid in aqueous solutions. *J. Pharm. Biomed. Anal.* **2006**, *41*, 1380-1385.

135. Cosmetic Ingredient Review Expert Final report on the safety assessment of Benzyl Alcohol, Benzoic Acid, and Sodium Benzoate. *Int. J. Toxicol.* **2001**, *20*, 23-50.

136. Scognamiglio, J.; Jones, L.; Vitale, D.; Letizia, C. S.; Api, A. M. Fragrance material review on benzyl alcohol. *Food Chem. Toxicol.* **2012**, *50*, S140-S160.

137. Belsito, D.; Bickers, D.; Bruze, M.; Calow, P.; Dagli, M. L.; Fryer, A. D.; Greim, H.; Miyachi, Y.; Saurath, J. H.; Sipes, I. G.; RIFM Expert Panel A toxicological and dermatological assessment of aryl alkyl alcohols when used as fragrance ingredients. *Food Chem. Toxicol.* **2012**, *50*, S52-S99.

138. Pinna, N.; Niederberger, M. Surfactant-free nonaqueous synthesis of metal oxide nanostructures. *Angew. Chem. Int. Ed.* **2008**, *47*, 5292-5304.

139. Bilecka, I.; Djerdj, I.; Niederberger, M. One-minute synthesis of crystalline binary and ternary metal oxide nanoparticles. *Chem. Commun.* **2008**, 886-888.

140. Garnweitner, G.; Niederberger, M. Nonaqueous and Surfactant-Free Synthesis Routes to Metal Oxide Nanoparticles. *J. Am. Ceram. Soc.* **2006**, *89*, 1801-1808.

141. Zhou, S.; Garnweitner, G.; Niederberger, M.; Antonietti, M. Dispersion Behavior of Zirconia Nanocrystals and Their Surface Functionalization with Vinyl Group-Containing Ligands. *Langmuir* **2007**, *23*, 9178-9187.

142. Garnweitner, G.; Goldenberg, L.; Sakhno, O.; Antonietti, M.; Niederberger, M.; Stumpe, J. Large-Scale Synthesis of Organophilic Zirconia Nanoparticles and their Application in Organic?Inorganic Nanocomposites for Efficient Volume Holography. *Small* **2007**, *3*, 1626-1632.

143. Pinna, N.; Grancharov, S.; Beato, P.; Bonville, P.; Antonietti, M.; Niederberger, M. Magnetite nanocrystals: Nonaqueous synthesis, characterization, and solubility. *Chem. Mater.* **2005**, *17*, 3044-3049.

144. Sun, S.; Zeng, H. Size-controlled synthesis of magnetite nanoparticles. *J. Am. Chem. Soc.* **2002**, *124*, 8204-8205.

145. Shultz, M.; Wilson, J.,; Fuller, C.; Zhang, J.; Dorn, H.; Fatouros, P. Metallofullerene-based Nanoplatform for Brain Tumor Brachytherapy and Longitudinal Imaging in a Murine Orthotopic Xenograft Model. *Radiology* **2011**, *261*, 136.

146. De Palma, R.; Peeters, S.; Van Bael, M. J.; Van den Rul, H.; Bonroy, K.; Laureyn, W.; Mullens, J.; Borghs, G.; Maes, G. Silane ligand exchange to make hydrophobic superparamagnetic nanoparticles water-dispersible. *Chem. Mater.* **2007**, *19*, 1821-1831.

147. Mohapatra, S.; Pal, D.; Ghosh, S. K.; Pramanik, P. Design of superparamagnetic iron oxide nanoparticle for purification of recombinant proteins. *J. Nanosci. Nanotechnol.* **2007**, *7*, 3193-3199.

148. van de Waterbeemd, M.; Sen, T.; Biagini, S.; Bruce, I. J. Surface functionalisation of magnetic nanoparticles: quantification of surface to bulk amine density. *Micro & Nano Letters* **2010**, *5*, 282-285.

149. Mohapatra, S.; Pramanik, N.; Mukherjee, S.; Ghosh, S. K.; Pramanik, P. A simple synthesis of amine-derivatised superparamagnetic iron oxide nanoparticles for bioapplications. *J. Mater. Sci.* **2007**, *42*, 7566-7574.

150. Salon, M. B.; Belgacem, M. N. Hydrolysis-Condensation Kinetics of Different Silane Coupling Agents. *Phosphorus Sulfur* **2011**, *186*, 240-254.

151. Ninjbadgar, T.; Brougham, D. F. Epoxy Ring Opening Phase Transfer as a General Route to Water Dispersible Superparamagnetic Fe3O4 Nanoparticles and Their Application as Positive MRI Contrast Agents. *Adv. Funct. Mater.* **2011**, *21*, 4769-4775.

152. Pal, S.; Alocilja, E. C. Electrically active polyaniline coated magnetic (EAPM) nanoparticle as novel transducer in biosensor for detection of Bacillus anthracis spores in food samples. *Biosens. Bioelectron.* **2009**, *24*, 1437-1444.

153. Wang, Y.; Dostalek, J.; Knoll, W. Magnetic Nanoparticle-Enhanced Biosensor Based on Grating-Coupled Surface Plasmon Resonance. *Anal. Chem.* **2011**, *83*, 6202-6207.

154. Kamikawa, T. L.; Mikolajczyk, M. G.; Kennedy, M.; Zhang, P.; Wang, W.; Scott, D. E.; Alocilja, E. C. Nanoparticle-based biosensor for the detection of emerging pandemic influenza strains. *Biosens. Bioelectron.* **2010**, *26*, 1346-1352.

155. Mukherjee, A.; Castanares, M.; Hedayati, M.; Wabler, M.; Trock, B.; Kulkarni, P.; Rodriguez, R.; Getzenberg, R. H.; DeWeese, T. L.; Ivkov, R.; Lupold, S. E. Monitoring nanoparticle-mediated cellular hyperthermia with a high-sensitivity biosensor. *Nanomedicine* **2014**, *9*, 2729-2743.

156. Haun, J. B.; Yoon, T.; Lee, H.; Weissleder, R. Magnetic nanoparticle biosensors. *Wiley Interdisciplinary Reviews-Nanomedicine and Nanobiotechnology* **2010**, *2*, 291-304.

157. Tartaj, P.; Morales, M. P.; Gonzalez-carreño, T.; Veintemillas-verdaguer, S.; Serna, C. J. The Iron Oxides Strike Back: From Biomedical Applications to Energy Storage Devices and Photoelectrochemical Water Splitting. *Adv. Mater.* **2011**, *23*, 5243-5249.

158. Haberl, J. M.; Sanchez-Ferrer, A.; Mihut, A. M.; Dietsch, H.; Hirt, A. M.; Mezzenga, R. Liquid-Crystalline Elastomer-Nanoparticle Hybrids with Reversible Switch of Magnetic Memory. *Adv. Mater.* **2013**, *25*, 1787-1791.

159. Batlle, X.; Labarta, A. Finite-size effects in fine particles: magnetic and transport properties. *J. Phys. D: Appl. Phys.* **2002**, *35*, R15-R42.

160. LesliePelecky, D.; Rieke, R. Magnetic properties of nanostructured materials. *Chem. Mater.* **1996**, *8*, 1770-1783.

161. Polshettiwar, V.; Luque, R.; Fihri, A.; Zhu, H.; Bouhrara, M.; Bassett, J. Magnetically Recoverable Nanocatalysts. *Chem. Rev.* **2011**, *111*, 3036-3075.

162. Yang, H.; Zhang, S.; Chen, X.; Zhuang, Z.; Xu, J.; Wang, X. Magnetite-containing spherical silica nanoparticles for biocatalysis and bioseparations. *Anal. Chem.* **2004**, *76*, 1316-1321.

163. Yi, D. K.; Lee, S. S.; Ying, J. Y. Synthesis and applications of magnetic nanocomposite catalysts. *Chem. Mater.* **2006**, *18*, 2459-2461.

164. Li, L.; Mak, K. Y.; Leung, C. W.; Ng, S. M.; Lei, Z. Q.; Pong, P. W. T. Detection of 10-nm Superparamagnetic Iron Oxide Nanoparticles Using Exchange-Biased GMR Sensors in Wheatstone Bridge. *IEEE Trans. Magn.* **2013**, *49*, 4056-4059.

165. Li, L.; Leung, C. W.; Pong, P. W. T. Magnetism of Iron Oxide Nanoparticles and Magnetic Biodetection. *Journal of Nanoelectronics and Optoelectronics* **2013**, *8*, 397-414.

166. Wang, J.; Zhu, Z.; Munir, A.; Zhou, H. S. Fe(3)O(4) nanoparticles-enhanced SPR sensing for ultrasensitive sandwich bio-assay. *Talanta* **2011**, *84*, 783-788.

167. Blanc-Beguin, F.; Nabily, S.; Gieraltowski, J.; Turzo, A.; Querellou, S.; Salaun, P. Y. Cytotoxicity and GMI bio-sensor detection of maghemite nanoparticles internalized into cells. *J. Magn. Magn. Mater.* **2009**, *321*, 192-197.

168. Frey, N. A.; Peng, S.; Cheng, K.; Sun, S. Magnetic nanoparticles: synthesis, functionalization, and applications in bioimaging and magnetic energy storage. *Chem. Soc. Rev.* **2009**, *38*, 2532-2542.

169. Coffey, W. T.; Kalmykov, Y. P. Thermal fluctuations of magnetic nanoparticles: Fifty years after Brown. *J. Appl. Phys.* **2012**, *112*, 121301.

170. Wabler, M.; Zhu, W.; Hedayati, M.; Attaluri, A.; Zhou, H.; Mihalic, J.; Geyh, A.; DeWeese, T. L.; Ivkov, R.; Artemov, D. Magnetic resonance imaging contrast of iron oxide nanoparticles developed for hyperthermia is dominated by iron content. *Int. J. Hyperthermia* **2014**, *30*, 192-200.

171. Park, J. Y.; Choi, H. J.; Nam, G.; Cho, K.; Son, J. In Vivo Dual-Modality Terahertz/Magnetic Resonance Imaging Using Superparamagnetic Iron Oxide Nanoparticles as a Dual Contrast Agent. *IEEE Trans. Terahertz Sci. Technol.* **2012**, *2*, 93-98.

172. Simeonidis, K.; Martinez-Boubeta, C.; Balcells, L.; Monty, C.; Stavropoulos, G.; Mitrakas, M.; Matsakidou, A.; Vourlias, G.; Angelakeris, M. Fe-based nanoparticles as tunable magnetic particle hyperthermia agents. *J. Appl. Phys.* **2013**, *114*, 103904.

173. Neuberger, T.; Schopf, B.; Hofmann, H.; Hofmann, M.; von Rechenberg, B. Superparamagnetic nanoparticles for biomedical applications: Possibilities and limitations of a new drug delivery system. *J. Magn. Magn. Mater.* **2005**, *293*, 483-496.

174. Vallejo-Fernandez, G.; O'Grady, K. Effect of the distribution of anisotropy constants on hysteresis losses for magnetic hyperthermia applications. *Appl. Phys. Lett.* **2013**, *103*, 142417.

175. Weiss, W.; Ranke, W. Surface chemistry and catalysis on well-defined epitaxial iron-oxide layers. *Prog. Surf. Sci.* **2002**, *70*, 1-151.

176. Li, X.; Elliott, D. W.; Zhang, W. Zero-valent iron nanoparticles for abatement of environmental pollutants: Materials and engineering aspects. *Crit. Rev. Solid State* **2006**, *31*, 111-122.

177. Zhang, Z.; Satpathy, S. Electron-States, Magnetism, and the Verwey Transition in Magnetite. *Phys. Rev. B* **1991**, *44*, 13319-13331.

178. Walz, F. The Verwey transition - a topical review. *J. Phys. Condens. Matter.* **2002**, *14*, R285-R340.

179. Cornell, R. M. *The iron oxides : structure, properties, reactions, occurrences, and uses;* Weinheim : Wiley-VCH: Weinheim, 2003; .

180. Zboril, R.; Mashlan, M.; Petridis, D. Iron(III) oxides from thermal processes-synthesis, structural and magnetic properties, Mossbauer spectroscopy characterization, and applications. *Chem. Mater.* **2002**, *14*, 969-982.

181. Makie, P.; Westin, G.; Persson, P.; Osterlund, L. Adsorption of Trimethyl Phosphate on Maghemite, Hematite, and Goethite Nanoparticles. *J. Phys. Chem. A* **2011**, *115*, 8948-8959.

182. Darken, L. S.; Gurry, R. W. The System Iron-Oxygen. I. The WÃ¼stite Field and Related Equilibria. *J. Am. Chem. Soc.* **1945**, *67*, 1398-1412.

183. Pankhurst, Q.; Connolly, J.; Jones, S.; Dobson, J. Applications of magnetic nanoparticles in biomedicine. *J. Phys. D: Appl. Phys.* **2003**, *36*, R167-R181.

184. Baumgartner, J.; Bertinetti, L.; Widdrat, M.; Hirt, A. M.; Faivre, D. Formation of Magnetite Nanoparticles at Low Temperature: From Superparamagnetic to Stable Single Domain Particles. *Plos One* **2013**, *8*, e57070.

185. Butler, R.; Banerjee, S. Theoretical Single-Domain Grain-Size Range in Magnetite and Titanomagnetite. *J. Geophys. Res.* **1975**, *80*, 4049-4058.

186. Langford, J.; Louer, D. Powder diffraction. *Rep. Prog. Phys.* **1996**, *59*, 131-234.

187. Harris, K.; Tremayne, M. Crystal structure determination from powder diffraction data. *Chem. Mater.* **1996**, *8*, 2554-2570.

188. Vickerman, J.; Gilmore, I. *Surface analysis the principal techniques;* Chichester, U.K. : Wiley: Chichester, U.K., 2009; .

189. Kasap, S. O. (. *Principles of electronic materials and devices;* Boston : McGraw-Hill: Boston, 2006; .

190. Lin, P.; Lin, S.; Wang, P. C.; Sridhar, R. Techniques for physicochemical characterization of nanomaterials. *Biotechnol. Adv.* **2014**, *32*, 711-726.

191. Lim, J.; Yeap, S. P.; Che, H. X.; Low, S. C. Characterization of magnetic nanoparticle by dynamic light scattering. *Nanoscale Res. Lett.* **2013**, *8*, 381.

192. Hiemenz, P. C., 1936- *Principles of colloid and surface chemistry;* New York : Marcel Dekker: New York, 1997; .

193. Wang, Z. Transmission electron microscopy of shape-controlled nanocrystals and their assemblies. *J. Phys. Chem. B* **2000**, *104*, 1153-1175.

194. Zhang, Z.; Miao, C.; Guo, W. Nano-solenoid: helicoid carbon-boron nitride hetero-nanotube. *Nanoscale* **2013**, *5*, 11902-11909.

195. Florini, N.; Barrera, G.; Tiberto, P.; Allia, P.; Bondioli, F. Nonaqueous Sol-Gel Synthesis of Magnetic Iron Oxides Nanocrystals. *J. Am. Ceram. Soc.* **2013**, *96*, 3169-3175.

196. Tu, Z.; Zhang, B.; Yang, G.; Wang, M.; Zhao, F.; Sheng, D.; Wang, J. Synthesis of poly(ethylene glycol) and poly(vinyl pyrrolidone) co-coated superparamagnetic iron oxide nanoparticle as a pH-sensitive release drug carrier. *Colloids Surf., A* **2013**, *436*, 854-861.

197. Yu, W.; Falkner, J.; Yavuz, C.; Colvin, V. Synthesis of monodisperse iron oxide nanocrystals by thermal decomposition of iron carboxylate salts. *Chem. Commun.* **2004**, 2306-2307.

198. Sangermano, M.; Allia, P.; Tiberto, P.; Barrera, G.; Bondioli, F.; Florini, N.; Messori, M. Photo-Cured Epoxy Networks Functionalized With Fe3O4 Generated by Non-hydrolytic SolGel Process. *Macromol. Chem. Phys.* **2013**, *214*, 508-516.

199. Fievet, F.; Lagier, J.; Blin, B.; Beaudoin, B.; Figlarz, M. Homogeneous and Heterogeneous Nucleations in the Polyol Process for the Preparation of Micron and Sub-Micron Size Metal Particles. *Solid State Ionics* **1989**, *32-3*, 198-205.

200. Katritzky, A.; Mu, L.; Lobanov, V.; Karelson, M. Correlation of boiling points with molecular structure .1. A training set of 298 diverse organics and a test set of 9 simple inorganics. *J. Phys. Chem.* **1996**, *100*, 10400-10407.

201. Nandwana, V.; Elkins, K.; Liu, J. Magnetic hardening in ultrafine FePt nanoparticle assembled films. *Nanotechnology* **2005**, *16*, 2823-2826.

202. Roca, A. G.; Morales, M. P.; O'Grady, K.; Serna, C. J. Structural and magnetic properties of uniform magnetite nanoparticles prepared by high temperature decomposition of organic precursors. *Nanotechnology* **2006**, *17*, 2783-2788.

203. Goss, C. Saturation Magnetization, Coercivity and Lattice-Parameter Changes in the System Fe3o4-Gamma-Fe2o3, and their Relationship to Structure. *Phys. Chem. Miner.* **1988**, *16*, 164-171.

204. Shultz, M. D.; Braxton, W.; Taylor, C.; Carpenter, E. E. One parameter control of the size of iron oxide nanoparticles synthesized in reverse micelles. *J. Appl. Phys.* **2009**, *105*, 07A522.

205. Finney, E. E.; Finke, R. G. Nanocluster nucleation and growth kinetic and mechanistic studies: A review emphasizing transition-metal nanoclusters. *J. Colloid Interface Sci.* **2008**, *317*, 351-374.

206. Wang, H.; Nann, T. Monodisperse Upconverting Nanocrystals by Microwave-Assisted Synthesis. *ACS Nano* **2009**, *3*, 3804-3808.

207. Rao, C. N. R.; Müller, A.; Cheetham, A. K. *Nanomaterials chemistry : recent developments and new directions;* Weinheim : Wiley-VCH ; Chichester : John Wiley, distributor: Weinheim : Chichester, 2007; .

208. Murray, C.; Norris, D.; Bawendi, M. Synthesis and Characterization of nearly Monodisperse Cde (E = S, Se, Te) Semiconductor Nanocrystallites. *J. Am. Chem. Soc.* **1993**, *115*, 8706-8715.

209. Symposium on Particle Growth in Suspensions (1972,: Brunel University *Particle growth in suspensions; proceedings;* London, New York, Academic Press: London, New York, 1973; .

210. Figuerola, A.; Fiore, A.; Di Corato, R.; Falqui, A.; Giannini, C.; Micotti, E.; Lascialfari, A.; Corti, M.; Cingolani, R.; Pellegrino, T.; Cozzoli, P. D.; Manna, L. One-pot synthesis and characterization of size-controlled bimagnetic FePt-iron oxide heterodimer nanocrystals. *J. Am. Chem. Soc.* **2008**, *130*, 1477-1487.

211. Tao, A. R.; Habas, S.; Yang, P. Shape control of colloidal metal nanocrystals. *Small* **2008**, *4*, 310-325.

212. Chen, Y.; Johnson, E.; Peng, X. Formation of monodisperse and shape-controlled MnO nanocrystals in non-injection synthesis: Self-focusing via. *J. Am. Chem. Soc.* **2007**, *129*, 10937-10947.

213. Huang, J.; Parab, H. J.; Liu, R.; Lai, T.; Hsiao, M.; Chen, C.; Sheu, H.; Chen, J.; Tsai, D.; Hwu, Y. Investigation of the growth mechanism of iron oxide nanoparticles via a seed-mediated method and its cytotoxicity studies. *J. Phys. Chem. C* **2008**, *112*, 15684-15690.

214. Hind, A. R.; Bhargava, S. K.; McKinnon, A. At the solid/liquid interface: FTIR/ATR - the tool of choice. *Adv. Colloid Interface Sci.* **2001**, *93*, 91-114.

215. Silverstein, R. M. (. M., 1916-2007 *Spectrometric identification of organic compounds;* New York, Wiley: New York, 1967; .

216. Motte, C.; Poelman, M.; Roobroeck, A.; Fedel, M.; Deflorian, F.; Olivier, M. -. Improvement of corrosion protection offered to galvanized steel by incorporation of lanthanide modified nanoclays in silane layer. *Prog. Org. Chem.* **2012**, *74*, 326-333.

217. Yue, Y.; Liu, Z.; Wan, T.; Wang, P. Effect of phosphate-silane pretreatment on the corrosion resistance and adhesive-bonded performance of the AZ31 magnesium alloys. *Prog. Org. Chem.* **2013**, *76*, 835-843.

218. Hu, J.; Liu, L.; Zhang, J.; Cao, C. Electrodeposition of silane films on aluminum alloys for corrosion protection. *Prog. Org. Chem.* **2007**, *58*, 265-271.

219. Chen, M.; Xie, X.; Zhang, X. Interactions of BTESPT silane and maleic anhydride grafted polypropylene with epoxy and application to improve adhesive durability between epoxy and aluminium sheet. *Prog. Org. Chem.* **2009**, *66*, 40-51.

220. Kim, C.; Wang, Z.; Choi, H.; Ha, Y.; Facchetti, A.; Marks, T. J. Printable cross-linked polymer blend dielectrics. Design strategies, synthesis, microstructures, and electrical properties, with organic field-effect transistors as testbeds. *J. Am. Chem. Soc.* **2008**, *130*, 6867-6878.

221. Mascher, P.; Boudreau, M.; Wallace, S.; Murugkar, S.; Balcaitis, G.; Wettlaufer, C.; Haugen, H. *Optical coatings for improved semiconductor diode laser performance;* Electrochemical Society Series; 1998; Vol. 98, pp 67.

222. Kim, W.; Ryu, J. Physical properties of epoxy molding compound for semiconductor encapsulation according to the coupling treatment process change of silica. *J. Appl. Polym. Sci.* **1997**, *65*, 1975-1982.

223. Kobayashi, Y.; Misawa, K.; Takeda, M.; Kobayashi, M.; Satake, M.; Kawazoe, Y.; Ohuchi, N.; Kasuya, A.; Konno, M. Silica-coating of AgI semiconductor nanoparticles. *Colloids Surf., A* **2004**, *251*, 197-201.

224. De Graeve, I.; Tourwe, E.; Biesemans, M.; Willem, R.; Terryn, H. Silane solution stability and film morphology of water-based bis-1,2-(triethoxysilyl)ethane for thin-film deposition on aluminium. *Prog. Org. Chem.* **2008**, *63*, 38-42.

225. Cao, H.; He, J.; Deng, L.; Gao, X. Fabrication of cyclodextrin-functionalized superparamagnetic Fe3O4/amino-silane core–shell nanoparticles via layer-by-layer method. *Appl. Surf. Sci.* **2009**, *255*, 7974-7980.

226. Sundar, S.; Mariappan, R.; Piraman, S. Synthesis and characterization of amine modified magnetite nanoparticles as carriers of curcumin-anticancer drug. *Powder Technol.* **2014**, *266*, 321-328.

227. Yamaura, M.; Camilo, R.; Sampaio, L.; Macedo, M.; Nakamura, M.; Toma, H. Preparation and characterization of (3-aminopropyl) triethoxysilane-coated magnetite nanoparticles. *J Magn. Magn. Mater.* **2004**, *279*, 210-217.

228. White, L. D.; Tripp, C. P. Reaction of (3-Aminopropyl)dimethylethoxysilane with Amine Catalysts on Silica Surfaces. *J. Colloid Interface Sci.* **2000**, *232*, 400-407.

229. Xu, Z.; Liu, Q.; Finch, J. A. Silanation and stability of 3-aminopropyl triethoxy silane on nanosized superparamagnetic particles: I. Direct silanation. *Appl. Surf. Sci.* **1997**, *120*, 269-278.

230. MORROW, B.; MCFARLAN, A. Surface Vibrational-Modes of Silanol Groups on Silica. *J. Phys. Chem.* **1992**, *96*, 1395-1400.

231. Yamashita, T.; Hayes, P. Analysis of XPS spectra of Fe2+ and Fe3+ ions in oxide materials. *Appl. Surf. Sci.* **2008**, *254*, 2441-2449.

232. McIntyre, N.; Zetaruk, D. X-Ray Photoelectron Spectroscopic Studies of Iron-Oxides. *Anal. Chem.* **1977**, *49*, 1521-1529.

233. Sahoo, B.; Devi, K. S. P.; Dutta, S.; Maiti, T. K.; Pramanik, P.; Dhara, D. Biocompatible mesoporous silica-coated superparamagnetic manganese ferrite nanoparticles for targeted drug delivery and MR imaging applications. *J. Colloid Interface Sci.* **2014**, *431*, 31-41.

234. Acres, R. G.; Ellis, A. V.; Alvino, J.; Lenahan, C. E.; Khodakov, D. A.; Metha, G. F.; Andersson, G. G. Molecular Structure of 3-Aminopropyltriethoxysilane Layers Formed on Silanol-Terminated Silicon Surfaces. *Journal of Physical Chemistry C* **2012**, *116*, 6289-6297.

235. Odio, O. F.; Lartundo-Rojas, L.; Santiago-Jacinto, P.; Martinez, R.; Reguera, E. Sorption of Gold by Naked and Thiol-Capped Magnetite Nanoparticles: An XPS Approach. *J. Phys. Chem. C* **2014**, *118*, 2776-2791.

236. Briggs, D.; Beamson, G. XPS Studies of the Oxygen-1s and Oxygen-2s Levels in a Wide-Range of Functional Polymers. *Anal. Chem.* **1993**, *65*, 1517-1523.

237. Stevens, J. S.; Byard, S. J.; Schroeder, S. L. M. Characterization of Proton Transfer in Co-Crystals by X-ray Photoelectron Spectroscopy (XPS). *Cryst. Growth Des.***2010**, *10*, 1435-1442.

238. Stevens, J. S.; de Luca, A. C.; Pelendritis, M.; Terenghi, G.; Downes, S.; Schroeder, S. L. M. Quantitative analysis of complex amino acids and RGD peptides by X-ray photoelectron spectroscopy (XPS). *Surf. Interface Anal.* **2013**, *45*, 1238-1246.

239. Stropoli, S. J.; Elrod, M. J. Assessing the Potential for the Reactions of Epoxides with Amines on Secondary Organic Aerosol Particles. *J. Phys. Chem. A* **2015**.

240. Chan, N.; Li, P.; Oh, J. K. Chain Length Effect of the Multidentate Block Copolymer Strategy to Stabilize Ultrasmall Fe3O4 Nanoparticles. *Chempluschem* **2014**, *79*, 1342-1351.

241. Tenzer, S.; Docter, D.; Rosfa, S.; Wlodarski, A.; Kuharev, J.; Rekik, A.; Knauer, S. K.; Bantz, C.; Nawroth, T.; Bier, C.; Sirirattanapan, J.; Mann, W.; Treuel, L.; Zellner, R.; Maskos, M.; Schild, H.; Stauber, R. H. Nanoparticle Size Is a Critical Physicochemical Determinant of the Human Blood Plasma Corona: A Comprehensive Quantitative Proteomic Analysis. *ACS Nano* **2011**, *5*, 7155-7167.

242. Paganelli, G.; Sansovini, M.; Ambrosetti, A.; Severi, S.; Monti, M.; Scarpi, E.; Donati, C.; Ianniello, A.; Matteucci, F.; Amadori, D. 177 Lu-Dota-octreotate radionuclide therapy of advanced gastrointestinal neuroendocrine tumors: results from a phase II study. *Eur. J. Nucl. Med. Mol. Imaging* **2014**, *41*, 1845-1851.

243. Piccin, A.; Grana, C. M.; Negri, G.; Pusceddu, I.; Paganelli, G.; Cortelazzo, S. Secondary acute myeloid leukaemia after peptide receptor radionuclide therapy. *Ann. Hematol.* **2012**, *91*, 299-300.

244. Pasha, S.; Gupta, K. Various drug delivery approaches to the central nervous system. *Expert Opin. Drug Deliv.* **2010**, *7*, 113-135.

245. Zhang, Y.; Kohler, N.; Zhang, M. Surface modification of superparamagnetic magnetite nanoparticles and their intracellular uptake. *Biomaterials* **2002**, *23*, 1553-1561.

246. Xu, Z.; Zeng, Q.; Lu, G.; Yu, A. Inorganic nanoparticles as carriers for efficient cellular delivery. *Chem. Eng. Sci.* **2006**, *61*, 1027-1040.

Appendix

Table A1. Descriptives for cell uptake study based on pg of Fe per cell values.

	N	Mean	Std. Deviation	Std. Error	95% Confidence Interval for Mean		Minimum	Maximum
					Lower Bound	Upper Bound		
Gly-FeOx	9	1.2770	.67894	.22631	.7551	1.7989	.55	2.50
Ser-FeOx	9	1.3263	.23690	.07897	1.1442	1.5084	.92	1.66
EDA-FeOx	9	96.1587	10.06934	3.35645	88.4187	103.8987	79.92	107.98
TEPA-FeOx	9	99.2303	35.11813	11.70604	72.2361	126.2245	62.38	153.77
ABA-FeOx	9	1.4106	.53743	.17914	.9975	1.8237	.83	2.50
SAHBA-FeOx	9	.6539	.12100	.04033	.5609	.7469	.52	.88
CMPVA-FeOx	9	1.3357	1.09110	.36370	.4970	2.1744	.34	3.05
APTS-FeOx	9	3.4168	.87460	.29153	2.7445	4.0891	2.10	4.60
APTES-FeOx	9	2.3539	.54045	.18015	1.9385	2.7694	1.45	3.05
Total	81	23.0181	41.81012	4.64557	13.7732	32.2631	.34	153.77

Table A2. Descriptives for cell uptake study based on percent uptake values.

	N	Mean	Std. Deviation	Std. Error	95% Confidence Interval for Mean		Minimum	Maximum
					Lower Bound	Upper Bound		
Gly-FeOx	9	.4615	.14989	.04996	.3463	.5767	.24	.67
Ser-FeOx	9	.3511	.06166	.02055	.3037	.3985	.25	.44
EDA-FeOx	9	71.7294	21.95533	7.31844	54.8531	88.6058	42.23	95.81
TEPA-FeOx	9	41.2559	9.61316	3.20439	33.8666	48.6452	33.31	55.85
ABA-FeOx	9	.4271	.14410	.04803	.3164	.5379	.28	.70
SAHBA-FeOx	9	.1937	.04216	.01405	.1613	.2261	.14	.27
CMPVA-FeOx	9	.4079	.32337	.10779	.1593	.6565	.11	.91
APTS-FeOx	9	.9150	.16723	.05574	.7865	1.0436	.63	1.08
APTES-FeOx	9	.5237	.13339	.04446	.4212	.6263	.38	.79
Total	81	12.9184	25.67111	2.85235	7.2420	18.5947	.11	95.81

Table A3. ANOVA values for cell uptake studies.

		Sum of Squares	df	Mean Square	F	Sig.
pg	Between Groups	129144.970	8	16143.121	108.607	.000
	Within Groups	10701.945	72	148.638		
	Total	139846.915	80			
Percent	Between Groups	48123.297	8	6015.412	94.212	.000
	Within Groups	4597.189	72	63.850		
	Total	52720.486	80			

Table A4. Tukey HSD post-hoc tests results for cell uptake study based on pg of Fe per cell values.

(I) Treatment	(J) Treatment	Mean Difference (I-J)	Std. Error	Sig.	95% Confidence Interval	
					Lower Bound	Upper Bound
Gly-FeOx	Ser-FeOx	-.04928	5.74723	1.000	-18.4292	18.3306
	EDA-FeOx	-94.88166*	5.74723	.000	-113.2615	-76.5018
	TEPA-FeOx	-97.95332*	5.74723	.000	-116.3332	-79.5734
	ABA-FeOx	-.13355	5.74723	1.000	-18.5134	18.2463
	SAHBA-FeOx	.62308	5.74723	1.000	-17.7568	19.0030
	CMPVA-FeOx	-.05872	5.74723	1.000	-18.4386	18.3212
	APTS-FeOx	-2.13980	5.74723	1.000	-20.5197	16.2401
	APTES-FeOx	-1.07693	5.74723	1.000	-19.4568	17.3030
Ser-FeOx	Gly-FeOx	.04928	5.74723	1.000	-18.3306	18.4292
	EDA-FeOx	-94.83238*	5.74723	.000	-113.2123	-76.4525
	TEPA-FeOx	-97.90404*	5.74723	.000	-116.2839	-79.5242
	ABA-FeOx	-.08427	5.74723	1.000	-18.4642	18.2956
	SAHBA-FeOx	.67236	5.74723	1.000	-17.7075	19.0522
	CMPVA-FeOx	-.00944	5.74723	1.000	-18.3893	18.3704
	APTS-FeOx	-2.09053	5.74723	1.000	-20.4704	16.2894
	APTES-FeOx	-1.02765	5.74723	1.000	-19.4075	17.3522
EDA-FeOx	Gly-FeOx	94.88166*	5.74723	.000	76.5018	113.2615
	Ser-FeOx	94.83238*	5.74723	.000	76.4525	113.2123
	TEPA-FeOx	-3.07166	5.74723	1.000	-21.4516	15.3082
	ABA-FeOx	94.74811*	5.74723	.000	76.3682	113.1280
	SAHBA-FeOx	95.50474*	5.74723	.000	77.1248	113.8846
	CMPVA-FeOx	94.82294*	5.74723	.000	76.4430	113.2028
	APTS-FeOx	92.74185*	5.74723	.000	74.3620	111.1217
	APTES-FeOx	93.80473*	5.74723	.000	75.4248	112.1846
TEPA-FeOx	Gly-FeOx	97.95332*	5.74723	.000	79.5734	116.3332
	Ser-FeOx	97.90404*	5.74723	.000	79.5242	116.2839
	EDA-FeOx	3.07166	5.74723	1.000	-15.3082	21.4516
	ABA-FeOx	97.81977*	5.74723	.000	79.4399	116.1997
	SAHBA-FeOx	98.57640*	5.74723	.000	80.1965	116.9563
	CMPVA-FeOx	97.89460*	5.74723	.000	79.5147	116.2745
	APTS-FeOx	95.81351*	5.74723	.000	77.4336	114.1934
	APTES-FeOx	96.87639*	5.74723	.000	78.4965	115.2563
ABA-FeOx	Gly-FeOx	.13355	5.74723	1.000	-18.2463	18.5134
	Ser-FeOx	.08427	5.74723	1.000	-18.2956	18.4642

	EDA-FeOx	-94.74811*	5.74723	.000	-113.1280	-76.3682
	TEPA-FeOx	-97.81977*	5.74723	.000	-116.1997	-79.4399
	SAHBA-FeOx	.75663	5.74723	1.000	-17.6233	19.1365
	CMPVA-FeOx	.07483	5.74723	1.000	-18.3051	18.4547
	APTS-FeOx	-2.00625	5.74723	1.000	-20.3861	16.3736
	APTES-FeOx	-.94338	5.74723	1.000	-19.3233	17.4365
SAHBA-FeOx	Gly-FeOx	-.62308	5.74723	1.000	-19.0030	17.7568
	Ser-FeOx	-.67236	5.74723	1.000	-19.0522	17.7075
	EDA-FeOx	-95.50474*	5.74723	.000	-113.8846	-77.1248
	TEPA-FeOx	-98.57640*	5.74723	.000	-116.9563	-80.1965
	ABA-FeOx	-.75663	5.74723	1.000	-19.1365	17.6233
	CMPVA-FeOx	-.68180	5.74723	1.000	-19.0617	17.6981
	APTS-FeOx	-2.76289	5.74723	1.000	-21.1428	15.6170
	APTES-FeOx	-1.70001	5.74723	1.000	-20.0799	16.6799
CMPVA-FeOx	Gly-FeOx	.05872	5.74723	1.000	-18.3212	18.4386
	Ser-FeOx	.00944	5.74723	1.000	-18.3704	18.3893
	EDA-FeOx	-94.82294*	5.74723	.000	-113.2028	-76.4430
	TEPA-FeOx	-97.89460*	5.74723	.000	-116.2745	-79.5147
	ABA-FeOx	-.07483	5.74723	1.000	-18.4547	18.3051
	SAHBA-FeOx	.68180	5.74723	1.000	-17.6981	19.0617
	APTS-FeOx	-2.08109	5.74723	1.000	-20.4610	16.2988
	APTES-FeOx	-1.01821	5.74723	1.000	-19.3981	17.3617
APTS-FeOx	Gly-FeOx	2.13980	5.74723	1.000	-16.2401	20.5197
	Ser-FeOx	2.09053	5.74723	1.000	-16.2894	20.4704
	EDA-FeOx	-92.74185*	5.74723	.000	-111.1217	-74.3620
	TEPA-FeOx	-95.81351*	5.74723	.000	-114.1934	-77.4336
	ABA-FeOx	2.00625	5.74723	1.000	-16.3736	20.3861
	SAHBA-FeOx	2.76289	5.74723	1.000	-15.6170	21.1428
	CMPVA-FeOx	2.08109	5.74723	1.000	-16.2988	20.4610
	APTES-FeOx	1.06288	5.74723	1.000	-17.3170	19.4428
APTES-FeOx	Gly-FeOx	1.07693	5.74723	1.000	-17.3030	19.4568
	Ser-FeOx	1.02765	5.74723	1.000	-17.3522	19.4075
	EDA-FeOx	-93.80473*	5.74723	.000	-112.1846	-75.4248
	TEPA-FeOx	-96.87639*	5.74723	.000	-115.2563	-78.4965
	ABA-FeOx	.94338	5.74723	1.000	-17.4365	19.3233
	SAHBA-FeOx	1.70001	5.74723	1.000	-16.6799	20.0799
	CMPVA-FeOx	1.01821	5.74723	1.000	-17.3617	19.3981
	APTS-FeOx	-1.06288	5.74723	1.000	-19.4428	17.3170

*. The mean difference is significant at the 0.05 level.

Table A5. Tukey HSD post-hoc tests results for cell uptake study based on percent uptake values.

(I) Treatment	(J) Treatment	Mean Difference (I-J)	Std. Error	Sig.	95% Confidence Interval	
					Lower Bound	Upper Bound
Gly-FeOx	Ser-FeOx	.11041	3.76681	1.000	-11.9360	12.1568
	EDA-FeOx	-71.26792*	3.76681	.000	-83.3143	-59.2215
	TEPA-FeOx	-40.79442*	3.76681	.000	-52.8408	-28.7480
	ABA-FeOx	.03437	3.76681	1.000	-12.0120	12.0808
	SAHBA-FeOx	.26779	3.76681	1.000	-11.7786	12.3142
	CMPVA-FeOx	.05358	3.76681	1.000	-11.9928	12.1000

	APTS-FeOx	-.45355	3.76681	1.000	-12.5000	11.5929
	APTES-FeOx	-.06224	3.76681	1.000	-12.1086	11.9842
Ser-FeOx	Gly-FeOx	-.11041	3.76681	1.000	-12.1568	11.9360
	EDA-FeOx	-71.37834*	3.76681	.000	-83.4247	-59.3319
	TEPA-FeOx	-40.90483*	3.76681	.000	-52.9512	-28.8584
	ABA-FeOx	-.07604	3.76681	1.000	-12.1225	11.9704
	SAHBA-FeOx	.15738	3.76681	1.000	-11.8890	12.2038
	CMPVA-FeOx	-.05683	3.76681	1.000	-12.1032	11.9896
	APTS-FeOx	-.56396	3.76681	1.000	-12.6104	11.4825
	APTES-FeOx	-.17265	3.76681	1.000	-12.2191	11.8738
EDA-FeOx	Gly-FeOx	71.26792*	3.76681	.000	59.2215	83.3143
	Ser-FeOx	71.37834*	3.76681	.000	59.3319	83.4247
	TEPA-FeOx	30.47351*	3.76681	.000	18.4271	42.5199
	ABA-FeOx	71.30229*	3.76681	.000	59.2559	83.3487
	SAHBA-FeOx	71.53571*	3.76681	.000	59.4893	83.5821
	CMPVA-FeOx	71.32151*	3.76681	.000	59.2751	83.3679
	APTS-FeOx	70.81438*	3.76681	.000	58.7680	82.8608
	APTES-FeOx	71.20569*	3.76681	.000	59.1593	83.2521
TEPA-FeOx	Gly-FeOx	40.79442*	3.76681	.000	28.7480	52.8408
	Ser-FeOx	40.90483*	3.76681	.000	28.8584	52.9512
	EDA-FeOx	-30.47351*	3.76681	.000	-42.5199	-18.4271
	ABA-FeOx	40.82879*	3.76681	.000	28.7824	52.8752
	SAHBA-FeOx	41.06220*	3.76681	.000	29.0158	53.1086
	CMPVA-FeOx	40.84800*	3.76681	.000	28.8016	52.8944
	APTS-FeOx	40.34087*	3.76681	.000	28.2945	52.3873
	APTES-FeOx	40.73218*	3.76681	.000	28.6858	52.7786
ABA-FeOx	Gly-FeOx	-.03437	3.76681	1.000	-12.0808	12.0120
	Ser-FeOx	.07604	3.76681	1.000	-11.9704	12.1225
	EDA-FeOx	-71.30229*	3.76681	.000	-83.3487	-59.2559
	TEPA-FeOx	-40.82879*	3.76681	.000	-52.8752	-28.7824
	SAHBA-FeOx	.23342	3.76681	1.000	-11.8130	12.2798
	CMPVA-FeOx	.01921	3.76681	1.000	-12.0272	12.0656
	APTS-FeOx	-.48792	3.76681	1.000	-12.5343	11.5585
	APTES-FeOx	-.09661	3.76681	1.000	-12.1430	11.9498
SAHBA-FeOx	Gly-FeOx	-.26779	3.76681	1.000	-12.3142	11.7786
	Ser-FeOx	-.15738	3.76681	1.000	-12.2038	11.8890
	EDA-FeOx	-71.53571*	3.76681	.000	-83.5821	-59.4893
	TEPA-FeOx	-41.06220*	3.76681	.000	-53.1086	-29.0158
	ABA-FeOx	-.23342	3.76681	1.000	-12.2798	11.8130
	CMPVA-FeOx	-.21420	3.76681	1.000	-12.2606	11.8322
	APTS-FeOx	-.72133	3.76681	1.000	-12.7677	11.3251
	APTES-FeOx	-.33002	3.76681	1.000	-12.3764	11.7164
CMPVA-FeOx	Gly-FeOx	-.05358	3.76681	1.000	-12.1000	11.9928
	Ser-FeOx	.05683	3.76681	1.000	-11.9896	12.1032
	EDA-FeOx	-71.32151*	3.76681	.000	-83.3679	-59.2751
	TEPA-FeOx	-40.84800*	3.76681	.000	-52.8944	-28.8016
	ABA-FeOx	-.01921	3.76681	1.000	-12.0656	12.0272
	SAHBA-FeOx	.21420	3.76681	1.000	-11.8322	12.2606
	APTS-FeOx	-.50713	3.76681	1.000	-12.5535	11.5393
	APTES-FeOx	-.11582	3.76681	1.000	-12.1622	11.9306
APTS-FeOx	Gly-FeOx	.45355	3.76681	1.000	-11.5929	12.5000
	Ser-FeOx	.56396	3.76681	1.000	-11.4825	12.6104
	EDA-FeOx	-70.81438*	3.76681	.000	-82.8608	-58.7680
	TEPA-FeOx	-40.34087*	3.76681	.000	-52.3873	-28.2945
	ABA-FeOx	.48792	3.76681	1.000	-11.5585	12.5343
	SAHBA-FeOx	.72133	3.76681	1.000	-11.3251	12.7677

	CMPVA-FeOx	.50713	3.76681	1.000	-11.5393	12.5535
	APTES-FeOx	.39131	3.76681	1.000	-11.6551	12.4377
APTES-FeOx	Gly-FeOx	.06224	3.76681	1.000	-11.9842	12.1086
	Ser-FeOx	.17265	3.76681	1.000	-11.8738	12.2191
	EDA-FeOx	-71.20569*	3.76681	.000	-83.2521	-59.1593
	TEPA-FeOx	-40.73218*	3.76681	.000	-52.7786	-28.6858
	ABA-FeOx	.09661	3.76681	1.000	-11.9498	12.1430
	SAHBA-FeOx	.33002	3.76681	1.000	-11.7164	12.3764
	CMPVA-FeOx	.11582	3.76681	1.000	-11.9306	12.1622
	APTS-FeOx	-.39131	3.76681	1.000	-12.4377	11.6551

*. The mean difference is significant at the 0.05 level.

Table A6. Descriptives for WST-1 cell proliferation assay at 24 hours.

	N	Mean	Std. Deviation	Std. Error	95% Confidence Interval for Mean		Minimum	Maximum
					Lower Bound	Upper Bound		
PBS	6	100.0000	3.11791	1.27288	96.7280	103.2720	95.67	104.30
Gly-FeOx	6	103.9668	2.43660	.99474	101.4097	106.5238	100.27	107.10
Ser-FeOx	6	103.6124	4.09556	1.67200	99.3143	107.9104	98.29	109.01
EDA-FeOx	6	104.1469	4.57737	1.86870	99.3432	108.9505	98.71	112.01
TEPA-FeOx	6	7.4513	1.03709	.42339	6.3629	8.5397	6.27	9.16
ABA-FeOx	6	102.0611	2.10804	.86061	99.8488	104.2733	98.78	104.45
SAHBA-FeOx	5	109.1063	3.50315	1.56666	104.7565	113.4560	103.93	111.86
CMPVA-FeOx	6	97.3286	3.54828	1.44858	93.6049	101.0523	92.98	102.38
APTS-FeOx	4	96.1010	17.67964	8.83982	67.9688	124.2333	69.67	106.72
APTES-FeOx	4	99.5506	35.46892	17.73446	43.1117	155.9896	47.06	122.74
Total	55	91.6280	31.46880	4.24325	83.1208	100.1352	6.27	122.74

Table A7. Descriptives for WST-1 cell proliferation assay at 48 hours.

	N	Mean	Std. Deviation	Std. Error	95% Confidence Interval for Mean		Minimum	Maximum
					Lower Bound	Upper Bound		
PBS	4	100.0000	17.95642	8.97821	71.4273	128.5727	74.86	114.99
Gly-FeOx	4	101.8516	18.16914	9.08457	72.9404	130.7627	79.07	118.77
Ser-FeOx	5	97.7795	20.18831	9.02849	72.7124	122.8466	67.57	123.76
EDA-FeOx	6	65.8497	9.11565	3.72145	56.2834	75.4160	56.20	82.92
TEPA-FeOx	6	8.4482	.97988	.40003	7.4198	9.4765	7.34	10.16
ABA-FeOx	5	90.8483	18.15668	8.11991	68.3038	113.3928	73.24	114.86
SAHBA-FeOx	4	94.9261	9.50615	4.75308	79.7997	110.0525	84.81	107.05
CMPVA-FeOx	6	98.2567	3.55627	1.45184	94.5246	101.9888	92.62	102.96
APTS-FeOx	6	108.2573	6.61101	2.69893	101.3194	115.1951	100.92	118.97
APTES-FeOx	6	96.7339	8.62068	3.51938	87.6871	105.7808	80.71	103.41
Total	52	84.5293	31.97574	4.43424	75.6272	93.4314	7.34	123.76

Table A8. ANOVA values for cell proliferation WST-1 assay at 24 and 48 hours.

	Sum of Squares	df	Mean Square	F	Sig.

Proliferation24	Between Groups	48357.024	9	5373.003	47.238	.000
	Within Groups	5118.400	45	113.742		
	Total	53475.424	54			
Proliferation48	Between Groups	45893.541	9	5099.282	34.260	.000
	Within Groups	6251.304	42	148.841		
	Total	52144.845	51			

Table A9. Tukey HSD post-hoc tests results for WST-1 cell proliferation assay at 24 hours.

(I) Treatment	(J) Treatment	Mean Difference (I-J)	Std. Error	Sig.	95% Confidence Interval	
					Lower Bound	Upper Bound
PBS	Gly-FeOx	-3.96677	6.15744	1.000	-24.4520	16.5185
	Ser-FeOx	-3.61236	6.15744	1.000	-24.0976	16.8729
	EDA-FeOx	-4.14688	6.15744	1.000	-24.6321	16.3384
	TEPA-FeOx	92.54869*	6.15744	.000	72.0635	113.0339
	ABA-FeOx	-2.06109	6.15744	1.000	-22.5463	18.4241
	SAHBA-FeOx	-9.10628	6.45798	.918	-30.5914	12.3788
	CMPVA-FeOx	2.67141	6.15744	1.000	-17.8138	23.1567
	APTS-FeOx	3.89897	6.88423	1.000	-19.0042	26.8022
	APTES-FeOx	.44937	6.88423	1.000	-22.4538	23.3526
Gly-FeOx	PBS	3.96677	6.15744	1.000	-16.5185	24.4520
	Ser-FeOx	.35441	6.15744	1.000	-20.1308	20.8396
	EDA-FeOx	-.18011	6.15744	1.000	-20.6653	20.3051
	TEPA-FeOx	96.51546*	6.15744	.000	76.0302	117.0007
	ABA-FeOx	1.90567	6.15744	1.000	-18.5796	22.3909
	SAHBA-FeOx	-5.13951	6.45798	.998	-26.6246	16.3456
	CMPVA-FeOx	6.63818	6.15744	.984	-13.8471	27.1234
	APTS-FeOx	7.86573	6.88423	.977	-15.0375	30.7689
	APTES-FeOx	4.41613	6.88423	1.000	-18.4871	27.3193
Ser-FeOx	PBS	3.61236	6.15744	1.000	-16.8729	24.0976
	Gly-FeOx	-.35441	6.15744	1.000	-20.8396	20.1308
	EDA-FeOx	-.53452	6.15744	1.000	-21.0198	19.9507
	TEPA-FeOx	96.16105*	6.15744	.000	75.6758	116.6463
	ABA-FeOx	1.55127	6.15744	1.000	-18.9340	22.0365
	SAHBA-FeOx	-5.49392	6.45798	.997	-26.9790	15.9912
	CMPVA-FeOx	6.28377	6.15744	.989	-14.2015	26.7690
	APTS-FeOx	7.51133	6.88423	.983	-15.3919	30.4145
	APTES-FeOx	4.06172	6.88423	1.000	-18.8415	26.9649
EDA-FeOx	PBS	4.14688	6.15744	1.000	-16.3384	24.6321
	Gly-FeOx	.18011	6.15744	1.000	-20.3051	20.6653
	Ser-FeOx	.53452	6.15744	1.000	-19.9507	21.0198
	TEPA-FeOx	96.69557*	6.15744	.000	76.2103	117.1808
	ABA-FeOx	2.08578	6.15744	1.000	-18.3995	22.5710
	SAHBA-FeOx	-4.95940	6.45798	.999	-26.4445	16.5257
	CMPVA-FeOx	6.81829	6.15744	.981	-13.6670	27.3035
	APTS-FeOx	8.04584	6.88423	.973	-14.8573	30.9490
	APTES-FeOx	4.59624	6.88423	1.000	-18.3069	27.4994
TEPA-FeOx	PBS	-92.54869*	6.15744	.000	-113.0339	-72.0635
	Gly-FeOx	-96.51546*	6.15744	.000	-117.0007	-76.0302

	Ser-FeOx	-96.16105*	6.15744	.000	-116.6463	-75.6758
	EDA-FeOx	-96.69557*	6.15744	.000	-117.1808	-76.2103
	ABA-FeOx	-94.60979*	6.15744	.000	-115.0950	-74.1245
	SAHBA-FeOx	-101.65497*	6.45798	.000	-123.1401	-80.1699
	CMPVA-FeOx	-89.87728*	6.15744	.000	-110.3625	-69.3920
	APTS-FeOx	-88.64973*	6.88423	.000	-111.5529	-65.7465
	APTES-FeOx	-92.09933*	6.88423	.000	-115.0025	-69.1961
ABA-FeOx	PBS	2.06109	6.15744	1.000	-18.4241	22.5463
	Gly-FeOx	-1.90567	6.15744	1.000	-22.3909	18.5796
	Ser-FeOx	-1.55127	6.15744	1.000	-22.0365	18.9340
	EDA-FeOx	-2.08578	6.15744	1.000	-22.5710	18.3995
	TEPA-FeOx	94.60979*	6.15744	.000	74.1245	115.0950
	SAHBA-FeOx	-7.04519	6.45798	.983	-28.5303	14.4399
	CMPVA-FeOx	4.73250	6.15744	.999	-15.7527	25.2177
	APTS-FeOx	5.96006	6.88423	.997	-16.9431	28.8633
	APTES-FeOx	2.51046	6.88423	1.000	-20.3927	25.4137
SAHBA-FeOx	PBS	9.10628	6.45798	.918	-12.3788	30.5914
	Gly-FeOx	5.13951	6.45798	.998	-16.3456	26.6246
	Ser-FeOx	5.49392	6.45798	.997	-15.9912	26.9790
	EDA-FeOx	4.95940	6.45798	.999	-16.5257	26.4445
	TEPA-FeOx	101.65497*	6.45798	.000	80.1699	123.1401
	ABA-FeOx	7.04519	6.45798	.983	-14.4399	28.5303
	CMPVA-FeOx	11.77769	6.45798	.717	-9.7074	33.2628
	APTS-FeOx	13.00525	7.15430	.721	-10.7964	36.8069
	APTES-FeOx	9.55565	7.15430	.940	-14.2461	33.3573
CMPVA-FeOx	PBS	-2.67141	6.15744	1.000	-23.1567	17.8138
	Gly-FeOx	-6.63818	6.15744	.984	-27.1234	13.8471
	Ser-FeOx	-6.28377	6.15744	.989	-26.7690	14.2015
	EDA-FeOx	-6.81829	6.15744	.981	-27.3035	13.6670
	TEPA-FeOx	89.87728*	6.15744	.000	69.3920	110.3625
	ABA-FeOx	-4.73250	6.15744	.999	-25.2177	15.7527
	SAHBA-FeOx	-11.77769	6.45798	.717	-33.2628	9.7074
	APTS-FeOx	1.22756	6.88423	1.000	-21.6756	24.1307
	APTES-FeOx	-2.22204	6.88423	1.000	-25.1252	20.6811
APTS-FeOx	PBS	-3.89897	6.88423	1.000	-26.8022	19.0042
	Gly-FeOx	-7.86573	6.88423	.977	-30.7689	15.0375
	Ser-FeOx	-7.51133	6.88423	.983	-30.4145	15.3919
	EDA-FeOx	-8.04584	6.88423	.973	-30.9490	14.8573
	TEPA-FeOx	88.64973*	6.88423	.000	65.7465	111.5529
	ABA-FeOx	-5.96006	6.88423	.997	-28.8633	16.9431
	SAHBA-FeOx	-13.00525	7.15430	.721	-36.8069	10.7964
	CMPVA-FeOx	-1.22756	6.88423	1.000	-24.1307	21.6756
	APTES-FeOx	-3.44960	7.54129	1.000	-28.5388	21.6396
APTES-FeOx	PBS	-.44937	6.88423	1.000	-23.3526	22.4538
	Gly-FeOx	-4.41613	6.88423	1.000	-27.3193	18.4871
	Ser-FeOx	-4.06172	6.88423	1.000	-26.9649	18.8415
	EDA-FeOx	-4.59624	6.88423	1.000	-27.4994	18.3069
	TEPA-FeOx	92.09933*	6.88423	.000	69.1961	115.0025
	ABA-FeOx	-2.51046	6.88423	1.000	-25.4137	20.3927
	SAHBA-FeOx	-9.55565	7.15430	.940	-33.3573	14.2461
	CMPVA-FeOx	2.22204	6.88423	1.000	-20.6811	25.1252
	APTS-FeOx	3.44960	7.54129	1.000	-21.6396	28.5388

*. The mean difference is significant at the 0.05 level.

Table A10. Dunnett two-sided post-hoc tests results for WST-1 cell proliferation assay at 24 hours.

(I) Treatment	(J) Treatment	Mean Difference (I-J)	Std. Error	Sig.	95% Confidence Interval	
					Lower Bound	Upper Bound
Gly-FeOx	PBS	3.96677	6.15744	.994	-13.3274	21.2609
Ser-FeOx	PBS	3.61236	6.15744	.997	-13.6818	20.9065
EDA-FeOx	PBS	4.14688	6.15744	.991	-13.1473	21.4410
TEPA-FeOx	PBS	-92.54869*	6.15744	.000	-109.8428	-75.2546
ABA-FeOx	PBS	2.06109	6.15744	1.000	-15.2331	19.3552
SAHBA-FeOx	PBS	9.10628	6.45798	.658	-9.0320	27.2445
CMPVA-FeOx	PBS	-2.67141	6.15744	1.000	-19.9656	14.6227
APTS-FeOx	PBS	-3.89897	6.88423	.997	-23.2344	15.4365
APTES-FeOx	PBS	-.44937	6.88423	1.000	-19.7848	18.8861

b. Dunnett t-tests treat one group as a control, and compare all other groups against it.

Table A11. Tukey HSD post-hoc tests results for WST-1 cell proliferation assay at 48 hours.

(I) Treatment	(J) Treatment	Mean Difference (I-J)	Std. Error	Sig.	95% Confidence Interval	
					Lower Bound	Upper Bound
PBS	Gly-FeOx	-1.85159	8.62672	1.000	-30.6548	26.9516
	Ser-FeOx	2.22047	8.18402	1.000	-25.1046	29.5456
	EDA-FeOx	34.15028*	7.87508	.003	7.8567	60.4439
	TEPA-FeOx	91.55184*	7.87508	.000	65.2582	117.8454
	ABA-FeOx	9.15172	8.18402	.980	-18.1734	36.4768
	SAHBA-FeOx	5.07392	8.62672	1.000	-23.7293	33.8771
	CMPVA-FeOx	1.74330	7.87508	1.000	-24.5503	28.0369
	APTS-FeOx	-8.25726	7.87508	.987	-34.5509	18.0363
	APTES-FeOx	3.26608	7.87508	1.000	-23.0275	29.5597
Gly-FeOx	PBS	1.85159	8.62672	1.000	-26.9516	30.6548
	Ser-FeOx	4.07205	8.18402	1.000	-23.2531	31.3972
	EDA-FeOx	36.00187*	7.87508	.002	9.7083	62.2955
	TEPA-FeOx	93.40343*	7.87508	.000	67.1098	119.6970
	ABA-FeOx	11.00330	8.18402	.937	-16.3218	38.3284
	SAHBA-FeOx	6.92551	8.62672	.998	-21.8777	35.7287
	CMPVA-FeOx	3.59489	7.87508	1.000	-22.6987	29.8885
	APTS-FeOx	-6.40567	7.87508	.998	-32.6993	19.8879
	APTES-FeOx	5.11766	7.87508	1.000	-21.1759	31.4113
Ser-FeOx	PBS	-2.22047	8.18402	1.000	-29.5456	25.1046
	Gly-FeOx	-4.07205	8.18402	1.000	-31.3972	23.2531
	EDA-FeOx	31.92981*	7.38748	.003	7.2642	56.5954
	TEPA-FeOx	89.33137*	7.38748	.000	64.6658	113.9970
	ABA-FeOx	6.93125	7.71597	.996	-18.8311	32.6936
	SAHBA-FeOx	2.85345	8.18402	1.000	-24.4717	30.1786
	CMPVA-FeOx	-.47716	7.38748	1.000	-25.1428	24.1884
	APTS-FeOx	-10.47773	7.38748	.915	-35.1433	14.1879
	APTES-FeOx	1.04561	7.38748	1.000	-23.6200	25.7112
EDA-FeOx	PBS	-34.15028*	7.87508	.003	-60.4439	-7.8567

	Gly-FeOx	-36.00187*	7.87508	.002	-62.2955	-9.7083
	Ser-FeOx	-31.92981*	7.38748	.003	-56.5954	-7.2642
	TEPA-FeOx	57.40156*	7.04369	.000	33.8838	80.9193
	ABA-FeOx	-24.99856*	7.38748	.045	-49.6642	-.3330
	SAHBA-FeOx	-29.07636*	7.87508	.020	-55.3700	-2.7828
	CMPVA-FeOx	-32.40698*	7.04369	.001	-55.9247	-8.8893
	APTS-FeOx	-42.40754*	7.04369	.000	-65.9253	-18.8898
	APTES-FeOx	-30.88420*	7.04369	.003	-54.4019	-7.3665
TEPA-FeOx	PBS	-91.55184*	7.87508	.000	-117.8454	-65.2582
	Gly-FeOx	-93.40343*	7.87508	.000	-119.6970	-67.1098
	Ser-FeOx	-89.33137*	7.38748	.000	-113.9970	-64.6658
	EDA-FeOx	-57.40156*	7.04369	.000	-80.9193	-33.8838
	ABA-FeOx	-82.40012*	7.38748	.000	-107.0657	-57.7345
	SAHBA-FeOx	-86.47792*	7.87508	.000	-112.7715	-60.1843
	CMPVA-FeOx	-89.80854*	7.04369	.000	-113.3263	-66.2908
	APTS-FeOx	-99.80910*	7.04369	.000	-123.3268	-76.2914
	APTES-FeOx	-88.28576*	7.04369	.000	-111.8035	-64.7680
ABA-FeOx	PBS	-9.15172	8.18402	.980	-36.4768	18.1734
	Gly-FeOx	-11.00330	8.18402	.937	-38.3284	16.3218
	Ser-FeOx	-6.93125	7.71597	.996	-32.6936	18.8311
	EDA-FeOx	24.99856*	7.38748	.045	.3330	49.6642
	TEPA-FeOx	82.40012*	7.38748	.000	57.7345	107.0657
	SAHBA-FeOx	-4.07780	8.18402	1.000	-31.4029	23.2473
	CMPVA-FeOx	-7.40841	7.38748	.990	-32.0740	17.2572
	APTS-FeOx	-17.40898	7.38748	.376	-42.0746	7.2566
	APTES-FeOx	-5.88564	7.38748	.998	-30.5512	18.7799
SAHBA-FeOx	PBS	-5.07392	8.62672	1.000	-33.8771	23.7293
	Gly-FeOx	-6.92551	8.62672	.998	-35.7287	21.8777
	Ser-FeOx	-2.85345	8.18402	1.000	-30.1786	24.4717
	EDA-FeOx	29.07636*	7.87508	.020	2.7828	55.3700
	TEPA-FeOx	86.47792*	7.87508	.000	60.1843	112.7715
	ABA-FeOx	4.07780	8.18402	1.000	-23.2473	31.4029
	CMPVA-FeOx	-3.33062	7.87508	1.000	-29.6242	22.9630
	APTS-FeOx	-13.33118	7.87508	.793	-39.6248	12.9624
	APTES-FeOx	-1.80784	7.87508	1.000	-28.1014	24.4858
CMPVA-FeOx	PBS	-1.74330	7.87508	1.000	-28.0369	24.5503
	Gly-FeOx	-3.59489	7.87508	1.000	-29.8885	22.6987
	Ser-FeOx	.47716	7.38748	1.000	-24.1884	25.1428
	EDA-FeOx	32.40698*	7.04369	.001	8.8893	55.9247
	TEPA-FeOx	89.80854*	7.04369	.000	66.2908	113.3263
	ABA-FeOx	7.40841	7.38748	.990	-17.2572	32.0740
	SAHBA-FeOx	3.33062	7.87508	1.000	-22.9630	29.6242
	APTS-FeOx	-10.00056	7.04369	.914	-33.5183	13.5172
	APTES-FeOx	1.52277	7.04369	1.000	-21.9949	25.0405
APTS-FeOx	PBS	8.25726	7.87508	.987	-18.0363	34.5509
	Gly-FeOx	6.40567	7.87508	.998	-19.8879	32.6993
	Ser-FeOx	10.47773	7.38748	.915	-14.1879	35.1433
	EDA-FeOx	42.40754*	7.04369	.000	18.8898	65.9253
	TEPA-FeOx	99.80910*	7.04369	.000	76.2914	123.3268
	ABA-FeOx	17.40898	7.38748	.376	-7.2566	42.0746
	SAHBA-FeOx	13.33118	7.87508	.793	-12.9624	39.6248
	CMPVA-FeOx	10.00056	7.04369	.914	-13.5172	33.5183
	APTES-FeOx	11.52334	7.04369	.823	-11.9944	35.0411
APTES-FeOx	PBS	-3.26608	7.87508	1.000	-29.5597	23.0275
	Gly-FeOx	-5.11766	7.87508	1.000	-31.4113	21.1759
	Ser-FeOx	-1.04561	7.38748	1.000	-25.7112	23.6200

	EDA-FeOx	30.88420*	7.04369	.003	7.3665	54.4019
	TEPA-FeOx	88.28576*	7.04369	.000	64.7680	111.8035
	ABA-FeOx	5.88564	7.38748	.998	-18.7799	30.5512
	SAHBA-FeOx	1.80784	7.87508	1.000	-24.4858	28.1014
	CMPVA-FeOx	-1.52277	7.04369	1.000	-25.0405	21.9949
	APTS-FeOx	-11.52334	7.04369	.823	-35.0411	11.9944

*. The mean difference is significant at the 0.05 level.

Table A12. Dunnett two-sided post-hoc tests results for WST-1 cell proliferation assay at 48 hours.

(I) Treatment	(J) Treatment	Mean Difference (I-J)	Std. Error	Sig.	95% Confidence Interval	
					Lower Bound	Upper Bound
Gly-FeOx	PBS	1.85159	8.62672	1.000	-22.0678	25.7710
Ser-FeOx	PBS	-2.22047	8.18402	1.000	-24.9124	20.4715
EDA-FeOx	PBS	-34.15028*	7.87508	.001	-55.9856	-12.3150
TEPA-FeOx	PBS	-91.55184*	7.87508	.000	-113.3871	-69.7165
ABA-FeOx	PBS	-9.15172	8.18402	.811	-31.8436	13.5402
SAHBA-FeOx	PBS	-5.07392	8.62672	.994	-28.9933	18.8455
CMPVA-FeOx	PBS	-1.74330	7.87508	1.000	-23.5786	20.0920
APTS-FeOx	PBS	8.25726	7.87508	.853	-13.5780	30.0926
APTES-FeOx	PBS	-3.26608	7.87508	1.000	-25.1014	18.5692

b. Dunnett t-tests treat one group as a control, and compare all other groups against it.

Table A13. Colony Assay Descriptive Statistics.

	N	Mean	Std. Deviation	Std. Error	95% Confidence Interval for Mean		Minimum	Maximum
					Lower Bound	Upper Bound		
No Particle - 0 min	6	100.017	26.4299	10.7899	72.280	127.753	66.1	137.6
Particle - 0 min	6	87.167	14.2152	5.8033	72.249	102.085	68.8	110.1
Extra Particle - 0 min	6	89.900	12.6366	5.1589	76.639	103.161	74.3	110.1
No Particle - 10 min	6	100.450	19.2761	7.8694	80.221	120.679	77.1	132.1
Particle - 10 min	6	62.850	13.4213	5.4792	48.765	76.935	44.0	85.3
Extra Particle - 10 min	6	55.033	10.8971	4.4487	43.598	66.469	44.0	71.6
No Particle - 15 min	6	107.333	22.4136	9.1503	83.812	130.855	71.6	137.6
Particle - 15 min	6	53.667	9.9631	4.0674	43.211	64.122	35.8	63.3

Extra Particle - 15 min	6	26.600	7.0798	2.8903	19.170	34.030	13.8	33.0
Total	54	75.891	30.1153	4.0982	67.671	84.111	13.8	137.6

Table A14. Colony Assay ANOVA Results.

	Sum of Squares	df	Mean Square	F	Sig.
Between Groups	36155.034	8	4519.379	17.072	.000
Within Groups	11912.472	45	264.722		
Total	48067.505	53			

Table A15. Colony Assay Dunnett (2-sided) Post Hoc Test Results.

Multiple Comparisons

Dependent Variable: Survival

Dunnett t (2-sided)[a]

(I) Group	(J) Group	Mean Difference (I-J)	Std. Error	Sig.	95% Confidence Interval	
					Lower Bound	Upper Bound
Particle - 0 min	No Particle - 0 min	-12.8500	9.3936	.644	-38.778	13.078
Extra Particle - 0 min	No Particle - 0 min	-10.1167	9.3936	.841	-36.045	15.811
No Particle - 10 min	No Particle - 0 min	.4333	9.3936	1.000	-25.495	26.361
Particle - 10 min	No Particle - 0 min	-37.1667*	9.3936	.002	-63.095	-11.239
Extra Particle - 10 min	No Particle - 0 min	-44.9833*	9.3936	.000	-70.911	-19.055
No Particle - 15 min	No Particle - 0 min	7.3167	9.3936	.965	-18.611	33.245
Particle - 15 min	No Particle - 0 min	-46.3500*	9.3936	.000	-72.278	-20.422
Extra Particle - 15 min	No Particle - 0 min	-73.4167*	9.3936	.000	-99.345	-47.489

*. The mean difference is significant at the 0.05 level.

a. Dunnett t-tests treat one group as a control, and compare all other groups against it.

Table A16. Colony Assay Tukey HSD Post Hoc Test Results.

Multiple Comparisons

Dependent Variable: Survival

(I) Group	(J) Group	Mean Difference (I-J)	Std. Error	Sig.	95% Confidence Interval	
					Lower Bound	Upper Bound
No Particle - 0 min	Particle - 0 min	12.8500	9.3936	.904	-17.746	43.446
	Extra Particle - 0 min	10.1167	9.3936	.975	-20.480	40.713
	No Particle - 10 min	-.4333	9.3936	1.000	-31.030	30.163
	Particle - 10 min	37.1667*	9.3936	.007	6.570	67.763
	Extra Particle - 10 min	44.9833*	9.3936	.001	14.387	75.580
	No Particle - 15 min	-7.3167	9.3936	.997	-37.913	23.280
	Particle - 15 min	46.3500*	9.3936	.000	15.754	76.946
	Extra Particle - 15 min	73.4167*	9.3936	.000	42.820	104.013
Particle - 0 min	No Particle - 0 min	-12.8500	9.3936	.904	-43.446	17.746
	Extra Particle - 0 min	-2.7333	9.3936	1.000	-33.330	27.863
	No Particle - 10 min	-13.2833	9.3936	.886	-43.880	17.313
	Particle - 10 min	24.3167	9.3936	.220	-6.280	54.913
	Extra Particle - 10 min	32.1333*	9.3936	.033	1.537	62.730
	No Particle - 15 min	-20.1667	9.3936	.456	-50.763	10.430
	Particle - 15 min	33.5000*	9.3936	.022	2.904	64.096
	Extra Particle - 15 min	60.5667*	9.3936	.000	29.970	91.163
Extra Particle - 0 min	No Particle - 0 min	-10.1167	9.3936	.975	-40.713	20.480
	Particle - 0 min	2.7333	9.3936	1.000	-27.863	33.330
	No Particle - 10 min	-10.5500	9.3936	.967	-41.146	20.046
	Particle - 10 min	27.0500	9.3936	.121	-3.546	57.646
	Extra Particle - 10 min	34.8667*	9.3936	.015	4.270	65.463
	No Particle - 15 min	-17.4333	9.3936	.646	-48.030	13.163
	Particle - 15 min	36.2333*	9.3936	.010	5.637	66.830
	Extra Particle - 15 min	63.3000*	9.3936	.000	32.704	93.896
No Particle - 10 min	No Particle - 0 min	.4333	9.3936	1.000	-30.163	31.030
	Particle - 0 min	13.2833	9.3936	.886	-17.313	43.880
	Extra Particle - 0 min	10.5500	9.3936	.967	-20.046	41.146
	Particle - 10 min	37.6000*	9.3936	.007	7.004	68.196
	Extra Particle - 10 min	45.4167*	9.3936	.001	14.820	76.013
	No Particle - 15 min	-6.8833	9.3936	.998	-37.480	23.713
	Particle - 15 min	46.7833*	9.3936	.000	16.187	77.380
	Extra Particle - 15 min	73.8500*	9.3936	.000	43.254	104.446
Particle - 10 min	No Particle - 0 min	-37.1667*	9.3936	.007	-67.763	-6.570
	Particle - 0 min	-24.3167	9.3936	.220	-54.913	6.280
	Extra Particle - 0 min	-27.0500	9.3936	.121	-57.646	3.546
	No Particle - 10 min	-37.6000*	9.3936	.007	-68.196	-7.004
	Extra Particle - 10 min	7.8167	9.3936	.995	-22.780	38.413
	No Particle - 15 min	-44.4833*	9.3936	.001	-75.080	-13.887

	Particle - 15 min	9.1833	9.3936	.986	-21.413	39.780
	Extra Particle - 15 min	36.2500*	9.3936	.010	5.654	66.846
Extra Particle - 10 min	No Particle - 0 min	-44.9833*	9.3936	.001	-75.580	-14.387
	Particle - 0 min	-32.1333*	9.3936	.033	-62.730	-1.537
	Extra Particle - 0 min	-34.8667*	9.3936	.015	-65.463	-4.270
	No Particle - 10 min	-45.4167*	9.3936	.001	-76.013	-14.820
	Particle - 10 min	-7.8167	9.3936	.995	-38.413	22.780
	No Particle - 15 min	-52.3000*	9.3936	.000	-82.896	-21.704
	Particle - 15 min	1.3667	9.3936	1.000	-29.230	31.963
	Extra Particle - 15 min	28.4333	9.3936	.087	-2.163	59.030
No Particle - 15 min	No Particle - 0 min	7.3167	9.3936	.997	-23.280	37.913
	Particle - 0 min	20.1667	9.3936	.456	-10.430	50.763
	Extra Particle - 0 min	17.4333	9.3936	.646	-13.163	48.030
	No Particle - 10 min	6.8833	9.3936	.998	-23.713	37.480
	Particle - 10 min	44.4833*	9.3936	.001	13.887	75.080
	Extra Particle - 10 min	52.3000*	9.3936	.000	21.704	82.896
	Particle - 15 min	53.6667*	9.3936	.000	23.070	84.263
	Extra Particle - 15 min	80.7333*	9.3936	.000	50.137	111.330
Particle - 15 min	No Particle - 0 min	-46.3500*	9.3936	.000	-76.946	-15.754
	Particle - 0 min	-33.5000*	9.3936	.022	-64.096	-2.904
	Extra Particle - 0 min	-36.2333*	9.3936	.010	-66.830	-5.637
	No Particle - 10 min	-46.7833*	9.3936	.000	-77.380	-16.187
	Particle - 10 min	-9.1833	9.3936	.986	-39.780	21.413
	Extra Particle - 10 min	-1.3667	9.3936	1.000	-31.963	29.230
	No Particle - 15 min	-53.6667*	9.3936	.000	-84.263	-23.070
	Extra Particle - 15 min	27.0667	9.3936	.121	-3.530	57.663
Extra Particle - 15 min	No Particle - 0 min	-73.4167*	9.3936	.000	-104.013	-42.820
	Particle - 0 min	-60.5667*	9.3936	.000	-91.163	-29.970
	Extra Particle - 0 min	-63.3000*	9.3936	.000	-93.896	-32.704
	No Particle - 10 min	-73.8500*	9.3936	.000	-104.446	-43.254
	Particle - 10 min	-36.2500*	9.3936	.010	-66.846	-5.654
	Extra Particle - 10 min	-28.4333	9.3936	.087	-59.030	2.163
	No Particle - 15 min	-80.7333*	9.3936	.000	-111.330	-50.137
	Particle - 15 min	-27.0667	9.3936	.121	-57.663	3.530

*. The mean difference is significant at the 0.05 level.

Table A17. The means and medians for survival time of each treatment group.

Treatment	Mean[a]				Median			
	Estimate	Std. Error	95% Confidence Interval		Estimate	Std. Error	95% Confidence Interval	
			Lower Bound	Upper Bound			Lower Bound	Upper Bound
PBS	29.375	1.085	27.249	31.501	28.000	.943	26.152	29.848
FeOx	26.625	.844	24.971	28.279	26.000	1.414	23.228	28.772
^{177}Lu-DOTA	31.375	.905	29.601	33.149	31.000	.306	30.400	31.600

^{177}Lu-D-SAHBA-FeOx	46.625	7.486	31.953	61.297	40.000	3.423	33.290	46.710
1^{77}Lu-D-CMPVA-FeOx	43.250	2.724	37.911	48.589	42.000	1.369	39.316	44.684
Overall	35.450	2.000	31.529	39.371	31.000	1.054	28.934	33.066

a. Estimation is limited to the largest survival time if it is censored.

Table A18. Results of pairwise comparison of log rank (Mantel-Cox) test for each treatment in the survival study.

Treatment	**PBS**		**FeOx**		**177Lu-DOTA**		**177Lu-D-SAHBA-FeOx**		**177Lu-D-CMPVA-FeOx**	
	Chi-Square	Sig.	Chi-Square	Sig.	Chi-Square	Sig.	Chi-Square	Sig.	Chi-Square	Sig.
PBS			3.586	.058	1.079	.299	12.479	.000	16.964	.000
FeOx	3.586	.058			12.494	.000	16.897	.000	16.897	.000
^{177}Lu-DOTA	1.079	.299	12.494	.000			11.396	.001	13.327	.000
^{177}Lu-D-SAHBA-FeOx	12.479	.000	16.897	.000	11.396	.001			.007	.933
^{177}Lu-D-CMPVA-FeOx	16.964	.000	16.897	.000	13.327	.000	.007	.933		

Vita

Stanley Eugene Gilliland III was born in Nashville, Tennessee on June 16, 1989 and is an American Citizen. He is a member of the Seneca-Cayuga Tribe of Oklahoma. In June 2007, he graduated from Bluestone Senior High School in Skipwith, Virginia. After high school, he attended James Madison University in Harrisonburg, Virginia where he received his Bachelor of Science in Biotechnology in December of 2010. In August 2011, he entered the Nanoscience and Nanotechnology PhD program at Virginia Commonwealth University. During his graduate studies he completed a MS degree in December of 2014.